University of Strathclyde
Engineering

Monitoring of Electrical Resistivity Changes in the Ground Laboratory Model Caused by Diesel Spillage and Injetion of Oxygen Release Compound

Antonio Montinaro

Submitted by Antonio Montinaro to the Civil Engineering Department, University of Strathclyde in part completion of the requirements for the MPhil in Geo-environmental Studies.

I, Antonio Montinaro, hereby state that this report is my own work and that all sources used are made explicit in the text.

September 2008

Abstract

The aim of this research is to verify the effectiveness of the electrical resistivity method in the study and monitoring of the pollutant dispersion and migration in the soil. In this particular study, Diesel has been used as the detection pollutant and a laboratory model was created in a tank comprised of a bottom clay layer covered by a sandy layer. Two narrow sectors separated by a permeable screen was included to allow permanent groundwater flow through the soil. In addiction, a permeable reactive barrier was made in the model with an oxygen release compound (i.e. ORC-Advanced by Regenesis®). When the model was used in the laboratory a mini electrical resistivity array was used to monitor the electrical resistivity properties that the media displayed.

In the laboratory model the pollutant was spilt on the top of the sandy layer on the left hand side and on the bottom of the sandy layer in the centre. This allowed simulation of very different situations and to study how these differences influence the migration and distribution dynamics of the pollutant.

Subsequently, the permeable reactive barrier was put in place by injecting an Oxygen Release Compound (i.e. ORC-Adv) in 24 mini boreholes along a cross section in the middle of the model tank.

Data concerning Dissolved Oxygen, pH and Conductivity of the water used in the laboratory model were collected with field probes and subjected to laboratory investigation. Apparent electrical resistivity was measured using an electrical resistivity meter and all data were analysed also using statistical analyses.

During the study period changes in electrical resistivity caused by pollutant dispersion in the sandy layer, water level fluctuations and presence of the reactive barrier were observed in detail. Data analysis showed that the electrical resistivity investigation method clearly detected the changes in resistivity due to pollutant spillage, influence of water level fluctuation, path of pollutant dispersion and effects of the permeable reactive barrier. The results of this study are summarized using graphs and several electrical resistivity images supported by RES2DINV® software.

Acknowledgments

I am sincerely grateful to Dr. Philippe Sentenac who, from the very beginning, has been an excellent supervisor, dedicating his time and enthusiasm to supporting my studies.
In this list of thanks I would like to mention a number of people for their contributions to this study:

- Dr. Franco Mazzotta and the *'Effemme' Chemical Laboratory* staff in Italy who provided the chemical analysis of water and soil samples and technical-scientific comment.

- Mr. Marcin Zielinski (*Ph.D. student*) for providing part of the material (clay soil) and technical information (soil geo-technical characteristics) which were central to my study; he also gave very good advice and I especially appreciate our chats over a cup of coffee at the end of the day.

- The technical staff of the Hydraulic Laboratory: Alex Brown (*Senior Technical Director of Resources & Facilities*), John Carlin, Christopher Bonner and Derek McNee (*Technicians),* and John Redgate (*Senior Electronics Technician*) with whom I spent much of my research time in Glasgow. I am grateful for their practical advice, technical solutions and, above all, for their high professionalism which made it possible build the physical laboratory model.

- The technical staff of the Environmental Laboratory: Francis McGilligan, Gavin Gibson and Gerry Carr (*Technicians*) for their valuable contributions towards the determination and evaluation of chemical-physical water parameters.

Table of Contents

Index

List of Figures

List of Tables

Chapter 1: Introduction

For decades humans have used the land for their own subsistence and civil-industrial development, generating wide areas that are highly polluted and of little further use. Future infrastructure expansion will not be sustainable if new, as yet uncontaminated areas of land are developed. As a result, recent national policies and new legislative directives (e.g. Part 2A of the Environmental Protection Act 1990; Contaminated Land Regulation 2000 and 2006 n° 1380; Landfill Directive 2004; Town and Country Planning Acts 2005; Radiactive Contaminated land Regulation 2006 n° 1379 etc.) focus on encouraging the reuse of contaminated land that has already been devastated and declared not suitable for living.

Land is defined as contaminated when any substance in a solid, liquid or gas phase is present in the soil, water, air or biomass in elevated concentrations such that it poses a threat to the whole ecosystem (Environmental Protection 2006). For this reason the need to correctly identify the presence of any dangerous substance in the environment is of vital importance; it is essential to map its spatial distribution, the kind of interactions it has with other environmental components (e.g. soil; water; air; etc.) and its transformations and distribution over time.

Contaminated land studies use several techniques to determine the source of a pollutant, its distribution in the environment and its pathway, thereby identifying potential risks to targets (e.g. workers, the general public, animals and plants etc.).

Most of these techniques are invasive (e.g. trial pit; boreholes; soil and water sampling etc.) and generally interact directly with the pollutant, giving point information about its concentration and risk. Subsequent evaluations are used to estimate its wider distribution within a certain accuracy margin.

In contrast to the techniques mentioned above, *electrical resistivity surveys* belong to the group of environmental geophysical methods that are defined as non-invasive or minimally invasive methods (e.g. resistivity method; electromagnetic method; radio or audio magnetotelluric method; ground probing radar method etc.).

Using this type of approach it is possible to identify pollutant presence, spatial dispersion in the soil over time and the effects of the remediation process (i.e. a permeable reactive barrier). All this can be done without interacting with or removing the dangerous substances.

The effectiveness of electrical resistivity survey method depends on several factors (Carrara et al. 2004; Loke 2001; Reynolds 1995). These factors include subsurface soil characteristics, water presence, and type of pollutant. The most important factor of this survey method is the effect on the electrical resistivity values of other substances present in the ground and on the materials that constitute the soil subsurface.

The aim of this study is to firstly identify a specific pollutant (i.e.diesel) in a physical laboratory model using the electrical resistivity method. The second part of this study will examine the distribution and evolution of the pollutant in the laboratory model over time. The third part of this study will monitor the changes in electrical resistivity in the model due to the injection of an Oxigen Release Compound (i.e. ORC-Adv).

This study continues and integrates the scientific work developed during the previous Master Research in Geo-environmentantal Engineering with title '*Monitoring Pollutant Plume (i.e. Diesel) in the ground Laboratory Model using Electrical Resistivity Array and Geographic Information System (G.I.S.)' (Montinaro A. 2007)*.

All the previously recorded data has been reviewed; new data has been acquired, analysed and new aspects of the research have been developed.

The physical ground laboratory model was built, comprising of a tank (270 x 60 x 45 cm) layered with two different kinds of soil (i.e. clay and sand). The model was subjected to continuous water flow that simulated free groundwater and divided the sandy layer into an inferior saturated portion and a superior unsaturated portion.

The diesel pollutant was leaked into the model both on the surface and on the bottom of the saturated zone in order to simulate two extreme kinds of leakage. The behaviour and spatial distribution of the diesel during this study period was analysed.

The electrical resistivity values of the analysis were measured, at regular intervals using an electrical array that was made with mini-electrodes (i.e. 5 cm long) connected by a multi-cable to the resistivity meter. The data was analysed using statistical analysis and inverse analysis. The results obtained are plotted on graphs and visualised by 2-D resistivity images.

1.1. Literature Review

The potential difference measured when an electric current with intensity, ***I*** passes through a material is determined by its chemical and physical properties.

This phenomenon has been used since the early twentieth century in several practical applications. The first studies identified variability in soil conductivity by fixing two electrodes in the surface layer and moving two other electrodes in order to measure the potential difference in the soil (Peterson 1907; Bergstrom 1913).

Subsequently, in 1912 Conrad Schlumberger in Europe and, at almost the same time, Wenner in the USA made significant advances in developing scientific and mathematical approaches to geo-physical prospecting surveys using information related to the electrical resistivity of the soil subsurface in one dimension (i.e. 1-D electrical resistivity) (Schlumberger 1920; Kunetz 1966).

Electrical resistivity values at different depths are measured by moving a set of four electrodes at constant distance along a line through the subsurface or by changing the distance between the electrodes (Gish and Rooney 1925).

Using matching curves, apparent resistivity values were plotted on a logarithmic scale which allowed geological sequences with several strata to be interpolated (Stefanescu et al, 1930; Langer 1933; Flathe 1955). This technique was developed much further in the 1970s with the advent of computer science (Ghosh 1971). The

Inverse Linear Theory was the basis of automatic *Inversion Method* software developed during subsequent years (Joansen 1977; Christensen 1986).

In the 1980s electrical resistivity data collection was exclusively manual; four electrodes were moved along the soil surface for each point of data measurement. The use of multi-electrode systems led to easier data collection, however, a manually operated switching system was still necessary (Barker 1981).

Computer controlled systems with automatic measurement and checking of data quality were critical in using this technique to carry out geo-electrical surveys for geo-physics prospecting and other practical applications (Overmeeren and Ritsema 1988; Dahlin 1989; Griffiths et al. 1990; Dahlin, 1993). Furthermore, electrodes connected with a multi-cable to an automatic switching system were able to relay electrical signals to a resistivity meter which, after calculations of resistivity values by computer software, allowed the development of two dimensional (2-D) resistivity imaging.

A particular technique, known as *"inverse numerical modelling"* enables very large quantities of data to be analysed (e.g. Olderburg and Li 1994; Tsourlos 1995; Loke and Barker 1996; Dahlin 1996). Using this approach it is possible to arrange electrodes on the soil surface in a grid pattern and integrate the data so as to obtain a 3-D resistivity image that contains information related to all spatial directions of the soil subsurface.

A limit of the surface resistivity survey is its decreasing resolution with depth. This can be overcome by using 2-D or 3-D borehole tomography with which a spaced vertical array of electrodes (i.e. Vertical Resistivity Probe) is used to supply detailed information at different depths (La Breque et al. 1996; Ramirez et al. 1996; Brown and Slater 1999).

Use of the multi-channel measuring technique continued and it is still being actively developed with the aim of deriving more efficient and powerful algorithms. This technique allows a greater depth of study and application of electrical resistivity

properties not only in “traditional settings” like the geological distribution of rocks and soil in the subsurface (Johansen 1977; Griffith et al., 1990; Mollerand Sorensen 1998; McDougal et al. 2004; Cardarelli and Fischanger 2006) but also in research studies of water quality and resources (e.g. Slater et al 1997; Christensen et al. 1998; Dahlin et al. 1999; Brown 1999; Koster 2005; Bowling et al. 2006). Furthermore, it is valuable in mining research (e.g. Sheets 2002; Johnson et al 2003), archaeological research (e.g. Li et al. 1992) and in environmental studies (e.g. Daily et al. 1995; Aristodemou et al. 2000; De La Vega et al.2003; Atekwana et al., 2005; Acworth 2006; Santos et al., 2006; Soupios et al., 2007).

1.2. Overview of Electrical Resistivity Theory

It is noted that, if a potential difference (***ΔV***) is applied across the two ends of a conductor, a current with intensity ***I*** passes through it. This current is related to the potential difference by Ohm’s Law:

$$\frac{\Delta V}{I} = R$$

Equation 1

where ***R*** is the electrical resistivity, which is dependent upon the nature and geometric characteristics of the conductor material.

Ohm’s law states that the potential gradient (electric field), ***E*** (***δV/δr)***, is the product of the current density ***j*** and the resistivity ***ρ***. Generally, in a linear conductor of length ***l*** and constant cross-section ***s*** the relationship is given by:

$$\frac{\delta V}{\delta r} = j\rho = \frac{I}{s}\rho$$

Equation 2

The potential difference, ***ΔV,*** between the ends of the conductor is calculated by integration of *equation 2*.

$$\Delta V = \frac{I}{s}\rho\int_0^l \delta r = \frac{I}{s}\rho l$$

Equation 3

Substitution of *equation 3* with the product, ***ρl/s,*** into *equation 1*gives:

$$\frac{\Delta V}{I} = R = \rho\frac{l}{s} = \rho K$$

Equation 4

where ***K*** is the geometric coefficient of the conductor and the resistivity constant (***ρ***) is an intrinsic property of the conductor.

In the subsurface when a current originating from the surface is applied, Ohm's Law assumes a different form due to a change in the geometric coefficient ***K***. Consequently, the resistivity is a parameter that influences the transit and distribution of the current in the conductor and, therefore, in the subsurface. For this reason it provides information about the nature and structure of the ground subsurface (Carrara et al.2004).

In practise, when a continuous current with intensity ***I*** is introduced through a single point as in surface ***C1*** (*Fig.1.1*), if the soil subsurface is electrically homogeneous, the current lines will symmetrically diffuse from that point and, therefore, the current (***I***) will be uniformly distributed within a circle of area $2\pi r^2$.

The current density, ***J,*** within the circle will be $I/2\pi r^2$. Given that the electric field ***E*** $(\delta V/\delta r)$ is equal to the product between the current density and electrical resistivity ***Jρ*** (*equation 2*) we have:

$$-\frac{\delta V}{\delta r} = -\frac{I}{2\pi r^2 \rho}$$

Equation 5

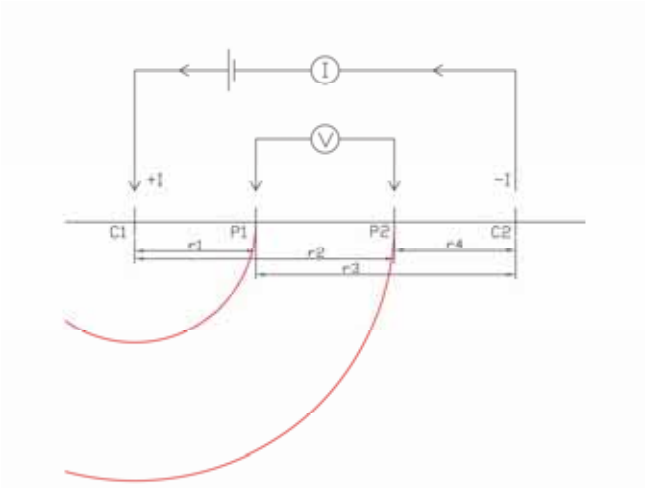

***Fig.1.1**: Diffusion of current lines when a continuous current with intensity **I** is introduced through a point as in surface C1.*

Therefore, with reference to *Fig 1.1*, the potential difference (ΔV^{C1}_{P1P2}) between points ***P1*** and ***P2*** at distances r_1 and r_2 from the source, ***C1,*** is obtained by integrating δV between the limits r_1 and r_2:

$$\Delta V^{C1}_{P1P2} = \int_{P1}^{P2} \delta V = \frac{I\rho}{2\pi}\int_{r_1}^{r_2} \frac{1}{r^2}\delta r = \frac{I\rho}{2\pi}\left(\frac{1}{r_1} - \frac{1}{r_2}\right)$$

Equation 6

If another point ***C2*** were to be connected to point ***C1*** by a direct current generator, in which ***C1*** is considered to be the positive pole and ***C2*** the negative pole and with r_3 and r_4 being the distances of ***C2*** from ***P1*** and ***P2***, the potential difference between ***P1*** and ***P2*** will be:

$$\Delta V^{C1}_{P1P2} = \frac{I\rho}{2\pi}\left(\frac{1}{r_3} - \frac{1}{r_4}\right)$$

Equation 7

such that the total possible potential difference ΔV that can be measured between points ***P1*** and ***P2*** as a result of the continuous current flowing from ***C1*** to ***C2***, is given by the algebraic sum of the previous formulas:

$$\Delta V = \Delta V_{P1P2}^{C1} - \Delta V_{MN}^{C2} = \frac{I\rho}{2\pi}\left(\frac{1}{r_1} - \frac{1}{r_2} - \frac{1}{r_3} + \frac{1}{r_4}\right)$$

Equation 8

Using *equation 8*, it is possible to obtain the resistivity of a homogeneous soil subsurface resulting from a passage of current:

$$\rho = \frac{\Delta V}{I} 2\pi \frac{1}{\frac{1}{r_1} - \frac{1}{r_2} - \frac{1}{r_3} + \frac{1}{r_4}} \Leftrightarrow \rho = \left(\frac{\Delta V}{I}\right) K$$

Equation 9

where ***K*** is the geometric coefficient. If ***ΔV*** is measured in *Volts*, ***I*** in *Amperes* and r_i in metres, the units of ***ρ*** are ***Ωm*** (Reynolds 1995). In the field points ***C1***; ***C2***; ***P1***; ***P2*** are metallic electrodes with high conductivity.

1.2.1. Apparent Resistivity

The calculated resistivity value is that which an isotropic and homogeneous subsurface will give with the same electrode arrangement, however, in reality the soil subsurface is not generally electrically homogenous. When the current is applied, therefore, any variation in conductivity can alter the flow, causing a variation in potential distribution compared to that which is given for a homogenous subsurface.

If ***ΔV*** is calculated using *equation 8*, and ***ΔV'*** is the potential difference measured in a real situation, the ratio ***ΔV/ΔV'*** gives the value of the disturbance product, **A**, in relation to the actual normal potential owing to heterogeneity in the subsurface. Consequently, the resistivity value measured in reality differs from the value measured in a uniform distribution. For this reason it is termed '*Apparent Resistivity*' and is indicated by ρ_a. In general, the resistivity measured on the surface is an *apparent resistivity* (Reynolds 1995; Carrara et al.2004).

The range in potential measured on a natural surface depends on the quantity, location, shape and resistivity of the soil layers in relation to current flow. By taking serial measurements of apparent resistivity it is possible to obtain information regarding the distribution and the nature of the soil subsurface.

1.3. Electrical Resistivity Properties of Substrate, Rock and Soil

Several factors and parameters can affect the electrical resistivity value of rocks or soil including the mineral composition, degree of fracturing, percentage of fractures filled, porosity and chemical composition of the groundwater (Carrara et al. 2004; Loke 2001; Reynolds 1995).

Depending upon the electrical properties of the medium, electric current can pass through the subsurface either by electronic conduction or by electrolytic conduction. In the former, the current flow occurs through free electrons (i.e. metals in the case of soil) and in the latter the current passes through the soil subsurface due to ion movement in the groundwater. Clearly, electronic conduction would be the principal means of current flow in mining activities where there is likely to be conductive natural minerals and in environmental studies where there could be industrial minerals present in the subsurface. In comparison, electrolytic conduction would be expected to be predominant in soil with groundwater flow.

In general, many naturally occurring minerals present in soils and rocks are bad conductors (e.g. quartz, feldspar etc.) with high electrical resistivity values (i.e. $> 10^7$ ohm*m). The groundwater that flows through the subsurface, however, is an efficient conductor with low resistivity (i.e. $1<\rho<100$ ohm*m), the value of which depends on the concentration of dissolved salts (i.e. sea water $\boldsymbol{\rho}$ = 0.2 ohm*m) (Carrara et al. 2004). Natural rocks and soils are composed of mineral associations and are characterised by a wide range of porosity values. In many cases they are permeated by a large volume of water which, if it is sufficient to form a continuous layer on the faces of pores, can completely change the resistivity of the subsurface since this

depends upon the electrical characteristics of the aqueous solution. Archie's Law (1942) describes how the $\boldsymbol{\rho}$ value changes in totally saturated conditions:

$$\rho = F \times \rho_W = \left(a\Phi^{-m}S^{-k}\right)\rho_w$$

Equation 10

where $\boldsymbol{F}$ is the *electric formation factor* which varies with porosity $\boldsymbol{\Phi}$; $\boldsymbol{\rho_w}$ is the fluid resistivity**;** $\boldsymbol{S}$ is the saturation level; $\boldsymbol{m}$ depends on the cementing level; $\boldsymbol{a}$ depends on the type of porosity and the form of the pores (Carrara et al.2004).

The resistivity of a selection of rocks, soils and minerals is shown in *Figure 1.2*, highlighting that there is overlap in the values of different classes. Igneous and metamorphic rocks generally have the highest resistivity values with a range that varies in the region of 1000 to 10^8 ohms*m according to the degree of fracturing and the percentage of fractures filled with groundwater. Sedimentary rocks and unconsolidated sediments, in comparison, have lower resistivity values varying from 10 to about 1000 ohm*m. They generally have high water content and their resistivity depends mainly on the porosity, fluid and clay content. In particular, clay soil normally has a lower resistivity value than sandy soil (Carrara et al. 2004; Loke 2001; Reynolds 1995).

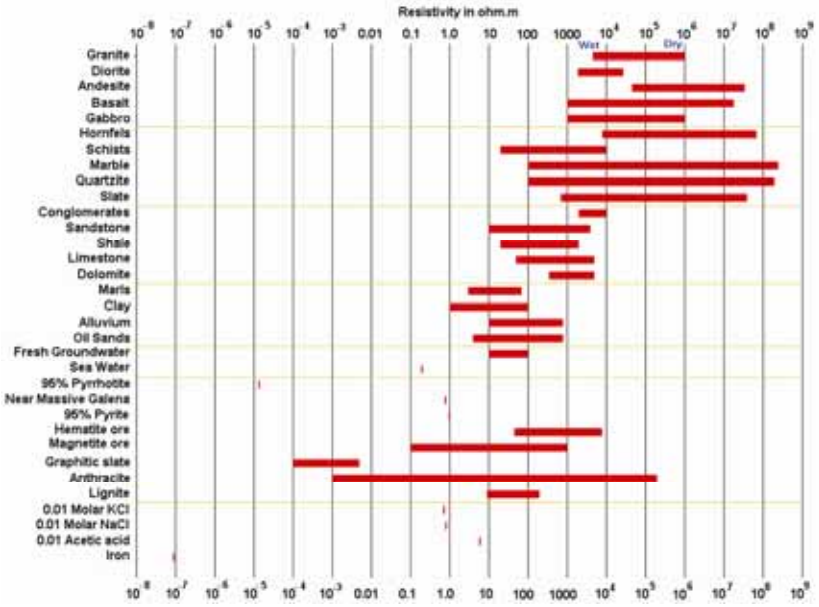

***Fig. 1.2**: Range of resistivity values for a selection of rocks, soils and minerals (Loke 2001).*

The presence of industrial contaminants in the soil can result in a variation from the normal electrical resistivity values. Metals (e.g. iron) have extremely low resistivity whereas chemicals that are strong electrolytes (e.g. potassium chloride, sodium chloride etc.) reduce the resistivity of groundwater, and hydrocarbons typically have very high resistivity values (Daily et al. 1995; Aristodemou et al. 2000; Loke 2001; De La Vega et al.2003; Atekwana et al., 2005; Acworth 2006; Santos et al., 2006; Soupios et al., 2007).

1.4. Depth of Measurement

The electrodes are distributed on the ground surface in simple patterns, symmetrically aligned in relation to the centre of measurement. In order to determine the investigation depth for each electrical resistivity measurement, many authors (e.g. Edwards 1977, Barker 1991, Merrick 1997) used *equation 11*, according to which the maximum value is reached at a depth of about ***0.35a*** where ***a*** is the electrodes spacing (*Fig. 1.3)*, thereafter decreasing asymptotically to zero.

$$F_{ID}(z) = \frac{2}{\pi} \cdot \frac{z}{\left(a^2 + 4z^2\right)^{1.5}}$$

Equation 11

In practice, however, Edwards (1977) and Barker (1991) used the "median depth of investigation", i.e. the depth above which the area under the curve is equal to half the total area above the curve.

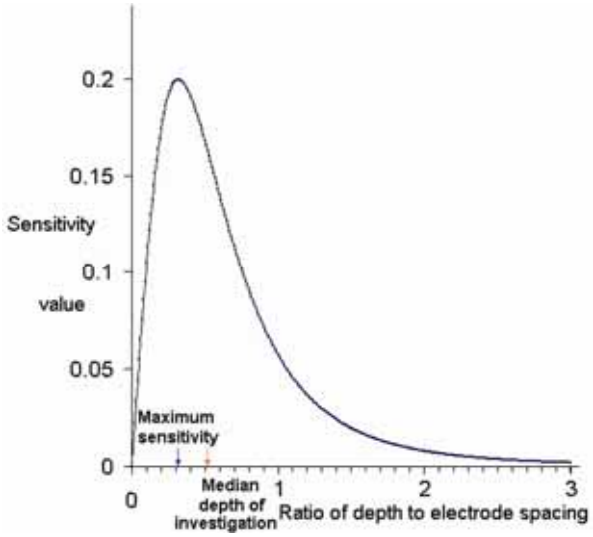

Fig. 1.3*: Curve described by equation 11 giving the sensitivity values of the resistivity method as a function of the ratio of depth to electrode spacing (Loke 2001).*

It is important to note that the previous theoretical estimation of the investigation depth (*equation 11*) is valid only for a homogeneous medium and, if there are large variations in resistivity on the subsurface, the effective depth of investigation could be different.

1.5. Traditional Resistivity Surveys

There are two main methods used to describe electrical arrays: the *Vertical Electrical Sounding* (***VES***) *Method* is used to determine the vertical variation in resistivity and the *Constant Separation Traversing* (***CST***) *Method* (also called *Electrical Resistivity Traversing* (***ETR***) *method*) is used to detect the horizontal variation in resistivity (Reynolds 1995).

1.5.1. Vertical Electrical Sounding (VES)

If, using the *Vertical Electrical Sounding* (***VES***) array, the distance between the current electrodes is increased, the depth to which the current penetrates is increased (Gish and Rooney 1925; Stefanescu et al, 1930; Langer 1933; Flathe 1955; Reynolds 1995). The position of measurement is taken as the midpoint of the electrode array.

Measurements of the resistance (***V/I***) are made at progressively larger spacings and at each electrode separation a value of apparent resistivity ($\boldsymbol{\rho_a}$) is calculated using the measured resistance in conjunction with the appropriate geometric factor for the electrode configuration being used. In this method, the centre point of the electrode array remains fixed, but the spacing between the electrodes is increased to obtain more information about the deeper sections of the subsurface.

The apparent resistivity values measured are normally plotted on log-log graph paper (*Fig.1.4*) and to interpret the data from such a survey, it is generally assumed that the subsurface consists of horizontal layers. In this case, the subsurface resistivity changes only with depth, but does not change in the horizontal direction. It should be noted that only a one-dimensional model of the subsurface is used to interpret the measurements. Despite this limitation, however, this method has given useful results for geological situations where the one-dimensional model is approximately true (e.g. assessing the water table location in the subsurface).

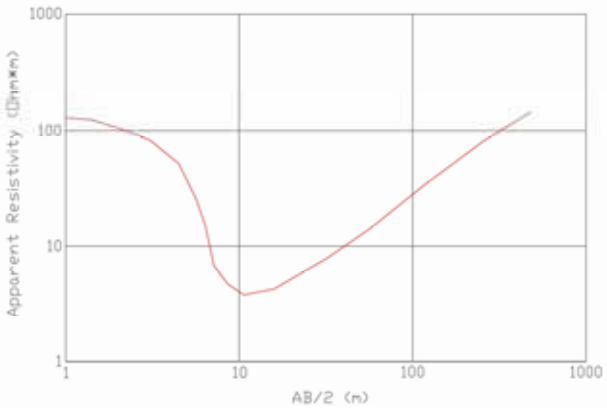

Fig. 1.4*: Example of log-log curve where the "Apparent resistivity" is measured at progressively larger electrodes spacing (i.e. AB/2) using the VES method and describing a horizontal geological structure composed of three strata.*

1.5.2. Constant Separation Traversing (CST)

With the *Constant Separation Traversing* (***CST***) *Method* the spacing between the electrodes remains fixed, but the entire array is moved along a straight line. The values of apparent resistivity are plotted on a linear graph as a function of distance along the profile (*Fig.1.5*) (Reynolds 1995). This gives some information about lateral changes in the data, but is mainly qualitative.

The most severe limitation of the ***CTS*** is that horizontal changes in subsurface resistivity are commonly found. Such changes will cause variations in the apparent resistivity values that might be, and frequently are, misinterpreted as changes with depth in the subsurface resistivity. In many engineering and environmental studies, the subsurface geology is very complex and the resistivity can change rapidly over short distances (Carrara et al.2004). This method might not be sufficiently accurate for such situations.

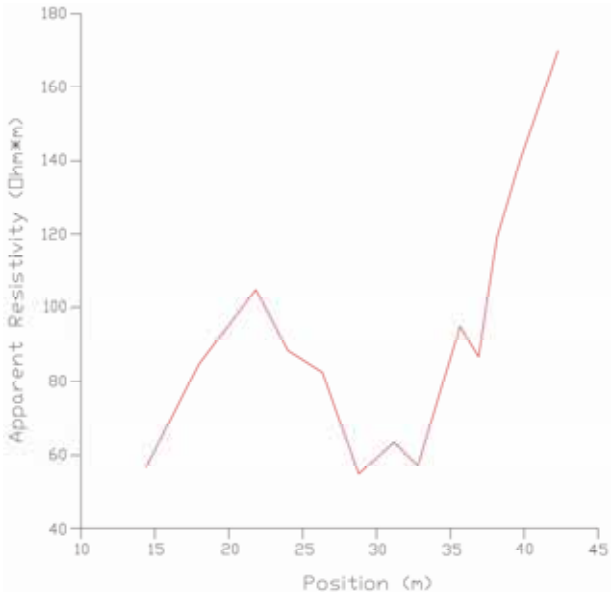

Fig. 1.5*: Example of "apparent resistivity" measurements taken using the CTS method, showing resistivity variations at a constant depth along a straight line.*

1.6. 2-D Imaging-Tomography Survey

A more effective way than VES or CST to investigate vertical and lateral resistivity changes is to complete a 2-D imaging-tomography survey. This is carried out using a large number of electrodes connected to a multi-core cable (*Fig.1.6*). An electronic switching unit, which is controlled by software that automatically selects the relevant four electrodes for each measurement in accordance with the resistivity meter and specific array adopted, records every resistivity measurement.

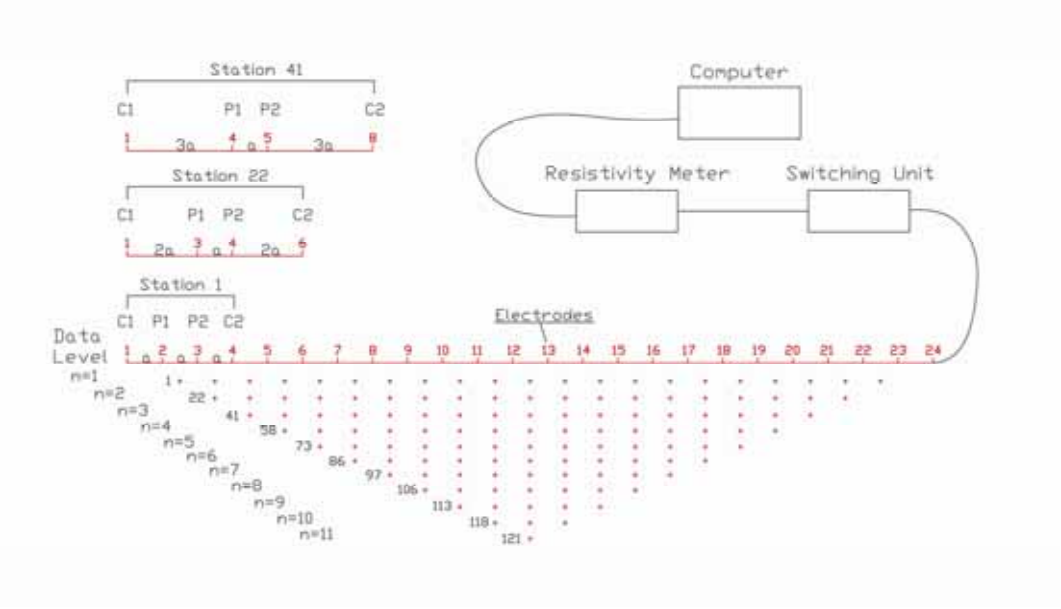

Fig. 1.6*: 2-D electrical resistivity survey composed by a large number of electrodes connected to a multi-core cable with electronic switching unit and resistivity meter controlled by software.*

The electrodes for a generic array are positioned along a straight line with a constant spacing, ***a***. The sequence of measurements uses the electrodes in turn as a current electrode (i.e. ***C1*** or ***C2***) and as a potential electrode (i.e. ***P1*** or ***P2***). In this way it is possible to obtain information about resistivity along the straight line and at different depths. It should be noted, however, that when the constant spacing, ***a***, increases, the number of measurements that can be made by a given number of electrodes along the survey line decreases (Loke 2001).

The apparent resistivity values can be plotted to produce a 'pseudosection contour' which displays the data and gives a very approximate picture of the true

subsurface resistivity distribution. This is, however, only an initial guide for later qualitative interpretations and the use of a different array to map the same region can give different contour shapes in the pseudosection plot.

1.6.1. Types of Electrical Resistivity Array

There are several kinds of resistivity arrays and those most commonly used for resistivity surveys are: Wenner (α-β-γ); Pole-Pole; Dipole-Dipole; Pole-Dipole; Wenner-Schlumberger and Equatorial Dipole-Dipole (*Fig.1.7*). For 2-D imaging tomography surveys the choice of the most appropriate array depends on the type of structure to be investigated, depth of investigation, lateral and vertical resistivity changes in the subsurface, background noise level, width of the investigated area and sensitivity of the array to vertical and orizontal changes in the subsurface resistivity.

The sensitivity fuction (Edwards 1997) describes the degree to which a change in the resistivity of a section of the subsurface influences the potencial measured by the array.

Certain electrical arrays are more sensitive to vertical resistivity changes, and others to lateral changes, whereas some are able to record both simultaneously.

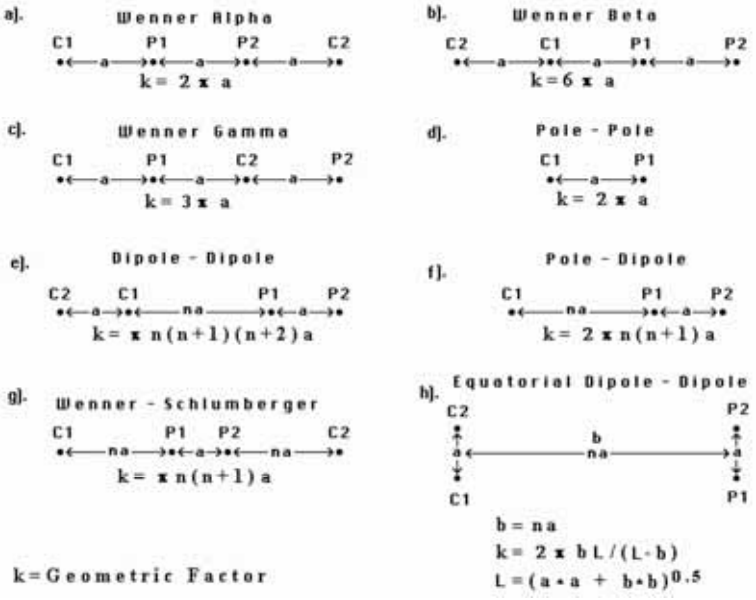

Fig. 1.7*: Electrode arrangements for the most common electrical resistivity arrays (Loke 2001).*

1.6.1.1. *Wenner Array*

There are three versions of the *Wenner* array, ***α***, ***β***, and ***γ*** (*Fig.1.7*), but the first is used most frequently. This array is characterised by a sensitivity described in *Figure1.8* (sensitivity plot) where it can be seen that the contour has an almost horizontal shape below the centre array. Due to this, the Wenner array is able to record vertical resistivity changes (horizontal structures) below its centre. Moreover the sensitivity plot shows wide areas with negative sensitivity values near the surface, between the ***C1***:***P1*** electrodes and the ***C2***:***P2*** electrodes. This implies that if a small object with a resistivity higher than the background medium is placed in such an area, the measured apparent resistivity value will decrease (anomaly inversion). Conversely, if an object with high resistivity is placed where the sensitivity plot shows positive high values, the measurement of apparent resistivity will increase.

In comparison with other arrays, the ***Wenner α*** array has a moderate investigation depth that is approximately equal to half the constant spacing between electrodes (***a***). Importantly, it also has the strongest signal strength in relation to other arrays and can be used in regions with high background noise. Of the other two ***Wenner*** arrays, the ***β*** is considered a special case of a dipole-dipole array where the spacing between the electrodes remains constant and with the ***Wenner γ*** the current and potential electrodes are equidistant and the deepest region mapped is below the ***C1*** and ***P2*** electrodes and not below the array centre (Loke 2001).

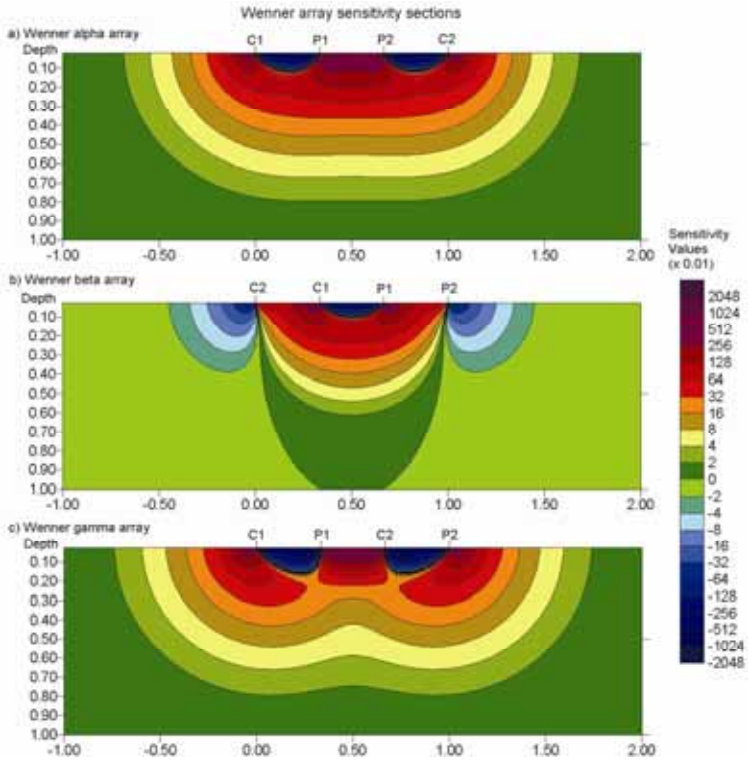

***Fig. 1.8**: Sensitivity plots of Wenner α, β, and γ arrays showing differences in their ability to record vertical or horizontal structures below the electrode arrangement (Loke 2001).*

1.6.1.2. Wenner-Schlumberger Array

Like the Wenner Array, this array also uses electrodes arranged with a constant spacing (*Fig.1.7*). However, it incorporates a factor "***n***" which is the ratio of the spacing between ***C1*** and ***P2*** electrodes (or ***P2*** and ***C2***) to the spacing between the ***P1***-***P2*** potential pair. The sensitivity pattern, (*Fig.1.9*), shows that the highest positive sensitivity values below the array centre increase from ***n***=1 (in the particular case of the Wenner array) to ***n***=6 (the classical Schlumberger array). Furthermore, near the location of the plotting point at the median depth of investigation, the sensitivity contours have a slight vertical curvature below the centre of the array. This means that it is moderately responsive to vertical resistivity changes (horizontal structures) for low ***n*** values and to lateral resistivity changes (vertical structures) for high "***n***" values. It can, therefore, be a good compromise to detect both structures.

The signal strength is weaker than the Wenner array but the median depth of investigation is about 10% larger; the horizontal coverage is slightly better and there

are more data points because, for the Wenner array, each successively deeper data level has 3 data points less than the previous level whereas, for the ***Wenner-Schlumberger*** array, there is a loss of only 2 data points with each deeper level.

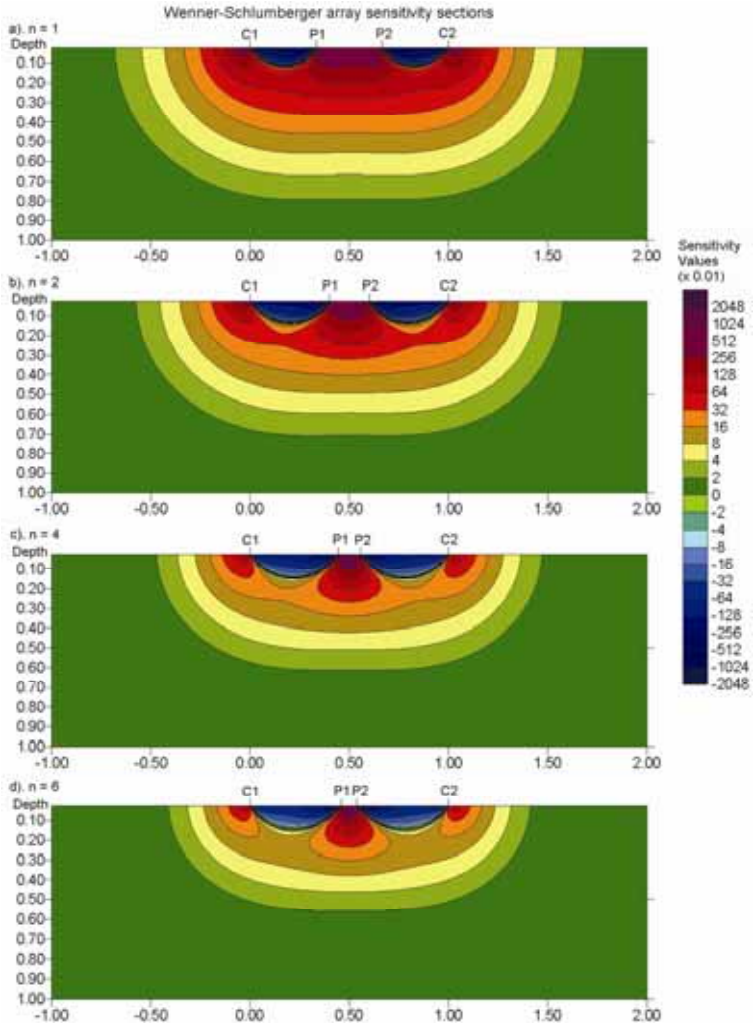

Fig. 1.9*: Sensitivity plots of the Wenner-Schlumberger array showing differences in their ability to record vertical or horizontal structures below the electrode arrangement (Loke 2001).*

1.6.1.3. <u>*Dipole-Dipole Array*</u>

In dipole-dipole arrays, the constant spacing, ***a***, between the ***C1*** and ***C2*** current electrodes is the same as that between the ***P1*** and ***P2*** potential electrodes (see *Fig.1.7*). In order to increase the investigation depth, the spacing between ***C1*** and ***P1*** electrodes is increased in accordance with the ***n*** factor (an integer).

The sensitivity plot (*Fig.1.10*) indicates that the largest sensitivity values are located between the ***C2-C1*** dipole pair and the ***P1-P2*** pair such that this array gives only minimal information about the resistivity of the region surrounding the plotting point. For this reason the distribution of data points in the pseudosection plot does not reflect the subsurface area mapped by the apparent resistivity measurements. When the ***n*** factor increases, the high sensitivity values become more concentrated below ***C1-C2*** current electrodes and the ***P1-P2*** potential electrodes, while the sensitivity values below the centre of the array between the ***C1-P1*** electrodes decrease. The sensitivity contour pattern becomes almost vertical for ***n*** values greater than 2 and this means that the dipole-dipole array is very sensitive to lateral changes in resistivity (vertical structures) but relatively insensitive to vertical changes in resistivity (horizontal structures).

In general, the dipole-dipole array has a shallower depth of investigation and smaller signal strength than the Wenner and Wenner-Schlumberger arrays, but it has better horizontal data coverage than the Wenner array. This can be an important advantage when the number of nodes available with the multi-electrode system is small. To use this array effectively, the resistivity meter should have high sensitivity and very good noise rejection circuitry, and there should be good contact between electrodes and ground.

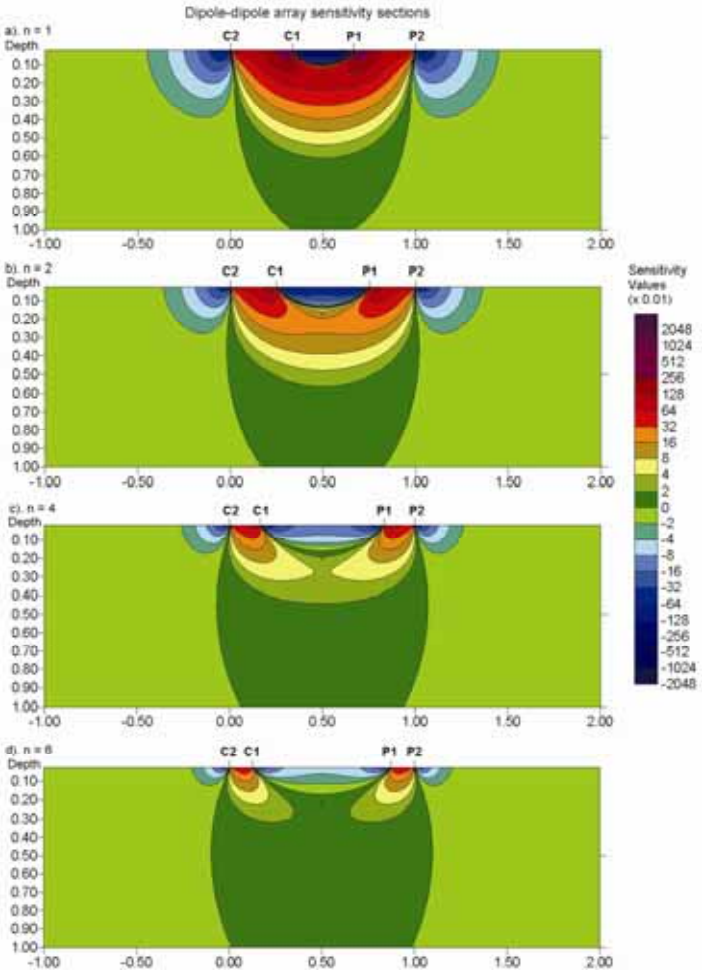

Fig. 1.10*: The dipole-dipole sensitivity plot. Largest sensitivity values are located between the* ***C2-C1*** *and* ***P1-P2*** *dipole pair. It gives minimal information about the resistivity of the region surrounding the plotting point and the high sensitivity values become more concentrated below* ***C1- C2*** *current electrodes and the* ***P1-P2*** *potential electrodes when the n factor increases (Loke 2001).*

1.6.1.4. Pole-Pole Array

This type of array, which is mainly used in archaeological surveys, is non-conventional because an array with only one current and one potential electrode cannot exist in reality (*Fig.1.7*). In practice with the pole-pole array, the second current and potential electrodes (***C2*** and ***P2***) should be placed at a distance that is more than 20 times the maximum separation between ***C1*** and ***P1*** electrodes used in the survey in order to ensure that the error is less than 5%. The effect of the ***C2*** electrode is approximately proportional to the ratio of the ***C1-P1*** distance to the ***C2-P1*** distance. A disadvantage of this array is that, as a result of the large distance

between the ***P1*** and ***P2*** electrodes, it can pick up a considerable amount of telluric noise that can severely diminish the quality of the measurements. It has, however, the widest horizontal coverage and deepest depth of investigation compared with other arrays, but the poorest resolution, which is indicated by the comparatively large spacing between the contours in the sensitivity function plot (*Fig.1.11*) (Loke 2001).

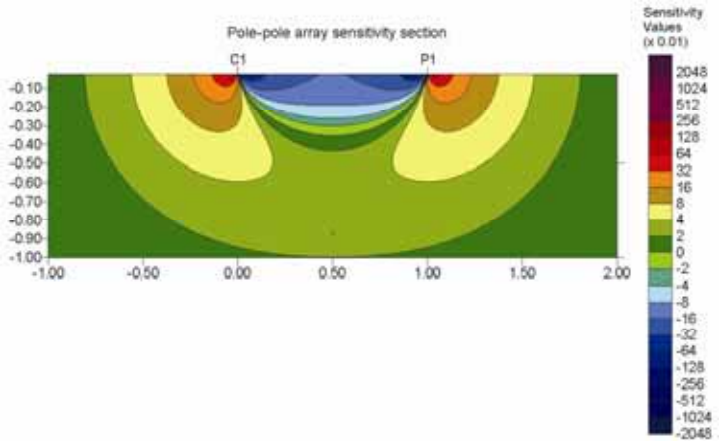

Fig. 1.11*: The pole-pole array arrangement. The second current and potential electrodes (**C2** and **P2**) are located far from **C1** and **P1** electrodes and it has the widest horizontal coverage and depth of investigation (Loke 2001).*

1.6.1.5. <u>*Pole-Dipole Array*</u>

The pole-dipole array is asymmetrical (*Fig.1.7*). By repeating the measurements with the electrodes arranged in the reverse configuration, (*Fig.1.12*), it is possible to eliminate the effect of this asymmetry, however, this procedure will double the number of data points and consequently the survey time. As with the pole-pole array, the pole-dipole array also requires a remote electrode (C2 electrode) which must be placed sufficiently far from the survey line.

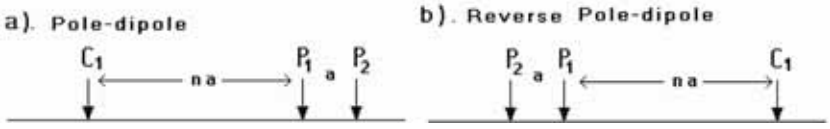

Fig. 1.12*: The Pole-Dipole array .By repeating measurements in a reverse configuration the effect of its asymmetry can be eliminated (Loke 2001).*

The sensitivity plot (*Fig.1.13*) shows that the area with the greatest sensitivity is below ***P1-P2*** dipole pair. For high **n** values (n>4), the high positive, sensitive region below the ***P1-P2*** dipole becomes increasingly vertical. It is also noted that the zone with negative sensitivity values between the ***C1*** and ***P1*** electrodes is to the right of the ***C1*** electrode and the smaller zone of high positive values is to the left of the same electrode. Thus, as for the dipole-dipole array, this array is probably more sensitive to vertical structures.

The pole-dipole array has a significantly higher signal strength compared to the dipole-dipole array although it is still lower than the Wenner and Wenner-Schlumberger arrays. It also has relatively good horizontal coverage and is not as sensitive to telluric noise as the pole-pole array.

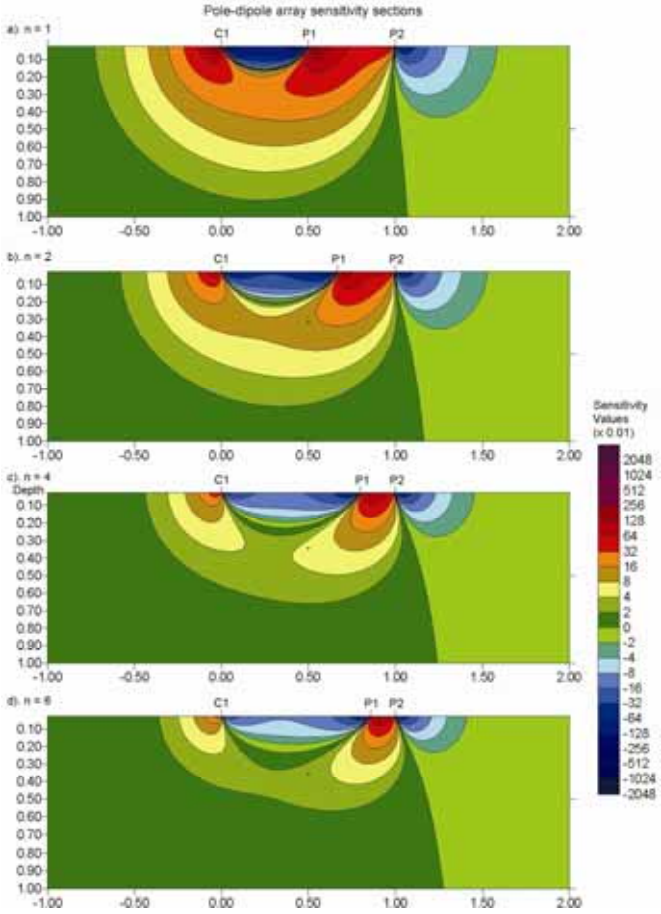

Fig. 1.13*: The pole-dipole sensitivity plot. The area with the greatest sensitivity is below* ***P1-P2*** *dipole pair; for high n values the zone with negative sensitivity values increase between the* ***C1*** *and* ***P1*** *electrodes and decrease on the right of the P2 electrode (Loke 2001).*

Chapter 2: Materials and Experimental Methods

2.1 Model Construction

The physical model used to study and monitor the migration and distribution of a pollutant in the soil comprises a tank made of plexiglass material divided into three sections by a permeable screen perforated with holes (1 mm diameter) and fine net.

The main section is located in the centre of the model and contains the soil (*Fig.2.1*). Two narrow sections either side of this main section form the areas where water comes in and out of the model and are used to control the water level to ensure correct groundwater flow. In particular, the narrow section on one side is fitted out with a tap on the top (*Fig. 2.2*), which allows water to flood this area, along with several overflow holes, which allow the water level to be set to different depths. The other narrow section is fitted out with a tap on its base (*Fig. 2.3*) from which water leaves the model and, like its partner, it also has several other overflow holes to adjust the water level. The selection of specific overflow holes at different levels in the two outer sections of the model allows either a constant groundwater flow to be maintained or can enable the groundwater velocity in the soil to be altered.

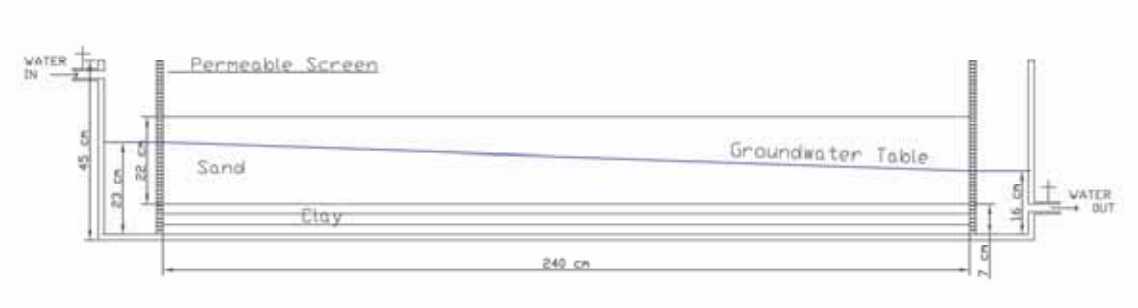

Fig. 2.1*: Cross-section of the laboratory model comprising a tank divided into three sections by permeable screens. The main section in the centre contains the clay and sandy soil and two narrow sections on each side allow a constant groundwater flow in the soil.*

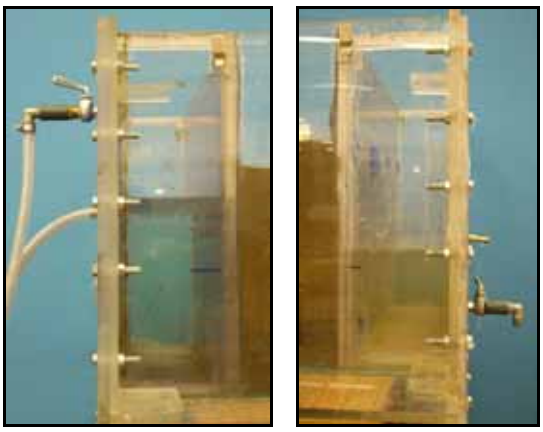

Figs. 2.2 & 2.3*: The "water-inlet" and "water-outlet" sections on the left and right side of the model with which it is possible to change the water level and manage the groundwater flow in the model.*

Since the electrical resistivity properties of soil depend on several factors (see *Section 1.3*), in this study the model has been built to try and recreate, as much as possible, an isotropic and homogeneous ground model so that the parameters measured can realistically identify physical and chemical alterations due to the controlled leakage of a contaminant (i.e. diesel). The soil is divided into several layers with the deepest formed by clay soil which is then overlaid by a sandy layer.

The groundwater level divides the sandy layer into two parts: a saturated zone on the base and an unsaturated (vadose) zone on the top. In this way, the basic model is comprised of three layers with different physical-chemical characteristics.

2.1.1 Soil Description: Clay Characteristics

The deepest soil layer in the model is composed of *Galston Clay* from Galston, East Ayrshire, Scotland (*Figs. 2.4-2.5*). It comes from a cave where the clay seam includes stones with different dimensions and a variety of mineralogical associations. This mixing of fine sediments (i.e. clay), coarse gravel, cobbles and boulders is likely to be of geological origin related to a glacial deposit.

Before laying the clay in the model, it was first air dried at ambient temperature (i.e. 19°C). The gravel and cobbles were removed and clods were crushed, pulverized and sieved through a 1 mm mesh. A representative specimen of this material was used to classify the soil on the basis of its particle size.

Figs. 2.4 & 2.5*: Galston Clay cave in Galston, East Ayrshire, Scotland. This kind of glacial clay deposit includes coarse gravel, cobbles and boulders as well.*

2.1.1.1 Particle size analysis

A combined sieving and sedimentation particle size analysis was carried out according to the ***British Standard 1377:1975, Test 7 (B)*** for the sediment portion with particle diameters bigger than 0.063 mm (i.e. Simple Dry Sieving) and the ***British Standard 1377:1975, Test 7 (D)*** for the sediment portion with particle diameters smaller than 0.063 mm (i.e. Hydrometer Analysis) (Head 1984) (*Fig. 2.6*). During these tests the specific gravity of the soil particles was determined (*Figs. 2.7-2.8*) along with the calibration of the specific hydrometer used (i.e. MED STS 50 PLS n°3793/P B.S. 718 weight = 23.8 g).

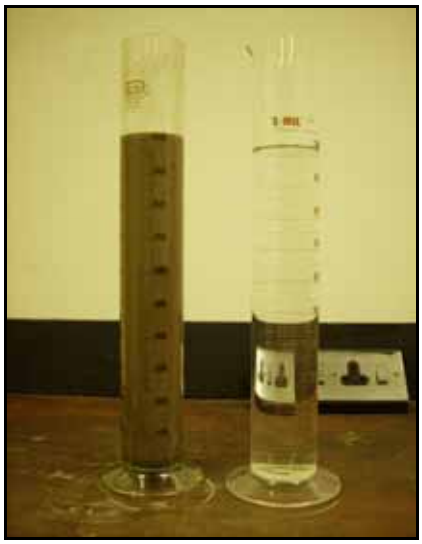

Fig. 2.6*: The sedimentation particle size method using a specific gravity hydrometer to measure the soil density in a suspension of water at various time intervals.*

Figs. 2.7 & 2.8*: Preparation and measurement phases related to the definition of the specific gravity of soil particles used in the hydrometer test.*

The test took several days to complete due to the relatively high percentage of fine silt and clay particles (i.e. 8days-7h-55'). In fact the *particle size curve* (*Fig. 2.9*) shows that almost 30% of the representative specimen is composed of medium and fine particles of sand; about 37% is formed by silt with the remaining 33% being clay. The full dataset can be found in *Appendix A*.

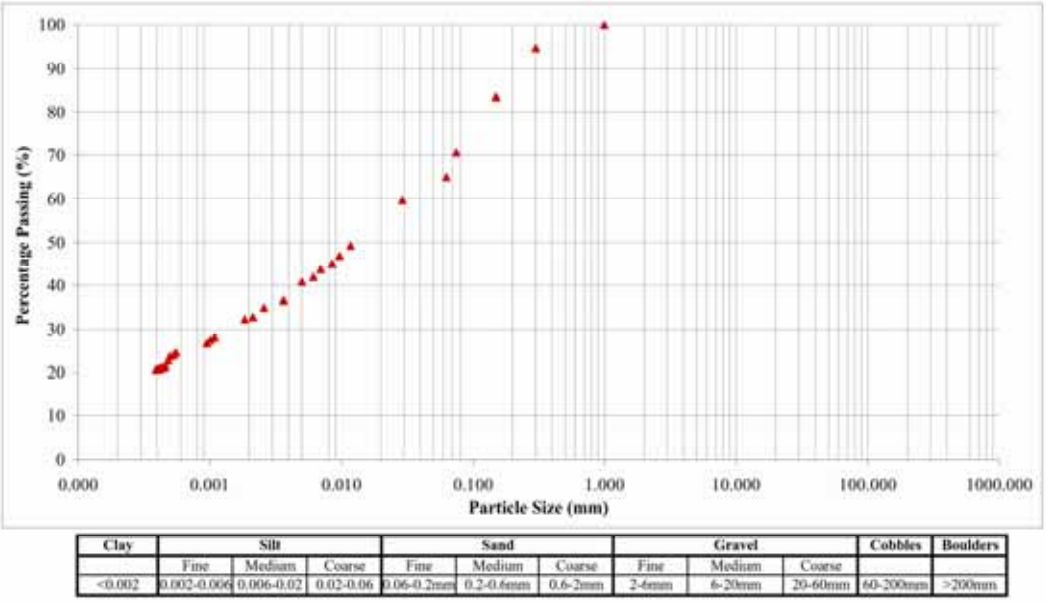

Fig. 2.9*: Particle size curve from hydrometer test and related sieving.*

2.1.2 Layering the Clay

As explained in the previous *Section 2.1*, the clay was laid on the base of the model after it had been dried and pre-treated. It was spread in thin layers of 1-1.5 cm thickness (*Fig. 2.10*) using a sieve with a mesh size of 1.00 mm. Each layer of clay was sprayed with 3 litres of tap water and covered with a plastic sheet for 24 hours before adding the next layer. This procedure was adopted to hydrate the clay and allow its particles to retain their natural moisture content.

During the procedure, which was repeated until the total clay thickness was 7 cm, no water seepage was observed from the clay layer through the permeable screen into the side sections of the model. The final, overall moisture content of this clay layer was measured at 18% with a portable moisture content meter (i.e. AT-Theta Kit).

***Fig. 2.10**: Clay layer on the base of the model in thin layers of 1-1.5 cm thickness.*

2.1.3 Soil Description: Sand Characteristics

Sand was specifically chosen and collected from the beach because this is, in fact, the most selective geo-sedimentary environment. The constant sea energy with its regular movements combined with wind energy and action sort the sedimentary deposit with an exceptionally homogeneous grain size and shape. For this study the sand was collected from Troon beach, South Ayrshire, Scotland following a preliminary site investigation (*Fig. 2.11*).

Fig. 2.11*: Sand collected from Troon Beach, South Ayrshire, Scotland.*

2.1.3.1 Particle size analysis

Adopting the *quartering procedure* a small, but representative, sand sample was used to classify the non-cohesive sediment on the basis of the particle size distribution.

Following ***British Standard 1377:1975, Test 7 (B)***, the sample was weighed, dried at 105°C for 24 hours in a thermostatically controlled drying oven. The grain size of the sand fraction was then determined by passing the sand sample through a series of sieves with decreasing mesh size (*Fig 2.12*) which separated it into different particle size ranges. The results of the cumulative percent finer by weight were plotted on an arithmetic scale and the grain size was plotted on a logarithmic scale (*Fig.2.13*). The particle size distribution chart was then used to determine the following parameters:

- *Uniformity Coefficient* (C_u) calculated from the curve (*equation 12*), shows how well sorted the sand is. This parameter is, in fact, the ratio of the grain size that is 60% finer by weight (***d_{60}***) to the grain size that is 10% finer by weight (***d_{10}***).

$$C_u = {d_{60}}/{d_{10}} = {0.17}/{0.12} = 1.416 \geq$$

Equation 12

In the present study, the sand can be defined as "*well sorted*" since a sample with a C_u greater than 6 is poorly sorted and a sample with a C_u less than 4 is well sorted.

- *Effective Size* (D_{10}) indicates the particle size in relation to which 10% of particles in the sample are finer and 90% are coarser. In this study, D_{10} = 0.12 mm, which defines this non-cohesive sediment as *Uniform Fine Sand* (*Fig. 2.14*).

***Fig. 2.12**: Sieve shaker used to determine the sand fraction passing through a series of sieves with decreasing mesh size.*

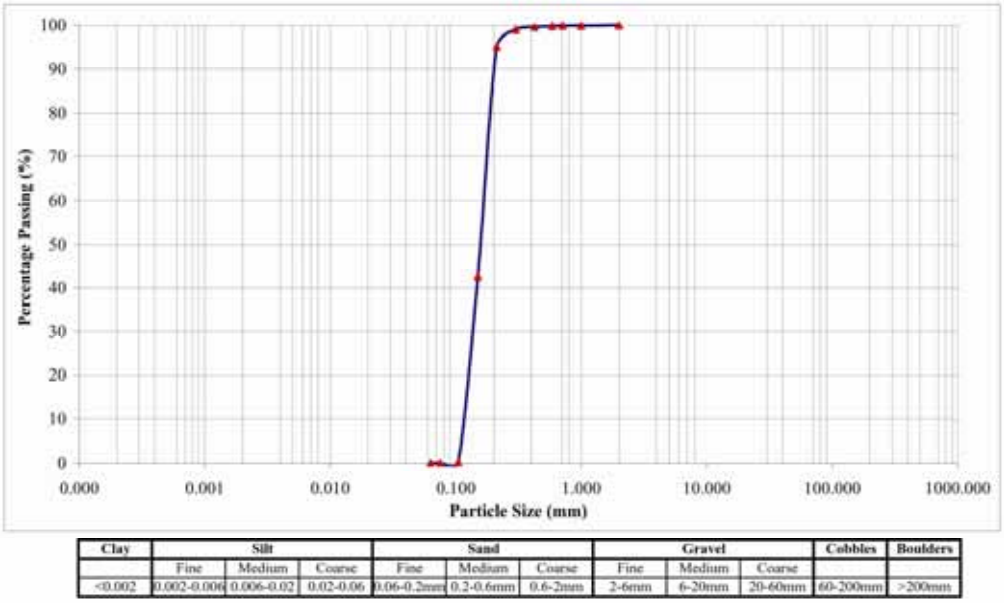

***Fig. 2.13**: Particle size curve from the sand sieving test.*

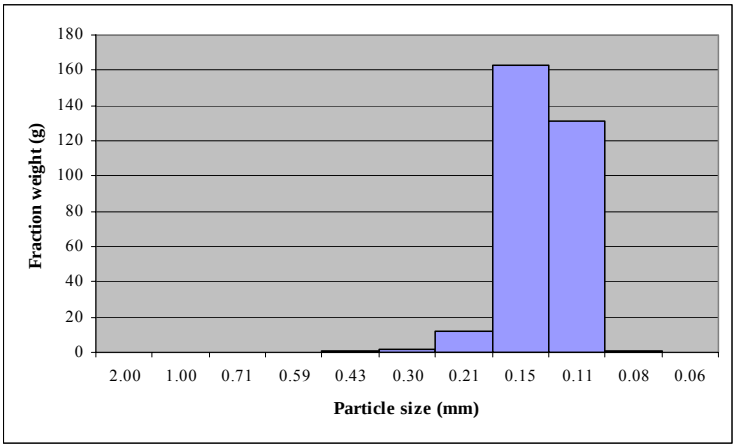

Fig. 2.14*: Istogram of sand fractions (in grams) with different grain size.*

2.1.4 Layering the Sand

Several layers of sand were spread on top of the clay using a sieve with a mesh size of 2 mm wide. The layers were scattered uniformly, removing any foreign bodies present (e.g. plastic; wood; etc) until the pre-determined depth of ≈ 20-22 cm was reached.

The sand was not artificially compacted but natural packing was achieved by slowly raising the groundwater level, flooding and gradually lowering the level again until it stabilised at 15 cm from the base on the "water inlet" side of the model and 13 cm from the base on the "water outlet" side of the model (*Fig. 2.15*). In this way any air bubbles in the soil were removed and the grains of sand settled on a horizontal plane.

Fig. 2.15*: Flooding the model to remove any air bubbles in the soil and settle the sand on a homogeneous horizontal plane.*

2.2 Choice of Model Array

The most appropriate electrical resistivity array for the 2-D imaging survey carried out in this study was chosen on the basis of the research objectives (see *Section 1 Introduction*). The array needed to be capable of identifying and describing the presence, distribution and diffusion of the pollutant in the model and the probable interaction between the model components (i.e. different kinds of soil, groundwater, pollutant, permeable reactive barrier). In addition, the model design was oriented to make use of the available equipment through an iterative process. In particular, the array was required to visualise:

- the horizontal soil stratification;
- the presence of groundwater flow that divided the sand layer into a higher unsaturated (vadose) zone and a lower saturated zone;
- the presence of pollutant spillage (leakage) on the surface and base of the sandy layer;
- the migration of pollutant over time;
- the effects of the remediation action (i.e. permeable rective barrier).

On the basis of previous (see *Section 1.6.1*) considerations, the Wenner-Schlumberger array was chosen. This array is sensitive to vertical resistivity changes (horizontal structures) in the soil strata and the groundwater table, and it is also more sensitive than other arrays to the horizontal resistivity changes (vertical structures) expected during pollutant migration particularly from areas of low spillage. Furthermore, the extensive horizontal coverage and greater number of data points than other arrays (e.g. Wenner) confirmed the choice of the Wenner-Schlumberger array for this research project.

This array is more sensitive to horizontal structures at low depth and, conversely, more sensitive to lateral resistivity changes at higher depth. To emphasize this physical characteristic and compare different pollutant migration behaviours, two leakage depths were assessed. Based on the pollutant (i.e. diesel) characteristics (see *Section 2.4.1*), the most superficial spillage was expected to settle in a thin horizontal

layer on top of the groundwater table or in the capillarity fringe. The deepest spillage, on the other hand, was expected to rise towards the surface and simultaneously travel down stream with the groundwater flow.

2.3 Experimental Setup for a 2-D Survey using the Wenner-Schlumberger Array

During the first part of this research (i.e. before diesel leakage; during diesel leakage and four weeks after leakage) 24 mini-electrodes, 5 cm long, made of copper with a constant spacing of 10 cm and subsequently during the second part of the research (i.e. monitoring of remediation action) 48 mini-electrodes, 5 cm spacing (*Fig.2.16 and 2.17*) were fixed along a straight, wooden bar connected to an electronic switching unit and a resistivity meter. The electrode arrangement for this specific array allows each electrode to be used as either a current electrode (e.g. ***C1***) or a potential electrode (e.g. ***P1***).

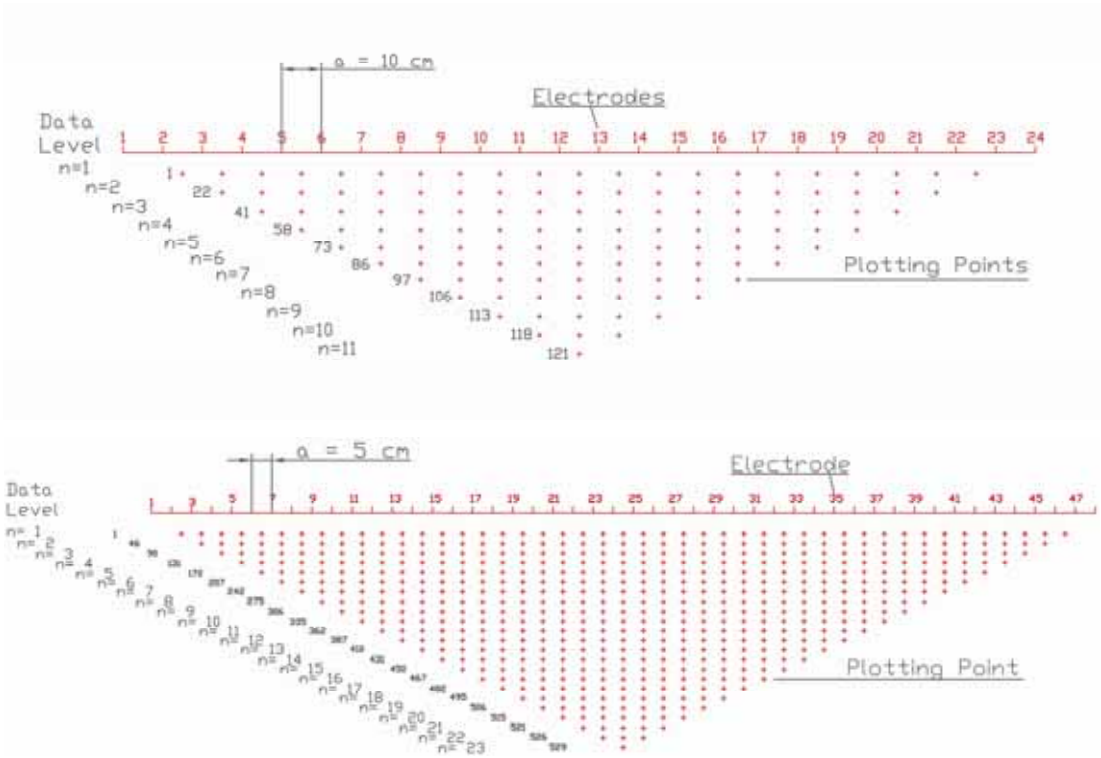

Fig. 2.16*: Wenner-Schlumberger electrical resistivity arrays with 24 electrodes; a = 10 cm spacing; 121 plotting points in 11 data levels and 48 electrodes; a = 5 cm spacing; 529 plotting points in 23 data levels.*

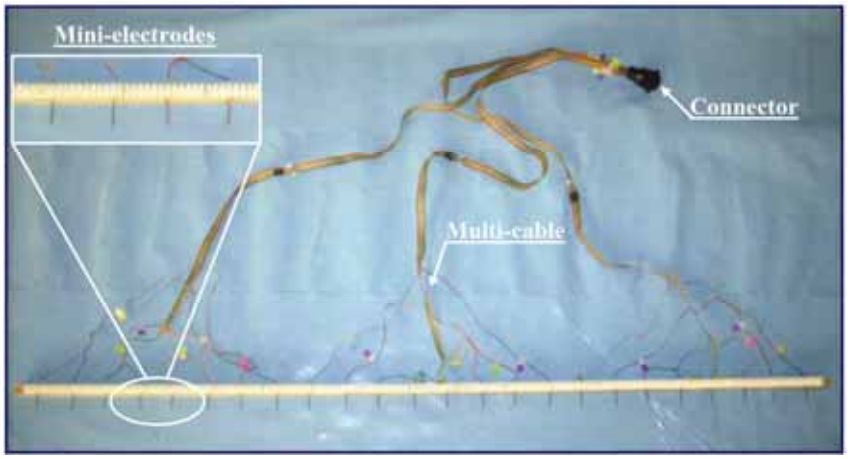

***Fig. 2.17**: Electrical resistivity array with 24 mini-electrodes at 10 cm spacing fixed along a straight, wooden bar 240 cm long and connected by an electrical multi-cable.*

For the first measurement electrodes 1, 2, 3 and 4 are used at spacing ***1a*** (a = 10 cm cm with 24 electrodes; a = 5 cm with 48 electrodes), where electrodes 1 and 4 are respectively the current electrodes (i.e. ***C1*** and ***C2)*** and electrodes 2 and 3 are the potential electrodes (i.e. ***P1*** and ***P2***) (*Fig.1.7g and Fig.2.18*). For the second measurement electrodes 2, 3, 4 and 5 are used for ***C1***, ***P1***, ***P2*** and ***C2*** respectively.

This measurement succession continues until the last electrodes (i.e. electrodes number 21-22-23-24 *Fig.2.18*) complete the first sequence of measurement at constant spacing ***1a***. In this way, the Wenner-Schlumberger array allows 21 measurements with 24 electrodes and 45 with 48 electrodes to be taken during the first sequence.

The second measurement sequence begins by using electrodes 1 and 3 as ***C1*** and ***P1*** at spacing ***2a*** (i.e. a = 20 cm with 24 electrodes; a = 10 cm with 48 electrodes), electrodes 3 and 4 as ***P1*** and ***P2*** at spacing ***1a*** (i.e. a = 10 cm with 24 electrodes; a = 5 cm with 48 electrodes) and electrodes 4 and 6 as ***P2*** and ***C2***, again at spacing ***2a***. In this second sequence electrodes 2, 4, 5 and 7 are designated as ***C1***, ***P1***, ***P2*** and ***C2*** respectively.

Successive sequences progress in a similar way, with electrodes chosen such that the spacing between ***C1*** and ***P1***, and ***P2*** and ***C2*** is always ***na*** and the spacing between ***P1*** and ***P2*** is always ***1a*** *(*e.g. Station 1; Station 22; Station 41 in *Fig.2.18*) . When all

possible combinations of 24 electrodes have been employed, 121 points of measurement are obtained at 11 different levels and when all possible combinations of 48 electrodes have been employed, 529 points of measurement are obtained at 23 different levels.

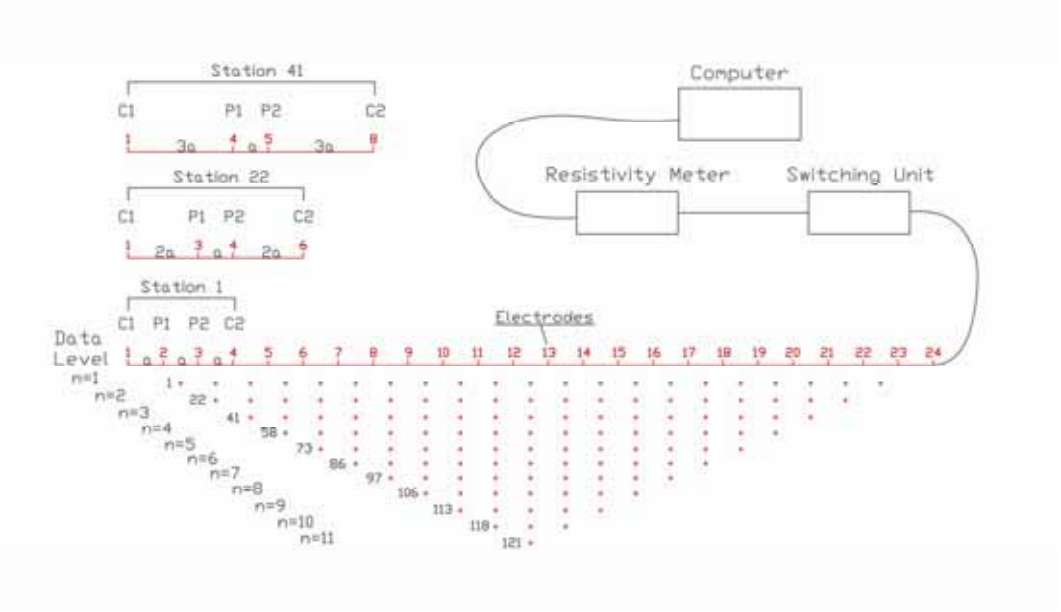

Fig. 2.18*: Example of electrical resistivity array equipment. 24 mini-electrodes connected by a multi-cable to the automatic switching unit and a resistivity meter supported by software. The switching unit selects the proper electrodes following the Wenner-Schlumberger measurement scheme; the resistivity meter records the potential difference and the software elaborates the data giving the electrical resistivity 2-D pseudosection image.*

2.4 Pollutant Used in the Physical Model

The pollutant used in this study was diesel which, when it is leaked in the soil, undergoes phase partitioning between gas, aqueous phases and a Light Non-Aqueous Phase Liquid (LNAPL) (Mayr and Hassnizadeh 2002).

Laboratory and field-scale experiments (e.g. Gajdos et al. 1995; Vanhala 1997) suggest that adding a small percentage of diesel to soil causes a remarkable decrease in resistivity (i.e. 15-30%). This results in an increase in hydrocarbons and, in some cases, hysteresis effects on the resistivity values were noted when pure water was added to the soil (Knight 1991). Conversely, in field observations the low resistivity value was due to a LNAPL of the diesel present in the subsurface (Sauck 2000).

In the current study two different modes of diesel spillage were adopted to investigate the migration and distribution of this pollutant plume. One controlled spillage of contaminant was simulated in the superficial (i.e. Zone A *Fig. 2.19*), unsaturated zone above the water table where it was expected that the contaminant would move predominantly in a vertical direction under the influence of gravity. In theory, capillarity forces would be expected to spread the pollutant laterally, displacing air due to its low density and viscosity (Sauck 2000; Mayr and Hassnizadeh 2002). When the contaminant is present in significant quantities, it can reach the capillarity fringe, where it starts to accumulate. Subsequently the contaminant should displace water from the capillarity and saturated zones, thereby penetrating the water table. It was expected that the pollutant would form a film that gradually spreads with the downstream groundwater flow and, when the spillage stops, the portion of pollutant that penetrates the saturated zone should be progressively removed by water.

A second controlled spill was simulated at a deeper level of the groundwater (i.e. Zone B *Fig. 2.19*). Due to the low density of diesel it was expected that it would rise to the surface through the soil pores, displacing the water present. It was also predicted that, simultaneously, a contaminated plume would be formed between the spillage point and the groundwater surface in the direction of downstream water flow.

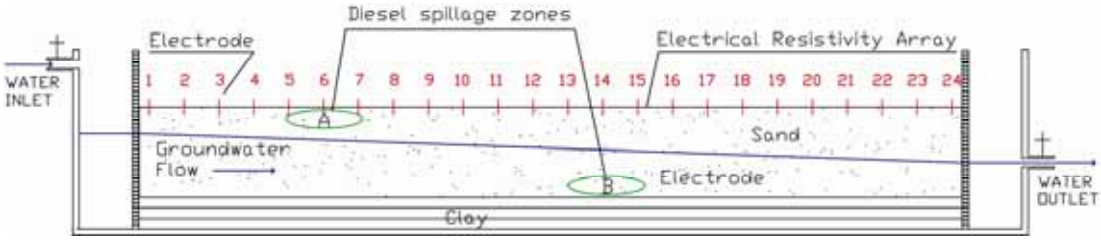

Fig. 2.19*: Controlled spillages of contaminant in the superficial and, unsaturated zones above the water table (Zone A) and at a deeper level of the groundwater on the bottom of the sandy layer (Zone B).*

2.4.1 Diesel Characteristics

A specific fraction of fuel oil from petroleum and a hydrocarbon mixture of thousands of individual compounds, most with carbon numbers between 10 and 22, is obtained when crude oil is distilled between 200°C and 350°C at atmospheric pressure. Most of these compounds are members of the paraffinic, naphthenic or aromatic class of organic hydrocarbons. These three classes of hydrocarbons have different chemical and physical properties (Baha et al. 1998):

- **Paraffins** have the general formula C_nH_{2n+2}, where "n" is the number of carbon atoms *(carbon number)* in the molecule. There are two subclasses of paraffins: *normal paraffins* and *isoparaffins*. Normal paraffins have carbon atoms linked to form chain-like molecules, with each carbon, except those at the ends, bonded to two others, one on either side. *Isoparaffins* have a similar carbon backbone, but they also have one or more carbons branching off from the backbone. Normal decane and 2,4-dimethyloctane have the same chemical formula, $C_{10}H_{22}$, but different chemical and physical properties. Compounds like this, with the same chemical formula but a different arrangement of atoms, are called *structural isomers*.

- **Naphthenes** have some of their carbon atoms arranged in a ring. The naphthenes in diesel fuel have rings of five or six carbons. Sometimes two or more rings are fused together, with some carbons shared by adjacent rings. *Naphthenes* with one ring have the general formula C_nH_{2n}.

- **Aromatics** have some of the carbon atoms arranged in a ring, but they are joined by aromatic bonds, not the single bonds found in naphthenes. Aromatic hydrocarbon rings contain six carbon atoms. *Benzene* is the simplest aromatic compound. Its structure was originally conceptualized as two equivalent structures with alternating single and double bonds. Each structure continually transformed itself into the other as the double bonds flipped back and forth between different pairs of carbon atoms. The

shorthand representation of benzene is a hexagon with a circle inside representing the aromatic bonds. One-ring aromatics have the general formula CnH2n-6. *Polycyclic aromatics* are compounds with two or more aromatic rings. These rings are often fused together, with some carbons being shared by adjacent rings. Paraffins and naphthenes are classified as *saturated hydrocarbons* because no more hydrogen can be added to them without breaking the carbon backbone. Aromatics and olefins are classified as *unsaturated hydrocarbons*. They contain carbon to carbon double bonds or aromatic bonds that can be converted to single bonds by adding hydrogen atoms to the adjacent carbons. When straight-chain olefins are saturated with hydrogen, they become paraffins. When aromatics are completely saturated with hydrogen, they become naphthenes; when they are partially saturated, they become cyclic olefins (Baha et al. 1998).

2.4.1.1 Diesel Properties

The following lists key properties of diesel:

- **Density:** For compounds of the same chemical class, density increases with carbon number. For compounds with the same carbon number, the order of increasing density is paraffin, naphthenes, and aromatics (*Tab. 2.1*) (*Fig.2.20*).

Compound	Hydrocarbon Class	Carbon Number	Density, 20°C, g/cm³
Naphthalene	Aromatic	10	1.175
Tetralin	Aromatic	10	0.9695
1, 3-Diethylbenzene	Aromatic	10	0.8639
n-Butylcyclohexane	Naphthene	10	0.7992
n-Pentylcyclopentane	Naphthene	10	0.7912
Decane	n-Paraffin	10	0.7301
2, 2-Dimethyloctane	Isoparaffin	10	0.7245
Anthracene	Aromatic	14	1.251
n-Nonylbenzene	Aromatic	15	0.8558
n-Nonylcyclohexane	Naphthene	15	0.816
n-Decylcyclopentane	Naphthene	15	0.811
n-Pentadecane	n-Paraffin	15	0.7684
n-Tetradecylbenzene	Aromatic	20	0.8549
n-Tetradecylcyclohexane	Naphthene	20	0.825
n-Pentadecylcyclopentane	Naphthene	20	0.8213
Eicosane	n-Paraffin	20	0.7843

***Table 2.1**: Density for representative diesel fuel hydrocarbons (Baha et al. 1998).*

Fig. 2.20*: Diesel on the top of the water table.*

- **Thermal expansion:** Like all liquids, diesel fuel slightly expands in volume as its temperature increases. The *coefficient of thermal expansion* measures the rate of expansion; a typical value for diesel fuel is 0.00046 cc per degree Fahrenheit.

- **Viscosity:** This is primarily related to molecular weight and not so much to hydrocarbon class. For a given carbon number, naphthenes generally have slightly higher viscosities than paraffins or aromatics (*Tab.2.2*).

- **Water solubility of diesel fuels**: This varies depending on factors such as the salinity of the water, the temperature and the concentration of hydrocarbons with long chains. At room temperature, it is within the range of 0.37-0.53 mg/litre in sea water (Boehm and Quinn 1974) and 0.7-11 mg/litre in tap water (Lysyj & Russell, 1974) (*Tab.2.2*).

Solubility and Viscosity of Representative Petroleum Products		
Product	**Solubility in cold water (at 20°C in ppm)**	**Viscosity in Centistokes**
Gasoline	50-100	0.5-0.6
1-Pentene	150	n/a
Benzene	1,791	0.5
toluene	515	0.5
Ethylbenzene	775	0.6
Xylenes	150	0.6
n-Hexene	12	0.4
Cyclohexane	210	n/a
i-Octane	0.008	n/a
JP-4 Jet Fuel	< 1	0.8-1.2
Kerosene	< 1	1.5-2
Diesel	< 1	2-4
Light Fuel Oil #1 and #2	< 1	1.4-3.6
Heavy Fuel Oil #4, #5 & #6	< 1	5.8-194
Lubricating Oil	< 0.001	400-600
Used Oil	< 0.001	40-60
Methanol	> 100,000	< 0.1

***Table 2.2**: Solubility and viscosity values of representative petroleum products (United-Tech 2007).*

2.4.2 Behaviour of Diesel in the Soil

The movement of diesel fuel spilt in the soil is directly correlated with its kinematic viscosity (i.e. 2-4 cSt at 20°C) (United-Tech 2007). It is higher than water viscosity (i.e. 1.003 x 10^{-3} Pa.s at 20°C) (Lide 1993). Similarly, the rate of percolation of diesel into soil is about half that of water (Stone, 1991). In effect, soil contaminated with diesel fuel acts like a filter that separates individual constituents on the basis of their adsorption. The movement of the diesel is also dependent on the moisture content of the soil. With increasing moisture content, the penetration rate of non-volatile components through the soil increases and the adsorption of more volatile components decreases. In contrast, upward mobility of the individual volatile and non-volatile constituents of the fuel decreases with increasing moisture content (Rosner 1996).

An indicator of the migration of substances into groundwater is the *retardation coefficient* (Rd) (i.e. *Rd= 1+(K_d x bulk density of soil)/porosity*; where k_d = *Partition Coefficient*). Considering the water Rd equals 1, *Tab.2.3* shows the calculated Rd from the adsorption isotherms of individual diesel constituents (Stone 1991):

Retardation Coeff. of individual diesel constituents		
Constituent	**Rd**	**Mobility**
fluorene	>100	low
phenanthrene	>100	low
pyrene	>100	low
benzanthracene	>100	low
benzo[*a*]pyrene	>100	low
fluoranthene	>100	low
naphthalene	100>Rd>10	medium
dimethylbenzenes	100>Rd>10	medium
ethylbenzene	100>Rd>10	medium
toluene	100>Rd>10	medium
benzene	<10	high
quinoline	<10	high
cresols	<10	high
phenol	<10	high

Table 2.3*: Retardation coefficient solubility and viscosity values of individual diesel components from representative petroleum products (Rosner 1996).*

2.5 Oxygen Release Compound Used in the Laboratory Model

There are several remedial technologies for contaminated land, however there is no one technology that can be applied to all contaminated land scenarios. Therefore, each reclamation case must be examined individually in order to identify the specific remedial technology requirements (Soesilo and Wilson 2000; Sharma and Reddy 2004).

Technologies used to remove and destroy the pollutants are defined on the basis of the groundmass to be reclaimed. The reclamation treatments are divided in two large classes: 'in-situ' and 'ex-situ'. In-situ methods do not involve contaminated soil or water to be removed where as, ex-situ methods, the contaminated material is removed and decontaminated with specific methods. This ex-situ method can take place either 'on-site' in the area to be reclaimed or 'off-site' when the reclamation action takes place outside of the contaminated area (CIRIA 1995).

This research, as described in Section 1, aims also to monitor the changes of the electrical resistivity value in the model caused by the presence of "*Oxygen Release Compound Advanced* by Regenesis®" injected in 24 mini-boreholes to simulate a permeable reactive barrier.

Permeable reactive barriers have opened up new horizons for 'in-situ' contaminated land reclamation treatments. It proposes a valid and economic alternative to the conventional remediation systems (Gavaskar et al. 1998, US.EPA 1998, Di Molfetta and Sethi 2005).

In its simplest form a reactive barrier is formed by a treatment zone (i.e. gate) perpendicular to the groundwater flow. The treatment zone can be made with several reactive materials (e.g. granular iron; activated carbon; zeolite; amorphous iron oxide; oxygen release compound; etc.) (CIRIA 1995, Gavaskar et al 1998, Sharma and Reddy 2004; Regenesis 2005). The pollutants are degraded, adsorbed or precipitated depending on the reactive materials used and the main benefit of this remediation system is that it doesn't require an external energy source because after its installation the barrier works passively (CIRIA 1995, US.EPA 1998).

2.5.1 Oxygen Release Compound Description

Oxygen Release Compound – Advanced (***ORC-Adv***) is a mixture of Calcium OxyHydroxide [$CaO(OH)_2$] and Calcium Hydroxide [$Ca(OH)_2$] (Regenesis 2007) and it is projected to treat 'in situ' soil and groundwater contaminated by petroleum hydrocarbons.

This compound involves intercalated (embedded) phosphates (i.e. Dipotassium Phosphate [HK_2O_4P]; Monopotassium Phosphate [H_2KO_4P]) (*Fig.2.21*) into the crystal structure of solid peroxygen molecules.

These phosphate ions slow the rate of hydration that liberates oxygen and forms exit pathways for the oxygen in an otherwise tightly packed crystals. These crystals can become even more "locked-up" when hydroxides begin to form as a reaction by-product following oxygen liberation and optimizes in this process peroxygen performance.

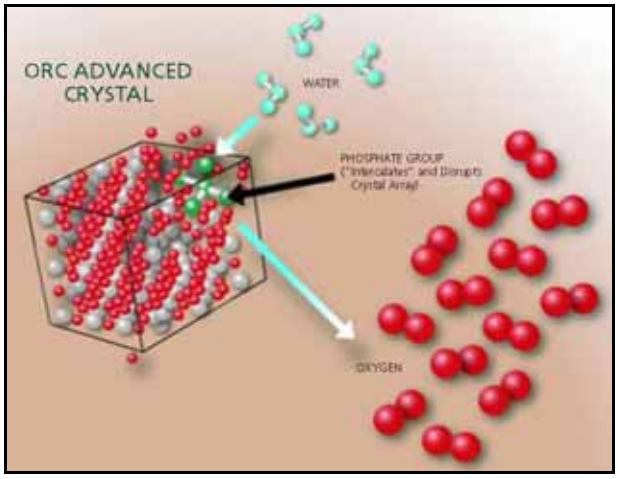

Fig. 2.21*: ORC-Adv Crystal that optimize peroxygen performance (Regenesis 2008).*

This compound formulation also minimizes "bubble off" which can waste the majority of oxygen available in common solid peroxygen chemicals, offering maximum oxygen release for periods up to 12 months on a single injection and minimizing oxygen waste while maximizing contaminated site remediation (Regenesis 2008).

The characteristics of this product improve and implement the bioremediation processes because, releasing its full amount of oxygen (17% by weight) over long period of time, allow to the aerobic microbes to accelerate the rates of natural attenuation degrading and removing pollutants from groundwater and soil.

Biodegradation can be part of the natural attenuation process that includes processes like dispersion, dilution and adsorption. All these processes reduce the contaminant concentrations in the soil but only biodegradation is able to physically degrade and destroy the pollutants (Sharma and Reddy 2004).

2.5.2 ORC-Adv dose rate for barrier application

For field based applications ***ORC-Adv*** can be mixed with water for slurry injection into the saturated zone for plume area treatment, source treatment, barrier treatment or added as backfill to excavations.

Design of the ***ORC-Adv*** bioremediation approach depends on the *volume of the aquifer* or vadose zone requiring treatment, *hydraulic characteristics* such as groundwater velocity, *site hydrogeology*, *contaminant plume constituents*, and *treatment goals* that generally take into account regulatory requirements and the responsible party's time frame for remediation (*Tab.2.4*) (Regenesis 2005).

Site Parameters for ORC-Adv Remediation Method	
Extend of impacted groundwater data	Volume of the aquifer
	Plume width, length and thickness
Hydro-geologic data	Soil type
	Groundwater dept
	Hydraulic conductivity
	Groundwater fluctuation
	Total and Effective porosity
	Seepage velocity
Contaminant constituents	Contaminant concentration within the plume area
	Dissolved phase concentration

Table 2.4*: Site parameters involved for ORC-Adv remediation process.*

For a barrier design the first stage in the ***ORC-Adv*** dose rate calculation is to determine the ***Contaminant Loading*** (kg/yr) following *Equation 13* (Crowley 2008):

Contaminant Loading *(kg/yr) = [Dissolved phase conc (mg/l)] x [Width of plume (intersecting gw flow direction) (m)] x [Thickness of contaminated saturated zone (m)] x [seepage velocity (m/day)] x [Effective Porosity] / (1000) x 365*

Equation 13

subsequently the **ORC-Advanced dose** can then be calculated as follows (*Equation 14*) (Crowley 2008):

ORC-Adv *= [Contaminant load (kg/yr)] x [3.2 (Stoichiometry (wt/wt) O2/contam.)] x [5.9 (ORC-A contains 17% oxygen, this 100 /5.9 = 17%)]*

Equation 14

In real cases a safety factor of between 2÷5 is applied, which takes into account heterogeneities in site conditions during field applications. It might be worth while if possible to consider a safety factor of 1.5÷2.

For a sand aquifer, a 30% solids mix of ***ORC-Adv*** and water is proposed. The slurry injection strategy for barrier installation is based upon the site litology. Also, the injection point spacing depends on aquifer permeability, groundwater velocity and for a sandy aquifer generally 2.4÷3.75 m spacing is used (Regenesis 2005).

2.5.3 ORC-Adv dose rate for barrier application in laboratory model

In Section 2.4 is reported that the pollutant (i.e. Diesel) in the laboratory model was spilt once on surface of the sandy layer (i.e. Source Zone A) (*Fig.2.19*) and once in the base of the sandy layer (i.e. Source Zone B) in July 2007 (see Section 1).

The barrier was planned to be located perpendicular the groundwater flow, just in Source Zone B in order to treat the pollutant present in this area and the pollutant that passed through the barrier breaking the contaminated plume (*Fig.2.22*).

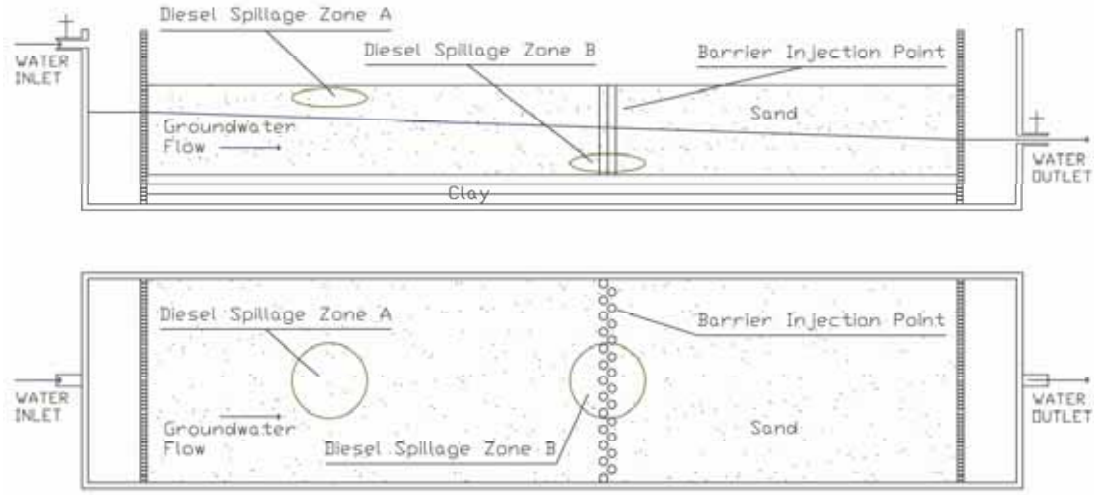

***Fig. 2.22**: Elevation and plan of the laboratory model with barrier location and diesel spillage Zone A-B location.*

Some soil and water specimens were sampled in the area where the pollutant was spilt (i.e. Source Zone A-B) before the ORC-Adv injection and further water specimens were collected also upstream and downstream the barrier location after ORC-Adv injection (*Fig. 2.23*).

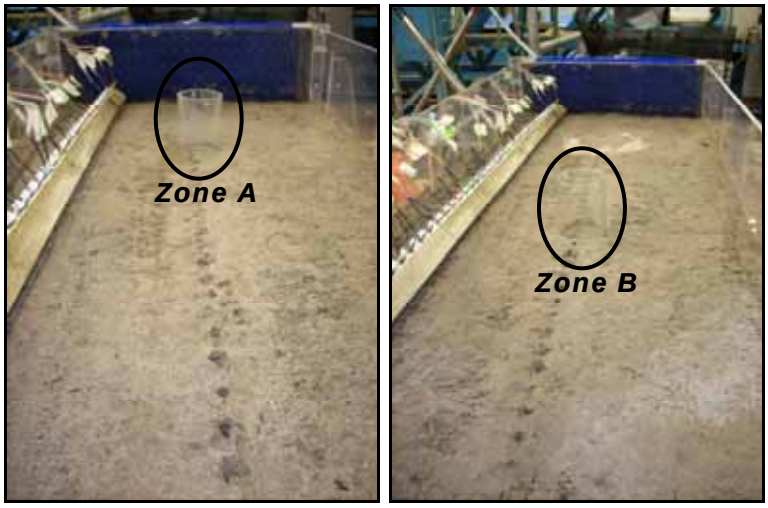

***Fig. 2.23**: Location of Zona A-B where water and soil specimens were sampled in order to determine the pollutant concentration before barrier installation.*

In this research the formulas of ***Contaminant Loading*** and ***ORC-Adv Dose*** used for field based application were adapted to the laboratory model and the following assumptions were done:

- Width of the contaminant plume was assumed equal to the tank's width (i.e. 0.6 m).

- Thickness of the contaminated saturation zone was assumed equal to the thickness of the sandy layer (i.e. 0.2 m).

- Effective porosity equal to 0.1 (Ref. McWorter, D.B., and D.K. Sunada, 1977, *Groundwater Hydrology and Hydraulics*, Water Resources Publications, Fort Collins, Colo).

- Seepage velocity equal to 0.5 m/day.
- Pollutant concentration in the water passing through the barrier equal to the pollutant concentration in the water sampled in Source Zone A (i.e. 5 mg/l).

- Pollutant concentration in the water present in the barrier location equal to the pollutant concentration in the water sampled in Source Zone B (i.e. 2.5 g/l).

- Pollutant concentration in the soil present in the barrier location equal to the pollutant concentration in the soil sampled in Source Zone B (i.e. 31 mg/kg).

- Homogeneous soil conditions with safety factor equal to 1.

Summary of Laboratory model parameters for *Contaminant Loading* (kg/yr) calculation			
Extend of impacted groundwater data	Width plume		*0.6 m*
	Thickness contaminated zone		*0.2 m*
Hydro-geologic data	Effective porosity		*0.1*
	Seepage velocity		*0.5 m/day*
Contaminant constituent	Contaminant concentration within the plume area	Hydrocarbons >12 in water sample Zone A	*5 mg/l*
		Hydrocarbons >12 in water sample Zone B	*2.5 g/l*
		Hydrocarbons >12 in soil sample Zone B	*31 mg/kg*

***Table 2.5**: Laboratory parameters involved for ORC-Adv remediation process.*

On the basis of the previous assumptions the contaminant loading was calculated considering:

1. ***Contaminant Loading*** in the water that passes through the barrier over one year equal to ***10.95 g/yr***
2. ***Contaminant Loading*** in the water present in the barrier installation area equal to ***1.5 g***
3. ***Contaminant Loading*** in the soil present in the barrier installation area equal to **0*.316 g***

Total ***Contaminant Loading*** to be treated is equal to ***12.766 g/yr.***

Using *Equation 14*, the ***ORC-Adv Dose*** was then calculated and it was equal to ***241 g***.

To provide an oxygen barrier the ***ORC-Adv Dose*** (i.e. 241 g ; 30%) was mixed with 563 g of water (i.e. 70%) and the resulting slurry was injected in 24 mini-boreholes, 1cm diameter perpendicular to the groundwater flow using two rows of injection point 2.5 cm spaced (*Fig.2.24*).

Fig. 2.24*: Location of 24 mini-boreholes before and after ORC-Adv injection.*

2.6 Model Performance and Data Acquisition

The physical model used in the current study was designed to detect the mode of pollutant (i.e. diesel) diffusion under different conditions by changing the following parameters: groundwater level, two different kinds of spillage in different locations and different spillage durations. It was designed also to detect and monitor the effects of a remediation action (i.e. permeable reactive barrier) on the electrical resistivity values and on the physical-chemical parameters (i.e. Dissolved Oxygen; Conductivity; pH).

Firstly, the data acquisition phase began by determining the hydrological model conditions. As already reported in *Section 2.3.2 & 2.3.4*, the process of layering the soil used in this model inherently means that factors such as grain packing, permeability and moisture content are different from natural conditions. It is important to emphasise, however, that sieving the soil in several layers along with the water action resulted in its own 'natural' packing (*Fig. 2.18 - Section 2.3.4*).

At the end of the construction phase of the model, the groundwater level was fixed at 15 cm from the base in the "water in" section and at 13 cm from the base in the "water out" section. Assuming that the clay layer is impermeable, the unconfined aquifer with a continuous steady groundwater flow is only in the sandy layer and the quantity of water flowing through the left hand side of the model is equal to that flowing through the right hand side, the ***Hydraulic Conductivity*** of the model was determined using Darcy's Law:

$$K = \frac{-Q}{A(\frac{h_a - h_b}{L})}$$

Equation 15

where $\boldsymbol{Q}$ (cm^3/s) is the water flow through the aquifer; $\boldsymbol{A}$ (cm^2) is the area of the saturated sandy layer; $\boldsymbol{h_a - h_b/L}$ (dimensionless) is the *hydraulic gradient* with $\boldsymbol{h_a}$ (cm) and $\boldsymbol{h_b}$ (cm) representing the difference in height between the "water inlet" and

"water outlet" model sections at **L** (cm) distance, i.e. the main length of the model section containing the soil.

Prior to leaking the diesel into the soil, a series of measurements were taken in order to delineate the baseline parameters when the model was at a steady state, i.e. at constant low groundwater flow. This allowed the baseline parameters of the model such as the electrical resistivity of the medium to be related to the physical-chemical groundwater parameters, where no pollutant is present. During week one, 500 ml of diesel was spilt onto the soil surface for 24 hours using a vertical plastic measuring cylinder with four pipes (*Fig.2.25)* buried in the soil at a depth of 4 cm, depositing the pollutant in the sandy layer (i.e. Zone A) (*Fig.2.19* – Section 2.4; *Fig.2.26*). During the next 24 hour period, a further 500 ml of diesel was spilt onto the surface and, simultaneously, 500 ml was spilt in the middle of the sandy model layer (near the top of the clay layer)(i.e. Zone B *Fig.2.19* – Section 2.4) at the dept of 20-22 cm using a syringe with a long needle (*Fig.2.27*).

Fig. 2.25*: Cylinder to spill pollutant in the sandy layer.*

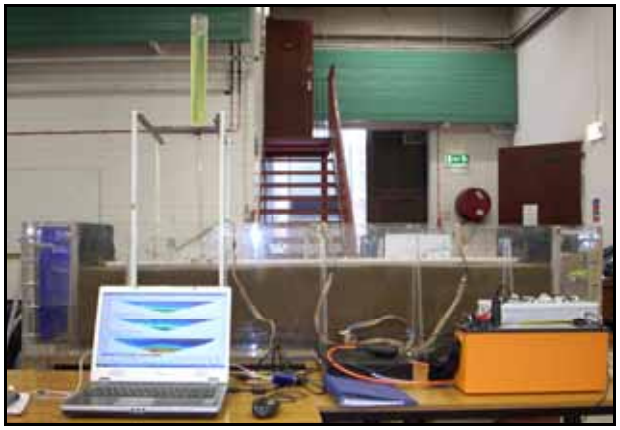

Figs. 2.26 & 2.27*: Spilling phase on top of the sandy layer using a measuring cylinder and, on the bottom of the sandy layer, using a syringe with a long needle.*

Forty-eight hours after the leakage phase, the water level was considerably elevated for the subsequent 36 hours in order to increase the groundwater flow in the model (to 23 cm from the base at the "water in" side of the model and 15 cm from the base at the "water out" side of the model).

During the first weekend the model was run again at the original low water levels for 64 hours and, thereafter, it constantly functioned at high groundwater level until the study was completed (i.e. 29th Jun. 2008) (*Tab. 2.6*).

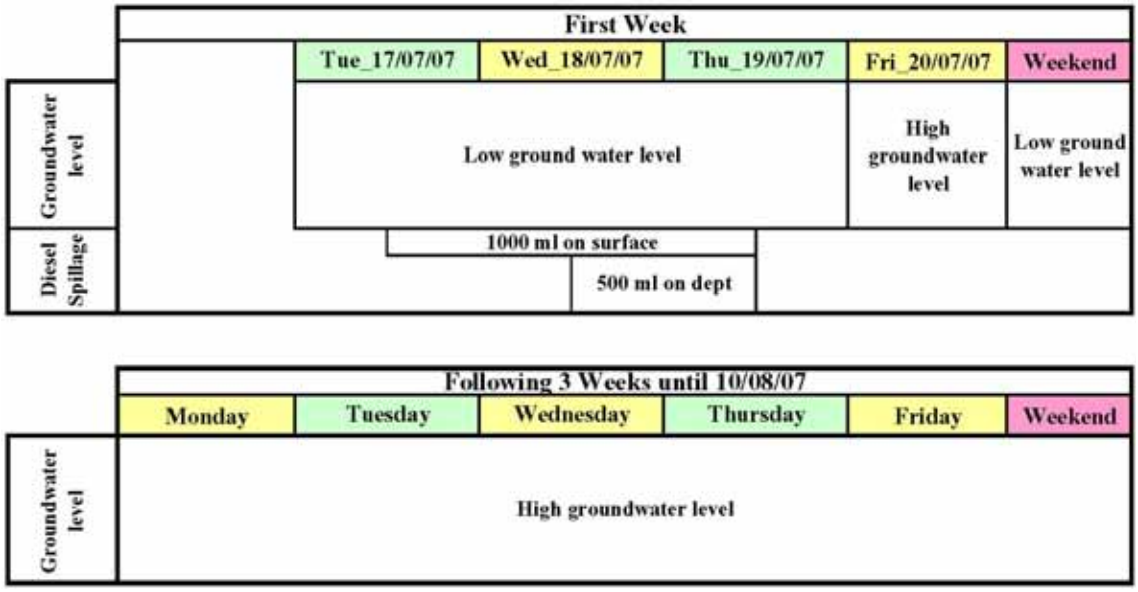

Table. 2.6*: Diesel spillages in two different areas of the model and water level changes during the study period.*

2.6.1 Electrical Resistivity Measurement

The electrical array with mini-electrodes 5 cm long, made of copper were fixed along a wooden bar at a constant spacing (*see Sector 2.2*). These were inserted into the soil, to a depth of 3 cm in the centre section of the model *(Fig. 2.28)*. The electrical resistivity was measured at regular time intervals (i.e. two electrical resistivity surveys per day during the first week; one electrical resistivity survey per day during following the three weeks) throughout this study period.

Fig. 2.28*: The electrical array with mini-electrodes 5 cm long inserted in the soil to a depth of 3 cm in the centre section of the model.*

The first measurement was taken to obtain the baseline of electrical resistivity in the model before diesel spillage to provide the necessary information for data analysis. During week one, these measurements were carried out twice per day at about 9.00 a.m. and 5.00 p.m. to ensure the consistency of detected resistivity changes. Subsequently, when the leaking phases finished and the hydraulic conditions in the model were maintained at a constant level, the measurements were taken only once per day at 9.00 a.m. for four weeks.

After this first monitoring period (i.e. 17/07/07 to 10/08/07), while the groundwater continuously flowed in the laboratory model, a new monitoring campaign (i.e. physical-chemical parameters; electrical resistivity survey) started at the 11th Jan. 2008 and the electrical resistivity of the model was measured once per week until the 27th Jun. 2008 using an array with 48 mini-electrodes.

2.6.2 Physical-chemical Measurements during the first Monitoring Campaign

Before commencing the leakage phase and after the groundwater level was fixed, three water samples were taken in order to define the chemical baseline characteristics of the water used in the model:

- ***Sample 1***: tap water before coming into contact with the model soil;
- ***Sample 1A***: water specimen taken in the sandy layer at approximately 11-12 cm from the model base and at 10 cm from the "water in" section, using a syringe with a long needle (*Fig.2.29*);
- ***Sample 1B***: water specimen taken in the sandy layer at approximately 11-12 cm from the model base and at 10 cm from the "water out" section using a syringe with a long needle.

Fig. 2.29*: Syringe with a long needle used to sample the groundwater with minimal disturbance to the physical-chemical trim of the model.*

The chemical analysis of the water samples was carried out by Dr. Franco Mazzotta at the "*Studio Effemme, Lecce, Italy*". The results are reported in *Appendix B*). Parts of the same samples were also used *in situ* (i.e. ***Samples 1a-1b***) in Glasgow to examine the pH, conductivity and dissolved oxygen using a field equipment probes.

In order to check if there was any trace of pollutant in the groundwater after 24 hours, after the 500 ml of diesel had been spilt on the surface, two other sets of water samples were taken for laboratory and field analysis. ***Sample 2A; Sample 2B – Sample 2a; Sample 2b*** and ***Sample 3A; Sample 3B – Sample 3a; Sample 3b*** were taken when the maximum spillage of diesel ceased at 1 litre on the surface near the electrode number 6 and at 500 ml from the base of the groundwater flow in the centre of the model. Additionally, two water samples were taken daily to continuously monitor the *in situ* groundwater parameters (i.e. pH; conductivity; dissolved oxygen). The final groundwater samples (i.e. ***Sample 4A; Sample 4B***) were taken 96 hours after the previous sampling again to detect signs of diesel in the groundwater.

2.6.2.1 *Moisture Content Measurements*

The moisture content on the surface of the sandy layer was measured at steady state (i.e. 14 cm depth near the "water inlet" sector; 16 cm depth near the"water outlet" sector) before starting the leaking phase and again, 24 hours later when the groundwater was raised to the maximum level (i.e. 6 cm depth near the "water inlet" sector; 14 cm depth near the "water outlet" sector) (*Fig.2.30*).

Fig. 2.30*: Moisture content meter used to determine the moisture in the sandy and clay soil in different model zones and with different groundwater levels*.

Table 2.7 summarises the model performance and the timing of all measurements during the first monitoring campaign (i.e. 17/07/07 to 10/08/07)

.

	First Week					
		Tue_17/07/07	Wed_18/07/07	Thu_19/07/07	Fri_20/07/07	Weekend
Goundwater level		Low ground water level			High groundwater level	Low ground water level
Diesel Spillage		1000 ml on surface				
				500 ml on dept		
Array		9.00 **07_17**; 16.30 **07_17a**	8.50 **07_18**; 16.30 **07_18a**	9.30 **07_19**; 17.00 **07_19a**	9.00 **07_20**; 17.00 **07_20a**	
Water Sample (Field)		10.00 **Sample 1-1a-1b**	9.00 **Sample 2a-2b**	9.00 **Sample 3a-3b**	10.00 **Sample 4a-4b;**	
Mointure Content	**Moins Cont 1** (on the clay layer)	**Moins Cont 2**				

	Second Week					
	Mon_23/07/07	Tue_24/07/07	Wed_25/07/07	Thu_26/07/07	Fri_27/07/07	Weekend
Goundwater level	High groundwater level					
Array	8.30 **07_23**	9.00 **07_24**	10.00 **07_25**	9.00 **07_26**	9.00 **07_27**	
Water Sample (Field)	10.00 Sample **5a-5b**	10.00 **Sample 6a-6b**	10.00 **Sample 7a-7b**	10.00 **Sample 8a-8b**	10.00 **Sample 9a 9b**	
Mointure Content		**Moins Cont 3**				

***Table. 2.7a**: Summary of events (i.e. diesel spillages, water level changes) involved in the model during the first and second week of the first monitoring campaign(i.e. 17/07/07-10/08/07).*

	Third Week					
	Mon_30/07/07	**Tue_31/07/07**	**Wed_01/08/07**	**Thu_02/08/07**	**Fri_03/08/07**	**Weekend**
Goundwater level	**High groundwater level**					
Array	10.00 **07_30**	9.00 **07_31**	9.00 **08_01**	10.30 **08_02**	9.00 **08_03**	
Water Sample (Field)	10.00 **Sample 10a-10b**	10.00 **Sample 11a-11b**	10.00 **Sample 12a-12b**	10.00 **Sample 13a-13b**	10.00 **Sample 14a-14b**	
Mointure Content						

	Fourth Week					
	Mon_06/08/07	**Tue_07/08/07**	**Wed_08/08/07**	**Thu_08/08/07**	**Fri_10/08/07**	**Weekend**
Goundwater level	**High groundwater level**					
Array	09.15 **08_06**	09.15 **08_07**	09.15 **08_08**	09.15 **08_09**	09.15 **08_010**	
Water Sample (Field)	10.00 **Sample 15a-15b**	10.00 **Sample 16a-16b**	10.00 **Sample 17a-17b**	10.00 **Sample 18a-18b**	10.00 **Sample 19a-19b**	
Mointure Content						

Table. 2.7b*: Summary of events (i.e. diesel spillages, water level changes) involved in the model during the third and fourth week of the first monitoring campaign(i.e. 17/07/07-10/08/07).*

2.6.3 Physical-chemical Measurements during the Second Monitoring Campaign

Before introducing the remediation action (i.e. Permeable reactive barrier made with ORC-Adv) into the model, a new monitoring campaign of the physical-chemical parameters (i.e. pH; Conductivity; Dissolved Oxygen) started in the 11th January 2008. Once per week water samples were collected in the "water inlet side" and in the "water outlet side" of the model using the same procedure already used during the first monitoring campaign (see *Sector 2.6.2*). Two days before the permeable barrier was installed (i.e. 22th May 2008) two water and soil samples (i.e. Water and Soil Samples Zone A-B) were collected in the areas (i.e. Zone A-B) of the model (Fig.2.23 *Section 2.5.3*). In July 2007 the diesel was spilt in order to determine (i.e. "*Studio Effemme, Lecce, Italy*") the pollutant concentration (i.e. Total

Hydrocarbon Content *THC*) still present in those areas. Five weeks after the barrier was installed, two extra water samples (i.e. Water upstream and downstream) were collected in order to monitor the *THC* concentration during the barrier performance.

Table 2.8 summarises the model performance and the timing of all measurements during the second monitoring campaign (i.e. 11/01/08 to 27/06/08).

	Jaunuary 2008				
		2nd week	3rd week	4th week	
Goundwater level	High groundwater level				
Array		01_11	01_18	01_25	
Water Sample (Field)		Sample 01-11a-b	Sample 01-18a-b	Sample 01-25a-b	

	February 2008				
	1st week	2nd week	3rd week	4th week	5th week
Goundwater level	High groundwater level				
Array	02_01	02_08	02_15	02_22	02_29
Water Sample (Field)	Sample 02-01a-b	Sample 02-01a-b	Sample 02-15a-b	Sample 02-22a-b	Sample 02-29a-b

	March 2008				
	1st week	2nd week	3rd week	4th week	
Goundwater level	High groundwater level				
Array	03_07	03_14	03_17	03_28	
Water Sample (Field)	Sample 03-07a-b	Sample 03-14a-b	Sample 03-17a-b	Sample 03-28a-b	

	April 2008				
	1st week	2nd week	3rd week	4th week	
Goundwater level	High groundwater level				
Array	04_04	04_11	04_18	04_25	
Water Sample (Field)	Sample 04-04a-b	Sample 04-11a-b	Sample 04-18a-b	Sample 04-25a-b	

	May 2008				
	1st week	2nd week	3rd week	4th week	5th week
Goundwater level	High groundwater level				
Array	05_02	05_09	05_16	05_26	05_30
Water Sample	Sample 05-02a-b	Sample 05-09a-b	Sample 05-16a-b	Sample 05-26a-b	Sample 05-30a-b
Water & Soil Sample (Lab)			Water & Soil 05-16A-B		

	June 2008				
	1st week	2nd week	3rd week	4th week	
Goundwater level	High groundwater level				
Array	06_06	06_13	06_20	06_27	
Water Sample (Field)	Sample 06-06a-b	Sample 06-13a-b	Sample 06-20a-b	Sample 06-27a-b	
Water Sample (Lab)				Water 06-27A-B	

Table 2.8: *Summary of events (i.e. water level; barrier installation) involved in the model during the second monitoring campaign (i.e. 11/01/08-27/06/08).*

Chapter 3: Data Collection, Analysis and Discussion

Data collected during this study is divided into four different groups on the basis of their origins:

1. Data related to characteristics of the materials used in the physical model (i.e. soil particles size; specific gravity; moisture content);

2. Data related to hydraulic characteristics of the model (i.e. hydraulic conductivity; water level; seepage velocity; volume of the aquifer);

3. Data related to characteristics of the groundwater samples (i.e. water conductivity; dissolved oxygen; pH; chemical concentrations);

4. Data related to electrical resistivity measurements (i.e. apparent resistivity).

The data analysis followed several steps:

- Observation and checking of raw data in context and evaluation of occasional anomalous data;

- Calculation of summary statistics pertaining to the raw data (e.g. mean; median; range etc.) and graphical representation (i.e. histograms; box plots etc).

- Elaboration of raw data in order to determine more useful information (i.e. mathematics subtraction of numerical data belonging to different datasets).

- Comparison of datasets with the same origin (e.g. water parameters relating to different time periods) and comparison of datasets with different origins (e.g. chemical-physical trends of the water parameters versus the trend of the electrical resistivity data during the same period of time).

3.1 Data related to Hydraulic Characteristics of the Model

As detailed in *Section 2.3.1 & 2.3.3,* during the construction phase of the model data was collected to describe the characteristics of the soils used (e.g. sand and clay characteristics). Before collecting experimental data, and during model operation, the groundwater flow was always calculated by measuring the water flow (i.e. ***Q***) and its ***Hydraulic Conductivity*** using *equation 15* (see *Section 2.6*). At the

steady state, when groundwater flow is determined by the different water levels 2 cm from each end of the model, the ***Q*** value was ***1.96x10^{-4} l/s***. This means that under these conditions almost ***16.9 litres*** of water passed through the model in 24 hours. Assuming the groundwater flowed only through the saturated part of the sandy layer (i.e. on average 14 cm above the bottom of the model) and again applying *equation 14*. The ***Hydraulic Conductivity*** was equal to ***0.039 cm/s***. Under these conditions the moisture content on the surface of the sandy layer measured with the moisture content meter AT-Theta Kit^{R} was equal to 41% of that at the "water in" side of the model and 38% of that at the "water out" side. When the water level was raised to 23 cm from the base at the "water in" side of the model and to 15 cm from the base at "water out" side; the ***Q*** value measured for the "water out" section was ***5.88x10^{-4} l/s*** and ***50.8*** litres per day. In this case the ***Hydraulic Conductivity*** was equal to ***0.017 cm/s***.

When the water level was raised during the first few minutes, groundwater appeared on the soil surface, visually highlighting the increase of water in the model. This phenomenon disappeared the day after but the moisture content on surface was nevertheless high, especially near the water input side (i.e. 45% saturated) indicating that the capillary fringe was so wide at soil surface that it probably almost totally saturated the sandy layer. This was confirmed during the diesel spillage. In fact, since the diesel is lighter than water, whether it was spilt on the surface or deep beneath it, in both cases it saturated the sandy sediment or floated above the groundwater, soon appearing on surface (*Fig. 3.1*).

Fig. 3.1*: At start of the superficial spilling phase the pollutant immediately flooded the sandy surface and ran off towards the "water-in" section.*

3.2 Data Related to Chemical-Physical Groundwater Characteristics

3.2.1 In-situ Data

The parameters chosen to define *in-situ* the characteristics of the groundwater were:

- ***Conductivity***: This is a good indicator of the impurity levels in the water. Pure water is a poor electrical conductor, but dissolved salts, leading to reduced purity, improve its conductivity. The measurement allows rapid evaluation, albeit in a 'rough and ready' way, of the overall mineral levels of the water (Donald and Kokes 1962). In this study the conductivity was measured using a Jennway PCMC® conductivity meter.

- ***Dissolved Oxygen***: This was measured using a portable instrument (model VWR DO200®). It describes the concentration (mg/l) of molecular oxygen that is in an aqueous state. It is an important parameter because it determines whether conditions are adequate for life of aerobic organisms in the water (Donald and Kokes 1962).

- ***pH***: This describes the acidity or alkalinity of the water and represents the cologarithm of hydrogen ion activity in a solution and affects most of the chemical processes in water ((Donald and Kokes 1962; Denney 1982). The pH meter used was a portable model HACH ONE®.

3.2.1.1 Discussion of results related to the first monitoring campaign

The daily *in situ* collected data for the research period between 17/07/07 to 10/08/07 is plotted for each parameter to enable the observation of trends over time *(Figs.3.2; 3.3 & 3.4*).

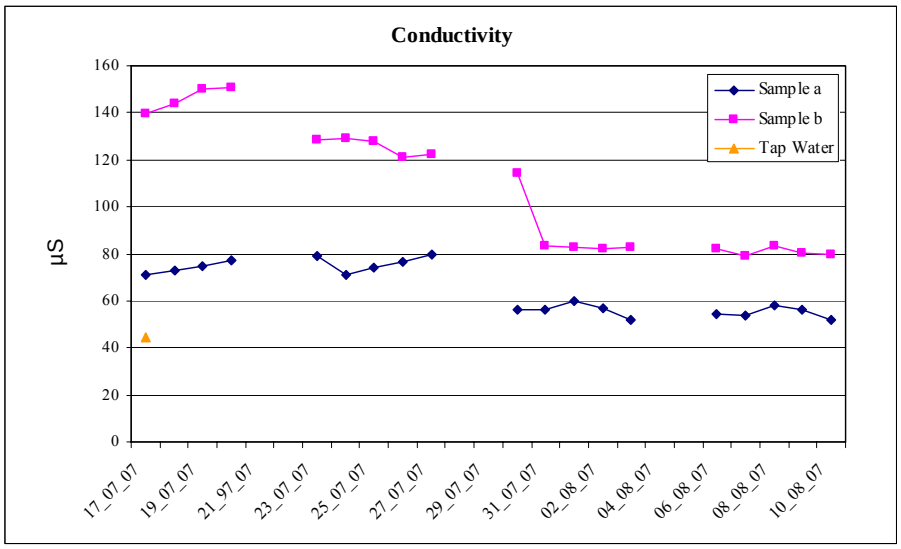

***Fig. 3.2**: The graphs shows the Electrical Conductivity variations in the ground water on the left side (Sample a) and the right side (Sample b) of the model.*

Electrical conductivity values increased from the left to the right side of the model. They exhibited an oscillating trend over time with a salt enrichment phase in the first week, a salt reduction during the second week and a stabilisation of the conductivity values during the remaining two weeks. The reduction in conductivity was accentuated in the water samples taken from right side compared to the left side of the model and even after four weeks of observation conductivity it did not return to the starting value (i.e. Sample 1a).

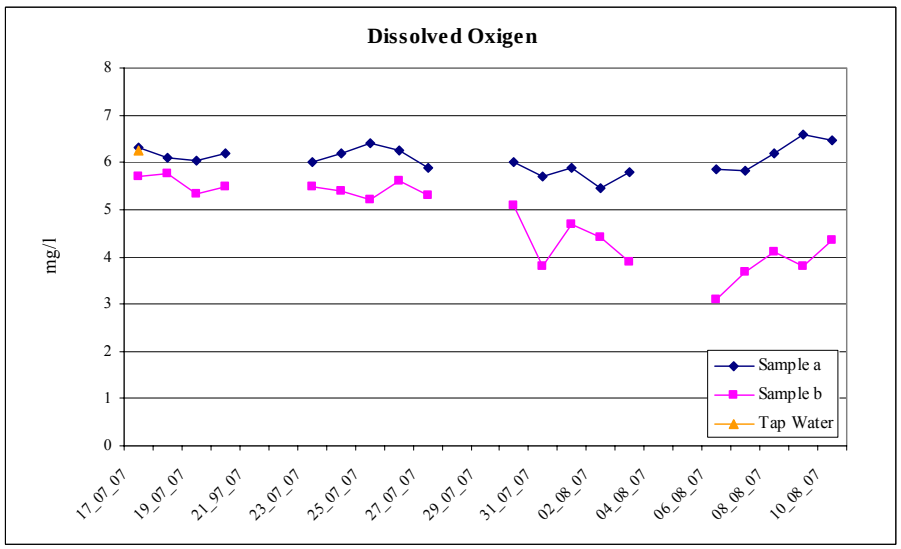

***Fig. 3.3**: The graph displays the Dissolved Oxygen variations in the groundwater on the left side (Sample a) and the right side (Sample b) of the model.*

Dissolved oxygen (***DO***) in the water on the left and right sides of the model differ. The DO value of tap water was almost identical to the water sampled on the left hand side of the model, which remained constant during the study period. Conversely, the DO values on the right hand side of the model decreased slowly during the first two weeks and then more dramatically during the remaining weeks. It may be hypothesised that the presence of pollutant on the surface of the left side of the model did not effect the DO value. Instead, the pollutant in the centre of the sandy layer resulted in aerobic bacteria using the oxygen present in the water. This allowed the bacteria to biodegrade the pollutant trapped in soil pores or aid adsorbtion of the pollutant around soil particles.

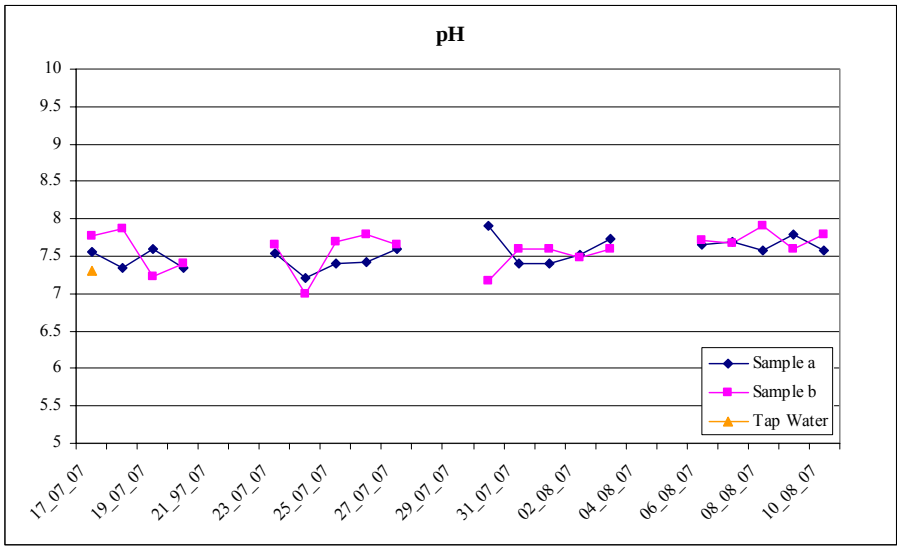

Fig. 3.4*: The graphs shows the pH variations in the ground water on the left side (Sample a) and the right side (Sample b)of the model..*

The ***pH*** values did not follow the trend exhibited by the other parameters. In fact, it was impossible to detect any differences in pH between water samples taken from different sides of the model with their values remaining almost constant during the study period.

The ***moisture content*** measurements of the soil contained in the model are summarised in *Table. 3.1*

Moisture Content				
Measurement	Soil	Location	water table depth (cm)	water %
MC 1A	Clay	near "water in"		17
MC 1B	Clay	near "water out"		18
MC 2A	Sand	near "water in"	14	41
MC 2B	Sand	near "water out"	16	38
MC 3A	Sand	near "water in"	6	45
MC 3B	Sand	near "water out"	14	41

Moisture content meter: **AT-Theta Kit**

Table. 3.1*: Summary the Moisure Content values with different water level and in different model zones.*

In particular the first two measurements are related to the moisture values of the clay soil after the layering phase on the left and right sides of the model; it can be seen that in the clay layer the moisture content is almost constant on both sides of the model. Values MC 2A-2B and MC 3A-3B respectively are related to the lower and higher groundwater levels which significantly influence the moisture content on the sandy soil surface.

3.2.1.2 Discussion of results related to the second monitoring campaign

Electrical conductivity during the observation period (i.e. 11/01/08 to 27/06/08) had different values on the basis of their sampling location (*Fig.3.5*). The specimens sampled from the tap water always had the lowest *Conductivity* values, however their values did increase a little during the observation period. The conductivity values from the water inlet and outlet side of the model both followed a general parallel trend to the tap water's conductivity. The outlet side conductivity values were always higher than all other values and the inlet values were generally in between the outlet and tap water values. The installation of the permeable reactive barrier affected the conductivity values only on the outlet side of the model. In fact, the water specimens sampled in this area (i.e. Water Sample 05/26b) had been recorded soon after the injection of the slurry. The slurry was made with 30% of ORC-Adv and 70% of water and after a stabilization phase the conductivity values increased again (i.e. Water Sample 05/30b and 06/06b) due to the dissolution of this new compound (i.e. ORC-Adv) present in the model.

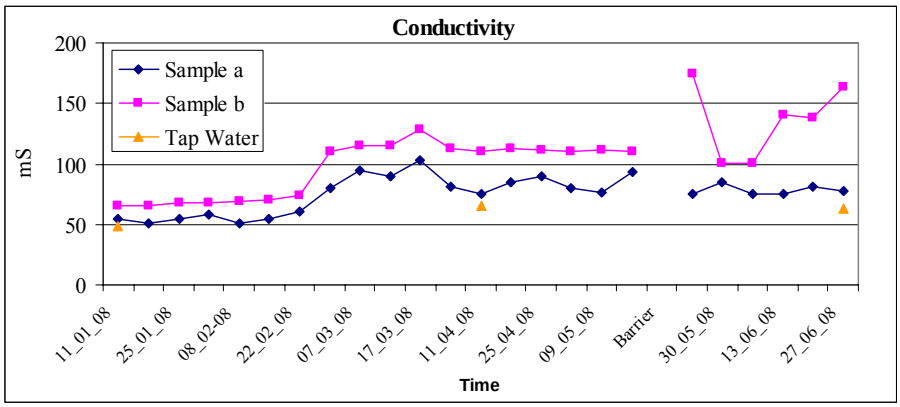

***Fig. 3.5**: The graphs shows the Conductivity variations in the groundwater on the left side (Sample a) and the right side (Sample b) of the model.*

Dissolved Oxygen values in the tap water samples were always higher than all other values (*Fig.3.6*). When the water entered the model (i.e. Water Samples a - the inlet) it lost part of its Dissolved Oxygen following the same trend of the Dissolved Oxygen in the tap water. The trend of the Dissolved Oxygen in the outlet (i.e. Water Samples b – outlet) of the model was rather constant until the installation of the permeable reactive barrier. In fact after the permeable reactive barrier was installed, the outlet Dissolved Oxygen values increased constantly during the following five weeks. On the contrary, the water inlet side the Dissolved Oxygen did not change from the usual trend of the water sampled in this area of the model.

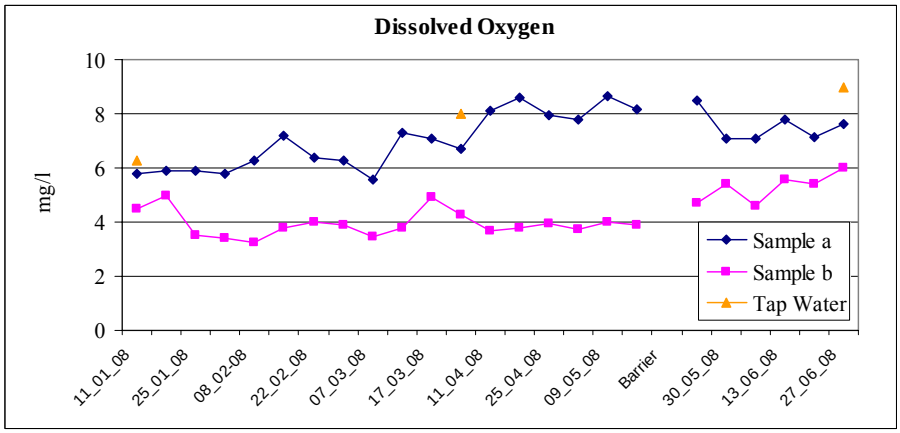

***Fig. 3.6**: The graphs shows the DO in the groundwater on the left side (Sample a) and the right side (Sample b) of the model.*

The trend of the ***pH*** values (*Fig.3.7*) remained almost constant during the observation period before the barrier installation. Until this moment it was

impossible to detect any differences in pH between water samples taken from different sides of the model. After the permeable reactive barrier settled the pH trend especially on the outlet model side changed and highlighted increasing values (i.e. Sample b) probably due to the Oxygen released from the barrier compound.

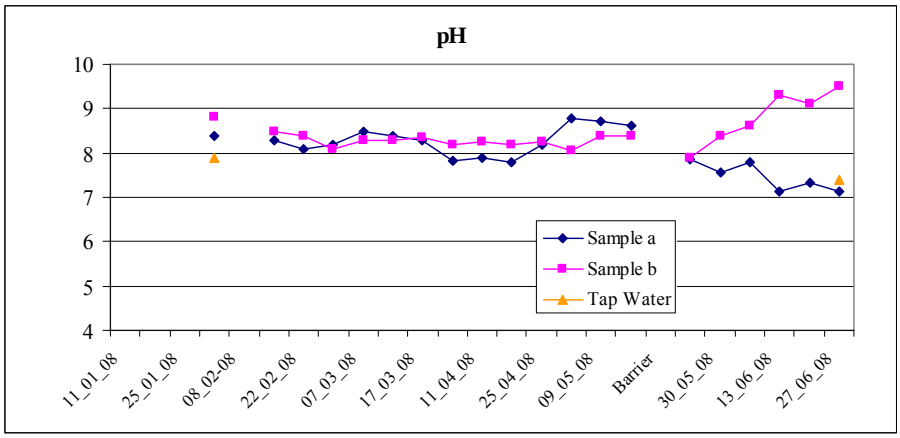

Fig. 3.7*: The graphs shows the pH variations in the groundwater on the left side (Sample a) and the right side (Sample b) of the model.*

3.2.2 Laboratory Data

The water samples analysed in the chemical laboratory (i.e. "*Studio Effemme, Lecce, Italy*") (see *Appendix B*) were divided in two groups:

- ***1° Group***: Water specimens taken during the first monitoring campaign to define the baseline characteristics of the water (i.e. ***Samples 1, 1A*** and ***1B***). These were: *pH; conductivity; dissolved oxygen; calcium; magnesium; sodium; potassium; chloride; ammonium; sulphite, fluorides; bromides; water hardness; total phosphorus; silica; aluminium; arsenic; cadmium; lead; antimony; copper; selenium; chromium; nickel; iron; manganese; zinc and boron*. Water specimen (i.e. ***Samples 2A-2B, 3A-3B*** and ***4A-4B***) were taken only to check for any traces of pollutant in the groundwater.

- ***2° Group***: Water and soil specimens (i.e. ***Water Sample Zone A***; ***Soil Sample Zone A***; ***Water Sample Zone B***; ***Soil Sample Zone B***; ***Water Upstream Barrier***; ***Water Downstream Barrier***) were taken during the

second monitoring campaign in order to check the pollutant concentration in the laboratory model.

3.2.2.1 Discussion of results 1° Group

The water samples i.e. ***Sample 1***; ***Sample 1A***; ***Sample 1B*** represent:

- ***Sample 1***: natural tap water;
- ***Sample 1A***: water from the model entrance and on contact with sandy soil;
- ***Sample 1B***: water from the end of the model.

From the analysis it is possible to deduce that the water was only in contact with the material (i.e. sand) that filled the model. In fact, the analysed parameters show that the water became rich in the typical sea water salts after passing through the sandy soil (i.e. Na^{+}, Cl^{-}, SO_4, K^{+}, and Mg^{++}) with a consequent increase in electrical conductivity.

It is interesting to note that whilst the ratio of Cl:Na is generally equal to 2:1, the sodium exceeds the absolute value of the chloride. Conversely, metals are distinctly absent from the water and also the sand, with the exception of aluminium, copper, iron, manganese and zinc which have a behaviour that requires further consideration:

- ***Aluminium***: remains constant during the first few minutes of the water/soil contact and then halves its concentration.
- ***Copper***: is generally present in water and is retained by the sand when the water enters the model, but is released again when the water leaves the model.
- ***Iron***: is not present in tap water but enrichment occurs during the first contact with sandy soil, and is thereafter always present in the water but decreases in concentration.
- ***Manganese***: is present in tap water, but disappears when passing through the soil that comprises the model.
- ***Zinc***: decreases during its transit through the model.

These analyses suggest that the concentration of heavy metals decreases in the water disproportionately to the time during which the water is in contact with the soil. This phenomenon can be explained as follows:

- Absorption or adsorption by the solid substrate of sand;
- Precipitation of metal salts due to clary-flocculation, which is facilitated by the presence of metals that are high in charge and an alkaline environment.

The chemical analysis of groundwater was sampled near the left and right hand sides of the model from the start of the experiment (i.e. 17th July) until 23rd July (i.e. ***2A-2B; 3A-3B; 4A-4B***). During this period the presence of hydrocarbons was not detected (i.e. Total Hydrocarbon Content < 2 μg/l).

3.2.2.2 Discussion of results 2° Group

The water and soil specimens collected during the second monitoring campaign were sampled to detect the pollutant concentration (i.e. ***TPH***) in the model before and after ORC-Adv injection (i.e. 16/05/08 and 27/06/08) . This allowed the correct Oxygen Realise Compound-Advanced® dose rate used to settle the permeable reactive barrier.

All the results are summarized in the following ***Table 3.2***:

Chemical Analysis			
Date		***Zone A***	
		Water Sample	Soil Sample
16/05/08	**TPH**	**5 mg/l**	**0.1 g/Kg**
		Zone B	
		Water Sample	Soil Sample
16/05/08	**TPH**	**2.5 g/l**	**31 mg/Kg**
		Barrier Upstream	
		Water Sample	
27/06/08	**TPH**	**10 mg/l**	
		Barrier Downstream	
		Water Sample	
27/06/08	**TPH**	**8 mg/l**	

3.3 Data Related to Electrical Resistivity Measurements

For each survey the electrical resistivity meter records a series of data (i.e. Current mA; Voltage mV; Standard Deviation %) (*Fig. 3.8*) and specific software (i.e. Areas 4.7 –GF Instruments®) records the electric field potential at two electrodes as the *Apparent Resistivity* value. A text file summarizes all the information related to the electrical survey and can be used to identify which electrodes are implicated with each apparent resistivity measurement (Res2Dinv 2007).

Fig. 3.8*: Resistivity meter displaying data recorded during the measurement process (i.e. Current mA; Voltage mV; Standard Deviation %).*

During the first monitoring campaign of four weeks (i.e. 17/07/07 to 10/08/07) twenty three electrical resistivity surveys were carried out using an electrical resistivity array with 24 mini-electrodes (see *Section 2.1*) and during the second monitoring campaign (i.e. 11/01/08 to 27/06/08) twenty five electrical resistivity surveys were carried out using an electrical resistivity array with 48 mini-electrodes. These were executed twice per day (i.e. 9.00 a.m.; 17.00 p.m.) during the first week in the first monitoring campaign when several physical model parameters were varied (see *Section 2.6.1* and *Table 2.7*), once per day (i.e. 9.00 am) during the following three weeks and once per week during the second monitoring campaign. During the weekend no measurements were taken. The Wenner-Schlumberger Array with 24 mini-electrodes provided for each electrical survey 121 apparent resistivity data points ordered in 11 levels (see *Fig. 2.1* – Section 2.1) and with 48 mini-electrodes the same array provided 529 apparent resistivity data points ordered in 23 levels (see *Fig. 2.1* – Section 2.1). The recorded data can be downloaded in several computer formats (i.e. text; excel; spss; res2dinv) and analyzed.

3.3.1 Analysis of Apparent Resistivity

Since the *apparent resistivity* is a continuous quantitative variable, descriptive statistics can be derived directly from the raw data. It should be noted that some of the data points were not included in the analysis because they are located outside the physical model and, therefore, do not relate to the parameters being investigated. These points are: 9 data point values arising from the last three measurement levels (i.e. n = 9; n = 10; n = 11) belonging to the first monitoring campaign and 81 data points values arising from the last 9 measurement levels (i.e. n = 15 to n = 23) belonging to the second monitoring campaign

3.3.1.1. Descriptive statistics of the first monitoring campaign : Discussion of results

Descriptive statistics of the Apparent Resistivity data belonging to the electrical resistivity surveys recorded during the first monitoring campaign presented in *Figs 3.9-3.10-3.11-3.12* and is also summarised in *Appendix D.*

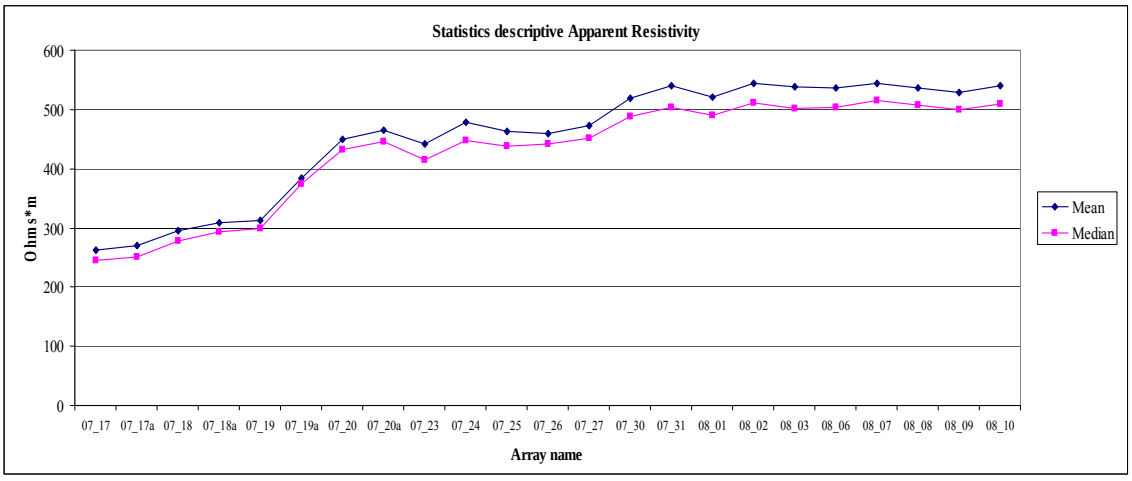

Figs. 3.9*: Trends of Mean; Median values related to the Apparent Resistivity values recorded during the first monitoring campaign.*

- ***Mean*** and ***Median*** values of apparent resistivity measure the central tendency of each dataset (Freund 1973). It can be seen that apparent resistivity generally increased after the addition of diesel and when the water level was elevated (*Fig. 3.9*). It was noted that the highest electrical

resistivity was found when, the quantity of diesel in the model was at it's highest or increasing (i.e. measurements ***07_17a-07_18***; ***07_19-07_20***) and so too was the water level (i.e. ***07_19-07_20***). Conversely, the mean and median values decreased when the water table was lowered during the first weekend (i.e. 20-23/07/07). All these changes in the resistivity values of the model were recorded with a retardation time that is inversely related to the magnitude of the 'alteration events' (i.e. addition of diesel and different groundwater levels). The mean values were always higher than median values, indicating that there was a positive skew as confirmed by the measure of skewness (*Fig.3.10*)

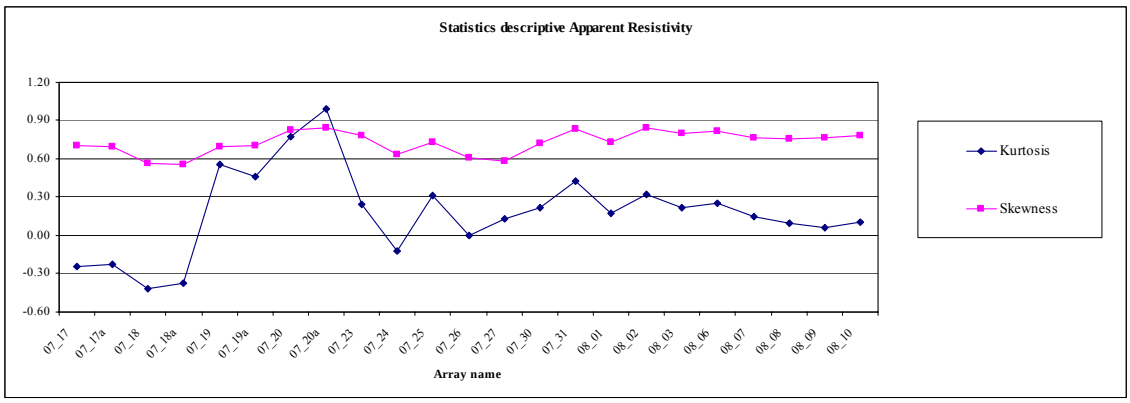

Figs. 3.10*: Trends of Kurtosis and Skewness values related to the Apparent Resistivity values recorded during the first monitoring campaign.*

- The ***kurtosis index*** (see *Appendix D* and *Fig.3.10*) measures the extent to which the peak of a uni-modal frequency distribution departs from the shape of a *Normal* distribution (Freund 1973). In this case the kurtosis values were always near zero indicating an almost *Normal* data distribution. At the same time this statistical parameters shows how it evidently changed after the pollutant spillage (i.e. 07_17a; 07_18a; 07_19) and groundwater level fluctuation (i.e. 07_19; 07_20; 07_20a; 07_23; 07_24; 07_25).
- The measures of dispersion and spread (i.e. ***Standard Deviation, Range, Standard Error and sample Variance***) (see *Appendix D)* describe the variability of the data. In particular, the ***Range*** (Freund 1973) (*Fig.3.11*) and ***Sample Variance*** (*Fig. 3.12*) emphasise how much the diesel and fluctuation

of the groundwater level affected the electrical resistivity in the model over time.

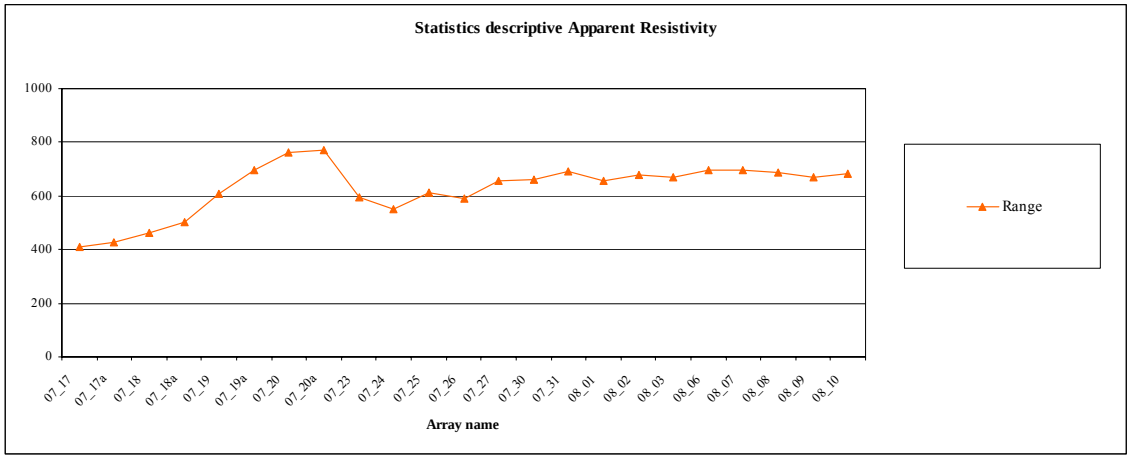

***Figs. 3.11**: Trends of the Range values related to the Apparent Resistivity values recorded during the first monitoring campaign.*

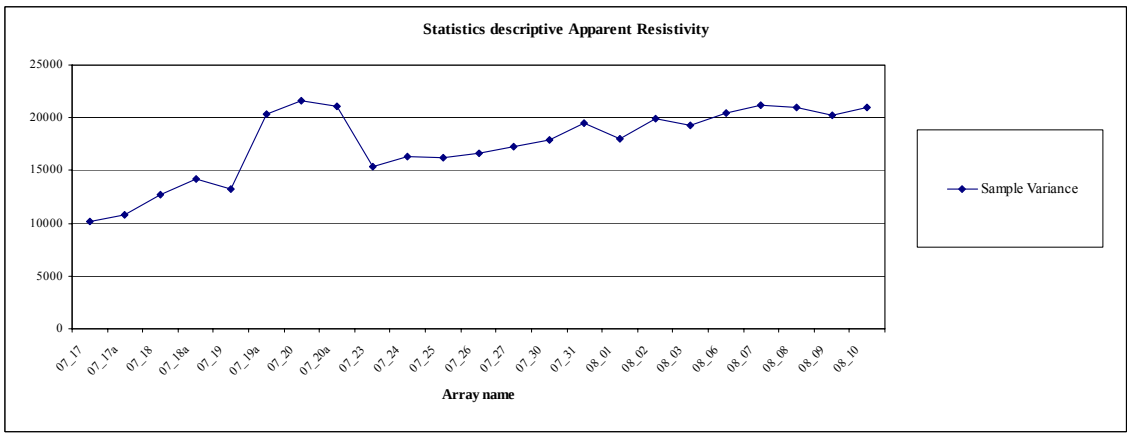

***Figs. 3.12**: Trends of Sample Variance values related to the Apparent Resistivity values recorded during the first monitoring campaign.*

These preliminary descriptive statistics clearly show that the resistivity values were closely linked to the presence of pollutant in the soil and to changes in the physical-chemical conditions of the model (e.g. different groundwater levels and spillage points).

In order to assess the extent to which the physical-chemical changes affected the resistivity values in the model, the apparent resistivity measured at steady-state was subtracted from the corresponding measurements taken when a disturbance was

induced. The obtained show the same behaviour as described above for the original apparent resistivity values, however, the changes associated with diesel addition and water table variation were more accentuated because all the resistivity measurements depart from the baseline values *(Fig 3.13)*.

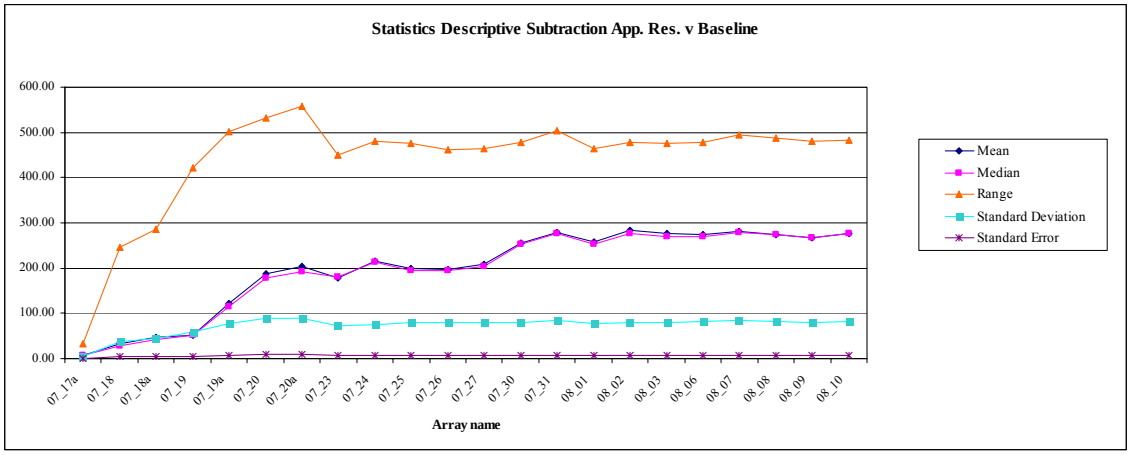

***Fig. 3.13**: Descriptive statistics showing the trend of values obtained by subtracting the resistivity values of the baseline electrical survey from the measures of apparent resistivity of each electrical survey relating to the experimental interventions.*

From *Fig 3.13* it can be seen that in the first assessment, where measurements were taken six hours after the addition of the first 200 ml of diesel to the model (i.e. survey ***07_17a***), no change in apparent resistivity values were clearly detected. At this time all the statistical parameters have values close to zero (i.e. 07_17a) despite the soil surface near the spillage point being immediately flooded by the pollutant (*Fig. 3.1 – Section 3.1*). This result may be due to the behaviour of diesel in the model; it was leaked at a depth of 4 cm across electrode six but, because of its physical-chemical characteristics and the high moisture content of the unsaturated sand surface (*Table 3.1 – Section 3.2.1.1*), it soon rose through the water causing flooding and stagnation of diesel LNAPL in the lightly depressed area close to the leakage point. With the Wenner-Schlumberger array the first measurement level in survey '***17_07a'***, at 5-6 cm depth, was too great to detect the start of the diesel spillage. Hence, it is not possible to verify whether the small recorded increase in resistivity is recorded by the electrode six in the spillage area or to background 'noise' of the physical model and the electrical resistivity meter.

The presence of diesel was recorded sixteen hours after its addition (i.e. survey ***07_18*** *Fig.3.13; Fig.3.14*) when all measures of apparent resistivity, especially the range and Kurtosis values, increase dramatically. The continuous increase in diesel levels was recorded in sequential assessments. Survey ***07_19*** recorded the second diesel spillage on the bottom of the model sixteen hours after its addition. Between the surveys ***07_19*** and ***07_20a*** the slope of the range curve is more than slope of the mean and median curve in fig 3.13 and the trend of the Kurtosis curve (*Fig.3.14*) decreases dramatically.

During this time period the leakage of diesel was stopped and the groundwater level increased. It can be seen that the range in electrical resistivity and Kurtosis values are directly correlated with the presence of pollutant in the model more than groundwater fluctuation. The mean and median values, however, are more influenced by the resistivity changes due to variation in groundwater level.

The following weekend (i.e. 21st-22nd July) the water level was lowered and then raised at start of the new week (i.e. 23rd July). Measurements of resistivity continued throughout this process and the concave region on all curves relating to surveys ***07_24*** - ***07_31*** (*Fig. 3.13*) represents the time required by the model to 're-set' following the effects of the previous events. During this period there was no diesel spillage and only simple water entered the model. This moderately increased the general electrical conductivity and established greater stability in the resistivity values.

During the following weeks, when there was no diesel addition, the range of resistivity measurements remained almost constant and always below the maximum value recorded during the first week. Similarly, in the same period, Mean, Median and Kurtosis values remain below the values achieved during week one and their trend slightly decreased (*Fig. 3.13; Fig.3.14*). This led to the hypothesis that the constant groundwater flow continued to transport and spread the contaminated plume

in the model thereby directly affecting the distribution of the electrical resistivity values in the model.

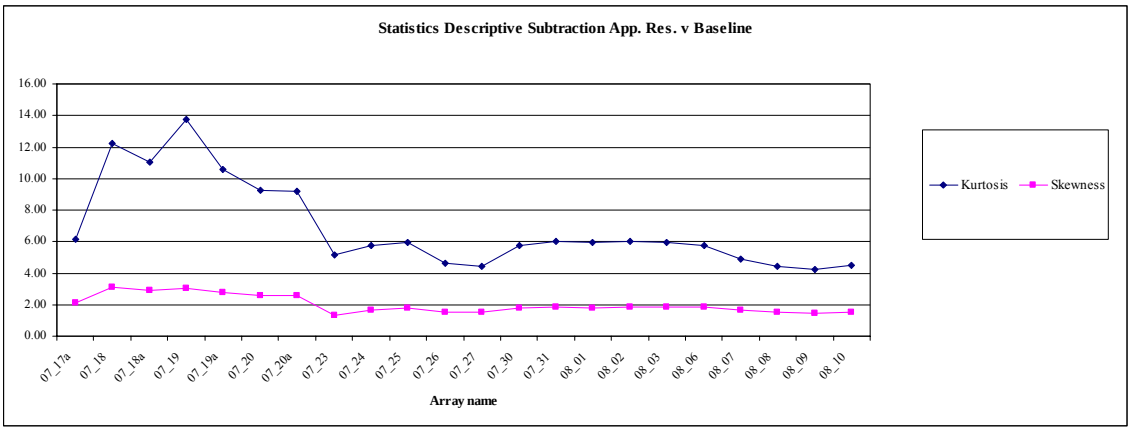

Fig. 3.14*: Trend of Kurtosis and Skewness values obtained by subtracting the resistivity values of the baseline electrical survey from the measures of apparent resistivity of each electrical survey relating to the experimental interventions.*

3.3.1.2 Graphical Presentation of Descriptive Statistics: Box Plot of first monitoring campaign

An alternative way to visualise summary statistics for quantitative variables is the 'box plot' in which a horizontal line represents the Median, a box extends to cover the inter-quartile range and a line extends away from the box to the extreme values. This has the advantage of comparing several datasets simultaneously.

The box plots for all the electrical resistivity surveys are grouped by week. During the first week, i.e. 17/07/07 to 20/07/07 (*Fig 3.15*), when the model was subjected to all disturbance events under consideration (i.e. diesel spillages; lifting and lowering of the water table in the sandy layer), some anomalous apparent resistivity values progressively appear in the top side of the graph, only two days after the experiment commenced, at which time most of the diesel was already spilt on surface. It may be that the second spillage on the bottom of the sandy layer on 18/07/07 and the rise in groundwater contributed to pollutant movement towards areas with high electrical resistivity visualised in the graph by higher values of the mean and range along with these anomalous values.

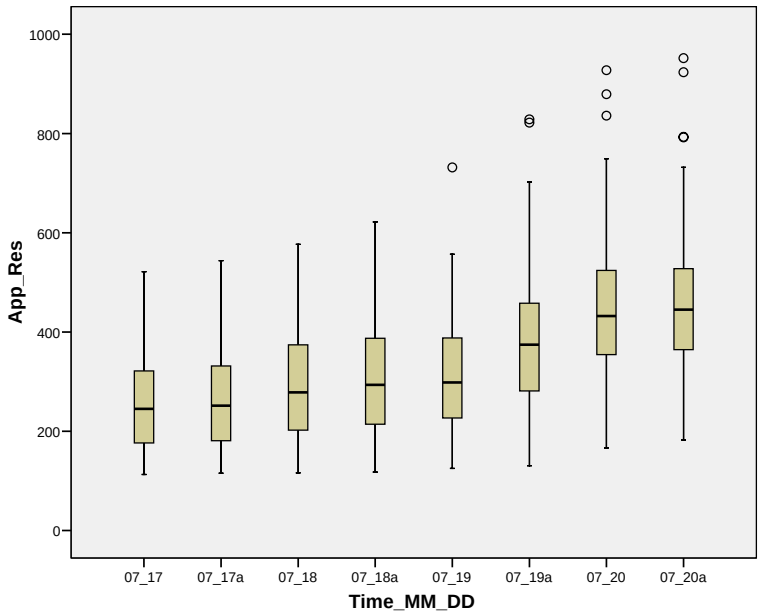

Fig. 3.15*: Box plot to show summary statistics of the apparent resistivity values measured by an electrical resistivity survey during the first week. Some anomalous apparent resistivity values appear in the top side of the graph.*

During the second week, i.e. 23/07/07 to 27/07/07, (*Fig. 3.16*) the general trend shows that there are still anomalous resistivity values (labelled with '○') but these are fewer and smaller than the first week confirming that without external inputs (i.e. pollutant addition or changes in the groundwater level) the model achieved a new internal chemical-physical equilibrium that persisted during the following two weeks (i.e. 30/07/07 to 03/08/07 and 06/08/07 to 10/08/07). During this time all the statistical parameters remained almost constant at higher resistivity values. The anomalous values continued to decrease, probably due to the pollutant spreading slowly to permeate more of the subsurface and encompass areas previously characterised by anomalous values.

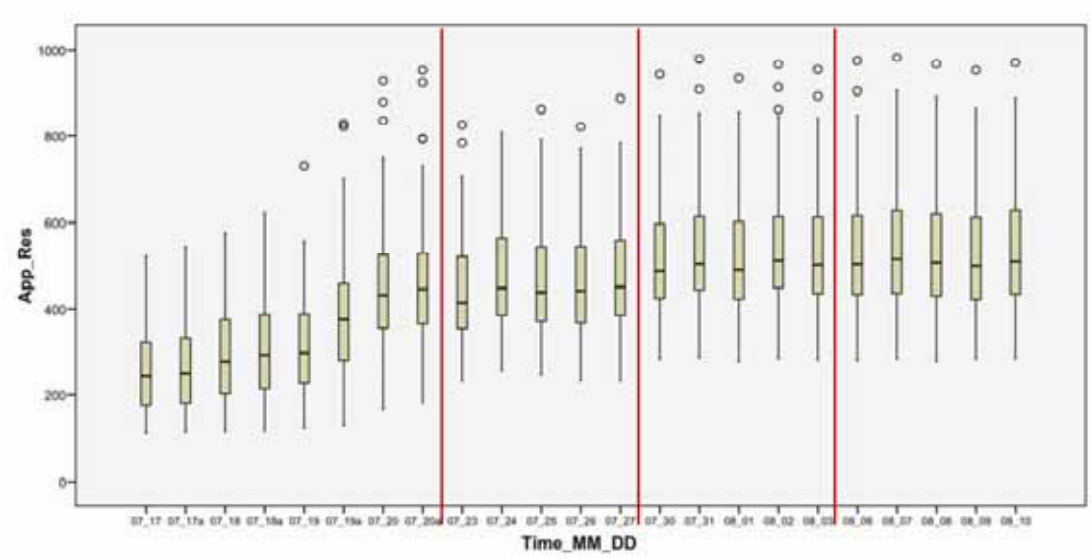

Fig. 3.16*: Box plot to show summary statistics of the apparent resistivity values measured by an electrical resistivity survey during the first monitoring campaign (divided into weeks by the red vertical lines).*

Using the departure of apparent resistivity from the baseline data of the model prior to starting the experiment, it was possible to observe how the presence of the anomalous data was amplified. In addition, anomalous values also appear on the lower part of the graph shown in *Fig 3.17* and there are a number of outliers (labelled with '*') in the upper part.

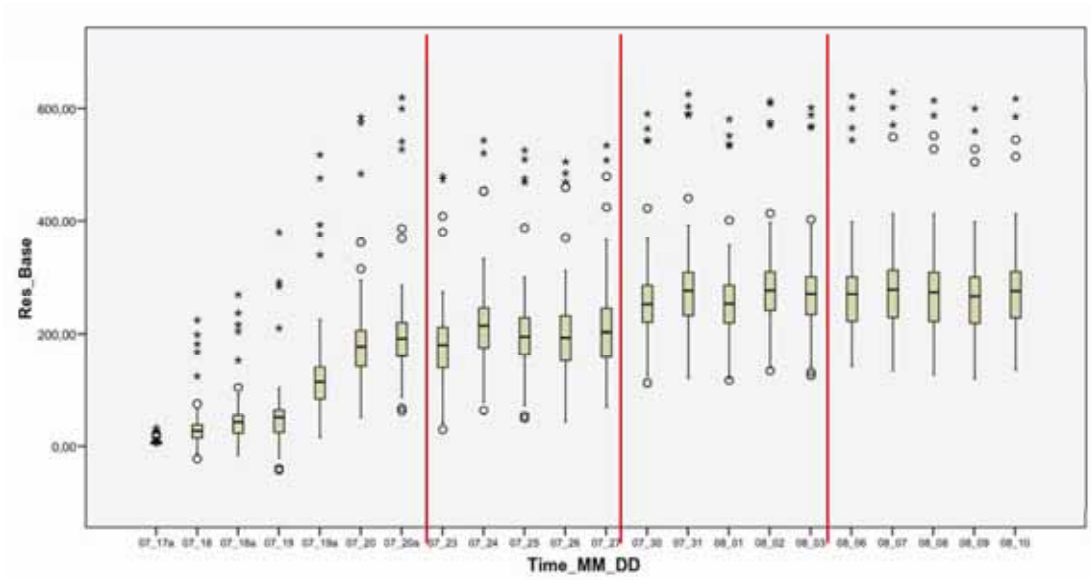

Fig. 3.17*: Box plot showing the trend of values obtained by subtracting the resistivity values of the baseline electrical survey from the measures of apparent resistivity of each electrical survey relating to the experimental interventions. The anomalous resistivity values are more evident.*

In order to specifically highlight the range of daily changes in the model, apparent resistivity data were subtracted from the resistivity values of the preceding survey and contrasted with the box plot (*Fig. 3.18*). It can be seen that the magnitude of the range is directly proportional to the time elapsed between two consecutive resistivity surveys and is related to the presence of the external inputs to the model. In particular, changes associated with diesel presence in the model are generally located in the positive area of the graph whilst changes associated with the water level are located towards the negative area of the graph. During the last two weeks of observation, when the model had reached its internal equilibrium, the range of daily resistivity values progressively reduced and the overall electrical resistivity of the model also decreased. Throughout this period the diesel continued to spread in the soil subsurface and dissolved a little in the water, thereby reducing its high concentration in the model. At the same time, some of the pollutant was leaving the model as it moved slowly towards the "water out" sector as indicated by a visible light stain of diesel. It is possible to hypothesise that new chemical-physical (e.g. dissolution of solids etc.) and biological conditions (e.g. microbial activity, natural attenuation etc.) were developing in the model which also contributed to lowering its overall electrical resistivity value.

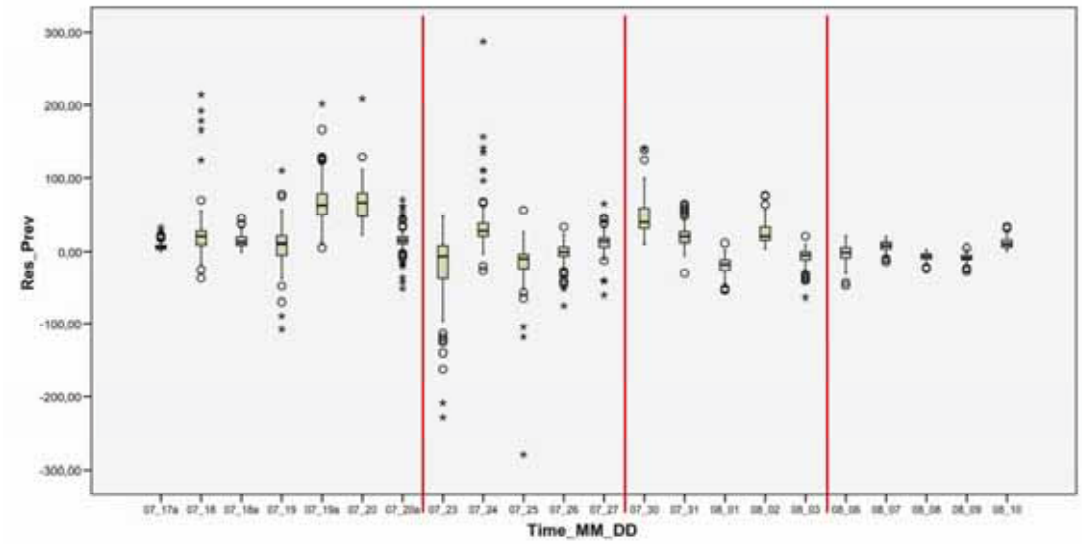

***Fig. 3.18**: Box plot showing the apparent resistivity data subtracted from the resistivity values of the preceding survey. Changes associated with diesel presence in the model are generally located in the positive area of the graph whilst changes associated with the water level are located towards the negative area of the graph.*

3.3.1.3. Descriptive statistics of the second monitoring campaign : Discussion of results

Descriptive statistics of the Apparent Resistivity data belonging to the electrical resistivity surveys, recorded during the second monitoring campaign, presented in the following figures and summarised in *Appendix D*. suggest that

- ***Mean*** and ***Median*** values of apparent resistivity (*Fig.3.19*) in this case also display a parallel trend that lightly decreases over the whole period, particularly after the permeable reactive barrier was installed. This trend is likely to be explained through dispersion of the pollutant by the groundwater and/or natual attenuation processes that occurred before the barrier was installed. Subsequently, the barrier installation contributed to the decreasing trend.

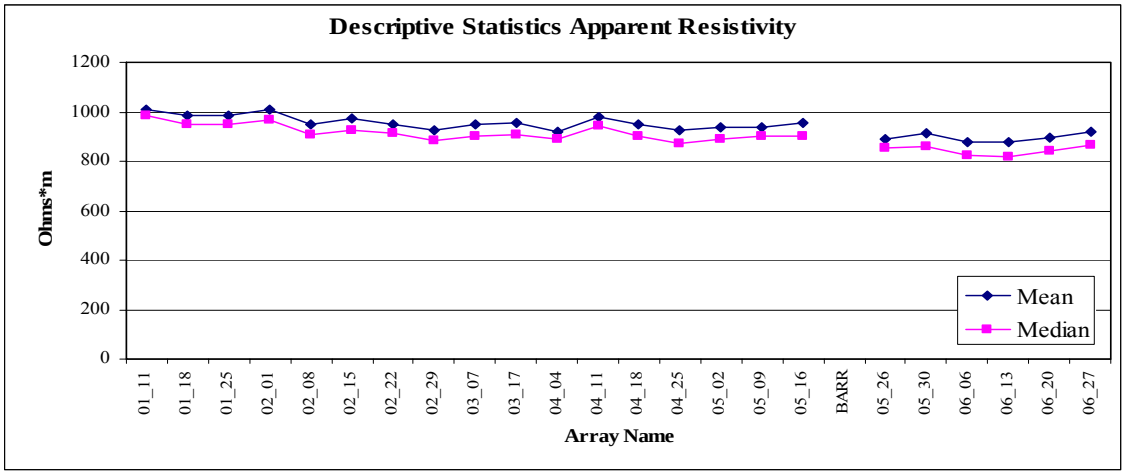

Figs. 3.19*: Trends of Mean; Median values related to the Apparent Resistivity values recorded during the second monitoring campaign.*

- ***The Range*** parameter (*Fig.3.20*) emphasises how much the barrier installation affects the electrical resistivity in the model. The range values are almost constant until the barrier is installed; once installed the range significantly increases but remains constant at this level for the remaining measuring time frame.

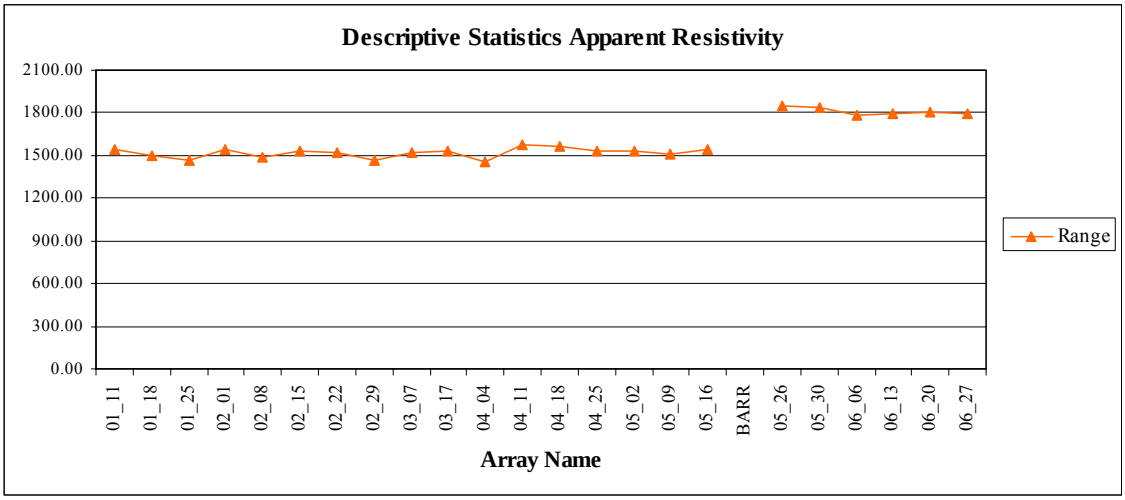

Figs. 3.20*: Trends of the Range values related to the Apparent Resistivity values recorded during the second monitoring campaign.*

- The ***Sample Variance*** parameter (*Fig.3.21*), also remained constant until the barrier was installed. Once the barrier was installed a jump in apparent resistivity is highlighted (i.e. 05_26 *Fig.3.21*) followed by fluctuation of its values.

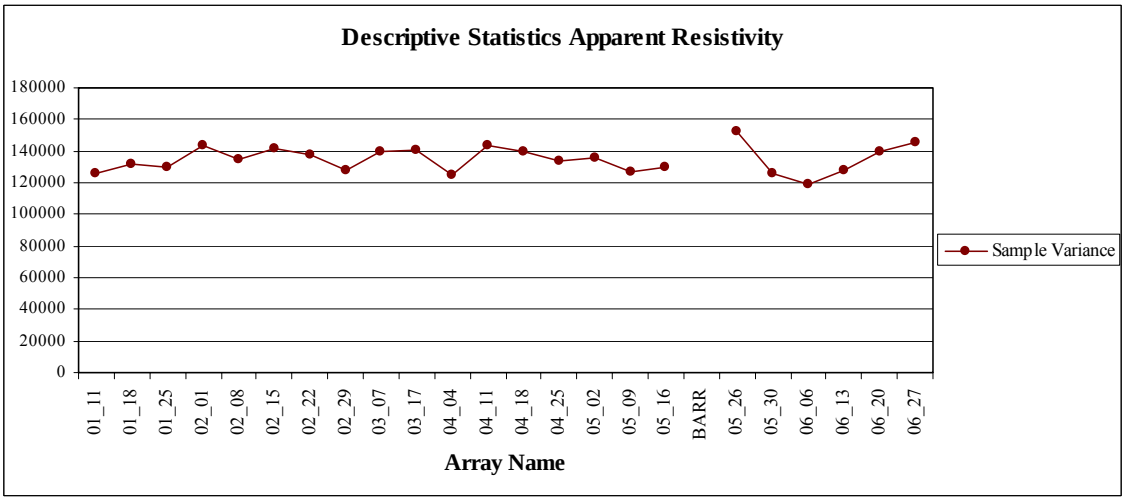

Figs. 3.21*: Trends of Sample Variance values related to the Apparent Resistivity values recorded during the second monitoring campaign.*

- ***Kurtosis Index*** and ***Skewness*** (*Fig.3.22*) in line with all other statistical parameters, displayed a constant or lightly increasing trend before the barrier was installed. This means that, under the same experimental conditions (i.e. no new pollutant spillage; no water level changes) and constant ***Range*** (*Fig.3.20*), the data with lower Apparent Resistivity values increased during

the time. These parameters did not record the barrier presence immediately after it's installation in the first electrical resistivity survey (i.e. 05_26), but in the following electrical resistivity surveys it displays a convex trend.

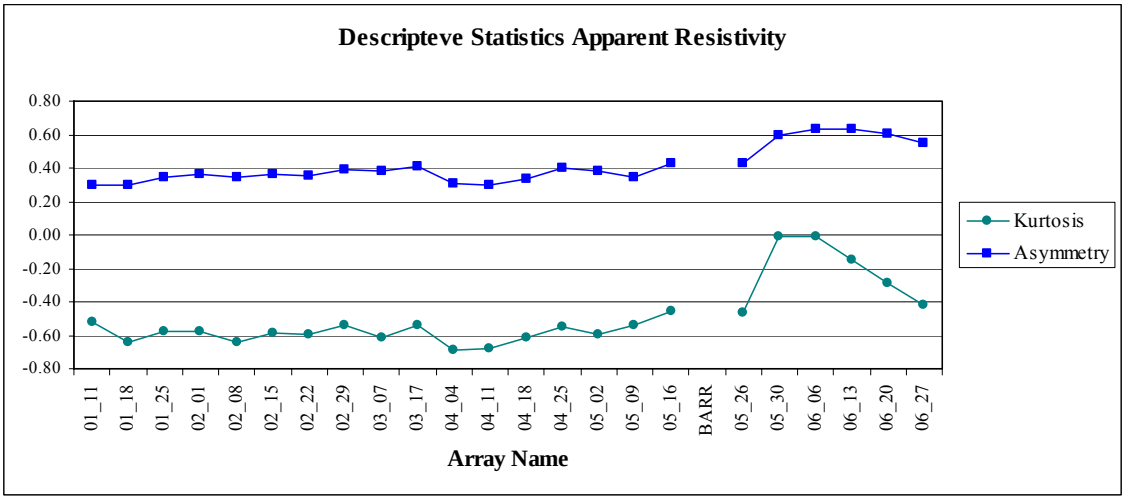

Figs. 3.22*: Trends of Kurtosis and Asymmetry values related to the Apparent Resistivity values recorded during the second monitoring campaign.*

During the second monitoring campaign all the electrical resistivity surveys were recorded using an electrical resistivity array equipped with more electrodes. The second campaign increased the number of electrodes from 24 electrodes to 48 electrodes and subsequently this changed the location of the measuring points (i.e. plotting point; see *Section 2.1*).

For this reason each Apparent Resistivity dataset related with '*48 electrodes array*' was not subtracted with 'baseline' Apparent Resistivity dataset collected with '*24 electrodes array*' but with the Apparent Resistivity dataset related to the first electrical resistivity survey collected starting the second monitoring campaign (i.e. Electrical Resistivity Survey *01_11*).

The analysis of the statistical descriptive parameters achieved with this subtraction reveals that:

Mean and ***Median*** of the Apparent Resistivity values subtracted to the first Apparent Resistivity dataset (i.e. *01_11*) are always negative and decrease over the second monitoring campaign (*Fig.3.23*) confirming and highlighting better that the

general Apparent Resistivity was decreasing. The barrier installation causes the differentiation of the Mean and Median subtraction values. In fact, before its installation the coincidence of the ***Mean*** and ***Median*** values of the Apparent Resistivity subtraction values describe a symmetrical normal distribution of their values (i.e. Apparent Resistivity subtraction values) in the frequency curves (*Fig.3.24*). However, after the barrier was installed, a clear decrement of the ***Mean*** and ***Median*** subtraction values is evident (i.e. 05_26). The differentiation of their values, show an asymmetrical distribution of the Apparent Resistivity subtraction values in the frequency curves (*Fig.3.24 and 3.25*).

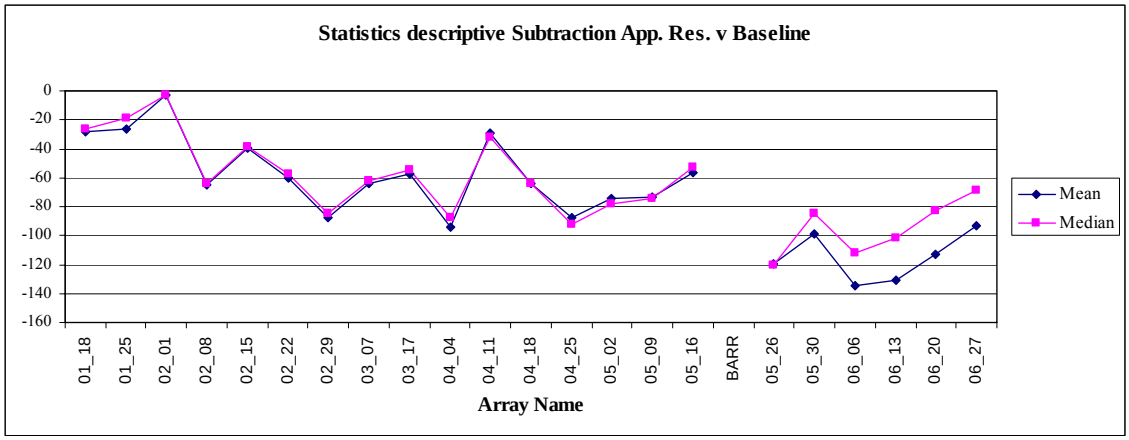

Fig. 3.23*: Trend of Mean and Median values obtained by subtracting the resistivity values of the first electrical survey of the second monitoring campaign from the measures of apparent resistivity of each electrical survey relating to the experimental interventions.*

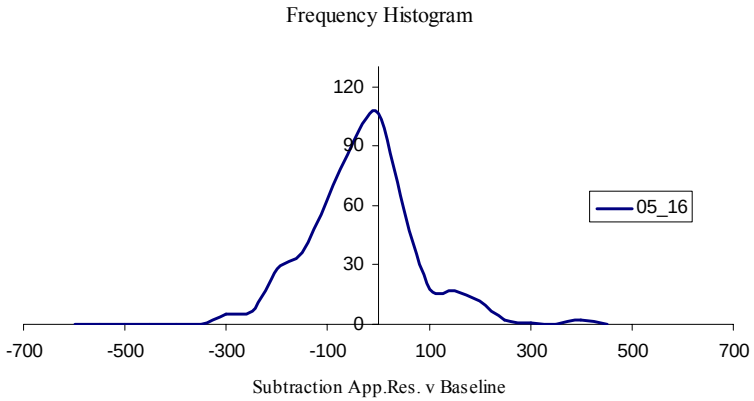

Fig. 3.24*: Example of the frequency curve describing the distribution of the subtracted apparent resistivity data before barrier installation.*

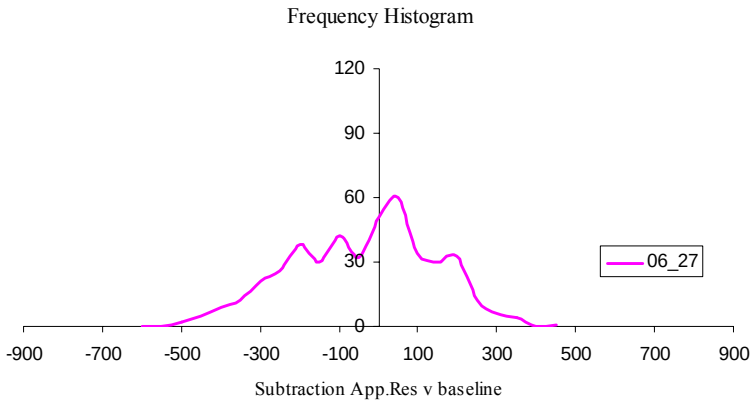

Fig. 3.25*: Example of the frequency curve describing the distribution of the subtracted apparent resistivity data after barrier installation.*

The measures of dispersion and spread before the barrier is installed, (i.e. ***Range*** and ***Sample Variance)*** of the Apparent Resistivity Subtraction dataset (*Fig.3.26* and *Fig.3.27*), show a similar parallel trend. However a small difference between these data sets, is that, the ***Sample Variance*** is generally decreasing, whereas the ***Range*** is generally increasing (*Fig.3.28*). After the barrier was installed the data sets display a drastic increment of their values that continued for many days (i.e. 05_26; 05_30; 06_06) before inverting this trend.

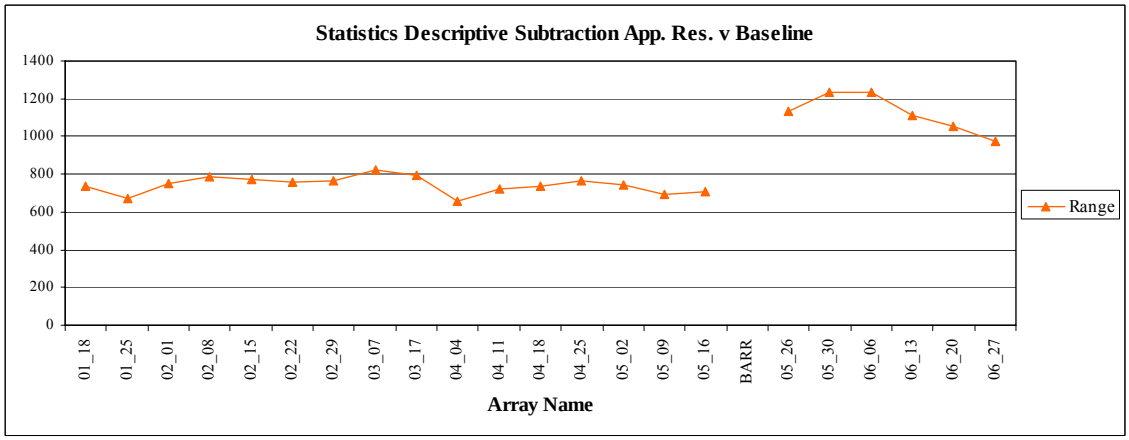

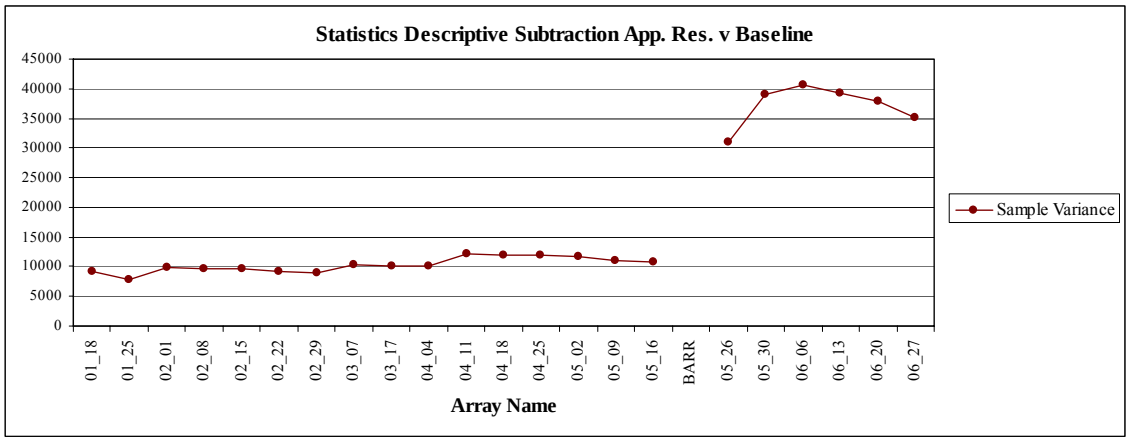

***Fig. 3.26-3.27**: Trend of Range and Sample Variance values obtained subtracting the resistivity values of the first electrical survey of the second monitoring campaign from the measures of apparent resistivity of each electrical survey relating to the experimental interventions.*

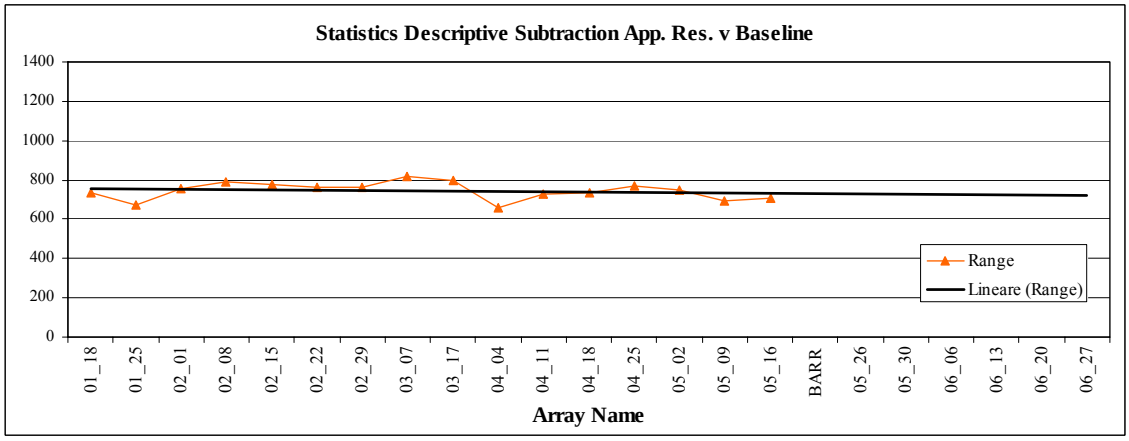

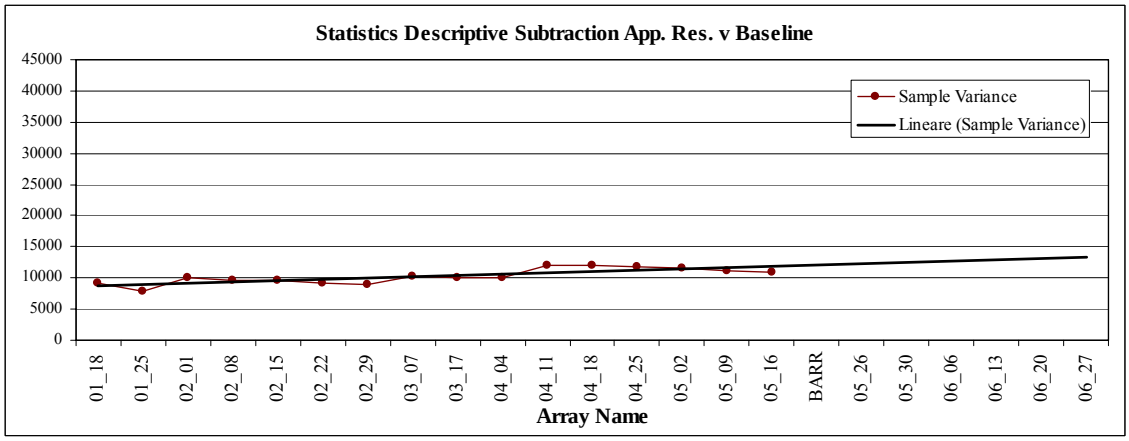

***Fig. 3.28-3.29**: Trend of Range and Sample Variance values obtained subtracting the resistivity values of the first electrical survey of the second monitoring campaign from the measures of apparent resistivity of each electrical survey relating to the experimental interventions before barrier installation.*

Kurtosis and ***Skewness*** parameters for this dataset displayed a general inverse trend until the barrier was installed; where, ***Kurtosis*** had a decreasing trend and ***Skewness*** at the same time had a light increasing trend (*Fig.3.30)*. This inverse trend between ***kurtosis*** and ***Skewness*** describes the frequency of the distribution curve of the Apparent Resistivity subtraction dataset; i.e. the ***Kurtosis*** became flatter and the ***Skewness*** more positively skewed. Although this trend is inverse, each single point from the same date is parallel to each other; i.e. they increased or decreased together. However, after barrier was installed the previous parallel trend between ***Kurtosis*** and ***Skewness***, was lost and instead they exhibit opposite movement (Fig.3.31).

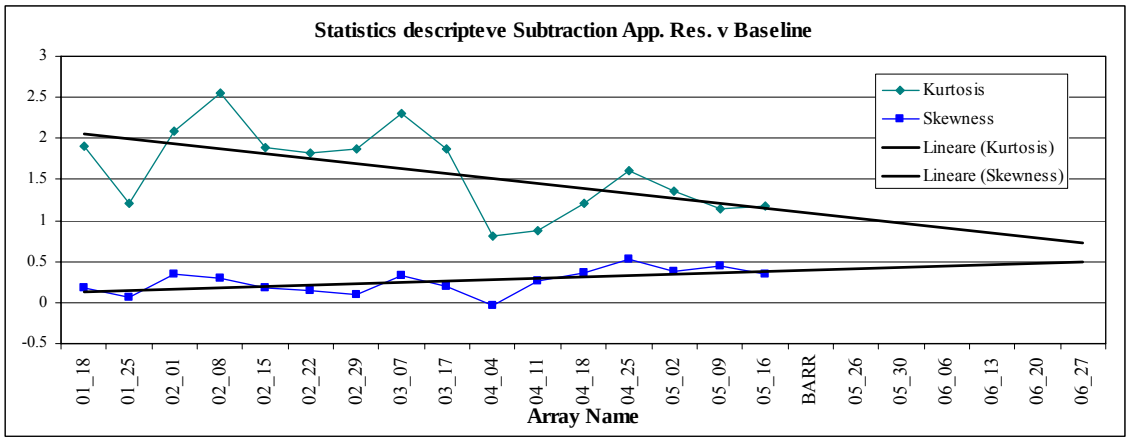

Fig. 3.30*: Trend of Kurtosis and Skewness values obtained subtracting the resistivity values of the first electrical survey of the second monitoring campaign from the measures of apparent resistivity of each electrical survey relating to the experimental interventions before barrier installation.*

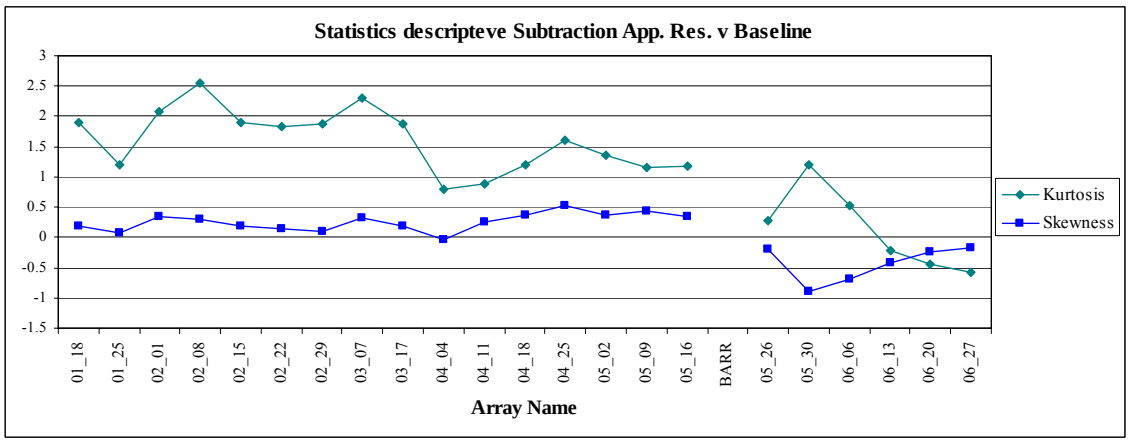

Fig. 3.31*: Trend of Kurtosis and Skewness values obtained subtracting the resistivity values of the first electrical survey of the second monitoring campaign from the measures of apparent resistivity of each electrical survey relating to the experimental interventions.*

3.3.1.4 Graphical Presentation of Descriptive Statistics: Box Plot of first monitoring campaign

As already discussed in Section 3.3.1.2, the Box Plot shows the five statistics (i.e. minimum, first quartile, median, third quartile, and maximum) and it is useful for displaying the distribution of a variable i.e. Apparent Resistivity Value ('App_Res') (Fig.3.32); Values resulting from subtraction of the Apparent Resistivity values of each electrical survey and Apparent Resistivity values of the first electrical resistivity survey during the second monitoring campaign ('Res – Base') (*Fig.3.33*). Values resulting from subtraction of the Apparent Resistivity values of each electrical survey and Apparent Resistivity values of the previous electrical survey ('Res – Prev') (*Fig.3.34*).

The *Figure 3.32* give a general view of all the Apparent Resistivity values related with each resistivity survey during the second monitoring campaign. The group of box-plots describing the resistivity surveys before the barrier installation (i.e. red dotted line in the figure) has a constant and stable trend with a light decrement of the mean as already showed in *Section 3.3.1.3* and *Fig.3.19*.

The barrier installation in the laboratory model enlarge the Range of the Apparent Resistivity dataset especially toward lower values but it is important to understand that this event (i.e. Barrier installation) isolates some high values shown in the "○" symbol in the figure below .

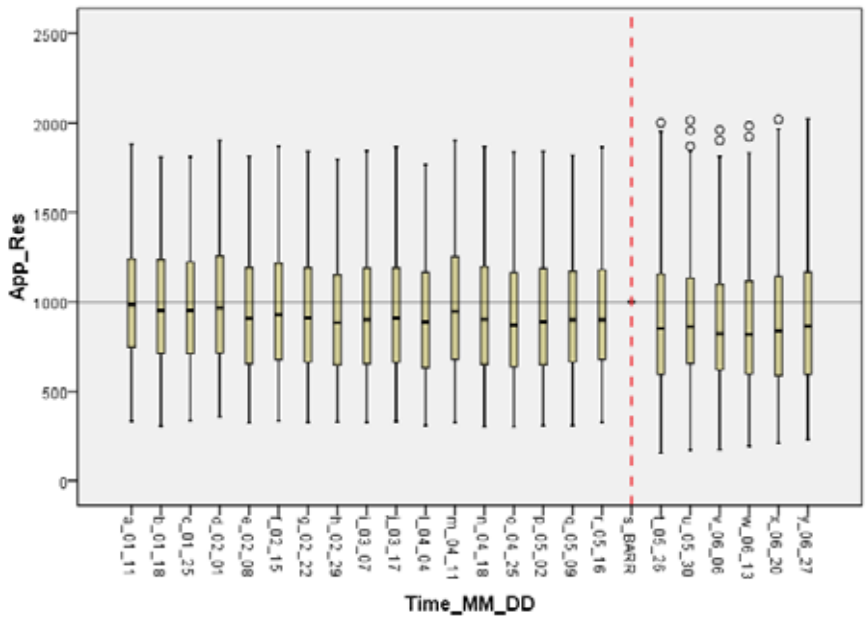

***Fig. 3.32**: Box plot to show summary statistics of the apparent resistivity values measured by an electrical resistivity survey during the second monitoring campaign.*

Subtracting the apparent resistivity values of the first electrical survey to the apparent resistivity values of each following resistivity survey, highlights and emphasizes the changes that occur in the laboratory model over the time. In fact, each box-plot in the *Figure 3.33* shows how much the Apparent Resistivity values changed in each electrical resistivity survey in comparison to the first survey. Most of the survey data, included a negative trend in the first and third quartile (i.e. yellow part of the box-plots), showing that at these points the Apparent Resistivity was progressively falling down over time before barrier installation. The outliers (labelled with "○" and/or "*" in *Fig.3.33*) are isolated points in the model that changed drastically in Apparent Resistivity in comparison with the first survey. This drastic change could be explained by the previous statistical analysis of the Apparent Resistivity data belonging to the first monitoring campaign; or it could be explained by a modification of the internal equilibrium after the pollution event; or it could also be explaied by an anomalous resistivity data due to an interaction between the resistivity equipment.

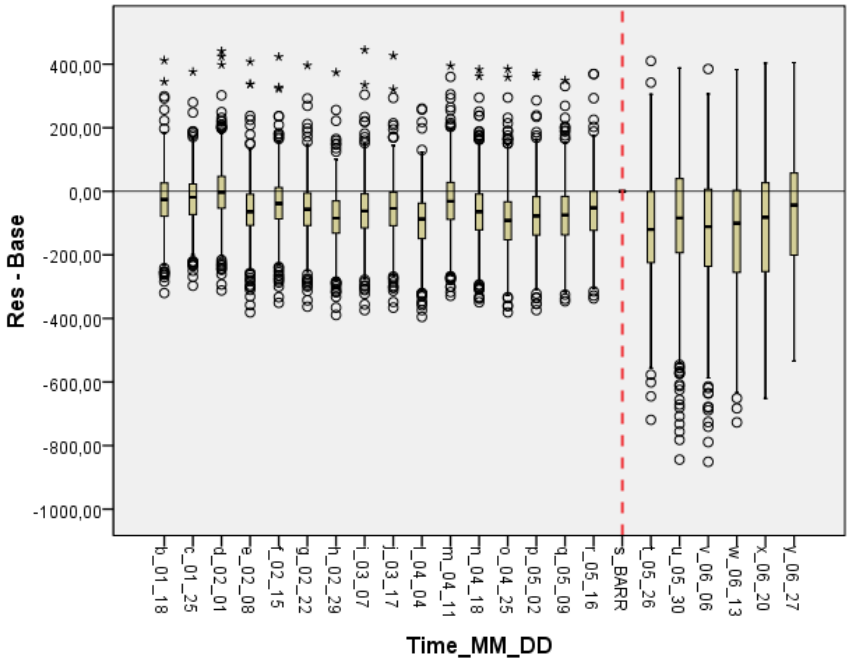

***Fig. 3.33**: Box plot showing the trend of values obtained subtracting the resistivity values of the first electrical survey of the second monitoring campaign from the measures of apparent resistivity of each electrical survey relating to the experimental interventions.*

The barrier installation brakes the previous almost constant trend causing firstly, a general and widespread reduction in Apparent Resistivity and secondly a rise in Apparent Resistivity for the reduced group of data points falling in the positive area of the graph. The reduction in resistivity in this case was probably caused by the injection of fresh water during the barrier installation. This injection of fresh water caused the pollutant to be displaced into new locations previously characterized by lower apparent resistivity.

The range of daily changes in apparent resistivity data obtained by subtracting the resistivity values of the each survey from its preceding survey is presented in *Figure 3.34*. In this Figure, it is possible to note that the range of the box-plots diminishes over time until the barrier is installed. After the barrier is installed the first survey (i.e.05-26) highlights two important events: a large and remarkable fall in resistivity and at the same time a less evident rise in resistivity. The following box-plot (i.e. 05_30), is when the greatest number of changes in resistivity occurred four days after the barrier was installed. This reduced considerably the range of the changes in resistivity for the most part of the data, but symmetrically recorded

outliers with high and low changes in resistivity. In the following box-plots it is possible to identify that the model is trying to re-establish its internal equilibrium after the barrier was installed.

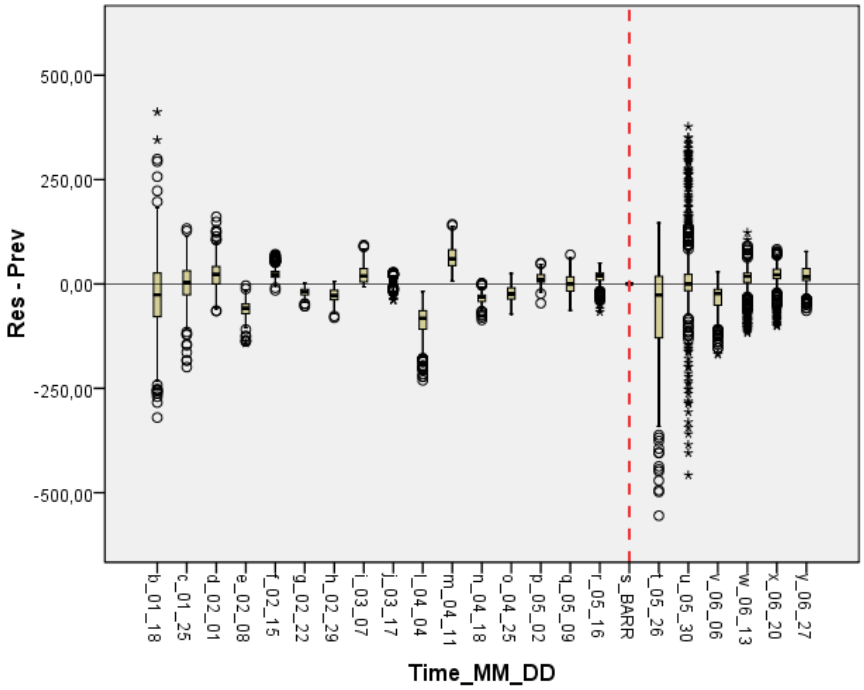

***Fig. 3.34**: Box plot showing the apparent resistivity data subtracted from the resistivity values of the preceding survey.*

3.3.3 Inverse Method Data Analysis

The calculated Apparent Resistivity value is not the 'true' resistivity of the subsurface, but rather an "apparent" value that is the resistivity of a homogeneous ground that will give the same resistance value for the same electrode arrangement (see *Section 1.2.1*). For this reason it is important to convert the apparent resistivity values into a resistivity model that can be used for the following geophysical interpretations (Loke 2001). In order to do so the recorded data was exported, into an appropriate format, to the software RES2DINV®.

This software divides the subsurface into rectangular cells of fixed dimensions, the cell size normally increasing with depth for which the resistivity is adjusted iteratively until an acceptable agreement is reached between the input data and the model (Loke and Baker 1996; Dahlin 1996) (*Fig. 3.35*). An 'inversion method',

elaborates the relationship between the "apparent" resistivity and the "true" resistivity giving an *Inverse Model Resistivity Section* which is an idealized mathematical representation of a cross-section of the earth (***2-D resistivity imaging***) that corresponds with the measured data.

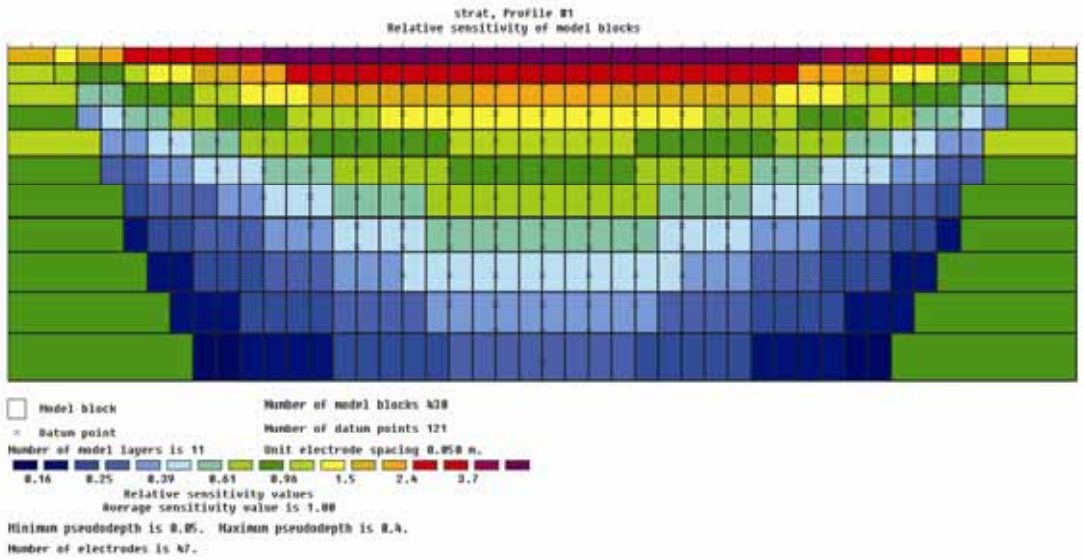

Fig. 3.35*: Division of the subsurface into rectangular cells of fixed dimensions. The cell size increases with depth and the resistivities are adjusted iteratively until an acceptable agreement between the input data and the model responses is reached.*

For each electrical resistivity survey the final result of this elaboration is an image (*Fig. 3.36*) divided in three parts where it is possible to visualize:

1) the measured apparent resistivity section;
2) the calculated apparent resistivity pseudosection;
3) the inverse model resistivity section from a survey that is a computer model for the subsurface that needs to be interpreted.

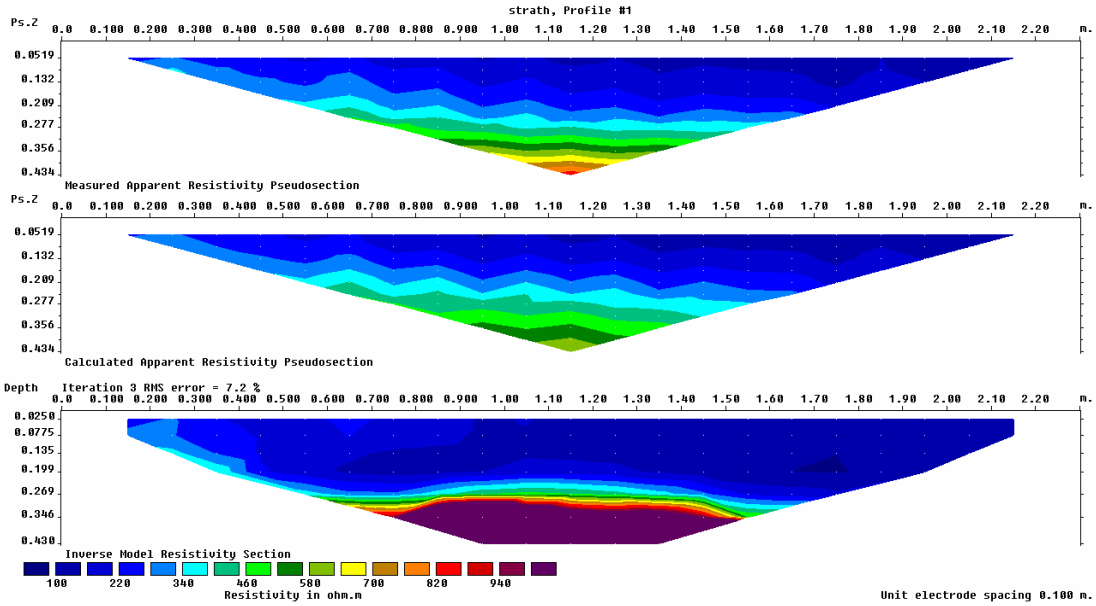

Fig. 3.36*: The three parts of this figure show respectively the 'measured apparent resistivity section', the 'calculated apparent resistivity section' and the 'inverse model resistivity section' which represent the result of the inversion method used by the software to elaborate the apparent resistivity values.*

3.3.3.1 Discussion of results: Apparent Resistivity Data First Monitoring Campaign

To analyse all the Apparent Resistivity data the RES2DINV® software was used by default except setting:

- defined linear contour intervals when it displayed the apparent resistivity pseudosections and the model resistivity section in least-squares inversion subroutines with "*Enter Minimum Contour Value*": 100 and "*Enter Contour Spacing Value*": 60;
- model cells with widths of half the unit spacing;
- use apparent resistivity values when carrying out the inversion.

The baseline map, obtained monitoring the resistivity of the model before the diesel injection (*Fig.3.37*), reflects the stratified structure of the physical model with its sandy and clay layers along with the different resistivity measurements between the left and right hand side due to the variable content of dissolved salts in the groundwater. The purple colour in the map represents the high resistivity values

recorded on the base that are not related to the soil but to the structure that support the physical model tank made of Perspex glass.

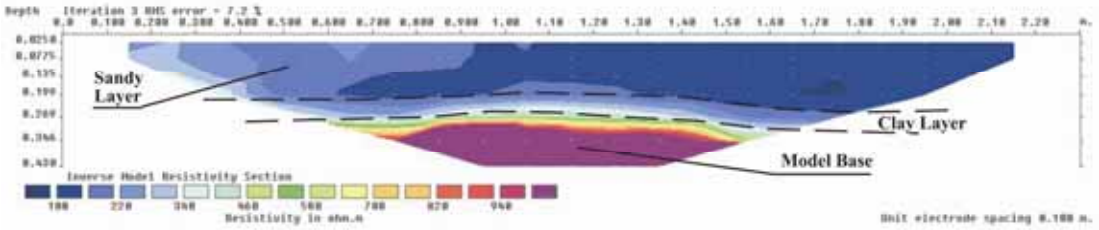

***Fig. 3.37**: The 'Inverse model' **07_17**' map shows the stratified structure of the sandy and clay layers and the different resistivity measurements between the left and right hand side of the physical model due to the variable content of dissolved salts in the groundwater.*

Six hour after the first diesel spillage the survey ***07_17a*** does not record any changes in the model how Figure 3.38 shows.

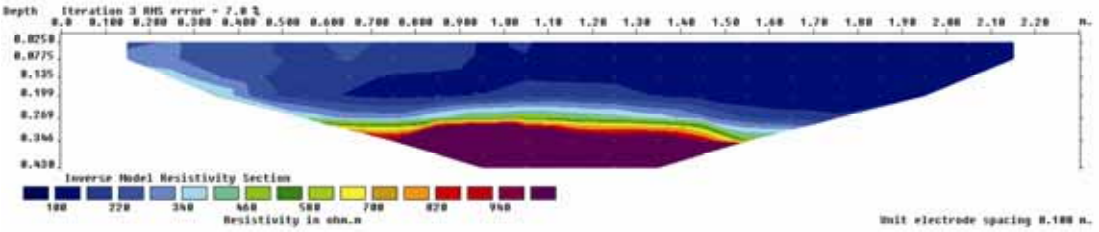

***Fig. 3.38**: The 'Inverse model '**07_17a**' map shows the stratified structure of the sandy and clay layers and the different resistivity measurements between the left and right hand side of the physical model but not the pollutant presence.*

The diesel spillage on the left hand side of the model was recorded after 24 hours with survey ***07_18*** when also more diesel started to be injected on the base of the sandy layer in the model centre. With the *Figure 3.39* it is possible to see the pollutant spillage zone on the left model side (i.e. Zone A) with horizontal plume on the top of the groundwater table that contributes to spread it but it was not still possible to highlight the second spillage zone (i.e. Zone B) in the centre of the model. At that moment the ground water was at lower level (i.e. 15 cm on the water inlet model side; 13 cm on the water outlet model side). The increase in resistivity on the upper part of the model caused also the deformation of the clay layer and the model base that in the previous map were almost horizontal. Besides, it is noted that electrical resistivity images are the outcome of data processing and for this reason they must not be interpreted as a direct representation of the field situation, but rather

as a guide for qualitative estimation of the electrical resistivity distribution in the soil model (Loke 2001).

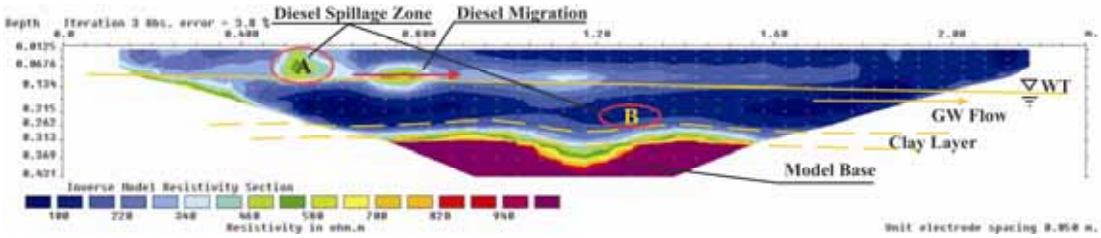

***Fig. 3.39**: 'Inverse model '**07_18**' map showing the diesel spillage in Zone A; the horizontal pollutant plume but not increasing in resistivity expected whit diesel spillage in Zone B.*

Finally, the diesel spilt in the centre of the model was recorded in map ***07_18a*** (*Fig.3.40*) when simultaneously the groundwater table was risen at higher level (i.e. 23 cm on the water inlet model side; 15 cm on the water outlet model side). The area where diesel was spilt in ***Zone A*** appears on the map more resistive than area where diesel was spilt at a deeper level of the sandy layer (i.e. ***Zone B***). On the left side much more diesel (i.e. 1000 ml) was spilt and its dissolved phase and LNAPL contributed to increase the resistivity values on the spillage point and downstream on the top of the groundwater flow. In ***Zone B*** less quantity of diesel (i.e. 500 ml) was spilt and the resistivity values never reached the same high levels as it is possible to note from the survey 07_18a and 07_19a. Due to the diesel's low density it partially rose to the surface through the saturated zone increasing the horizontal plume and partially remaining trapped in the soil pores. The spillage effects in the centre of the saturated zone were manifested by a general increase in resistivity and presence of a vertical plume indicating a sudden rise in pollutant (*Fig.3.41*).

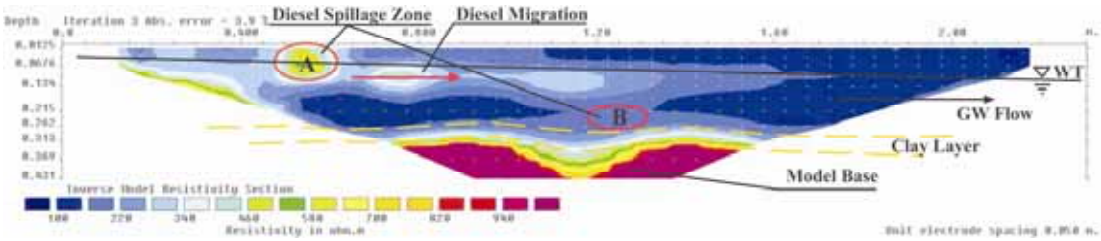

***Fig. 3.40**: 'Inverse model '**07_18a**' map showing the diesel spillage in Zone A; the horizontal pollutant plume and the increase in resistivity expected whit diesel spillage in Zone B.*

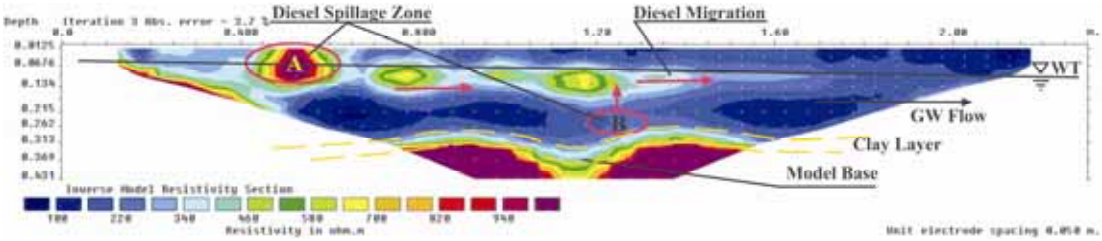

***Fig. 3.41**: 'Inverse model '**07_19a**' map showing the diesel spillage in Zone A; the horizontal and vertical pollutant plume and the increase in resistivity expected whit diesel spillage in Zone B. The clay layer on the model base appears deformed because of the high resistivity values on surface.*

After a previous observation phase during which the water table was at higher level it was lowered to detect its influence on the pollutant dispersion. The 07_23 map (*Fig.3.42*) related with this observation phase does not highlight any specific changes directly correlated with water level fluctuation. In fact the resistivity continued to increase in the model and especially in the horizontal plume even though the pollutant spillage was stopped some days before. On the contrary, statistical analysis highlighted very well the influence of the water level lowering on the resistivity values related with ***07_23*** survey (see *Section 3.3.1.1*).

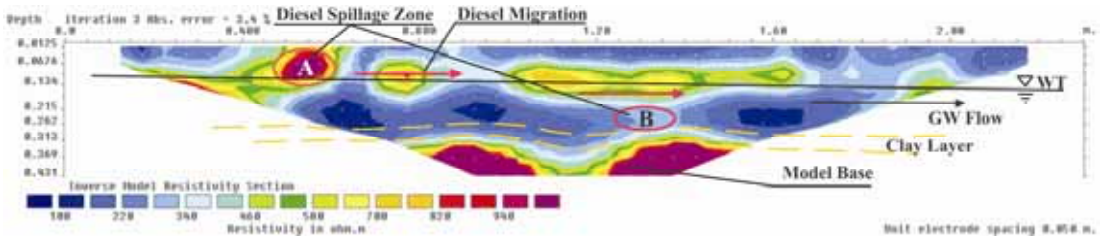

***Fig. 3. 42**: 'Inverse model '**07_23**' map showing the diesel spillage in Zone A; the horizontal and vertical pollutant plume and the increase in resistivity expected whit diesel spillage in Zone B. The groundwater was at lower level.*

When then the groundwater table was permanently fixed at high level during the second week of the monitoring campaign (*Fig.3.43*), the method of analysis recorded how the pollutant concentration was increasing and penetrating the soil. This was especially true on the left hand side of the physical model and on the top of the sandy layer, below the groundwater level. Whereas in the model centre, the pollutant was ascending to the top of the groundwater, forming a plume following the water flow.

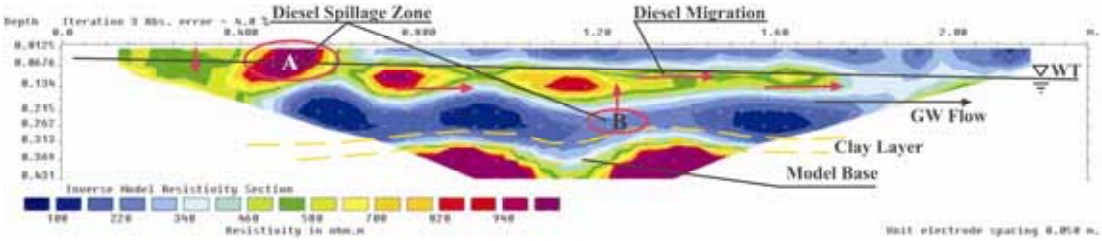

***Fig. 3.43**: 'Inverse model '**07_24**' map showing the diesel spillage in Zone A; the horizontal and vertical pollutant plume in diesel spillage Zone B. The groundwater was fixed at high level.*

For LNAPL release in the unsaturated zone, the capillary fringe and the water table tends to act as a hydraulic barrier for further downward migration (see section) (Mayer 2002).

In the present study, initially the LNAPL stagnated on surface (*Fig.3.1*) and then displaced the water beneath the water table. At the same time, horizontal spreading took place in all directions, although this could not be seen very clearly with this kind of data analysis and maybe because there were few data points. During this sequence of events, the increasing resistivity on the top and in the centre of the physical model continued to alter the form of its base and it was no longer possible to recognise the original horizontal shape of the clay layer that was still present.

At the end of the first monitoring campaign (i.e. fourth week) when there were no external events (i.e. pollutant injection end/or changes in water level) to disturb the model, it seemed to achieve an internal equilibrium. However, the statistical analysis already showed in *Figures 3.9-10-11-13-16-17* (*Section 3.3.1*) that the last seven daily electrical surveys (i.e. 08_02; 08_3; 08_06; 08_07; 08_08; 08_09; 08_10) ***Mean*** and ***Median*** curves have horizontal trends. In fact, the inverse model map '***08_10***' (*Fig.3.44*) is almost the same in comparison with the last *Figure 3.40.* Only this time (*Fig.3.44*), the diesel spillage zone on the left of the model (i.e. Zone A) and the horizontal pollutant plume are less intense in colour. This is likely to have happened because the pollutant didn't feed the spillage zones any more and from these zones the pollutant dispersion was spreading to the remaining parts of the model. It is also likely that, the outliers on the top of the box-plots in *Figures 3.16-17* were directly related with the resistivity of the spillage point. In fact when the resistivity values decreased in this area, the outliers simultaneously also diminished,

into a number that maintained a constant ***Range*** (*Fig.3.11-12*) of resistivity in the model.

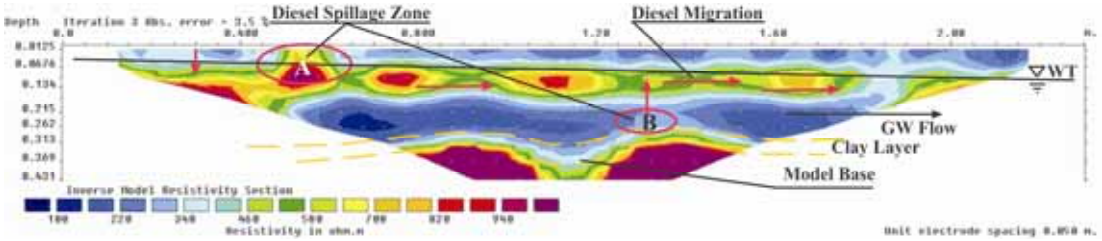

Fig. 3.44*: 'Inverse model '**08_10**' map showing the diesel spillage in Zone A; the horizontal and vertical pollutant plume in diesel spillage Zone B. The diesel spillage zone on the left model side (i.e. Zone A) and the horizontal pollutant plume are less intense in colour in comparison with previous maps.*

3.3.3.2 Discussion of results: first set of Subtracted Apparent Resistivity Data

As already reported in the statistical analysis section (see *Section 3.3.1*) the data obtained by subtracting each electrical resistivity survey from the Apparent Resistivity data of the baseline survey, before the diesel spillage has been converted into a resistivity model (i.e. *Inverse Method Resisitivity Analysis*).

The images obtained represent the changes in electrical resistivity can be exclusively detemined by the influence of the pollutant presence. The pollutant presence can influence the electrical resistivity through its dispersion and movement in the laboratory model The introduction of the pollutant and it's subsequent dispersion, affects the visual reading. For example, when the model has no pollutant in the tank, it is possible to see the Perspex tank highlighted as high resistivity in a horizontal line at the bottom of the tank. However when the pollutant is introduced, the horizontal lines are skewed due to the presence of the pollutant and it's plume.

The first image, subtracting the '***Baseline***' survey to the ***07_17a*** survey recorded six hours after the first diesel spillage in the model (*Fig.3.45*), shows an increasing resistivity only on the left side of the map. This increase in resistivity is probably due to the diesel spillage on the left side of the model, however on the base of the laboratory model, the higher resistivity is also likely due to anomalous data, interacting with the Perspex.

It is important to specify that the colours of the defined contour interval in the following 'subtracted' maps represent exclusively the increase in resistivity values.

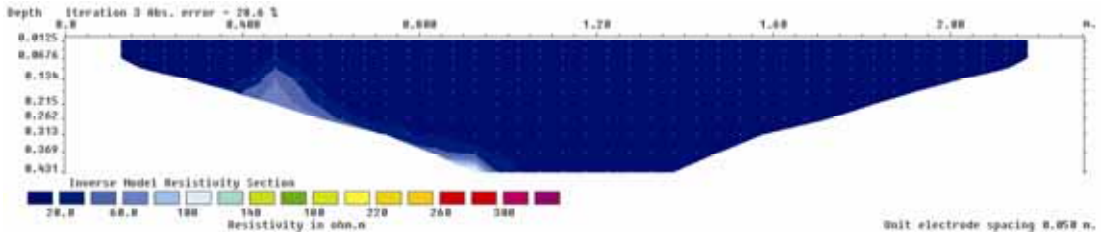

***Fig. 3.45**: 'Inverse model '**07_17a-baseline**' map six hours after the first diesel spillage in the model. Increase in resistivity only on the left side of the map due probably to the diesel spillage and on the base of the laboratory model due probably to anomalous data.*

.

Using the subtracted data was not possible to clearly define the first diesel spillage location six hours after the splillage of diesel. However, an increase in resistivity was recorded in the light blue colour above and is a significant breakthrough in comparison with the previous equivalent inverse image (*Fig.3.38*). The previous image (*Fig.3.38*) obtained using the original apparent resistivity data, found it impossible to note any change in resistivity six hours after the diesel spillage in the same area.

Figure 3.46 represents the difference map obtained using the data recorded when the diesel was abundantly spilt on the left side (i.e. Zone A), when the pollutant started to be split on the centre of the model (i.e. Zone B) and when the groundwater was fixed at low level. The first spillage zone (i.e. Zone A) was increasing its shape and the resistivity values were also increasing in the centre of the model (i.e. Zone B). On the contrary of the previous correspondent *Figure 3.39* in this map (*Fig.3.46*), identified the increasing resistivity, particularly below the water table. This is likely to be related to the diesel spillage in Zone B and it was not as easy to clearly identify the horizontal plume.

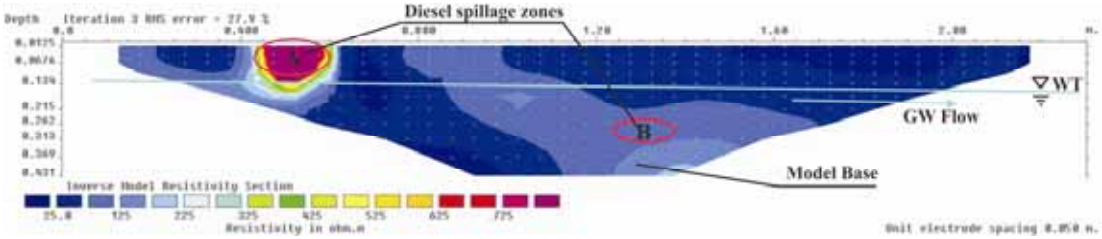

***Fig.3.46**: Image '**07_18-Baseline**' obtained subtracting the apparent resistivity values of the electrical resistivity baseline survey to the apparent resistivity values of the electrical resistivity survey (**07_18**) recorded with low water level and diesel spillage on left model side.*

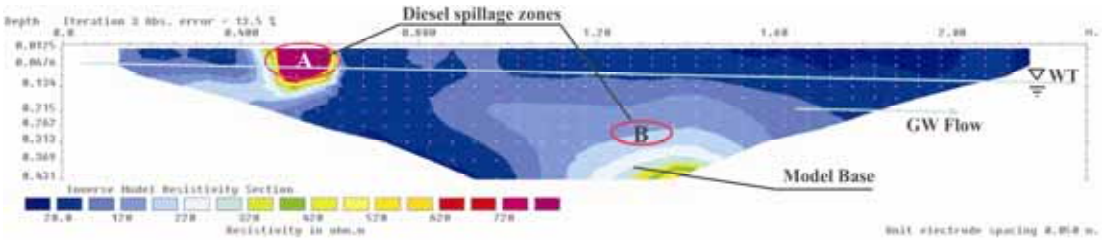

***Fig.3.47**: Image '**07_18a-Baseline**' obtained subtracting the apparent resistivity values of the electrical resistivity baseline survey to the apparent resistivity values of the electrical resistivity survey (**07_18a**) recorded with high water level and diesel spillage on left model side.*

At the end of the diesel spillage in Zone B and when the water level was at a higher level (*Fig.3.47*), the resistivity values continued to increase especially below the water table in the centre of the model. Subsequently in *Figure 3.48* the resistivity continued to increase and a similar trend was observed.

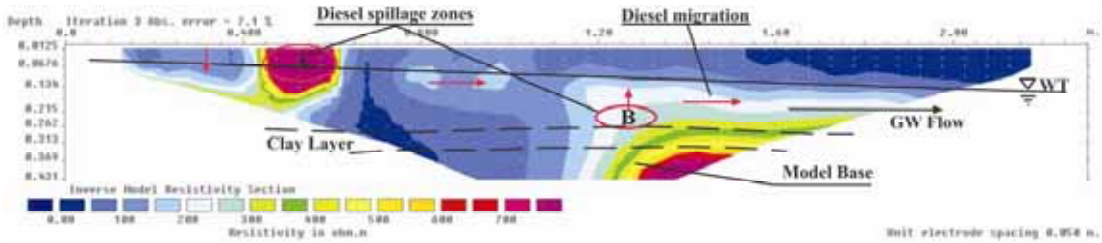

***Fig.3.48**: Image '**07_19a-Baseline**' obtained subtracting the apparent resistivity values of the electrical resistivity baseline survey to the apparent resistivity values of the electrical resistivity survey (**07_19a**) recorded with high water level and any diesel spillage in the model.*

During the new water level lowering (*Fig.3.49*) the increasing resistivity continued in most areas in the model especially close to the Zone B. It did not

increase, however in the left side of the model, here the resistivity decreased on the top of the water table. It is possible to hypothesize that the horizontal pollutant plume mingled with a vertical plume in the model centre.

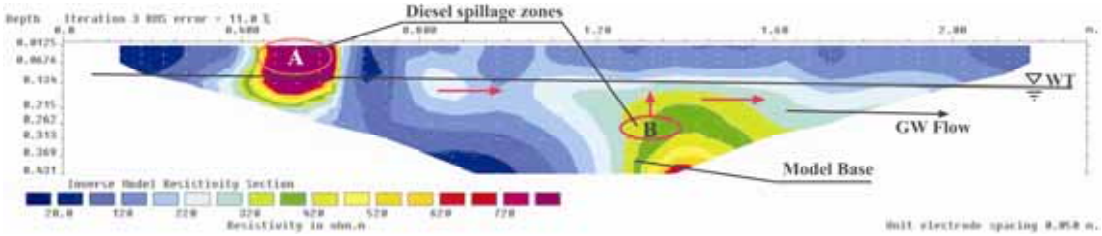

***Fig.3.49**: Image '**07_23-Baseline**' obtained subtracting the apparent resistivity values of the electrical resistivity baseline survey to the apparent resistivity values of the electrical resistivity survey (**07_23**) recorded with low water level and any diesel spillage in the model.*

With the new stable high water level (*Fig.3.50*) the resistivity in the model continued to increase, deforming the shape of the resistivity distribution in the diesel spillage zones and delineating better than before the horizontal e vertical pollutant dispersion.

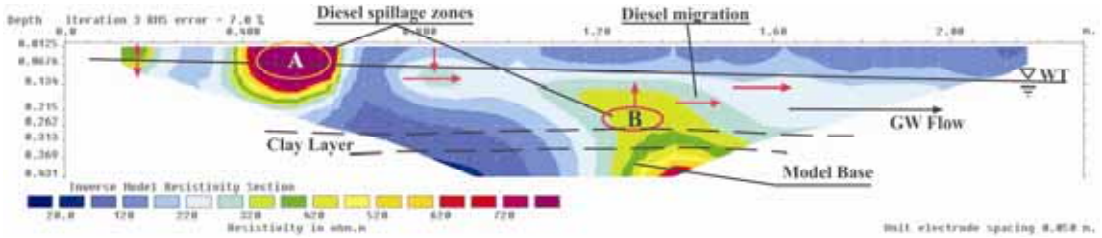

***Fig.3.50**: Image '**07_24-Baseline**' obtained subtracting the apparent resistivity values of the electrical resistivity baseline survey to the apparent resistivity values of the electrical resistivity survey (**07_24**) recorded with new high water level and any diesel spillage in the model.*

The following electrical resistivity survey map (i.e. *Fig.3.51*) confirms the effect related to the rising water level shown in the previous map (*Fig.3.44*; *Survey 08_10*). In addition, it identifies that a consistent reduction in resistivity is related to the diesel spillage zones. This can be clearly seen in the left hand side of the Zone A, confirming that the reduction in outliers in the last box-plots in *Figure 3.17* are related with diesel spillage zones.

On the contrary, below and above the water table and on the right hand side of the Zone B the resistivity continues to increase due to the wide distribution of the pollutant in the laboratory model.

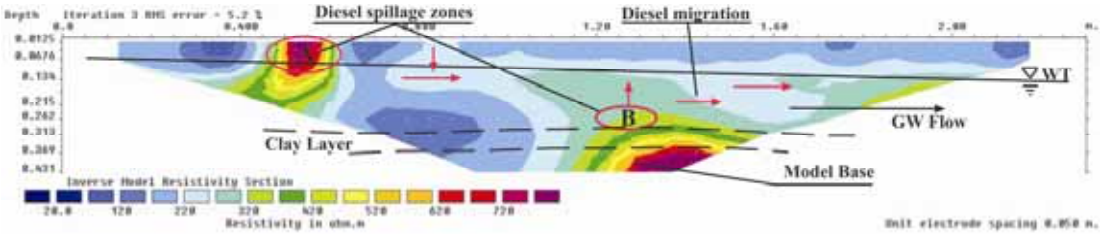

***Fig.3.51**: Image '**08_10-Baseline**' obtained subtracting the apparent resistivity values of the electrical resistivity baseline survey to the apparent resistivity values of the electrical resistivity survey (**08_09**) recorded with constant high water level and any diesel spillage in the model.*

3.3.3.3 Discussion of results: Apparent Resistivity Data Second Monitoring Campaign

The analysis of the Apparent Resistivity data belonging to the electrical resistivity survey of the second monitoring campaign was carried out using the '*Inverse Method*' and the same software (i.e. RES2DINV®) used in the Apparent Resistivity data from the first monitoring campaign. The only change was the "*Enter Minimum Contour Value*": ***350*** and "*Enter Contour Spacing Value*": ***100.*** This change was made to adapt the colours of the defined contour interval for the inverse model resistivity maps to the new range of data.

In fact the range of Apparent Resistivity data belonging to the first monitoring campaign was different from the Apparent Resistivity data belonging to the second monitoring campaign (see *Section 3.3.1 Fig.3.11 and 3.20*). This was due to the different electrode spacing (i.e First Monitoring Campaign: 24 electrodes – 10 cm spacing; Second Monitoring Campaign: 48 electrodes – 5 cm spacing) in the same model length (i.e. 240 cm).

The first inverse model resistivity map (*Fig.3.52; Survey 11_01*) of the second monitoring campaign appeared quite similar to the last inverse resistivity map (*Fig.3.44; Survey 08_10*) of the first monitoring campaign. In fact, it was possible to identify the spillage zones (i.e. Diesel Spillage Zone A-B); the groundwater level; the

horizontal plume; the deformed clay layer and some anomalous areas due to the interference of the electrical resistivity arrays with model boundaries on its left side, right side and on its base.

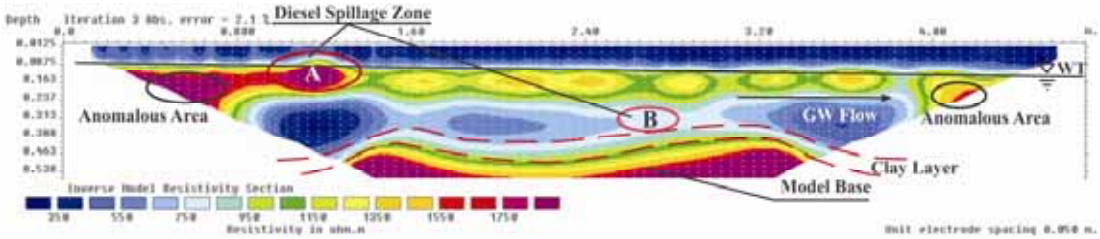

***Fig.3.52**: 'Inverse model '**01_11**' map showing the diesel spillage in Zone A; the horizontal and vertical pollutant plume in diesel spillage Zone B.*

During the second monitoring camping and before the barrier installation (i.e. 11/01/08 to 22/05/08) the laboratory model was monitored once per week maintaining the groundwater constantly at high level. The last inverse resistivity map (*Fig.3.53; Survey 05_22*) before the barrier installation (see all the maps in *Appendix E*) shows that the general resistivity distribution in the model was decreasing over time especially the horizontal plume on the top of the groundwater flow and the resistivity in the model centre were decreasing toward lower values.

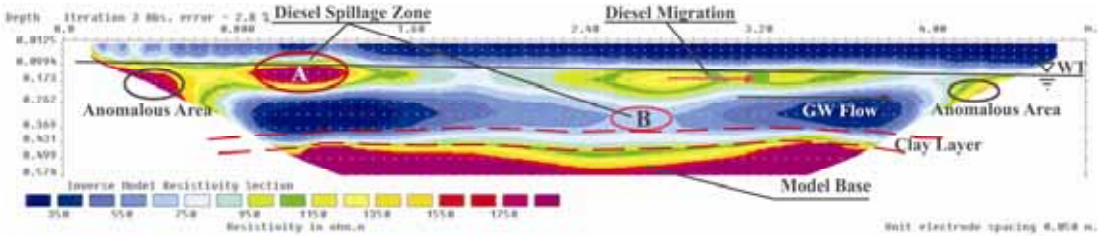

***Fig.3.53**: 'Inverse model '**05_22**' map showing the diesel spillage in Zone A; the horizontal and vertical pollutant plume in diesel spillage Zone B.*

Subtracting the Apparent resistivity data from the 01_11 electrical survey to the Apparent Resistivity data from the last electrical survey ***05_22*** before the barrier was installed, it was possible to achieve the Inverse model resistivity map (*Fig.3.54*). This figure displays that generally the resistivity was decreasing in the model (i.e. deep blue colour) except in the areas where there were anomalous resistivity values. Again this can be explained by the interaction among electrodes (i.e. on soil surface);

model boundaries (i.e. model base) and soil that caused the resistivity increased over four months (i.e. 01_11 to 05_22).

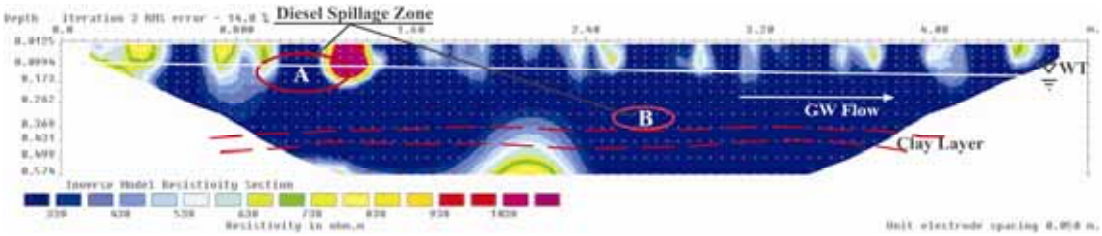

***Fig.3.54**: Image '**05_22-01_11**' obtained subtracting the apparent resistivity values of the electrical resistivity survey **01_11** to the apparent resistivity values of the electrical resistivity survey **05_22** recorded with constant high water level and any diesel spillage in the mode during the second monitoring campaign.*

The new event in the model was the instalment of the permeable reactive barrier in the middle of the model following the procedure already described in *Section 2.5.3*.

The statistical analysis and its descriptive parameters (i.e. Mean; Media; Range; Sample Variance; Kurtosis; Skewnees) (see *Section 3.3.1.3; 3.3.1.4*) of the Apparent Resistivity data, revealed the barrier effects on the resistivity in the laboratory model. In addiction, it also displayed where these effects occurred in the Inverse Model Resistivity Analysis.

Fixing the diesel spillage zone locations, i.e. clay layer location already identified in the previous maps and setting the barrier almost in the middle of the model, the *Figure 3.55* shows the sequence of maps obtained after the barrier was installed.

In survey 05_26 map it is possible to see how the injection of the ORC-Ad in 24 mini-boreholes caused a clear-cut breaking of the previous resistivity distribution. In the following phases (i.e. *Survey 05_30* to *06_27*) the horizontal plume of low resistivity (i.e. blue colour) expanded on the right side of the model reducing also, the resistivity distribution of the horizontal plume on the top of the ground water table.

On the contrary, on the left side of the model there are no relevant changes in resistivity over the testing period.

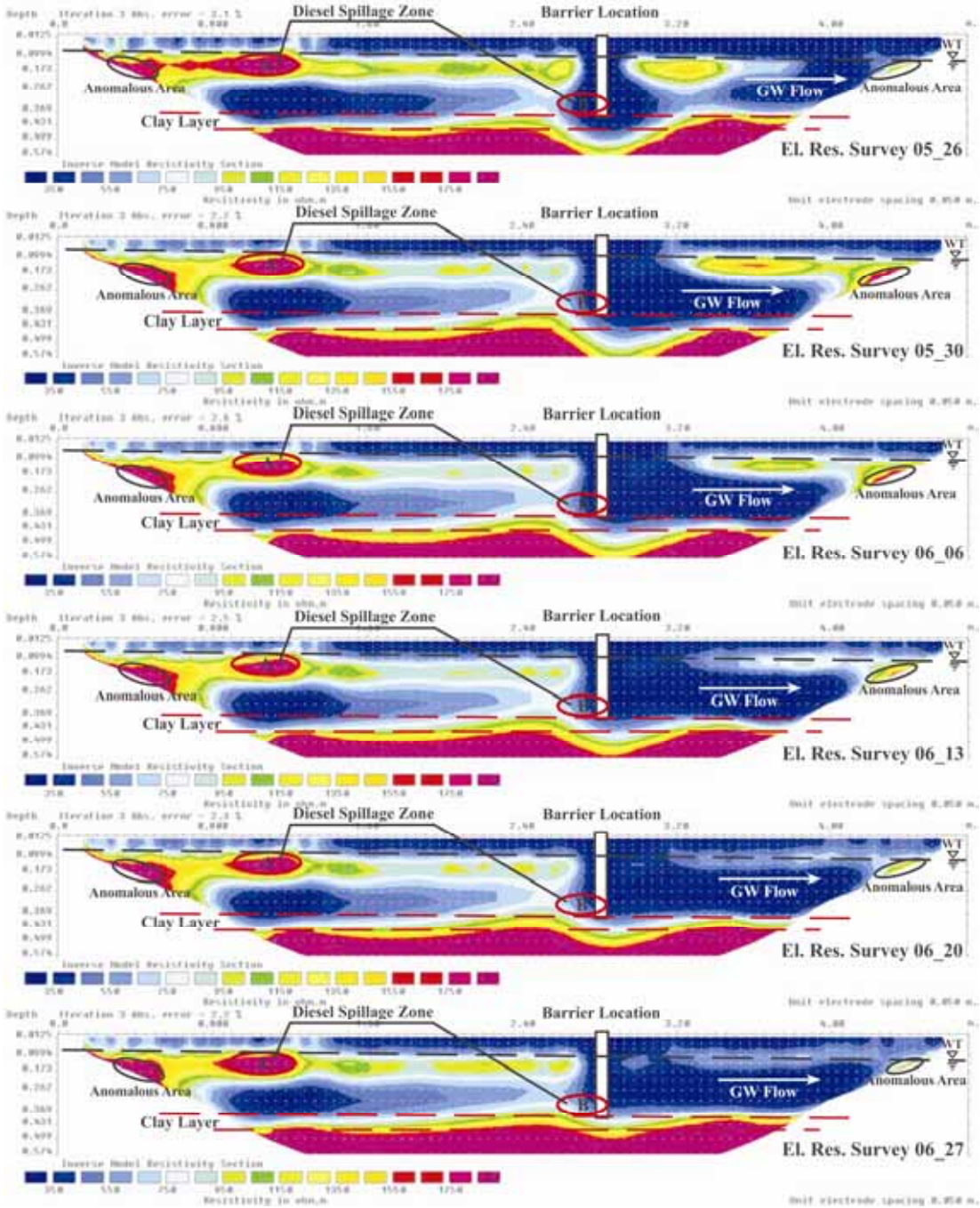

***Fig.3.55**: Sequence of the Inverse Resistivity model maps obtained after the barrier installation until the research end.*

3.3.3.4 Discussion of results: second set of Subtracted Apparent Resistivity Data

The Apparent Resistivity data belonging to the last electrical resistivity surveys (i.e. *Survey 05_22*) before the barrier was installed, were subtracted to the Apparent Resistivity data belonging to the resistivity surveys after the barrier installation in order to highlight only the changes in resistivity occurred.

The subtraction gave positive and negative values and because the inverse resistivity model is not able to use negative values, all the data were treated in order to have two different kinds of images. The first sequence of maps (*Fig.3.56*) shows only areas of the cross-sections involved in resistivity increase and the second sequence of images (*Fig.3.57*) shows only the areas of the cross-sections involved in resistivity decrease.

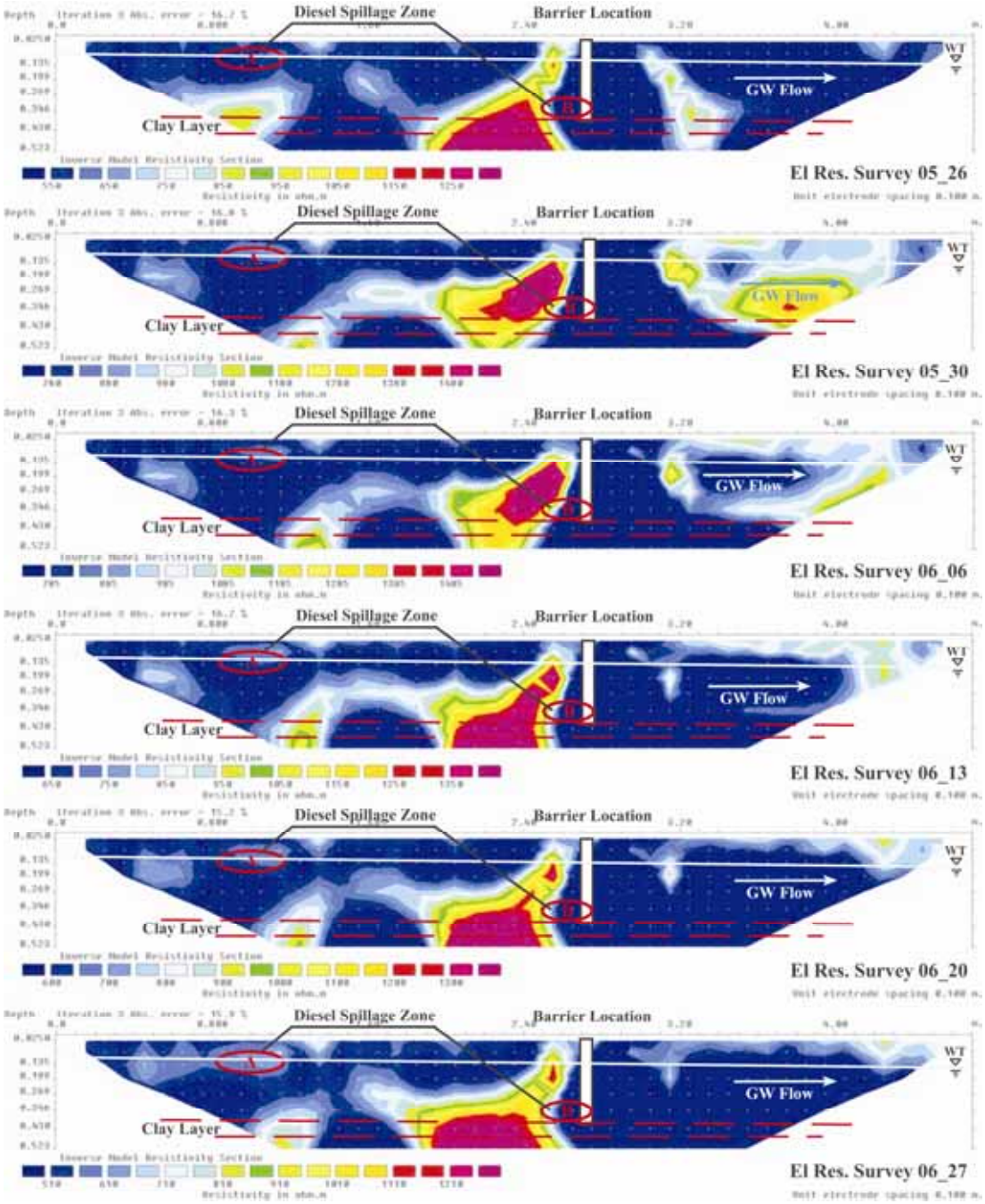

Fig.3.56*: Sequence of the Inverse Resistivity model maps obtained subtracting the last resistivity values recorded before barrier installation to the apparent resistivity values recorded after barrier installation until the research end. This maps show only areas of the cross-sections involved in resistivity increase.*

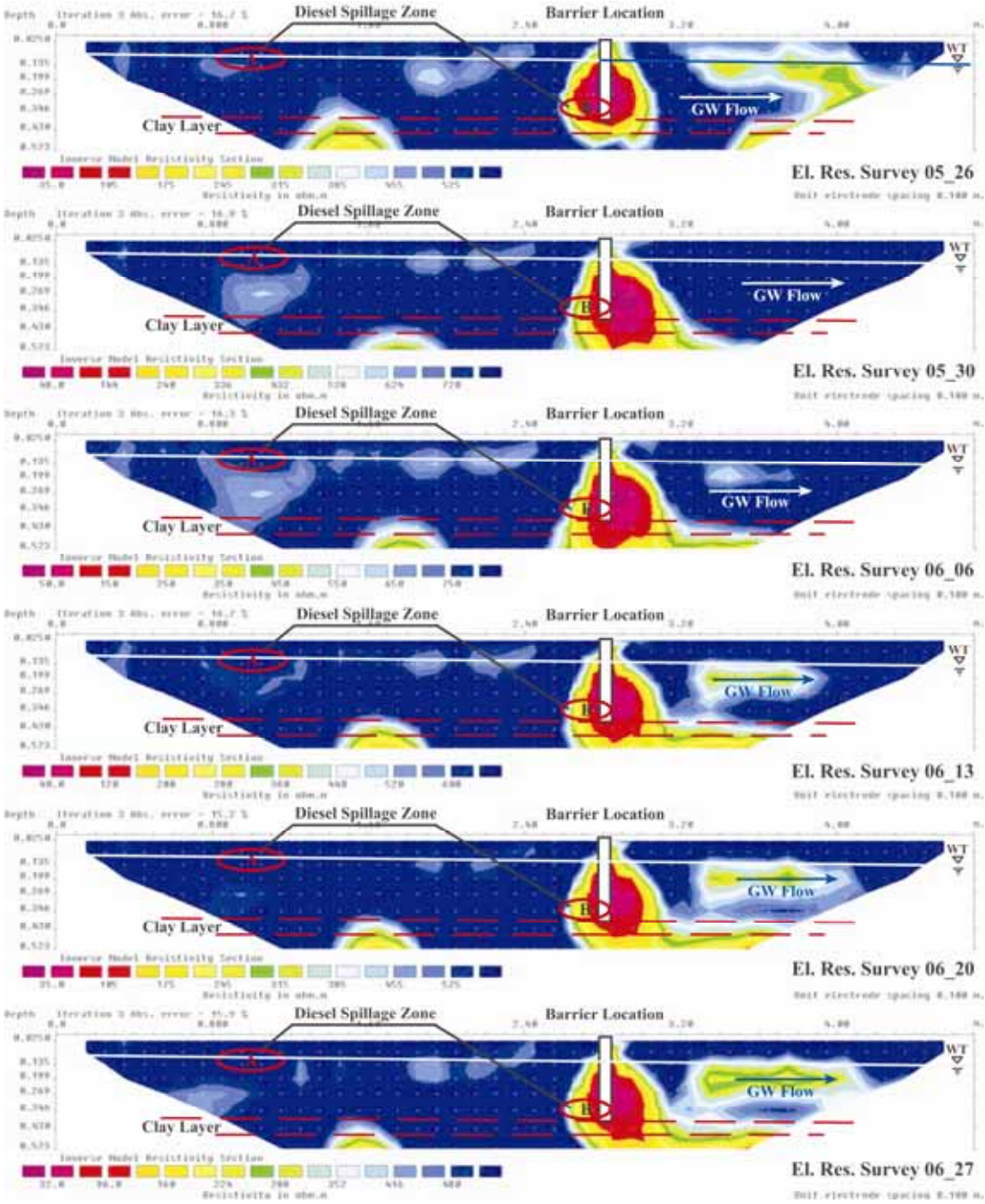

Fig.3.57*: Sequence of the Inverse Resistivity model maps obtained subtracting the last resistivity values recorded before barrier installation to the apparent resistivity values recorded after barrier installation until the research end. This maps show only areas of the cross-sections involved in resistivity decrease.*

The ORC-Ad injection probably moved the pollutant previously located in the barrier area upstream and downstream the barrier location causing an increasing in resistivity in these new areas (i.e. *Survey 05_26 Fig.3.53*). The outliers (labelled '○') on the top of box-plots in Figure 3.32 - 3.33 (see *Section 3.3.1.4*) also showed

increasing resitivity. Subsequently the area with low resistivity extended itself downstream toward the outlet water side (i.e. *Survey 05_30 to 06_27 Fig.3.56*).

Upstream of the barrier the high resistivity went up in the second map (i.e. *Survey 05_30 Fig.3.56*) and subsequently decreased its intensity in the area between water table and clay layer (i.e. *Survey 06_06 to 06_27*) (see *Sect 3.3.1.4 Fig. 3.32 - 3.33*).

Also in these maps there are some areas with anomalous resistivity related to the anomalous interaction among electrical resistivity array, model boundaries and soil. This is particularly seen on the left side of the model (i.e. yellow spot on the base of the clay layer) and on the soil surface not directly related to the pollutant distribution or barrier effects.

In order to clearly display the model areas with a resistivity decrement, the maps in *Figure 3.57* were achieved by inverting the colour scale and focusing the inverse model analysis and its representation in the data with decrement in resistivity.

In the first *Survey 05_26* (*Fig.3.57*) the ORC-Ad injection area had an elliptic shape with the main axis coincident with barrier. Successively the elliptic shape change moving downstream and contemporaneously the area with low resistivity expanded itself just below groundwater table toward outlet water model side (i.e. *Survey 05_30* to *06_27 Fig.3.57*).

The anomalous areas are located in these maps especially on the model base (i.e. yellow spot on the left model side) and on the model surface.

In addiction, in this specific case was interesting to observe the the '*Apparent Resistivity Pseudo-section*' maps (*Fig.3.58*) achieved during the inverse analysis.

The simple distribution of the apparent resistivity values in the cross-section probably gives a better representation of the barrier effects over time. In the first map (i.e. *Survey 05_26 Fig 3.58*) the barrier zone was represented as a parallelepiped that successively changes its shape involving all the area on the right barrier side (i.e. *Survey 05_30* to *06_27*).

On the contrary the left model side was not involved in relevant resistivity changes.

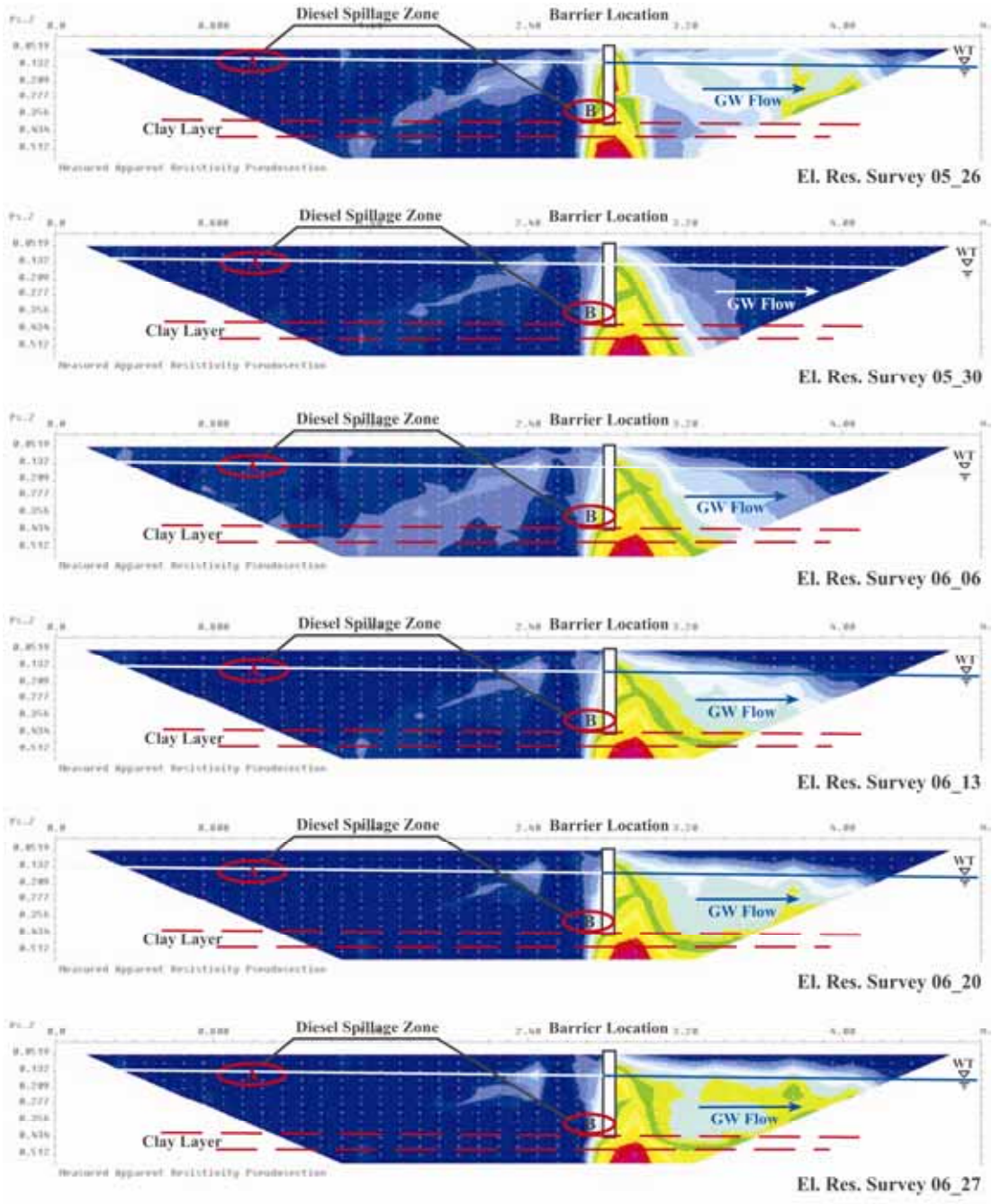

***Fig.3.58**: Sequence of the Measured Apparent Resistivity maps obtained subtracting the last resistivity values recorded before barrier installation to the apparent resistivity values recorded after barrier installation until the research end. This maps show only areas of the cross-sections involved in resistivity decrease.*

Chapter 4: Conclusions and Future Work

The aim of this research was to verify the effectiveness of the electrical resistivity method in:

- The study of the pollutant (i.e. diesel) dispersion in the soil;
- The monitoring of the changes in resistivity due to the fluctuation of the groundwater level;
- The monitoring of the changes in resistivity due to the injection of the Oxygen Release Compound in a permeable barrier settled in the ground laboratory model.

A the end of the data collection and data analysis it is possible to affirm that the electrical resistivity survey method based on the Wenner-Schlumberger array was effective in:

1) detecting the horizontal stratification of the soil in the model,
2) detecting the pollutant effects on the surface and lower soil levels;
3) detecting the presence of groundwater and the effects of its fluctuations,
4) detecting the effects of the barrier instalment made with ORC-Adv.

4.1 Horizontal Stratification of the Laboratory Subsurface

The *Inverse Resistivity Analysis* of apparent resistivity in the model prior to pollutant spillage confirmed a uniform horizontal soil stratification and homogeneity of electrical resistivity in all strata.

The scientific literature generally suggests (Carrara et al. 2004; Loke 2001; Reynolds 1995) that clay is characterized by lower resistivity values than a sandy soil. In this study, however, the reverse was observed. The sandy soil has lower resistivity than clay soil and there is no overlap between soil types. It is probable that this is directly attributable to the presence of dissolved salts in the sandy soil (i.e. NaCl) which are transported by the groundwater flow. For the same reason, resistivity values on the water inlet hand side of the baseline map (i.e. *Fig.3.37*

Survey 07_17) are slightly higher than the values on the water outlet hand side as indicated by the conductivity values reported in the results of the chemical laboratory analysis and "in situ" analysis of the water sampled in the model (see *Section 3.2.1*; *3.2.2* & *Appendix B*).

4.2 Influence of Diesel Spillage on Electrical Resistivity Changes

Diesel was spilt on surface on the 'water inlet' model side [*Zone A*] and in the centre of the sandy layer [*Zone B*] and the electrical resistivity investigation method detected and recorded single spillage events and overlap between events.

The pollutant spillage on the surface (i.e. Zone A) was detected six hours after its introduction within a restricted area a few centimetres deep in the sandy layer, near the spillage point (see *Fig. 3.45 Section 3.3.3.2*) with a map achieved subtracting the apparent resistivity data of the '*Baseline*' electrical survey to the apparent resistivity data of the survey '*07_17a*'. From the start of the pollutant spillage, however, flooding of the surface pollutant was noted running off towards the 'water inlet' model side in the opposite direction to the groundwater flow (*Fig.3.1 Section 3.1*), and this then settled on the surface. This pollutant behaviour was not recorded by the electrical resistivity meter due to the interaction between the soil, water and physical-chemical pollutant characteristics.

Only when the spilt pollutant reached an adequate quantity it was recorded by the electrical resistivity meter. In fact the diesel was able to displace water from the capillarity fringe and settle on the top of the saturated zone (see *Fig. 3.43*).

The dispersion and diffusion dynamics of the pollutant spilt on the bottom of the sandy layer in the centre of the model (i.e. Zone B) have different characteristics than the earlier, superficial spillage and this is reflected in the resistivity meter readings. In this area less diesel was spilt (500 ml in 24 hours c.f. 1000 ml on the left model site) and it is for this reason that the resistivity values never reached the same high levels as recorded on the left hand side of the model and the pollutant in the central area is involved more with the dynamics of the groundwater flow.

The spillage effects were soon noted on the surface but were not registered by the resistivity meter until some hours after the spillage commenced. They were

manifested by a general increase in resistivity in the centre of the saturated zone and presence of a vertical plume indicating a sudden rise in pollutant (see *Section 3.3.1* and *Fig. 3.43*). In the subsequent surveys the diffusion area of the pollutant became larger, increasing the resistivity on the bottom of the sandy layer and heightening the movement of the pollutant plume movement in accordance with the direction of groundwater flow. This is due to the rapid reappearance of pollutant on the model surface, the pollutant becoming trapped in soil pores, the adsorption of some pollutant components by soil particles and to the action of the groundwater flow which favours pollutant dispersion toward the left hand side of the model.

4.3 Influence of Groundwater Fluctuation on Electrical Resistivity Changes

Groundwater level was changed only during the first monitoring campaign and in general the greatest resistivity levels occurred during the first week and coincided with the overlap of effects due to attaining the maximum diesel spillage and maximum water level. In the weeks following the diesel spillage phase, the effects were exclusively due to the groundwater fluctuations, which are illustrated in the box plots (*Fig.3.16* and *3.17 Section 3.3.1.2*). From these plots, it is also possible to see that the effect of lowering the water level is to concomitantly lower the moisture content of the soil surface and the penetration rate of non volatile components through the soil. These are always manifested by a general decrease in resistivity.

When the water level was suddenly increased, it caused an initial maximum increment in resistivity followed by an adjustment phase characterised by spontaneous fluctuations in resistivity values that reached a stable equilibrium some days after the last water level change. This is due to the elevation in water level causing some of the pollutant which had already settled on the groundwater to rise to the surface and merge with the pollutant already trapped in the unsaturated zone. The rise in groundwater stimulates movement of the contaminant which, being slower than the groundwater flow tends to accumulate in model zones that then have high resistivity values.

4.4 Influence of ORC-Adv injection on Electrical Resistivity Changes

During the second monitoring campaign and before the barrier installation the electrical resistivity method was able to record in the model a general decreasing in electrical resistivity over the time (see *Section 3.3.1.3* and *3.3.1.4*; *Section 3.3.3.1 Fig.3.52* to *3.54*) probably due to the continued pollutant dispersion that allows part of dissolved pollutant transported by groundwater to leave the model or due to probable biological reaction that could support natural attenuation actions.

The ORC-Adv injection during the barrier installation suddenly caused new drastic changes in resistivity. All the statistical parameters recorded this event, especially when analysing the data obtained from subtracting the apparent resistivity data of each electrical survey after barrier installation, from the apparent resistivity data belonging to the last survey before barrier installation.

The box-plot graphs (see *Section 3.3.1.4; Fig.3.32* to *3.34*) emphasized the reduction in resistivity. This is probably caused by the injection of ORC-Adv with fresh water and a local increased resistivity caused by the pollutant displacement present in the soil pores during the barrier instalment.

The *Inverse Model Analysis* allowed to visualize in which part of the model the changes occurred (*Fig.3.55* to *3.57*). The barrier installation acted like a break and divided the laboratory model in two different parts. All the main changes in resistivity are located on the right model side (i.e. barrier downstream side) and the left model side (i.e. barrier upstream side) remained almost unchanged in resistivity.

The injection of ORC-Adv and water caused a drastic decrement in resistivity around the barrier location that broke the pollutant plume. The pollutant present in the pores of the soil was displaced into new locations downstream and upstream of the barrier. This caused an increase in resistivity in these new areas. Subsequently a low resistive plume expanded in the right side of the model, reducing the resistivity distribution in this part of the model.

At this research stage the effects (i.e. cutting of the pollutant plume; reduction in resistivity) should be attributed not to the real reduction in pollutant concentration but to:

- The injection action that was introduced into the model slurry with low electrical resistivity;and the,
- Oxygen liberation during the slow hydration of the ORC-Adv.

In fact chemical analysis of two water specimens sampled upstream and downstream of the barrier 5 weeks after the barrier was installed, revealed that the pollutant concentrations are still almost the same (i.e. 10 mg/l upstream; 8 mg/l downstream) in both barrier's edges.

It is important to remember that electrical resistivity images are the outcome of data processing (i.e. they are based on apparent resistivity values) and for this reason they must not be interpreted as a direct representation of the field situation, but rather as a guide for qualitative estimation of the electrical resistivity distribution in the soil model.

The chosen Wenner-Schlumberger array has been confirmed as valid not invasive investigation method in a given situation but the accuracy of electrical resistivity images can be improved determining a three-dimensional (3-D) resistivity model for the subsurface using the data obtained from a 3-D electrical imaging survey (Li and Oldenburg 1992, White et al. 2001). Ideally, the electrodes for such a survey should be arranged not along a cross-section but in a rectangular grid.

In this specific study it was relatively easy to follow and interpret the changes in resistivity values but in 'life' situations geological structures are generally more complex and the spillage location and pollutant composition in the soil may not be known. Therefore, it is an efficient survey method in environmental investigations in the field and the accuracy of electrical resistivity images can be improved determining a three-dimensional (3-D) resistivity model for the subsurface using the data obtained from a 3-D electrical imaging survey (Li and Oldenburg 1992, White et al. 2001). Ideally, the electrodes for such a survey should be arranged not along a cross-section but in a rectangular grid.

Chapter 5: References

Abdul Nassir, S.S., Loke, M.H., Lee, C.Y., Nawawi, M.N.M., 2000. Salt-water intrusion mapping by geoelectrical imaging surveys. *Geophysical Prospecting*, Vol. 48, pp. 647-661.

Acworth, R.I., Jorstad, L.B., 2006. Integration of multi-channel piezometry and electrical tomography to better define chemical heterogeneity in a landfill leachate plume within a sand aquifer. *Journal of Contaminant Hydrology* Vol. 83 pp. 200– 220.

Balba, T., Dore, S., Pope, D., Weston, A. 2006. Feasibility Assessment of Organic and Iron-Based Permeable Reactive Barriers for Treatment of Chlorobenzenes. *Fifth International Conference on Remediation of Chlorinated and Recalcitrant Compounds,*Monterey, CA. Published by *Battelle Press*, ISBN 1-57477-157-4.

Aristodemou, E., Thomas-Betts, A., 2000. DC resistivity and induced polarisation investigations at a waste disposal site and its environments. *Journal of Applied Geophysics* Vol. 44 pp. 275–302.

Atekwana, E.A., Sauck, W.A., Werkema, D.D., 2000. Investigations of geoelectrical signatures at a hydrocarbon contaminated site. *Journal of Applied Geophysics* Vol. 44, pp. 167–180.

Atekwana, E. Atekwana, E.A., Legall, F.D., Krishnamurthy, R.W., Sauck, W.A., 2004. Relationship Between Biodegradation and Bulk Electrical Conductivity. SAGEEP 2004: *Symposium on the Application of Geophysics to Engineering and Environmental Problems*, 22-26 February 2004, Colorado Springs, Colorado. Environmental and Engineering Geophysical Society, Denver, CO. CD-ROM, pp. 354-362.

Atekwana, E.A., Atekwana, E.A, Rowe, R.S. Werkema, D.D., Legall, F., 2004. The relationship of total dissolved solids measurements to bulk electrical conductivity in an aquifer contaminated with hydrocarbon. *Journal of Applied Geophysics* Vol. 56 pp. 281– 294.

Atekwana, E.A., Atekwana, E., Legall, F.D., Krishnamurthy, R.V., 2005. Biodegradation and mineral weathering controls on bulk electrical conductivity in a shallow hydrocarbon contaminated aquifer. *Journal of Contaminant Hydrology* Vol.80, pp. 149– 167.

Bacha, J., Blondis, L., Freel, J., Hemighaus, G., Hoekman, K., Hogue, N., Horn, J., Lesnini, D., McDonald, C., Nikanjam, M., Olsen, E., Scott, B., Sztenderowicz, M., 1998. Technical Review Diesel Fuel. *(FTR-2) Chevron Products Company*, a division of Chevron U.S.A. Inc.

Ball, L.B., Kress, W.C. Anderson, E.D., Teeple, A.P., Ferguson, J.W., Colbert, C.R., 2004. Surface Geophysical Investigation of the Areal and Vertical Extent of Metallic Waste at the Former Tyson Valley Powder Farm near Eureka, Missouri, Spring 2004. *Scientific Investigations Report* 5208. Geological Survey, USA.

Barker, R., 1981. The offset system of electrical resistivity sounding and its use with a multicore cable. *Geophysical Prospecting* Vol. 29, pp. 128-143.

Barker, R.D., 1991. Depth of investigation of collinear symmetrical four-electrode arrays. *Geophysics*, Vol. 54, pp. 1031-1037.

Barker, R., Venkateswara Rao, T., Thangarajan, M., 2001.Delineation of contaminant zone through electrical imaging technique. *RESEARCH COMMUNICATIONS, CURRENT SCIENCE*, Vol. 81, no. 3, 10.

Batayneh, A.T., 2001. Resistivity imaging for near-surface resistive dyke using two-dimensional DC resistivity techniques. *Journal of Applied Geophysics* Vol. 48 pp. 25–32.

Bauer, P., Supper, R., Zimmermann, S., Kinzelbach, W., 2006. Geoelectrical imaging of groundwater salinization in the Okavango Delta, Botswana. *Journal of Applied Geophysics* 60 (2006) 126–141.

Bergström, G., 1913. Försök med elektrisk maimletning. *Svering Geoliska Undersöknings Arsbok* Stockholm 7 (6), pp.1-10.

Bermjo, J., Sauck, W.A., Atekwana, E.A., 1997. Geophysical discovery of an LNAPL plume at Wurtsmith AFB. *Ground Water Monitoring and Remediation* vol 17, pp. 131-137.

Berryman, J.G., 1997. Surface and Borehole Electromagnetic Imaging of Conducting Contaminant Plumes. *Project Report*. Lawrence Livermore National Laboratory (LLNL), Livermore, California, U.S.A.

Boehm, P.D., Quinn, J.G., 1974. The solubility behavior of No. 2 fuel oil in sea water. Mar Pollut Bull, Vol. 5, pp. 101-105.

Boopathy, R., 2003. Use of anaerobic soil slurry reactors for the removal of petroleum hydrocarbons in soil. *International Biodeterioration & Biodegradation* Vol. 52, pp. 161 – 166.

Boopathy, R., 2004. Anaerobic biodegradation of no. 2 diesel fuel in soil: a soil column study. *Bioresource Technology* Vol. 94, pp. 143–151.

Børresen, M., Breedveld G.D., Rike, A.G., 2003. Assessment of the biodegradation potential of hydrocarbons in contaminated soil from a permafrost site. *Cold Regions Science and Technology* Vol. 37, pp. 137– 149.

Bowling, J.C., Zheng, C., Rodriguez, A.B., Harry, D.L., 2006. Geophysical constraints on contaminant transport modeling in a heterogeneous fluvial aquifer. *Journal of Contaminant Hydrology* Vol. 85, pp. 72–88.

Bowling1, J.C., Rodriguez, A.B., Harry, D.L., Zheng, C., 2006. Delineating Alluvial Aquifer Heterogeneity Using Resistivity and GPR Data. *Groundwater Summit*, San Antonio, Texas.

Buettner, M., Daily, W., Ramirez, A., Bussod, G., 1999. Electrical Resistance Tomography of Unsaturated Flow and Transport in Yucca Mountain. *Symposium on the Application of Geophysics to Engineering and Environmental Problems Oakland, CA*. Preprint UCRL-JC-131761, Lawrence Livermore National Laboratory (LLNL), Livermore, California, U.S.A.

Bratton, W., Maresca, J., Dickerson, W., Ramirez, A., Daily, W., 2004. Monitoring Permeable Reactive Barriers Using Electrical Resistance Tomography. *Journal of Geophysical Research* 201355, Lawrence Livermore National Laboratory (LLNL), Livermore, California, U.S.A.

Brown, D., Slater, L.D. 1999. Focused packer testing using geophysical tomography and CCTV in a fissured aquifer. *Quarterly Journal of engineering Geology* Vol. 32, pp. 173-183.

Bruno, R., Raspa, G., 2001: La pratica della Geostatistica lineare. *Guerini Studio,* Bologna.

Buettner, M., Daily, W., Ramirez, A., Bussod, G., 1999. Electrical Resistance Tomography of Unsaturated Flow and Transport in Yucca Mountain. *Symposium on the Application of Geophysics to Engineering and Environmental Problems Oakland*, CA March 14-18,1999. UCRL-JC-131761, Lawrence Livermore National Laboratory (LLNL), Livermore, California, U.S.A.

Buselli, G., Lu, K., 2001. Groundwater contamination monitoring with multichannel electrical and electromagnetic methods. *Journal of Applied Geophysics* Vol. 48 11 – 23.

Cardarelli, E., Fischanger, F., 2006. 2D data modelling by electrical resistivity tomography for complex subsurface geology. *Geophysical Prospecting,* 54 pp. 121–133.

Carle, S.F., Ramirez, A., Daily, W.D., Newmark, R.L. Tompson, A.F.D., 1998. Integration of Geologic Interpretation, Geostatistics, Parallel Computing, and Electrical Resistance Tomography for Characterization of 3-D Aquifer System Heterogeneity. *UCRL-JC-131552 Abs*, Lawrence Livermore National Laboratory (LLNL), Livermore, California, U.S.A.

Carle, S.F., Ramirez, A., Daily, W.D., Newmark, R.L., Tompson, A.F.D., 1998. A Geostatistical Approach to Obtaining Geologically Plausible ERT Inversions. *UCRL-JC-132053 Abs*, Lawrence Livermore National Laboratory (LLNL), Livermore, California, U.S.A.

Carrara, E., Rapolla, A., Roberti, N., 2004. Le indagini geofisiche per lo studio del sottosuolo: Metodi geoelettrici e sismici. *Liguori Editore*, Napoli.

Carrigan, C.R., Martins, S.A., Ramirez, A., Daily, W.D., Hudson, G.B., Ralston, D., Ekwurzel, B., 2001. Characterization of Contaminant Transport by Gravity, Capillarity and Barometric Pumping in Heterogeneous Vadose Zones. *Preprint UCRL-ID-142784,* Lawrence Livermore National Laboratory (LLNL), Livermore, California, U.S.A.

Carrigan, C.R., Martins, S.A., Ramirez, A., Daily, W.D., 2002. A Laboratory Approach Relating Complex Resistivity Observations to Flow and Transport in Saturated and Unsaturated Hydrologic Regimes (Tracking Code: 01-FS-006). *UCRL.ID-146986*, Lawrence Livermore National Laboratory (LLNL), Livermore, California, U.S.A.

Chambers, J.E., Loke, M.k., Ogilvy, R.D., Meldrum, P.I., 2004. Noninvasive monitoring of DNAPL migration through a saturated porous medium using electrical impedance tomography. *Journal of Contaminant Hydrology*, Vol. 68 pp. 1– 22.

Christensen, N.B., 1986. The geoelectrical sounding method: a historical review of interpretation techniques and the interpreter's evaluation of the method, in twentyfive years of geology in Aashus. In Møller, J.T. (Ed), *Geological Essays, GeoSkrifter* Vol.24, Aarhus University, pp. 91-102.

Construction Industry Research and information Association (CIRIA), 1995. Remedial treatment for contaminated land. *Special Publication* 104 London, Vol. 4, pp. 12-21.

Crowley, O., 2008. *Calculation of Contaminant loading (kg/yr) and ORC-Advanced dose*. [email] (Personal communication, 7 April 2008).

Curtis, F., Lammey, J., 1998. Intrinsic remediation of a diesel fuel plume in Goose Bay, Labrador, Canada. *Environmental Pollution* Vol. 103, pp. 203-210.

Dady, W., Ramlrez, R., LaBrecque, D., Barber, W., 1995. Electrical resistance tomography experiments at the Oregon Graduate Institute. *Journal of Applied Geophysics* Vol. 33, pp. 227-237.

Daffy, W., Ramirez, A., 1995. Electrical resistance tomography during in-situ trichloroethylene remediation at the Savannah River Site. *Journal of Applied Geophysics* 33 pp. 239- 249.

Dahlin, T., 1989. The development of a cable system for vertical electrical sounding and a comparison of the Schlumberger and Offset Wenner methods. *Licentiate Thesis TUTVDG/(TVTG-1005)*/1-77, Lind University, pp. 77.

Dahlin, T., 1993. On the automation of 2D resistivity surveying for engineering and environmental applications. *Doctoral Thesis*, ISRN TUTVDG/TVTG-1007-SE, ISBN 91-628-1032-4, Lund University, pp. 187.

Dahlin, T., 1996. 2D resistivity surveying for environmental and engineering applications. *First Break* 14 (7), pp. 275-283.

Dahlin, T., Glatz, D., Persoon, N., Gwaze, P., Owen, R., 1999. Electrical and magnetic investigation of deep aquifers in North Matabeland, Zimbabwe. Proceedings of the fifth *Meeting on Environmental and Engineering Geophysics*, Budapest, 5-9 Sept., 2 pp.

Dahlin, T., 2001. The development of DC resistivity imaging techniques. *Computers & Geosciences* Vol. 27 pp. 1019–1029.

Daily, W., Ramirez, A., 1995. Environmental Process Tomography in the United States. *The Chemical Engineering Journa*l, Vol. 56, pp. 159-165.

Daily, W., Ramirez, A., Newmark, R., George V., Randall, J., 1999. Imaging UXO Using Electrical Impedance Tomography. *Preprint UCRL-JC-136407*, Lawrence Livermore National Laboratory (LLNL), Livermore, California, U.S.A.

Daily, W., Ramirez,A., 2000. Calibration of Electrical Impedance Tomography. *UCRL-ID-139413*, Lawrence Livermore National Laboratory (LLNL), Livermore, California, U.S.A.

Daily, W., Ramirez,A., 2003. Electrical Impedance Tomography at the A-014 Outfall for Detection of DNAPL. *Journal of Geophysical Research* 153535 Lawrence Livermore National Laboratory (LLNL), Livermore, California, U.S.A.

De La Vega, M., Osella, A., Lascano, E., 2003. Joint inversion of Wenner and Dipole-Dipole data to study a gasolina-contaminant soil. *Journal of Applied Geophysics*, Vol. 54 pp. 97-109.

De Lima, A.L., Sato, H.K., Porsani, M.J., 1995. Imaging industrial contaminant plumes with resistivity techniques. *Journal of Applied Geophysics* Vol.34, pp. 93-108.

De Lima, A.L., Niwas, S., 2000. Estimation of hydraulic parameters of shaly sandstone aquifers from geoelectrical measurements. *Journal of Hydrology* Vol. 235, pp. 12–26.

Department of the Environment and Water Resources, 2006. Diesel Fuel Quality Standard. *AustralianGovernment*,http://www.environment.gov.au/atmosphere/fuelquality/standards/diesel/index.html.

Di Molfetta A., Sethi, R., 2005. "Barriere reattive permeabili." In *Bonifica di siti contaminati. Caratterizzazione e tecnologie di risanamento*. *Luca Bonomo, McGraw Hill*, ISBN 88-386-6278-9.

Edwards L.S., 1977. A modified pseudosection for resistivity and induced-polarization. *Geophysics*, Vol.42, pp. 1020-1036.

Ferguson, I.J., Ristau, J.P., Maris, V.G. Hosain, I., 1998. Geophysical imaging of a kaolinite deposit at Sylvan, Manitoba, Canada. *Journal of Applied Geophysics* Vol. 41 pp. 105–129.

Ferguson, S.H., Franzmann, P.D., Revill, A.T., Snape, I., Rayner, J.L., 2003. The effects of nitrogen and water on mineralisation of hydrocarbons in diesel-contaminated terrestrial Antarctic soils. *Cold Regions Science and Technology* Vol. 37, pp. 197– 212.

Ferguson, S.H., Woinarski, A.Z., Snape, I., Morris, C.E., Revill, A.T., 2004. A field trial of in situ chemical oxidation to remediate long-term diesel contaminated Antarctic soil. *Cold Regions Science and Technology* Vol. 40, pp. 47– 60.

Flathe, H., 1955. A practical method of calculating geoelectrical model graphs for horizontally stratified media. *Geophisical Prospecting* Vol. 3 (3), pp. 268-294.

Frohlich, R.K., Urish, D.W., 2002. The use of geoelectrics and test wells for the assessment of groundwater quality of a coastal industrial site. *Journal of Applied Geophysics* 50 (2002) 261– 278.

Gajdos, V., Kral, V., 1995. Influence of hydrocarbon pollution to soil conductivity. In: Bell, R.S. Proceeding of the *Symposium on the Application of Geophysics to Engineering and Environmental Problems* (SAGEEP 1995), Orlando Fl, pp. 785-789.

Gavaskar, A. R., N. Gupta, B. M. Sass, R. J. Janosy, and D. O'Sullivan. 1998. Permeable barriers for groundwater remediation: design, construction, and monitoring. Columbus, OH. *Battelle Press*.

Ghazali, F.M., Zaliha, N.R., Rahman, A., Salleh, A.B., Basri, M., Biodegradation ofhydrocarbons in soil by microbial consortium. *International Biodeterioration & Biodegradation* Vol. 54 pp. 61 – 67.

Gish, O.H., Rooney, W.J., 1925. Measurement of resistivity of large masses of undisturbed earth. *Terrestrial Magnetism and Atmospheric Electricity* Vol 30 (4), pp. 161-188.

Ghosh, D.P., 1971. The application of linear filter theory to the direct interpretation of geoelectrical resistivity sounding measurements. *Geophysical Prospecting* Vol. 19, pp. 192-217.

Green, R.T., 2004. GEOPHYSICAL SURVEY TO DETERMINE THE DEPTH AND LATERAL EXTENT OF THE LEONA AQUIFER AND EVALUATION OF DISCHARGE THROUGH THE LEONA RIVER FLOODPLAIN, SOUTH OF UVALDE, TEXAS. *CNWRA Southwest Research Institute*, San Antonio, Texas, USA.

Grellier, S., Robain, H., Bellier, G., Skhiri, N., 2006. Influence of temperature on the electrical conductivity of leachate from municipal solid waste. *Journal of Hazardous Materials* B137 (2006) 612–617.

Griffiths, D.H., Turnbull, J., Olayinka, A.I., 1990. Two-dimensional resistivity mapping with a computer-controlled array. *First Break* 8 (4), pp. 121-129.

Head, K.H., 1984. Manual of soil laboratory trsting Volume 1 soil classification and compaction tests. *Pentech Press,* London.

Hoffmann, r., Dietrich, P., 2004. An approach to determine equivalent solutions to the geoelectrical 2D inversion problem. *Journal of Applied Geophysics* Vol. 56 pp. 79– 91.

Hunkeler, D., Hohener, P., Zeyer, J., 2002. Engineered and subsequent intrinsic in situ bioremediation of a diesel fuel contaminated aquifer. *Journal of Contaminant Hydrology* Vol. 59 pp. 231– 245.

Johansen, H.K., 1977. A man computer interpretation system for resistivity sounding over a horizontally stratified earth. *Geophysical Prospecting* Vol. 25 (4), pp. 667-691.

Johnson, W.J., 2003.APPLICATIONS OF THE ELECTRICAL RESISTIVITY METHOD FOR DETECTION OF UNDERGROUND MINE WORKINGS. *Geophysical Technologies for Detecting Underground Coal Mine Voids*, Lexington, KY, USA.

Johnston, K., Ver Hoef, J.M., Krivoruchko, K., Lucas, N., 2002: Manual ArcGis Geoststistical Analyst. *ESRI* USA.

Knight, R., 1991, Hysteresis in the electrical resistivity of partially saturated sandstones. *Geophysics* Vol. 56, pp. 2139-2147.

Koster, J.W., Harry, D.L., 2005. Effects of water saturation on a Resistivity Survey of an Unconfined Fluvial Aquifer in Columbus, MS. *Hydrology Days*, Dept. of Geosciences Colorado State University.

Kunetz, G., 1966. Principles of Direct Current Resistivity prospecting. *Gebüder Borntraeger*, Brelin 103 pp.

Imparato, V., Raffaelli, L., Rizzi, S., Zelioli, A., Pagano, A., 2003. LA PROSPEZIONE GEOFISICA IN CAMPO AMBIENTALE. *Linee Guida*, Direzione centrale ambiente, Provincia di Milano.

La Breque, D.J., Miletto, M., Daily, W., Ramirez, A., Owen, E., 1996. The effects of noise on Occam's inversion of resistivitytomography data. *Geophysics* Vol. 61, pp. 538-548.

Langbehn, A., Steinhart H., 1995. BIODEGRADATION STUDIES OF HYDROCARBONS IN SOILS BY ANALYZING METABOLITES FORMED. *Chemosphere,* Vol. 30, No. 5. pp. 855-868.

Langer, R.E., 1933. An inverse problem in differential equations. *America Society of Mathematics Journal* Vol. 39 pp. 14-28.

Lee, M.W., Collett, T.S., 2006. A Method of Shaly Sand Correction for Estimating Gas Hydrate Saturations Using Downhole Electrical Resistivity Log Data. *USGS Scientific Investigations Report 2006* -5121, Reston, Virginia, USA.

Legall, F.D., Atekwana E.A., Krishnamurthy R.V., Werkema, D.D., Sauck, W.A., 2003. Geochemical and Isotopic Characteristics Associated with High Electrical Conductivities in a Shallow Hydrocarbon-Contaminated Aquifer. *Geophysical Research Abstracts*, Vol. 5, 07225.

Li, Y., Oldenburg, D.W., 1992. Approximate inverse mappings in DC resistivity problems. *Geophysical Journal International* Vol. 109, pp. 343-362.

Lide, D.R, 1993., Handbook of Chemistry and Physics (73rd edn.). *Lide, D.R Editor - CRC Press*, Boca Raton, FL.

Loke, M.H., Barker, R.D., 1996. Rapid least-squares inversion of apparent resistivity pseudosections by a quasi-Newton method. *Geophysical Prospecting* Vol. 44 (1), pp. 131-152.

Loke, M.H., 2001. Electrical imaging survey for environmental and engineering studies. *A practical Guide to 2D and 3D surveys.*

Lysyj, I., Russell, E.C. 1974. Dissolution of petroleum-derived products in water. *Water Res*, Vol. 8, pp. 863-868.

Marescot, L., Rigobert, S., Lopes S.P., Lagabrielle R., Chapellier, D., 2006. A general approach for DC apparent resistivity evaluation on arbitrarily shaped 3D structures. *Journal of Applied Geophysics* Vol. 60pp. 55–67.

Margesin, R., Schinner, F., 1999. BIODEGRADATION OF DIESEL OIL BY COLD-ADAPTED MICROORGANISMS IN PRESENCE OF SODIUM DODECYL SULFATE. *Chemosphere*, Vol. 38. No. 15. pp. 3463-3472.

Marin, M., Pedregosa, A., Rios, S., Ortiz, M.L., Laborda, F., 1995. Biodegradation of Diesel and Heating Oil by *Acinetobacter calcoaceticus* MM5: its Possible Applications on Bioremediation. *International Biodeterioration & Biodegradation*) pp. 269-285.

Matheron, G., 1963. Traité de la geostatiquée. *Editions Technip*, France.

Matheron, G., 1965. Les variables régionalisées et leur estimation: une application de la théorie des functions aléatores aux sciences de la nature. *PhD. Thesis, Masson*, Paris.

Mayer, A., Hassanizadeh, S.M., 2002. Contamination of soil and groundwater by Nonaqueous Phase Liquids (NAPLs). *Dept of Earth sciences*, Utrecht University.

McDougal, R.R., Abraham, J.D.. Bisdorf, R.J., 2004. Results of Electrical Resistivity Data Collected near the Town of Guernsey, Platte County, Wyoming. *Open File Report* -1095 Geological Survey U.S.

Meju, M.A., 2000. Geoelectrical investigation of oldrabandoned, covered landfill sites in urban areas: model development with a genetic diagnosis approach. *Journal of Applied Geophysics*, Vol. 44, pp. 115–150.

Merrick, N.P., 1997. A new resolution index for resistivity electrode arrays. *Exploration Geophysics*, Vol. 28, pp. 106-109.

Molina-Barahona, L., Rodr´ıguez-Vázquez, R., Hernández-Velasco, M., Vega-Jarquin C., Zapata-Pérez, O., Mendoza-Cantú, A., Albores, A., 2004. Diesel removal from contaminated soils by biostimulation and supplementation with crop residues. *Applied Soil Ecology* Vol.27, pp. 165–175.

Møller, I., Sørensen, K.I., 1998. A new approach for last 2-D geoelectrical mapping of near-surface structures. *European Journal of Environmental and Engineering Geophysics* Vol. 2 (3), pp. 247-261.

Monteiro Santos, F.A. Mateus, A., Figueiras, J., Gonçalves, M.A., 2006. Mapping groundwater contamination around a landfill facility using the VLF-EM method — A case study. *Journal of Applied Geophysics* 60 (2006) 115–125.

Wan Namkoong, Hwang, E.Y, Park, J.S., Choi, J.Y., 2002. Bioremediation of diesel-contaminated soil with composting. *Environmental Pollution* 119 pp. 23–31.

Nath, S.K., Shahid, S., Dewangan, P., 2000. SEISRES - a Visual C++ program for the sequential inversion of seismic refraction and geoelectric data. *Computers & Geosciences* Vol.26, pp. 177-200.

Newmark, L.R., Daily, W.D., Kyle, K.R., Ramirez, A., 1997. Monitoring DNAPL Pumping Using Integrated Geophysical Techniques. UCRL-ID-122215, *Lawrence Livermore National Laboratory* (LLNL), Livermore, California, U.S.A.

Newmark, L.R., Ramirez, A, Daily, W.D., 2002. Monitoring Carbon Dioxide Sequestration using Electrical Resistance Tomography (ERT): A Minimally Invasive Method. *6th International Conference on Greenhouse Gas Control Technologies, Kyoto, Japan*, Lawrence Livermore National Laboratory (LLNL), Livermore, California, U.S.A.

Nocentini, M., Pinelli D., Fava, F., 2000. Bioremediation of a soil contaminated by hydrocarbon mixtures: the residual concentration problem. *Chemosphere* Vol. 41, pp. 1115-1123.

Oldenburg, D.W., Li, Y., 1994. Inversion of induced polarization data. *Geophysics* Vol. 59, pp. 1327-1341.

Overmeeren, R.A., Van Ritsema, I.L., 1988. Continuous vertical electrical sounding. *First Break* Vol. 6 (10), pp. 313-324.

Peterson, W., 1907. Om malmsokande medelst elektricitet. *Jern-Kontorets Annaler* Vol. 2-3, pp. 153-171

Porsani, J.L., Filho, W.M., Elis, V.S., Shimeles, F., Dourado, J.C., Moura, H.P.,2004. The use of GPR and VES in delineating a contamination plume in a landfill site: a case study in SE Brazil. *Journal of Applied Geophysics*, Vol.55 pp. 199– 209.

Ramirez, A., Daily, W.D., LaBreque, D.J., Roelant, D., 1996. Detection of leaks in underground storage tanks using electrical resistance methods. *Journal of environmental and Engineering Geophysics* Vol. 1, pp. 189-203.

Ramirez, A., Daily, W.D., Newmark, R.L., George, V., Randall, J., 1999. Imaging UXO Using Electrical Impedance Tomography. *Annual Meeting of the Environmental and Engineering Geophysical Society Arlington*, VA February 20-24, 1999. Preprint UCRL-JC-136407, Lawrence Livermore National Laboratory (LLNL), Livermore, California, U.S.A.

Ramirez, A., Friedmann, J., Dyer, K., Aines, R., 2006. SITE CHARACTERIZATION USING JOINT RECONSTRUCTIONS OF DISPARATE DATA TYPES. *Journal of Geophysical Research* 155048-REV-3 *Lawrence Livermore National Laboratory (LLNL)* Livermore, California, U.S.A.

Ramirez, A., Nitao, J., Hanley, W., Aines, R., Glaser, R., Sengupta, S., Dyer, K, Hickling, T., Daily, W., 2004. Stochastic Inversion of Electrical Resistivity Changes Using a Markov Chain, Monte Carlo Approach. *Journal of Geophysical Research* 155048-REV-3 Lawrence Livermore National Laboratory (LLNL), Livermore, California, U.S.A.

Ramirez, A., Daily, w.D., 2002. Determination of S-112 and Mock Tank Electrical Resistivities using Numerical Forward and Inverse Solutions. *Journal of Geophysical Research* 148652 Lawrence Livermore National Laboratory (LLNL), Livermore, California, U.S.A.

Ramirez, A., Daily, W., LaBrecque, D., 1996. Complex Electrical Resistance Tomography of a Subsurface PCE Plume. *Symposium on the Application of Geophysics to Engineering and Environmental Problems* Keystone, CO April 28-May 1, 1996. UCRL-JC-122874, Lawrence Livermore National Laboratory (LLNL), Livermore, California, U.S.A.

Ramirez, A., Daily, W., LaBrecque, D., 1996. Tank Leak Detection Using Electrical Resistance Methods. *Symposium on the Application of Geophysics to Engineering and Environmental Problems* Keystone, CO April 28-May 1, 1996. UCRL-JC- 122875, Lawrence Livermore National Laboratory (LLNL), Livermore, California, U.S.A.

Ramirez, A., Daily, W., 2001. Electrical imaging at the large block test—Yucca Mountain, Nevada. *Journal of Applied Geophysics* Vol. 46 pp. 85–100.

Ramirez, A., Daily, W., Binley, A., 2002.Tank Leak Experiment at the Mock Tank Site, 200 East Area: Electrical Resistance Tomography- Preliminary Results. *UCRL-ID-145662-REV-1",* Lawrence Livermore National Laboratory (LLNL), Livermore, California, U.S.A.

Ramirez, A., Daily, W., 2002. Determination of S-112 and Mock Tank Electrical Resistivities using Numerical Forward and Inverse Solutions. *UCRL-ID-148652*, Lawrence Livermore National Laboratory (LLNL), Livermore, California, U.S.A.

Regenesis. 2005. Design Manual for In Situ Accelerated Bioremediation. From CD Advanced Cost Effective Technologies for Contaminated Site Remediation – *A Collection of Selected Battelle Conference Papers 2001-2007 compiled by Regenesis®*.

Regenesis. 2007. Oxygen release Compound – Advanced. Material Safety Data Sheet (MSDS) – material identification and composition. *Regenesis®* [Online]. Availableat: http://www.regenesis.com/library/ORC-A_MSDS_3_12_2007.pdf [accessed 05 April 2008]

Regenesis. 2008. Oxygen release Compound – Advanced. Product Brochure. *Regenesis*®[Online].Availableat:*http://www.regenesis.com/library/ORC_Adv_Bro_Dec0303F.pdf* [accessed 05 April 2008].

Reynolds, J.M., 1995. An introduction to Applied Environmental Geophysics. *Wiley and Sons*, Chister, Weste sussex, UK.

Richard, J.Y., Vogel, T.M., 1999. Characterization of a soil bacterial consortium capable of degrading diesel fuel. *International Biodeterioration & Biodegradation* Vol. 44, pp. 93-100.

Rosner, G., 1996. Diesel fuel and exhaust emissions – Environmental health criteria 171- *international programme on chemical safety United Nations*, International labour organisation, Geneva.

Sauck, W.A., 2000. A model for the resistivity structure of LNAPL plumes and their environs in sandy sediments. *Journal of Applied Geophysics* 44 2000 151–165.

Schlumberger, C., 1920. Etude sur la Prospection Electrique du Sous-sol, *Gaultier-Villars et Cie*., Paris, 94 pp.

Scott, A., Lundegard, S.& P., 1998. Intrinsic biodegradation of diesel fuel in an interval of separate phase Hydrocarbons. *Applied Geochemistry*, Vol. 13, No. 7, pp. 851-859.

Sepic, E., Leskovsek, H., Trier, C., 1995. Aerobic bacterial degradation of selected polyaromatic compounds and n-alkanes found in petroleum. *Journal of Chromatography* A, 697 pp. 515-523.

Sharma, H.D., Reddy, K.R., 2004. Geoenvironmental Engineering: Site Remediation, Waste Containment, and Emerging Waste Management Technologies. *Wiley, J. and Sons inc*, ISBN-13: 9780471215998.

Sheets, R.A., 2002. Use of Electrical Resistivity to Detect Underground Mine Voids in Ohio. Water-Resources *Investigations Report* 02-4041, USGS. USA.

Slater, L., Binley, M.A., Brown, D., 1997. Electrical imaging of fractures using groundwater salinity change. *Ground Water* Vol. 35, pp. 436-442.

Slater, L., Binley, M.A, Daily, W., Johnson, R., 2000. Cross-hole electrical imaging of a controlled saline tracer Injection. *Journal of Applied Geophysics* Vol. 44, pp. 85–102.

Schneider, G.W., De Ryck, S.M., Rerre, P.A., 1993. The application of automated high resolution DC resistivity in monitoring hydrogeological field experiments. In: Bell, R.S., Lepper, C.M. Proceeding of the *Symposium on the Application of Geophysics to Engineering and Environmental Problems* (SAGEEP 1993), san Diego, CA pp. 145-162.

Soesilo, J.A., Wilson, S.R., 2000. Site Remediation Planning and Management. *Lewis Publishers London*.

Soupios, P., Papadopoulos, I., Kouli, M., Georgaki, I., Vallianatos, F., Kokkinou, E., 2007. Investigation of waste disposal areas using electrical methods: a case study from Chania, Crete, Greece. *Environmental Geology* vol. 51 pp. 1249–1261.

Sjödahl, P., 2006. Resistivity investigation and monitoring for detection of internal erosion and anomalous seepage in embankment dams. *Doctoral Thesis* Engineering Geology Lund University Sweden.

Stefanescu, S., Schlumberger, C., Schlumberger, M., 1930. Sur la distribution electrique potentielle autor d'une prise de terre pontuelle dans un terrain à couches horizontals, homogènes et isotropes. *Journal de Physique et du Radium* Vol. 1 (4), pp. 132-140.

Stewart, M., North, L., 2006. A borehole geophysical method for detection and quantification of dense, non-aqueous phase liquids (DNAPL) in saturated soils. Journal of Applied Geophysics 60 (2006) 87–99.

Stone, W.A., 1991. Assessing health risks associated with diesel contaminated soils and groundwater. In: Calabrese EJ & Kostecki PT, eds, *Hydrocarbon contaminated soils*, Vol. 1, Remediation techniques, environmental fate, risk assessment, analytical methodologies, regulatory considerations. Chelsea, MI, Lewis Publishers, pp. 167-179.

Suzuki, K., Toda, S., Kusunoki, K., Fujimitsu, Y., Mogi, T., Jomori, A., 2000. Case studies of electrical and electromagnetic methods applied to mapping active faults beneath the thick quaternary. *Engineering Geology* Vol. 56, pp.29–45.

Taylor, C., Viraraghavan, T., 1999. A BENCH-SCALE INVESTIGATION OF LAND TREATMENT OF SOIL CONTAMINATED WITH DIESEL FUEL. *Chemosphere,* Vol. 39, No. 10, pp.1583-1593.

Tsourlos, P., 1995. Modelling, interpretation and inversion of multielectrode resistivity survey data. *Ph.D. dissertation*, Dept. of Electronics, University of York, York, U.K. 315 pp.

United-Tech, Inc. 2007. Bioremediation and Contaminates - Biotechnology Company - Industry - aquaculture supply waste water sludge Biodegradable product oil spill cleaning soil remediation waste water. ww.united-tech.com/obt-bioremediation.html. 22.04.07.

U.S. Department of Labor Occupational Safety & Health Administration 2007. Chemical Sampling Information Diesel Fuel. *www.osha.gov*. http://www.osha-slc.gov/dts/chemicalsampling/data/CH_234655.html. 25.05.07

US.EPA. 1998. Permeable reactive barrier technologies for contaminated remediation. Remedial Technology Forum. *U.S.EPA/600/R-98/125.*

Vanhala, H., 1997. Mapping oil-contaminated sand and till with the spectral induced polarization (SIP) method. *Geophisical Prospecting* Vol. 45, pp. 303-326.

Van Schoor, M., 2002. Detection of sinkholes using 2D electrical resistivity imaging. *Journal of Applied Geophysics* 50 (2002) 393– 399.

Webster, R., Oliver, M., 1999. Geostatistics for Enviromental Scientists. *John Wiley & Sons*, LTD.

Weller, A., Frangos, W., Seichter, M., 2000. Three-dimensional inversion of induced polarization data from simulated waste. *Journal of Applied Geophysics* Vol. 44, pp. 67–83.

Werkema, D.D., Aterkawana, E.A., Endres, A., Sauck, W.A., Cassidy, D.P., 2003. Investigating the geoelectrical response of hydrocarbon contamination undergoing biodegratation. *Geophys. Res. Lett*. Vol. 30, pp 1647-1654.

Werkema, D.D., Dale, D., 2005. Can geoelectrical methods be used to monitor NAPL remediation effort? *E.P.A. Science Forum –May 2005*, Washigton, DC.

White, R.M.S., Collins, S., Denne, R., Hee, R. and Brown, P., 2001. A new survey design for 3D IP modelling at Copper hill. Exploration Geophysics, 32, 152-155.

WORLD HEALTH ORGANIZATION INTERNATIONAL AGENCY FOR RESEARCH ON CANCER, IARC Monographs on the Evaluation of Carcinogenic Risks to Humans, 1998. Volume 45, Occupational Exposures in Petroleum Refining; Crude Oil and Major Petroleum Fuels. *Summary of Data Reported and Evaluation*.

Xia, J., Miller, R.D., 2005. Applications of Integrated Geophysical Survey in Mapping Subsurface to a Depth of 80 ft at a Landfill in Salina, Kansas. *Kansas Geological Survey Open-file* Report 48, 150 pp.

Yang, C., Wang, Z., Yun, C., Liu, H.,2006. Delineating underground structures using geoelectrical methods and 3-D laser scanning technology at Tai-Pen Bay, Taiwan. *SEG/New Annual Meeting*, Orleans.

Appendices

Appendix A

Clay Particle Size Analysis

Sand Particle Size Analysis

Particle Size Distribution by Hydrometer Sedimentation

Data: **30.05.07**

Sample: **Glalstone clay** **Galstone -East Ayershire- Scotland**

Calibration and Sample Data

	Symbol	Units	Value
Hydrometer No	-	-	3793/P
Meniscus correction	C_m	-	0.5
Reading in dispersant	R_0'	-	1.0
Dry mass of soil	m	g	71.025
Particle density	ρ_s	g/cm^3	2.46
Room Temperature	T	^{o}C	20
Viscosity of water @ T	η	mPa.s	1.0019

Calibration Equation:

$H_r = 105.59 - 1.097\ R_h$

$$D = 0.00553\sqrt{\frac{\eta H}{(G_s - 1)t}}$$

$$K = \frac{G_s}{m(G_s - 1)} \times R \times 100$$

Test Data

Water Viscosity η (mPa.s)	Elapsed Time t (mins)	Temp T (^{o}C)	Reading R_h'	$R_h'+C_m$ R_h	Effective Depth H_r (mm)	Particle Diameter D (mm)	$R_h'-R_0'$ R_d	% Finer than D K (%)	K Proportioned (%)
1.002	0	20	47	47.50	55.1	0.0630	46.00	100.00	65.13
1.002	5	20	40	40.50	62.8	0.0161	39.00	91.76	59.77
1.002	10	20	36	36.50	67.2	0.0118	35.00	82.35	49.22
1.002	15	20	34.3	34.80	69.1	0.0097	33.30	78.35	46.83
1.002	20	20	33	33.50	70.5	0.0085	32.00	75.29	45.00
1.002	30	20	32.1	32.60	71.5	0.0070	31.10	73.17	43.73
1.002	40	20	30.8	31.30	72.9	0.0061	29.80	70.12	41.91
1.002	60	20	30	30.50	73.8	0.0050	29.00	68.23	40.78
1.002	120	20	27	27.50	77.1	0.0036	26.00	61.18	36.56
1.002	240	20	25.9	26.40	78.3	0.0026	24.90	58.59	35.01
1.002	360	20	24.3	24.80	80.0	0.0021	23.30	54.82	32.76
1.002	480	20	24	24.50	80.4	0.0019	23.00	54.12	32.34
1.002	1440	20	21	21.50	83.6	0.0011	20.00	47.06	28.12
1.002	1680	20	20.5	21.00	84.2	0.0010	19.50	45.88	27.42
1.002	1920	20	19.5	20.00	84.7	0.0010	18.50	44.70	26.72
1.002	5790	20	18.5	19.00	86.4	0.0006	17.50	41.18	24.61
1.002	6240	20	18.05	18.55	86.9	0.0005	17.05	40.12	23.98
1.002	7200	20	17.9	18.40	87.0	0.0005	16.90	39.76	23.77
1.002	7680	20	17.2	17.70	87.8	0.0005	16.20	38.12	22.78
1.002	8640	20	16.3	16.80	88.8	0.0005	15.30	36.00	21.52
1.002	9120	20	16.05	16.55	89.1	0.0004	15.05	35.41	21.16
1.002	10080	20	16	16.50	89.1	0.0004	15.00	35.29	21.09
1.002	10560	20	15.8	16.30	89.4	0.0004	14.80	34.82	20.81
1.002	11520	20	15.75	16.25	89.4	0.0004	14.75	34.71	20.74
1.002	12000	20	15.7	16.20	89.5	0.0004	14.70	34.59	20.67

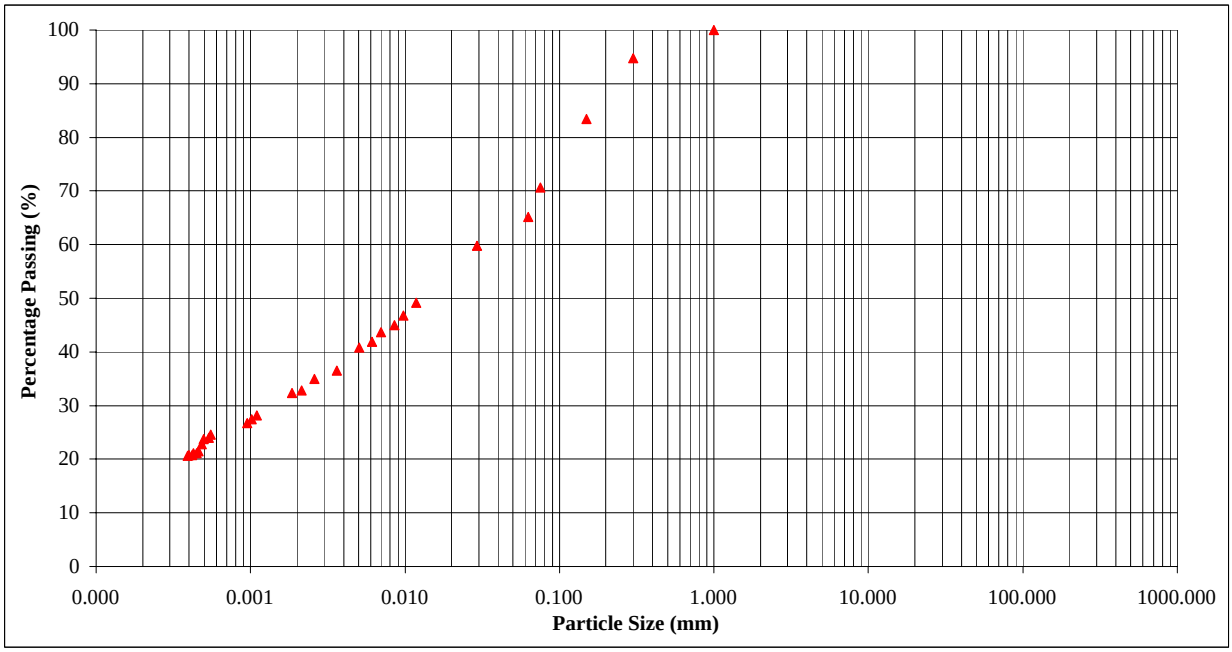

Clay	Silt			Sand			Gravel			Cobbles	Boulders
	Fine	Medium	Coarse	Fine	Medium	Coarse	Fine	Medium	Coarse		
<0.002	0.002-0.006	0.006-0.02	0.02-0.06	0.06-0.2mm	0.2-0.6mm	0.6-2mm	2-6mm	6-20mm	20-60mm	60-200mm	>200mm

Particle Size Distribution

Data: **4.05.07**

Sample: **Sand** Troon beach -East Ayshire- Scotland

Dry mass of soil: **309.44** g

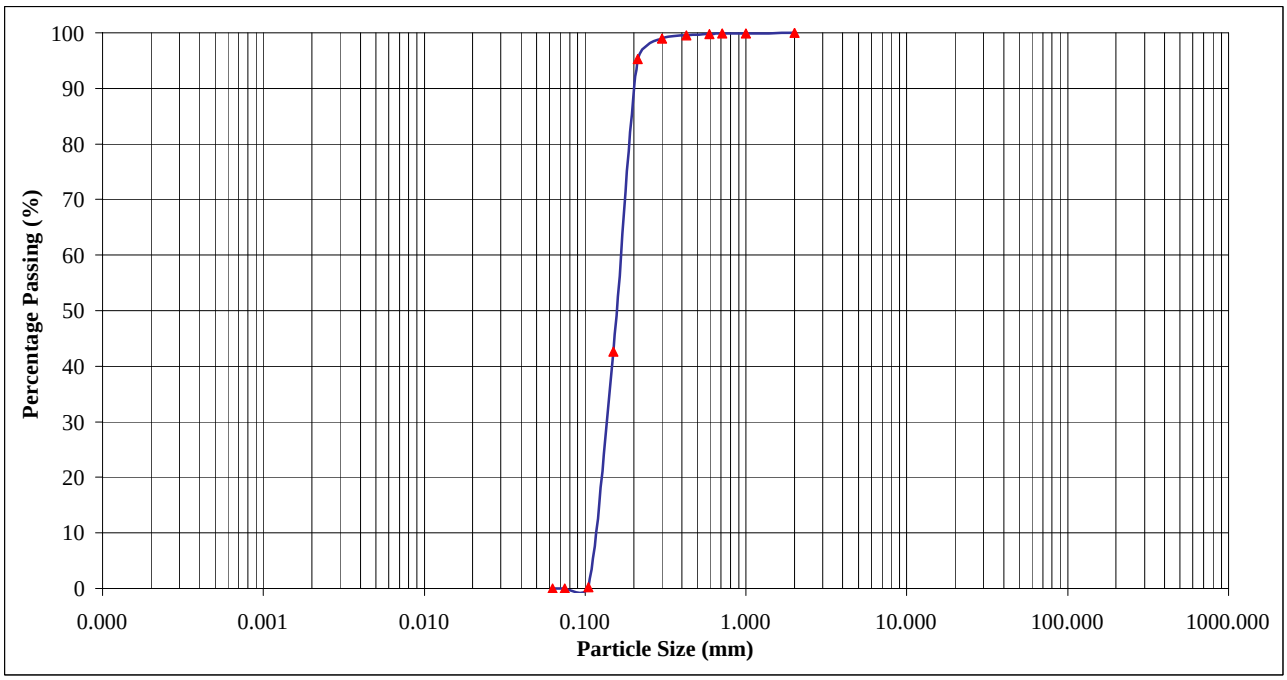

Clay	Silt			Sand			Gravel			Cobbles	Boulders
	Fine	Medium	Coarse	Fine	Medium	Coarse	Fine	Medium	Coarse		
<0.002	0.002-0.006	0.006-0.02	0.02-0.06	0.06-0.2mm	0.2-0.6mm	0.6-2mm	2-6mm	6-20mm	20-60mm	60-200mm	>200mm

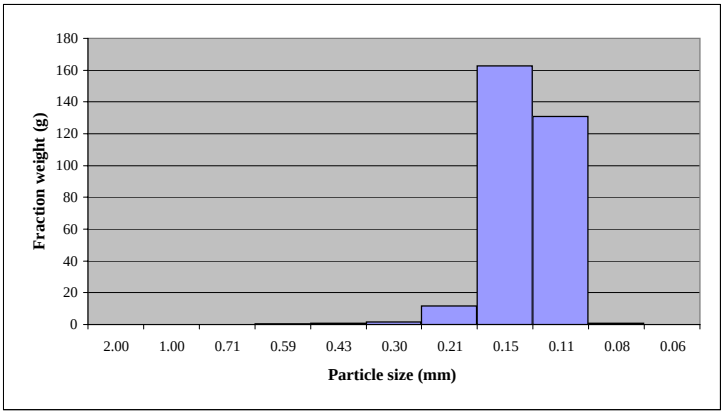

Appendix B

Data of Laboratory Analysis of Soil and Water Samples

Data of "In-situ" Analysis of Water Samples

STUDIO EFFEMME S.r.l.
CHIMICA APPLICATA
ANALISI – CONSULENZE – RICERCHE

AZIENDA CON SISTEMA QUALITÀ CERTIFICATO DA DNV =UNI EN ISO 9001/2000=
AZIENDA CON SISTEMA DI GESTIONE AMBIENTALE CERTIFICATO DA DNV = UNI EN ISO 14001:2004 =

P.zza Aldo Moro s.n. - 73018 Squinzano (LE)
tel. 0832-787358-781801 fax 0832-788128
E-mail: info@studioeffemme.com
p.iva e cod. fisc. 03447670757

SQUINZANO, 19/07/2007

I tre campioni di acqua analizzata rappresentano:

- acqua dell'acquedotto comunale - campione 1
- acqua a contatto con la sabbia, all'entrata nel modello - campione 1A
- acqua prelevata all'uscita del modello - campione 1B

Da quanto sopra si evince che l'acqua è stata in contatto soltanto con il materiale di riempimento del modello (sabbia); infatti dai parametri analizzati risulta che l'acqua durante l'attraversamento della sabbia si arricchisce in sali tipici dell'acqua marina (ad esempio l'aumento di Na^{+} e Cl^{-} di SO_4, K^{+} e Mg^{++}) con conseguente aumento della conducibilità elettrica.

Interessante, inoltre, è notare l'arricchimento di NaCl dove il rapporto Cl/Na abitualmente è 2:1, in questo caso il sodio supera, in valore assoluto i cloruri; invece, per quanto riguarda i metalli, fondamentalmente sono assenti sia nell'acqua che nella sabbia eccetto che per alluminio, rame, ferro, manganese e zinco che hanno un comportamento degno di attenzione durante il contatto dell'acqua con la sabbia.

- **Alluminio**

L'alluminio fondamentalmente rimane costante nei primi minuti di contatto acqua/sabbia poi dimezza la sua concentrazione.

- **Rame**

Il rame è presente nell'acqua, viene trattenuto dalla sabbia all'entrata, poi viene nuovamente ceduto all'uscita.

- **Ferro**

Il ferro non è presente nell'acqua dell'acquedotto, si arricchisce nel primo contatto con la sabbia poi diminuisce ma è sempre presente.

- **Manganese**

Il manganese è presente nell'acqua dell'acquedotto, mentre non è più presente all'uscita del modello.

- **Zinco**

Lo zinco diminuisce all'aumentare del tempo di contatto con la sabbia.

Dalle analisi effettuate sui metalli pesanti si può dedurre che il loro valore diminuisce quanto piu' aumenta il tempo di contatto acqua/sabbia.
Questo fenomeno può essere spiegato in due modi:
o chemi assorbimento da parte del sub-strato solido, oppure una precipitazione dei sali dei singoli metalli summenzionati dovuta ad una chariflocculazione agevolata dalla presenza di metalli ricchi in carica e da un pH basico.

Dr. Franco Mazzotta

STUDIO EFFEMME S.r.l.
CHIMICA APPLICATA
ANALISI – CONSULENZE – RICERCHE

AZIENDA CON SISTEMA QUALITÀ CERTIFICATO DA DNV =UNI EN ISO 9001/2000=
AZIENDA CON SISTEMA DI GESTIONE AMBIENTALE CERTIFICATO DA DNV = UNI EN ISO 14001:2004 =

P.zza Aldo Moro s.n. - 73018 Squinzano (LE)
tel. 0832-787358-781801 fax 0832-788128
E-mail: info@studioeffemme.com
p.iva e cod. fisc. 03447670757

SQUINZANO, 04/07/2008

Chemical Analysis		
	Zone A	
	Water Sample	Soil Sample
TPH	**5 mg/l**	**0.1 g/Kg**
	Zone B	
	Water Sample	Soil Sample
TPH	**2.5 g/l**	**31 mg/Kg**
	Barrier Upstream	
	Water Sample	
TPH	**10 mg/l**	
	Barrier Downstream	
	Water Sample	
TPH	**8 mg/l**	

Dr. Franco Mazzotta

Environmental Laboratory

Dept. Civil Engineering University of Strathclyde -Glasgow-

First Monitoring Campaign (17/07/07 - 10/08/07)

	In situ Groundwater Parameters								
	Conductivity			DO			pH		
Time	Tap Water	Sample a	Sample b	Tap Water	Sample a	Sample b	Tap Water	Sample a	Sample b
17_07_07	44.7	71	139.7	6.26	6.3	5.7	7.3	7.55	7.77
18_07_07		73.1	143.8		6.1	5.75		7.34	7.86
19_07_07		75	149.9		6.05	5.33		7.6	7.22
20_07_07		77.3	150.5		6.19	5.5		7.35	7.40
21_97_07									
22_97_07									
23_07_07		79.3	128.3		6	5.5		7.53	7.66
24_07_07		71.3	129		6.2	5.4		7.2	7
25_07_07		74.3	128		6.4	5.2		7.4	7.7
26_07_07		76.7	121.2		6.26	5.6		7.42	7.8
27_07_07		79.8	122.2		5.9	5.3		7.6	7.65
28_07_07									
29_07_07									
30_07_07		56.3	114.2		6	5.1		7.9	7.17
31_07_07		56.1	83.5		5.7	3.8		7.4	7.6
01_08_07		59.7	82.5		5.89	4.7		7.4	7.6
02_08_07		56.6	82.4		5.45	4.42		7.51	7.48
03_08_07		52.1	82.8		5.78	3.879		7.74	7.6
04_08_07									
05_08_07									
06_08_07		54.3	82.3		5.86	3.10		7.66	7.72
07_08_07		53.9	79.3		5.81	3.69		7.7	7.68
08_08_07		58.1	83.3		6.20	4.10		7.58	7.9
09_08_07		56.2	80.5		6.60	3.80		7.8	7.6
10_08_07		52.1	80		6.46	4.35		7.58	7.8

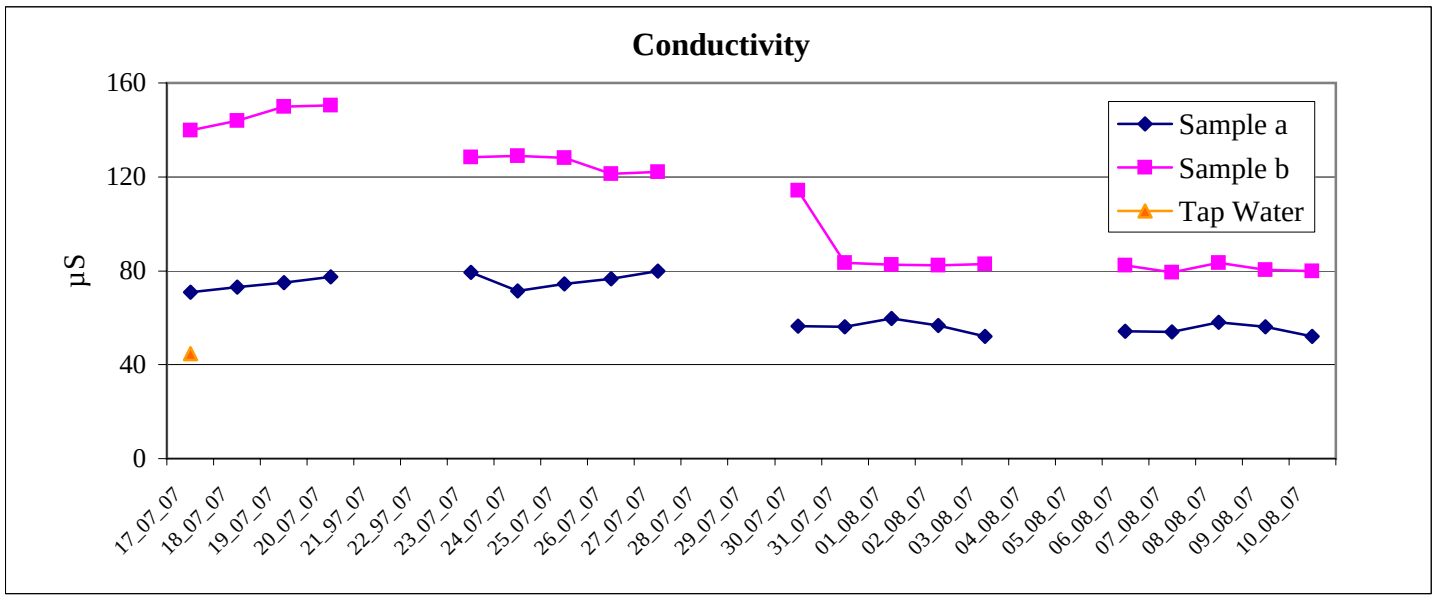

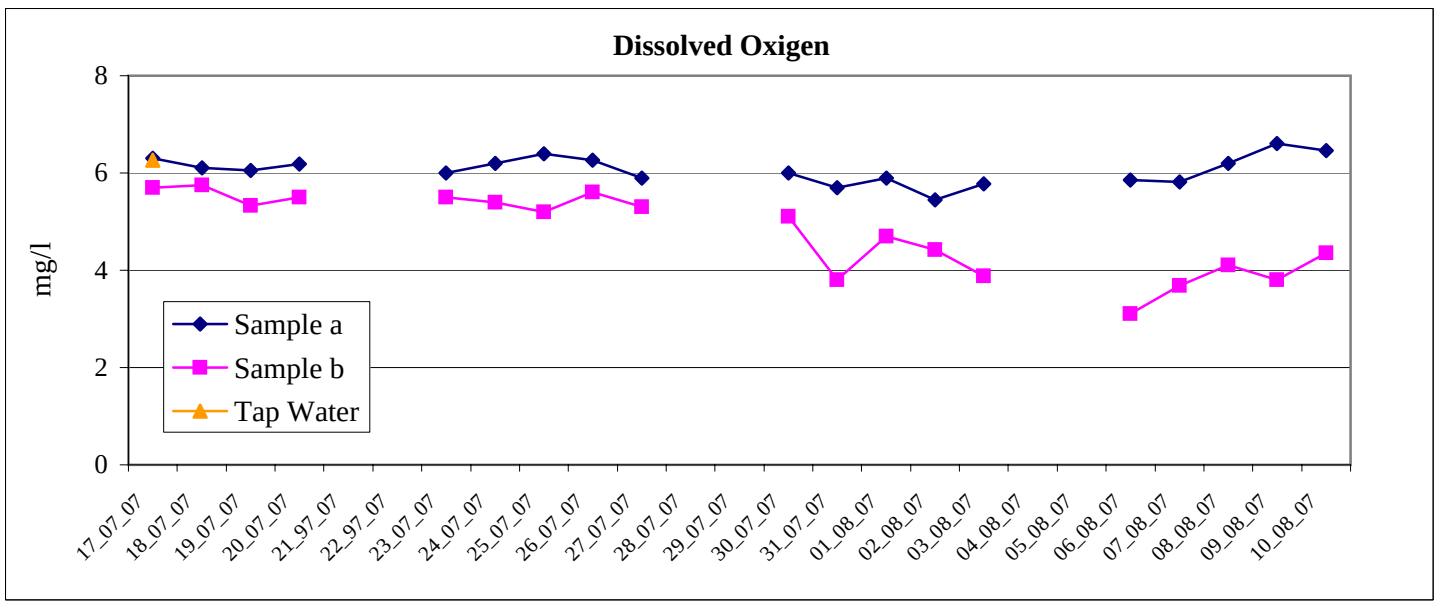

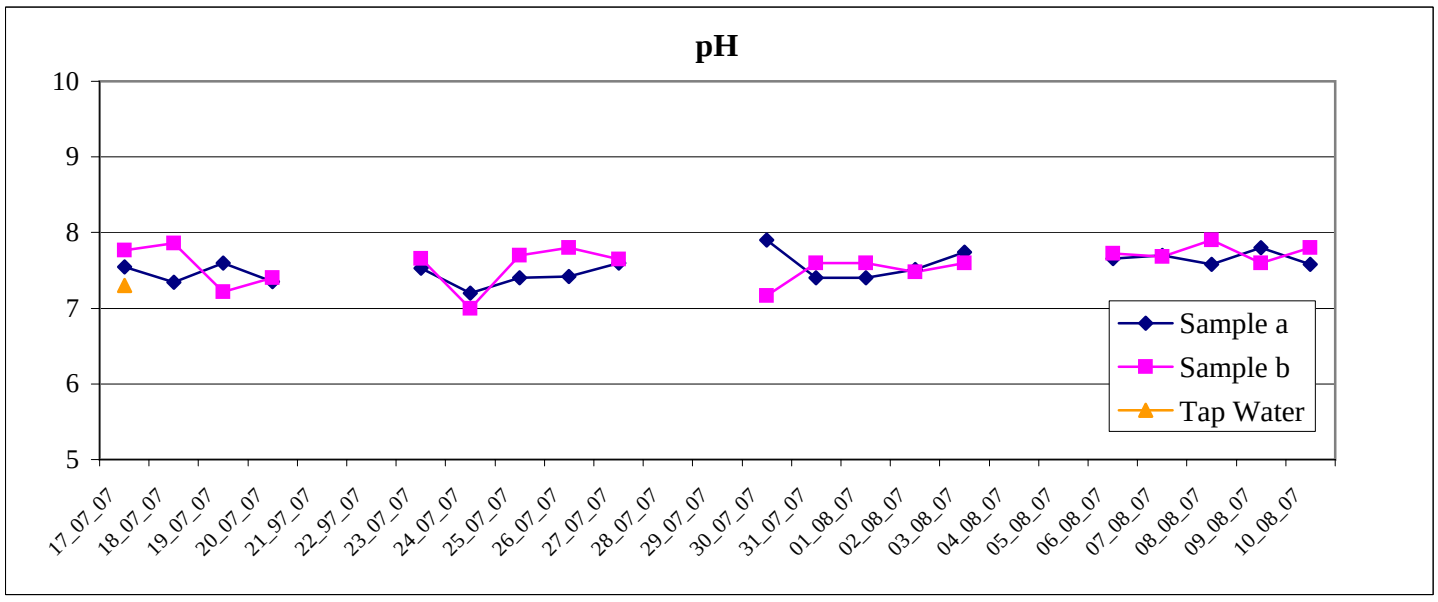

Environmental Laboratory

Dept. Civil Engineering University of Strathclyde -Glasgow-

Second Monitoring Campaign (11/01/08 - 27/06/08)

	In situ Groundwater Parameters								
	Conductivity			DO			pH		
Time	Tap Water	Sample a	Sample b	Tap Water	Sample a	Sample b	Tap Water	Sample a	Sample b
11_01_08	48.2	54.5	66	6.26	5.8	4.5			
18_01_08		51	65.8		5.9	4.95			
25_01_08		55	67.5		5.88	3.5			
01_02-08		57.8	67.4		5.79	3.4	7.9	8.4	8.8
08_02-08		50.5	69.2		6.26	3.22			
15_02_08		54.5	70.9		7.2	3.8		8.3	8.5
22_02_08		61.2	74.2		6.38	4.02		8.1	8.4
29_02_08		80.3	110		6.29	3.9		8.2	8.1
07_03_08		94.5	115.5		5.57	3.47		8.5	8.3
14_03_08		89.1	115.6		7.28	3.78		8.4	8.3
17_03_08		103	128.4		7.09	4.92		8.3	8.36
04_04_08		81	113	8	6.7	4.26		7.83	8.2
11_04_08	65	75.4	110.4		8.11	3.66		7.88	8.25
18_04_08		85	112.8		8.6	3.78		7.8	8.2
25_04_08		90	111		7.97	3.92		8.2	8.24
02_05_08		80	110.7		7.8	3.71		8.77	8.05
09_05_08		76.5	111.2		8.63	4		8.7	8.37
16_05_08		93	110.1		8.16	3.9		8.6	8.4
Barrier									
26_05_08		74.9	175		8.5	4.7		7.87	7.89
30_05_08		85.2	100.9		7.09	5.41		7.55	8.4
06_06_08		74.9	101		7.09	4.6		7.8	8.6
13_06_08		75.3	141.1		7.8	5.55		7.13	9.3
20_06_08		80.8	138.1		7.14	5.41		7.34	9.1
27_06_08	62.8	77	163.7	9	7.64	5.98	7.4	7.14	9.5

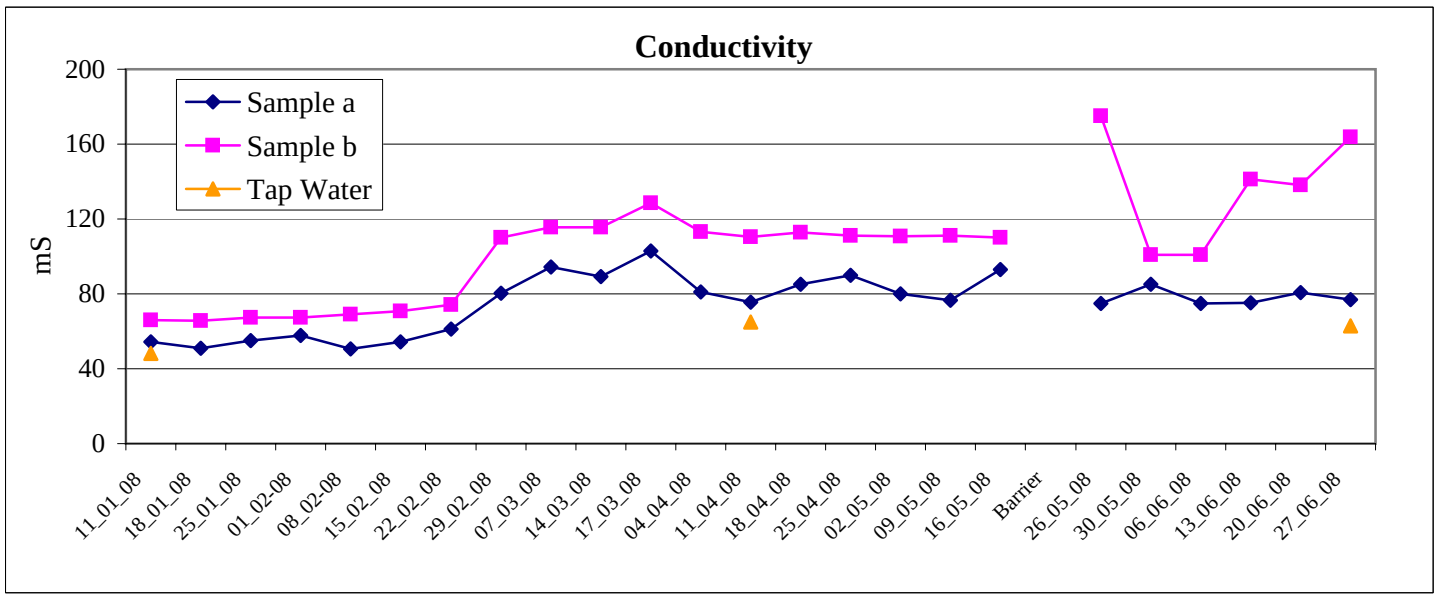

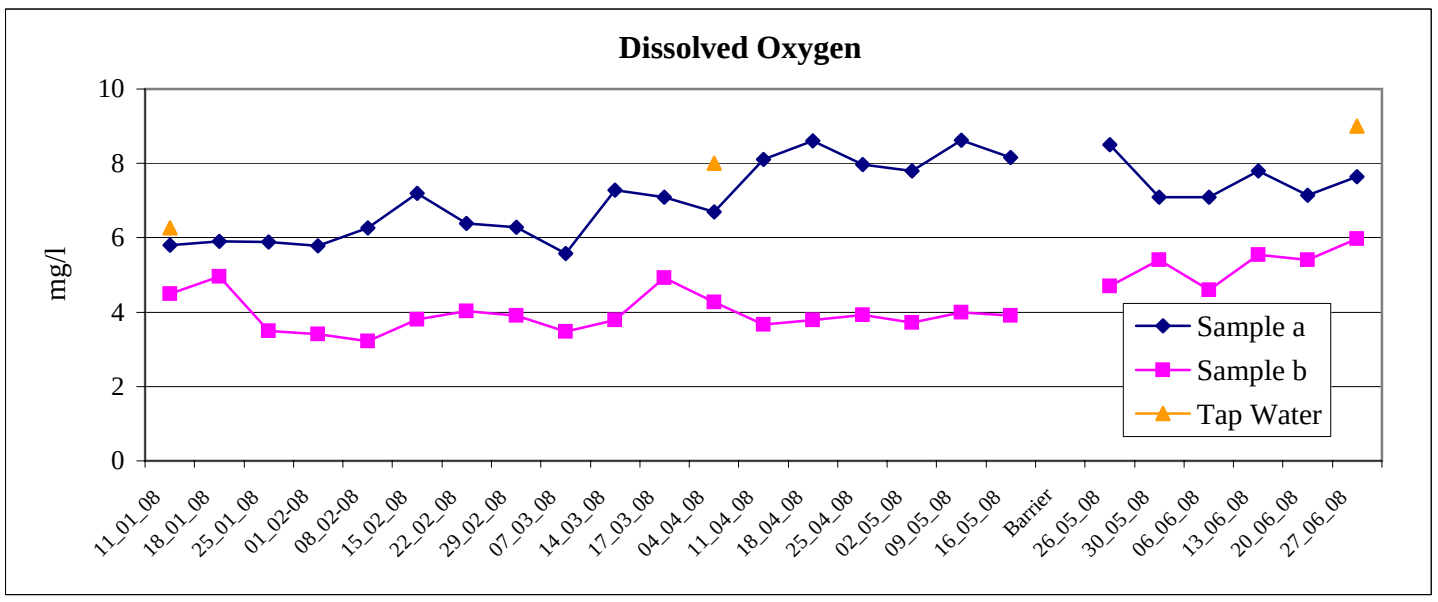

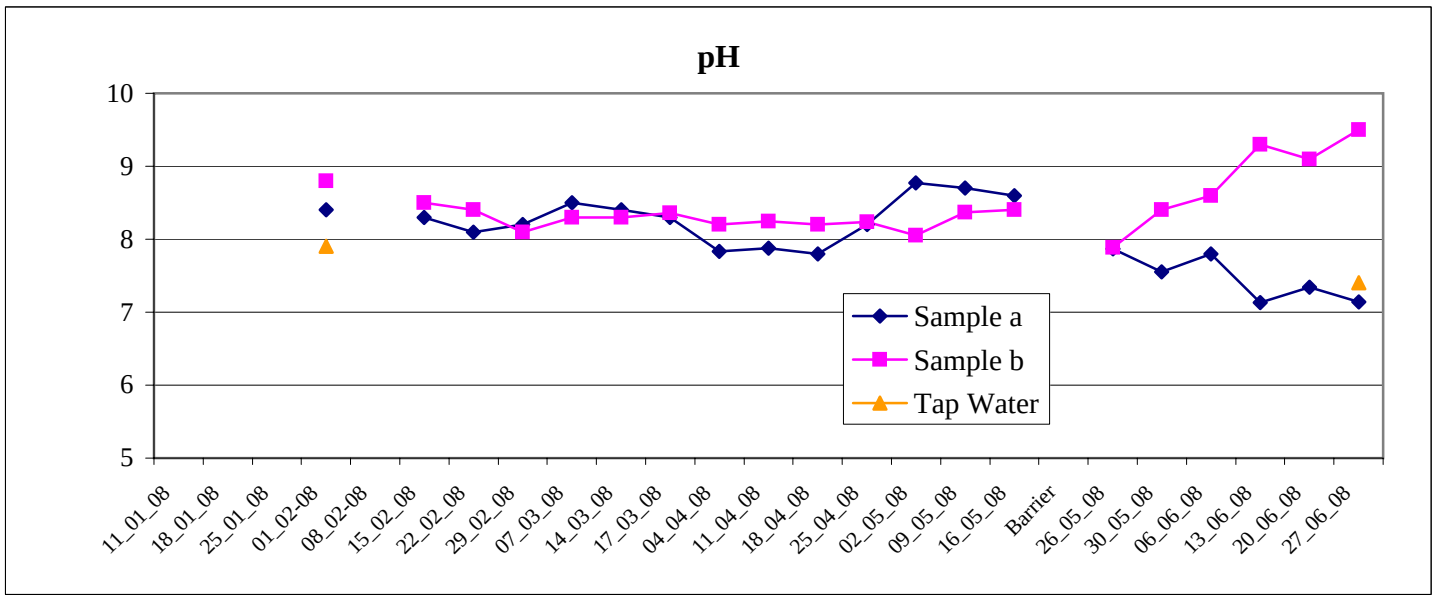

Appendix C

Electrical Resistivity Equipment

ARES AUTOMATIC RESISTIVITY SYSTEM

1100 Vp-p - 2 A - 300 W

Resistivity & IP
up to 10 adjustable IP windows

2D/3D Resistivity Tomography
Multi - Electrode Arrays, VES, RP, SP

Easy-Control System

Applications:
groundwater explorations, geotechnical investigations, measurements on dams and dikes, environmental studies, geological surveys, mineral prospecting, archaeology and many others.

ARES represents a new well equipped resistivity and IP imaging system of the third generation designed by GF Instruments.
Its variability, easy operation (without PC), feeding from a standard 12 V battery and compatibility with widespread interpretation software makes ARES a cost effective and useful tool for working groups and research teams.

GF Instruments

ARES - Technical Specifications

One ruggedized weatherproof unit integrates a powerful transmitter and a sensitive receiver completed with rich software support for a variety of measuring methods.

Transmitter	
Power	up to 300 W (ARES-G4), up to 200 W (ARES-G3)
Current	up to 2.0 A (ARES-G4), up to 1.25 A (ARES-G3)
Voltage	10 - 550 V (1100 Vp-p)
Protection	full electronic
Precision	0.5%
Receiver	
Input impedance	20 MΩ
Input voltage range	5 V
Mains frequency filtering	50 or 60 Hz
Precision	0.1%
Supported methods	
2D/3D Multi-Electrode Resistivity Tomography	Wenner Alpha / Beta / Gamma, Wenner-Schlumberger, Dipole-Dipole, Pole-Dipole, Reverse Pole-Dipole, Pole-Pole, MSG, user defined configurations possibility of simultaneous measurement of up to 8 methods
VES - Vertical Electrical Sounding	Schlumberger, Wenner, dipole-dipole, pole-dipole, pole-pole, user defined configurations
RP - Resistivity Profiling SP - Self Potential	Wenner Alpha / Beta / Gamma, Wenner-Schlumberger, Dipole-Dipole, Pole-Dipole, Pole-Pole, MSG
Measurement - features	self-adapting control system, automatic ranging and calibration automatic checking of measured values easy interruption of the measurement (for the first view of measured structures) capability of profile prolongation by means of multi-electrode cable rolling
IP - Induced Polarization (Chargeability)	available for all 1D / 2D / 3D methods up to 10 adjustable IP windows, each max. 30 s, step 20 / 16.66 ms
Pulse	0.3 s - 30 s, step 0.1 s
SP compensation	constant and linear, time-invariant
Stacking	manual or automatic self-adaptive setting
Measurement optimization	adjustable optimum measured voltage and maximum acceptable measurement error
Stored values	position of the measured point, output current, input voltage, SP, apparent resistivity, standard deviation, chargeability with standard deviation for all 10 IP windows
Output data format	RES2DINV / RES3DINV, Surfer (and others)
Maximum number of electrodes	200 for 2D, 1000 for 3D arrays
Maximum profile length	10 km
Control unit	Easy-Control system, no need of PC for the measurement alphanumeric keyboard, large LCD display safety switch
Memory	16 Mbit, up to 100 files, 70000 readings
Interface	RS232 or USB
Power supply	12 V car battery or attachable battery pack
Connectors	for PC, battery and a universal one for all measuring accessories (Multi-Electrode Cable, VES-Adapter …)
Dimensions	13 x 17 x 39 cm
Weight	3.5 kg

Standard Accessories:

- Transport case
- T-piece (for connection of multi-electrode cable sections and cables for current and potential electrodes)
- Cable for external 12 V battery
- RS232 and USB cables
- Measuring software ARES

Optional accessories:

(subject to continuous development)

- 12 V battery pack
- Fast 3-stage battery charger
- AC adapter (for all countries)
- 2D / 3D multi-electrode cable sections
- Accessories for measurement of large 3D multi-electrode arrays
- VES-adapter (for 5 pairs of potential electrodes)
- Cable reels
- Standard electrodes, non-polarisable electrodes
- Interpretation and mapping software

GF Instruments, s.r.o.
Geophysical Equipment and Services

Ječná 29a, 621 00 Brno, Czech Republic
Tel.: +420 541634 366, 285
Fax: +420 541634 260
E-mail: gregor@gfinstruments.cz
www.gfinstruments.cz

REPRESENTED BY:

With reservations for changes

Appendix D

Descriptive Statistics of the Apparent Resistivity Data

Descriptive Statistics: Apparent Resistivity First Monitoring Campaign

Resistivity Array	07_17	07_17a	07_18	07_18a	07_19	07_19a	07_20	07_20a	07_23	07_24	07_25	07_26	07_27	07_30	07_31	08_01	08_02	08_03	08_06	08_07	08_08	08_09	08_10
Mean	262.09	269.31	294.24	308.85	312.85	384.35	450.42	464.77	441.11	478.93	462.28	459.51	471.93	518.14	539.97	520.12	544.82	537.78	535.96	543.35	536.63	528.28	539.50
Standard Error	9.54	9.84	10.66	11.26	11.09	13.55	14.01	13.90	11.87	12.33	12.12	12.35	12.53	12.63	13.18	12.68	13.34	13.13	13.52	13.75	13.68	13.43	13.69
Median	245.01	251.52	278.13	293.42	298.16	374.47	432.24	445.20	414.64	447.48	438.24	441.58	450.66	487.15	503.18	489.46	511.66	501.38	502.86	515.12	506.59	498.85	509.37
Standard Deviation	100.99	104.12	112.84	119.15	115.26	142.71	146.89	145.11	123.94	127.59	127.12	128.98	131.45	133.67	139.50	134.18	141.21	138.92	143.04	145.47	144.75	142.10	144.92
Sample Variance	10199.54	10840.76	12732.21	14195.81	13285.81	20364.89	21577.59	21058.20	15360.84	16278.21	16160.25	16634.60	17279.14	17866.69	19459.62	18003.72	19939.00	19298.82	20459.55	21161.85	20952.75	20193.03	21002.25
Kurtosis	-0.24	-0.23	-0.41	-0.38	0.56	0.46	0.77	0.99	0.24	-0.12	0.31	0.00	0.13	0.22	0.43	0.18	0.32	0.21	0.25	0.15	0.10	0.06	0.11
Skewness	0.70	0.70	0.57	0.56	0.70	0.71	0.83	0.84	0.78	0.63	0.73	0.61	0.58	0.72	0.83	0.73	0.84	0.80	0.81	0.77	0.75	0.77	0.78
Range	408.81	428.13	460.75	503.87	606.54	697.96	761.06	769.26	594.74	550.58	614.09	589.99	655.79	658.93	691.36	654.95	680.19	671.21	694.39	697.68	688.08	668.24	684.68
Minimum	112.85	115.48	115.90	117.78	125.21	130.61	166.53	182.57	231.33	257.94	248.23	231.88	231.42	283.70	286.97	278.58	285.52	282.69	280.26	284.14	278.77	283.81	285.42
Maximum	521.66	543.61	576.65	621.65	731.75	828.57	927.59	951.83	826.07	808.52	862.32	821.87	887.21	942.63	978.33	933.53	965.71	953.90	974.65	981.82	966.85	952.05	970.10
Sum	29354.02	30162.23	32954.94	34591.53	33788.05	42662.70	49546.08	50659.51	48081.23	51245.90	50850.31	50086.31	51912.31	58031.37	60476.34	58253.68	61020.11	60231.77	60027.85	60855.12	60102.45	59167.55	60424.54
Count	112	112	112	112	108	111	110	109	109	107	110	109	110	112	112	112	112	112	112	112	112	112	112

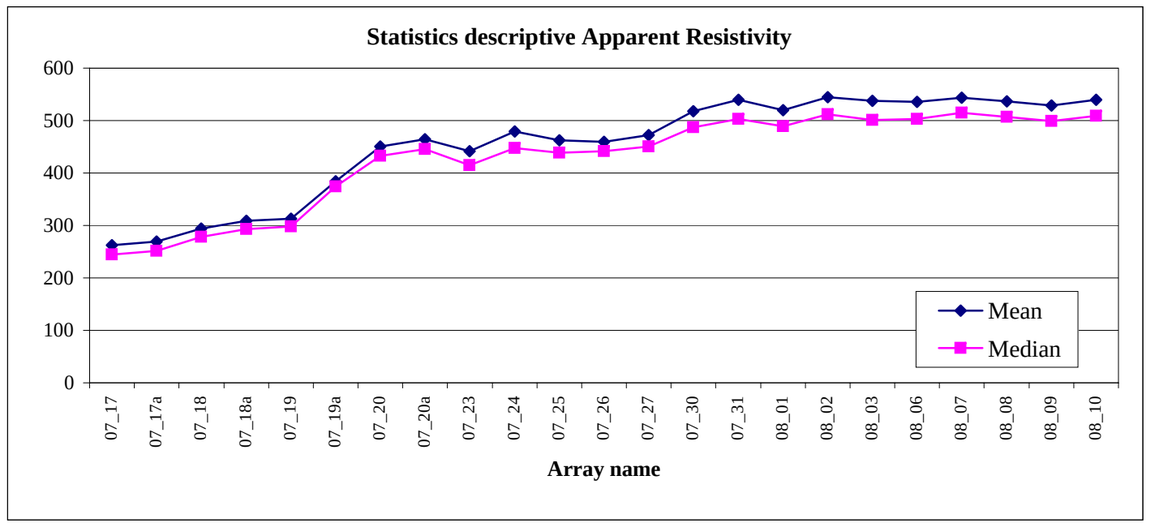

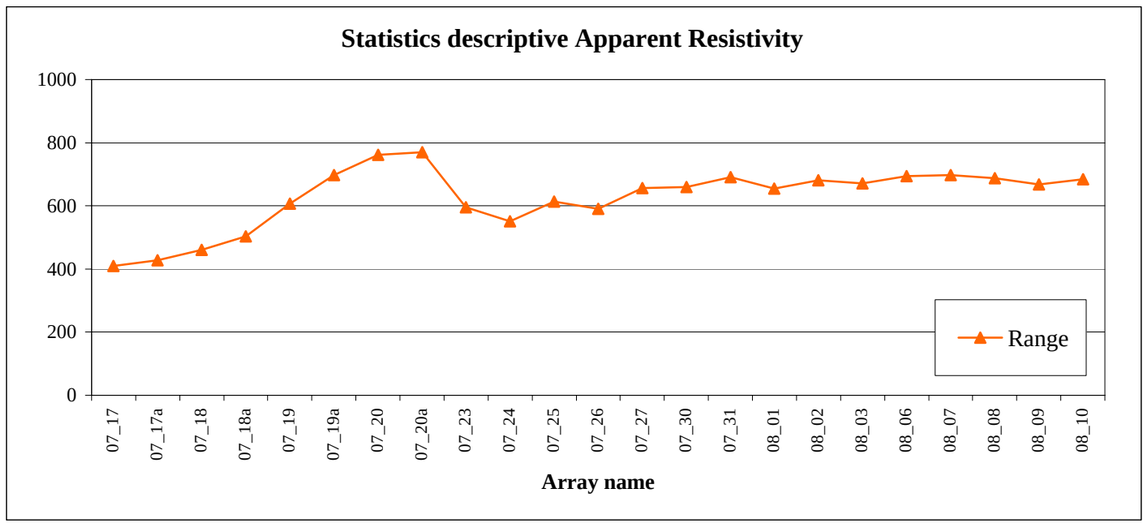

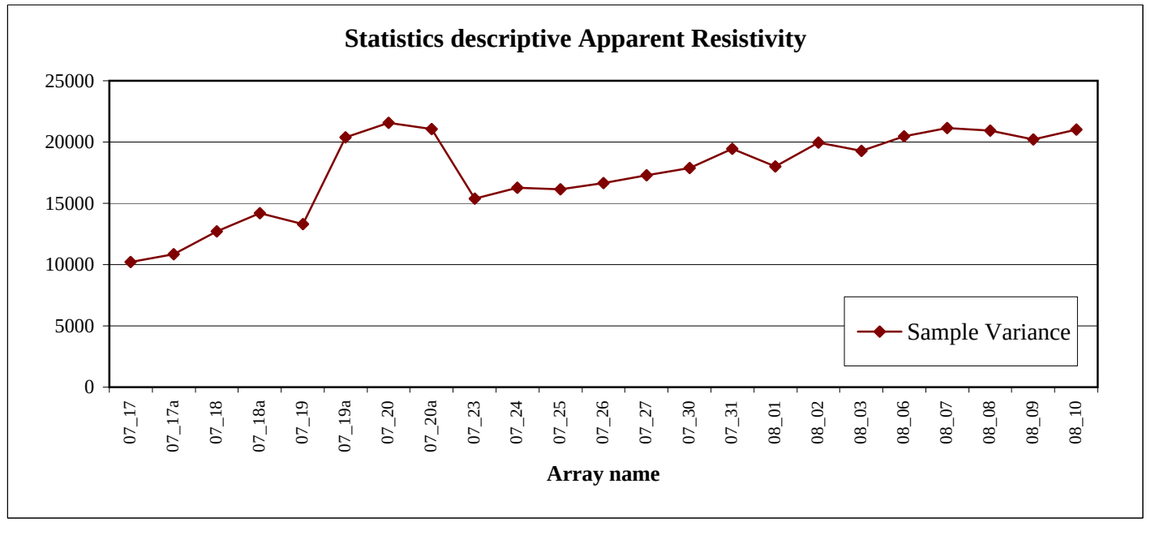

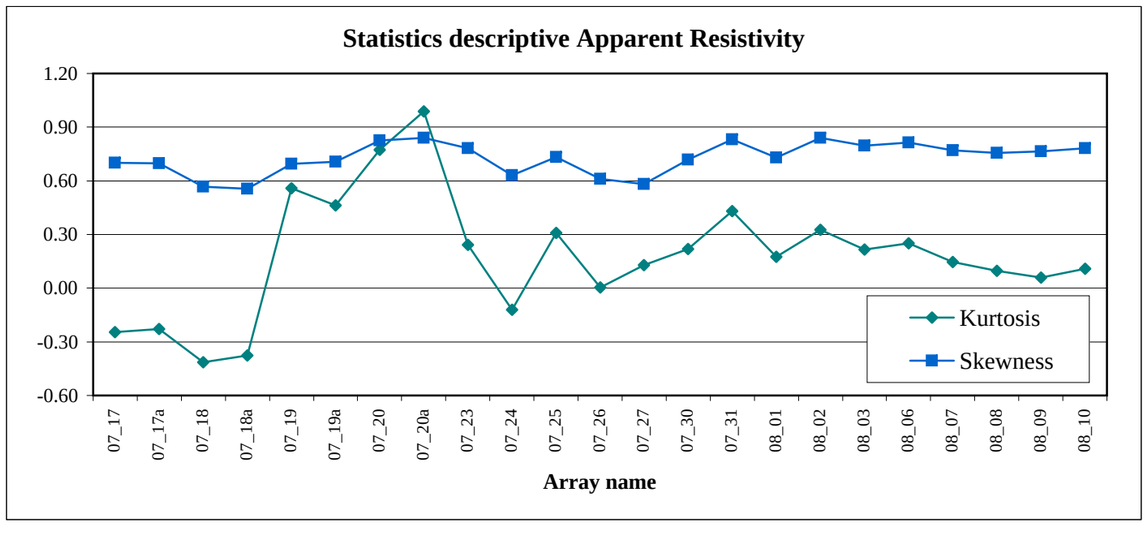

Descriptive Statistics: Subtraction Apparent Resistivity v Baseline Data First Monitoring Campaign

Resistivity Array	*07_17a*	*07_18*	*07_18a*	*07_19*	*07_19a*	*07_20*	*07_20a*	*07_23*	*07_24*	*07_25*	*07_26*	*07_27*	*07_30*	*07_31*	*08_01*	*08_02*	*08_03*	*08_06*	*08_07*	*08_08*	*08_09*	*08_10*
Mean	7.22	32.15	46.76	51.49	122.48	188.29	202.93	178.15	215.96	200.14	197.87	209.50	256.05	277.88	258.03	282.73	275.69	273.87	281.26	274.54	266.19	277.42
Standard Error	0.50	3.52	4.13	5.51	7.41	8.50	8.64	6.95	7.34	7.49	7.53	7.52	7.61	7.98	7.26	7.64	7.54	7.73	7.91	7.82	7.57	7.65
Median	6.16	27.26	42.93	51.04	114.52	177.71	191.76	180.19	214.17	195.04	193.52	203.15	252.53	276.52	253.30	276.89	270.47	270.11	278.15	273.58	266.69	276.01
Standard Deviation	5.30	37.24	43.73	57.50	78.07	89.17	90.23	72.55	75.96	78.57	78.57	78.91	80.58	84.50	76.85	80.82	79.76	81.80	83.75	82.71	80.07	80.95
Sample Variance	28.06	1387.15	1912.44	3306.77	6095.36	7951.84	8141.70	5263.42	5770.59	6173.29	6172.48	6227.16	6493.47	7139.50	5906.26	6532.09	6361.27	6690.51	7013.99	6840.64	6411.49	6552.35
Kurtosis	6.16	12.24	11.04	13.76	10.58	9.26	9.18	5.15	5.73	5.94	4.60	4.45	5.72	6.04	5.96	5.99	5.97	5.78	4.91	4.44	4.20	4.52
Skewness	2.10	3.13	2.90	3.04	2.78	2.60	2.59	1.35	1.64	1.79	1.54	1.54	1.75	1.85	1.81	1.82	1.83	1.82	1.63	1.52	1.45	1.52
Range	32.57	246.72	285.52	422.25	502.50	532.91	557.32	449.97	479.98	476.31	461.55	464.78	477.69	504.92	463.81	478.70	475.58	479.12	494.50	487.38	479.55	482.05
Minimum	0.01	-22.59	-16.39	-43.02	15.42	51.34	62.14	29.49	63.68	49.58	44.10	69.91	112.42	120.89	117.20	134.49	125.80	143.01	134.80	126.95	119.98	135.53
Maximum	32.58	224.13	269.13	379.23	517.92	584.25	619.46	479.46	543.66	525.89	505.65	534.69	590.11	625.81	581.01	613.19	601.38	622.13	629.30	614.33	599.53	617.58
Sum	808.21	3600.92	5237.51	5612.43	13595.07	20711.62	22119.80	19418.53	23107.65	22015.85	21567.32	23044.69	28677.35	31122.32	28899.66	31666.09	30877.75	30673.83	31501.10	30748.43	29813.53	31070.52
Count	112	112	112	109	111	110	109	109	107	110	109	110	112	112	112	112	112	112	112	112	112	112

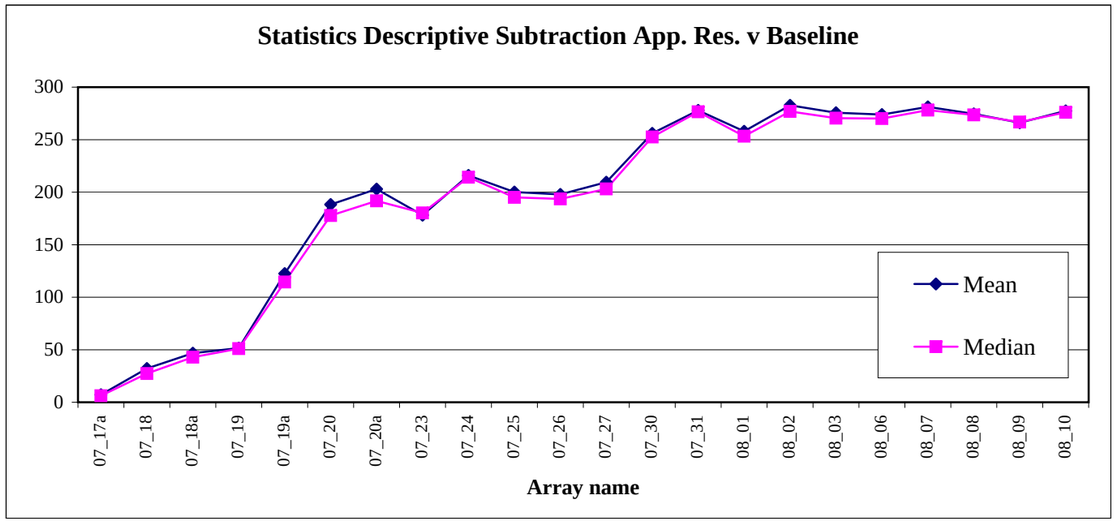

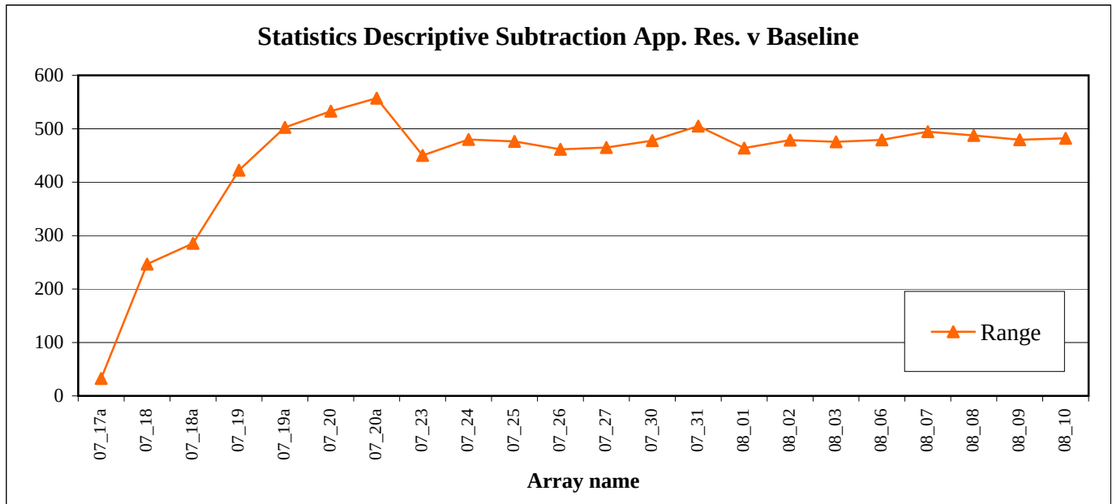

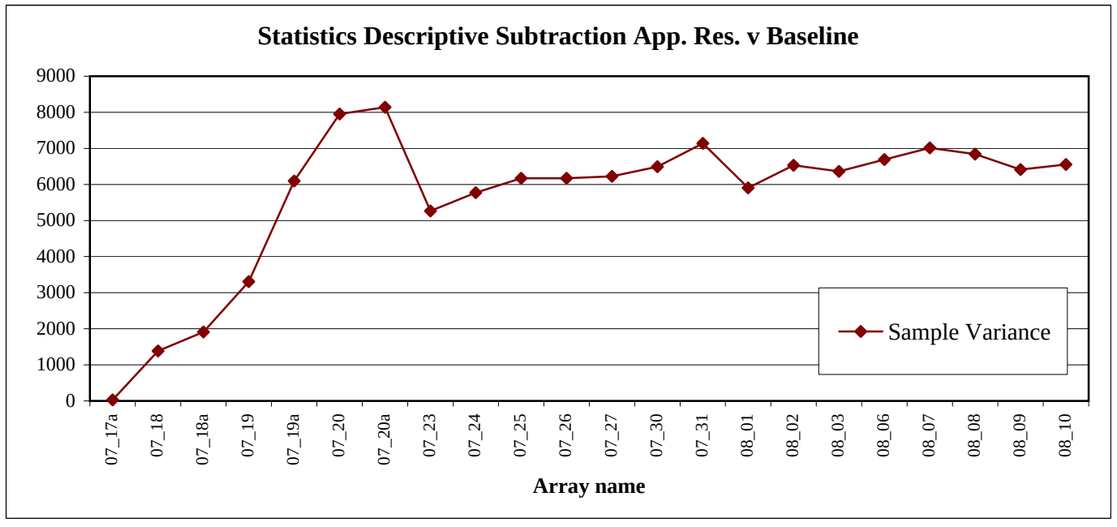

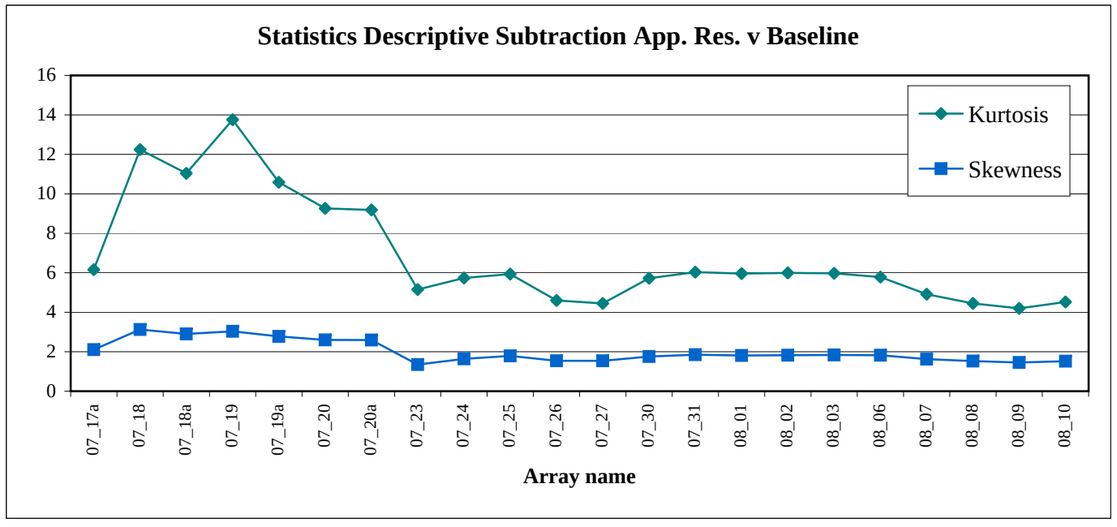

Descriptive Statistics: Apparent resistivity Data Second Monitoring Campaign

Resistivity Array	*01_11*	*01_18*	*01_25*	*02_01*	*02_08*	*02_15*	*02_22*	*02_29*	*03_07*	*03_17*	*04_04*	*04_11*	*04_18*	*04_25*	*05_02*	*05_09*	*05_16*	*BARR*	*05_26*	*05_30*	*06_06*	*06_13*	*06_20*	*06_27*
Mean	1010.88	982.75	984.13	1007.73	946.29	971.36	950.87	923.53	946.51	953.05	917.18	981.73	947.07	923.64	936.70	937.46	954.48		891.17	911.97	876.23	880.34	897.90	917.77
Standard Error	16.76	17.14	17.02	17.88	17.34	17.76	17.53	16.90	17.68	17.72	16.71	17.92	17.69	17.27	17.39	16.84	17.00		18.45	16.75	16.33	16.92	17.63	18.02
Median	984.82	949.89	950.34	965.25	907.06	926.88	912.03	883.57	901.93	909.28	887.50	945.44	903.22	874.11	889.13	901.65	901.60		851.84	861.92	822.54	820.17	839.13	864.61
Standard Deviation	354.74	362.74	360.35	378.54	366.95	375.93	371.03	357.70	374.21	375.00	353.58	379.27	374.37	365.64	368.02	356.54	359.81		390.57	354.55	345.59	358.04	373.12	381.50
Sample Variance	125841	131579	129850	143290	134652	141321	137667	127946	140036	140624	125018	143847	140150	133691	135442	127121	129461		152543	125706	119434	128191	139219	145540
Kurtosis	-0.52	-0.64	-0.57	-0.57	-0.64	-0.59	-0.60	-0.54	-0.61	-0.54	-0.69	-0.68	-0.62	-0.55	-0.59	-0.54	-0.46		-0.46	-0.01	-0.01	-0.15	-0.28	-0.42
Skewness	0.29	0.30	0.35	0.36	0.34	0.37	0.36	0.39	0.38	0.41	0.30	0.29	0.34	0.40	0.38	0.35	0.43		0.42	0.59	0.64	0.64	0.60	0.55
Range	1545.38	1499.96	1469.46	1540.04	1489.49	1535.19	1515.69	1469.85	1519.57	1534.70	1456.53	1574.16	1567.11	1535.35	1533.66	1509.10	1538.13		1845.48	1841.23	1786.11	1789.02	1809.69	1793.52
Minimum	335.54	307.26	339.72	360.20	323.77	337.47	327.26	329.00	327.12	333.53	310.30	326.71	303.85	302.43	309.26	310.58	328.82		156.97	175.02	176.38	196.16	211.19	229.61
Maximum	1880.92	1807.22	1809.18	1900.24	1813.26	1872.66	1842.95	1798.85	1846.69	1868.23	1766.83	1900.87	1870.96	1837.78	1842.92	1819.68	1866.95		2002.45	2016.25	1962.49	1985.18	2020.88	2023.13
Sum	452875	440271	440890	451462	423938	435171	425988	413743	424037	426965	410896	439813	424287	413792	419642	419983	427608		399244	408561	392552	394393	402258	411162
Count	448.00	448.00	448.00	448.00	448.00	448.00	448.00	448.00	448.00	448.00	448.00	448.00	448.00	448.00	448.00	448.00	448.00		448.00	448.00	448.00	448.00	448.00	448.00

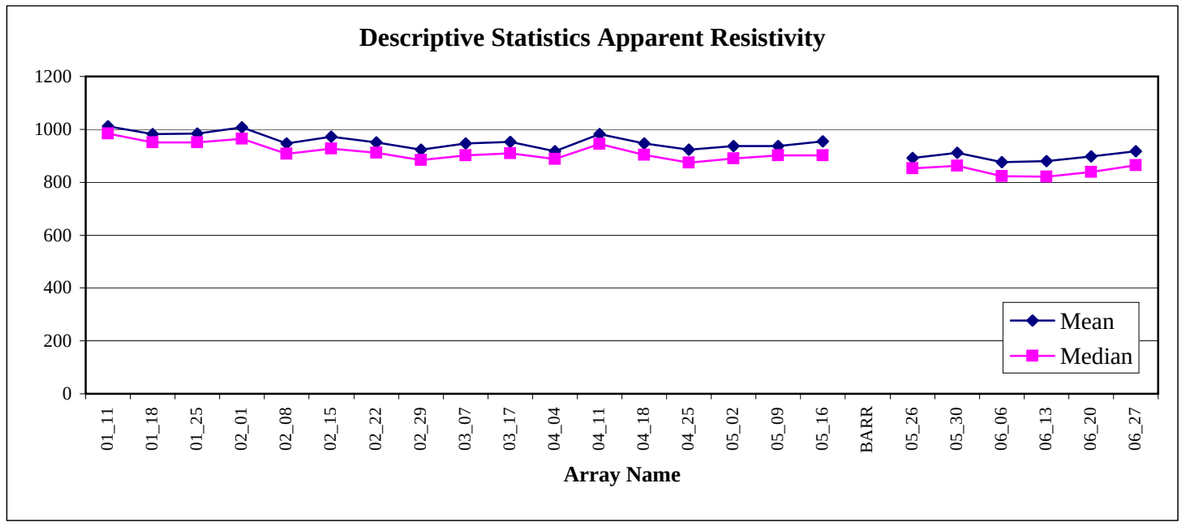

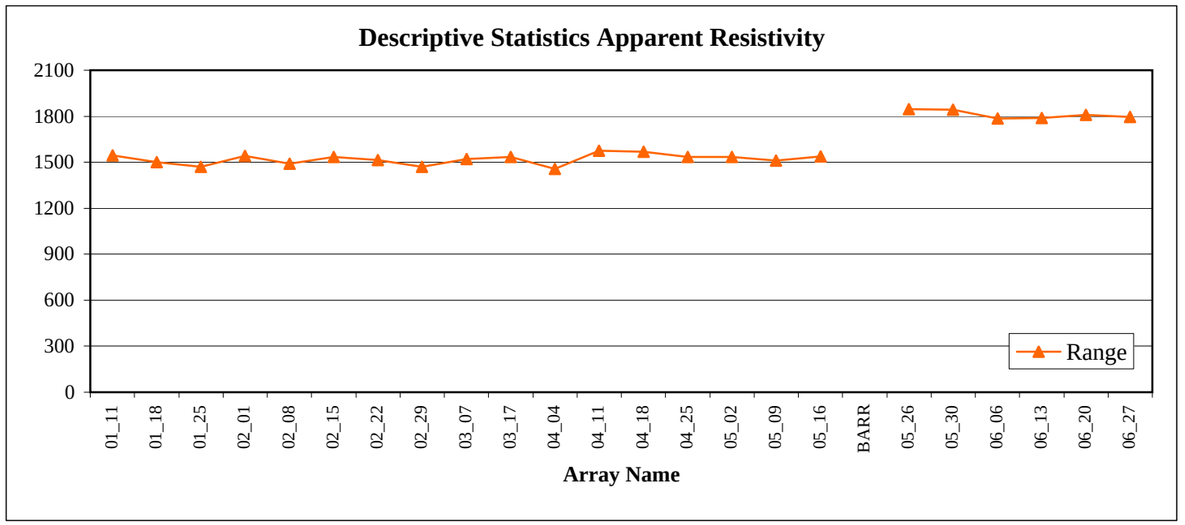

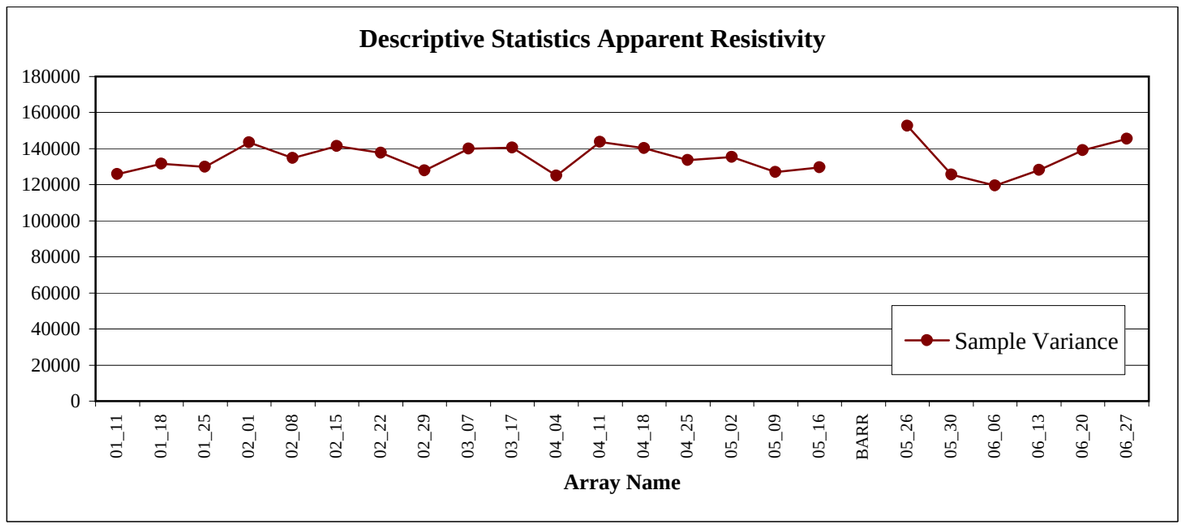

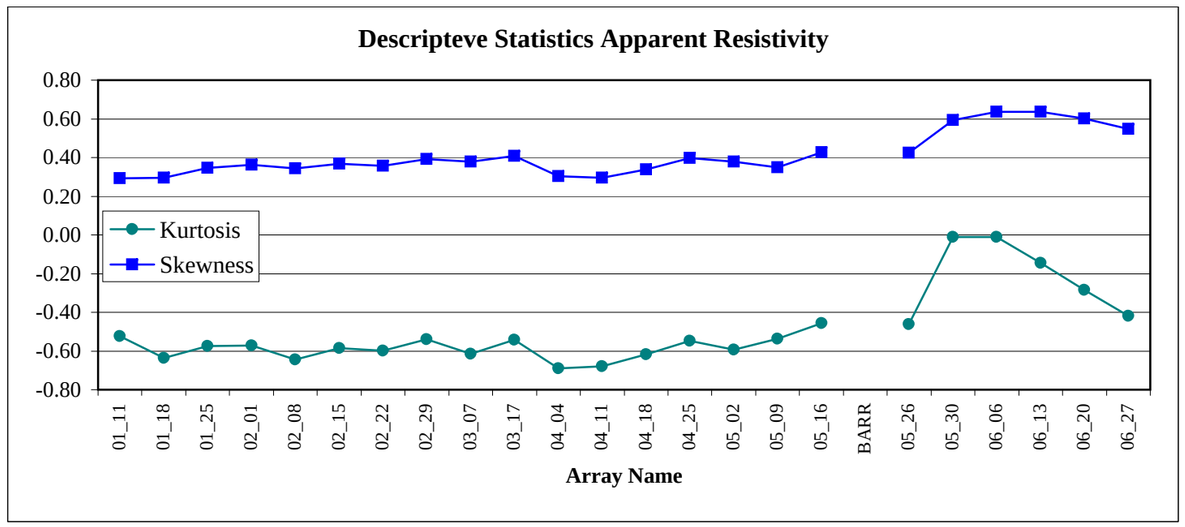

Descriptive Statistics: Subtraction Apparent Resistivity v First Survey Second Monitoring Campaign

Resistivity Array	*01_18*	*01_25*	*02_01*	*02_08*	*02_15*	*02_22*	*02_29*	*03_07*	*03_17*	*04_04*	*04_11*	*04_18*	*04_25*	*05_02*	*05_09*	*05_16*	*BARR*	*05_26*	*05_30*	*06_06*	*06_13*	*06_20*	*06_27*
Mean	-28.13607	-26.7533	-3.154664	-64.59339	-39.51844	-60.01596	-87.3502	-64.37092	-57.83493	-93.70433	-29.15752	-63.81444	-87.24082	-74.18089	-73.42129	-56.40138		-119.7124	-98.91685	-134.6502	-130.5404	-112.9853	-93.11036
Standard Error	4.507442	4.190273	4.716847	4.61631	4.636792	4.536881	4.470834	4.776462	4.739069	4.756799	5.191477	5.183466	5.152606	5.101124	4.982923	4.916069		8.327977	9.337358	9.511121	9.359703	9.204416	8.850193
Median	-26.065	-19.02	-3.05	-64.08	-38.785	-57.28	-84.64005	-62.47	-54.85	-87.70005	-31.7	-64.295	-91.79495	-78.23005	-74.72	-52.68		-120.43	-84.26995	-111.635	-101.37	-82.775	-68.635
Standard Deviation	95.40457	88.69137	99.83683	97.70886	98.14238	96.02767	94.62972	101.0986	100.3072	100.6825	109.8829	109.7133	109.0601	107.9704	105.4686	104.0536		176.2701	197.6346	201.3125	198.1076	194.8208	187.3233
Sample Variance	9102.032	7866.159	9967.393	9547.022	9631.927	9221.313	8954.783	10220.94	10061.53	10136.96	12074.24	12037.01	11894.11	11657.62	11123.62	10827.14		31071.13	39059.44	40526.71	39246.61	37955.13	35090.01
Kurtosis	1.898927	1.205071	2.080246	2.550582	1.891764	1.824305	1.867077	2.309398	1.876069	0.80443	0.88477	1.206496	1.6	1.362845	1.146784	1.173962		0.286844	1.197059	0.51693	-0.217184	-0.44477	-0.574894
Asymmetry	0.178912	0.064208	0.339085	0.290202	0.179398	0.139599	0.089044	0.323606	0.188449	-0.032113	0.26335	0.369644	0.52341	0.372546	0.443081	0.345316		-0.201086	-0.890357	-0.681227	-0.413364	-0.250211	-0.171203
Range	733.28	674.6698	753.5499	789.7299	774.6399	760.1999	763.4799	819.2599	793.8499	655.5099	725.0999	732.8599	767.2699	746.6099	696.1099	707.2099		1130.74	1233.08	1236.83	1111.38	1055.98	974.8199
Minimum	-320.32	-297.8399	-312.2699	-381.3799	-351.6199	-363.7099	-389.0499	-374.1999	-366.3299	-395.3799	-329.2299	-349.0899	-381.3099	-374.8799	-346.5799	-337.8999		-719.7799	-844.58	-851.47	-727.7801	-652.1	-575.1599
Maximum	412.96	376.8299	441.28	408.35	423.02	396.49	374.43	445.06	427.52	260.13	395.87	383.77	385.96	371.73	349.53	369.31		410.9599	388.5	385.36	383.6	403.88	399.66
Sum	-12604.96	-11985.48	-1413.289	-28937.84	-17704.26	-26887.15	-39132.89	-28838.17	-25910.05	-41979.54	-13062.57	-28588.87	-39083.89	-33233.04	-32892.74	-25267.82		-53631.15	-44314.75	-60323.28	-58482.11	-50617.42	-41713.44
Count	448	448	448	448	448	448	448	448	448	448	448	448	448	448	448	448		448	448	448	448	448	448

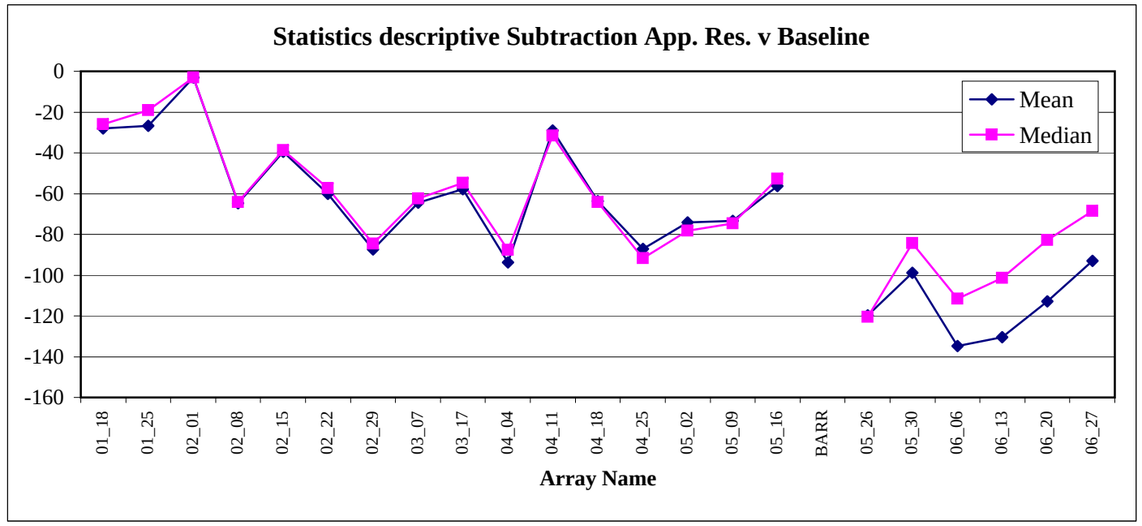

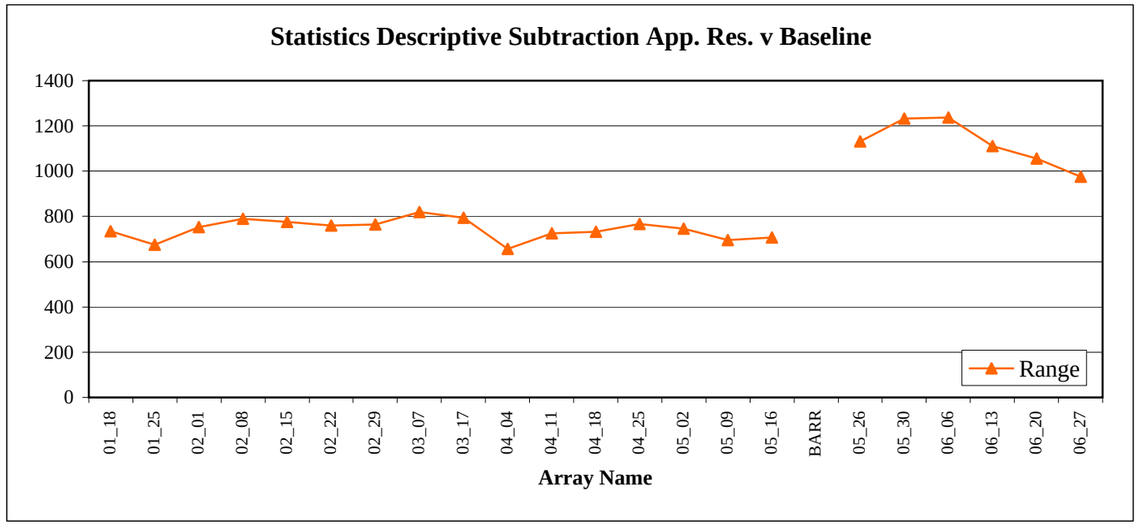

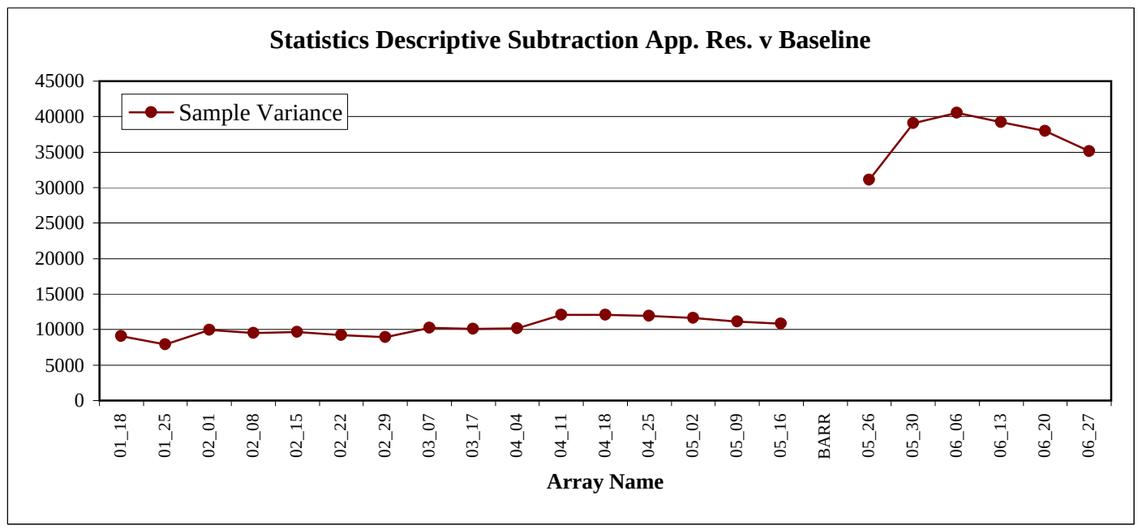

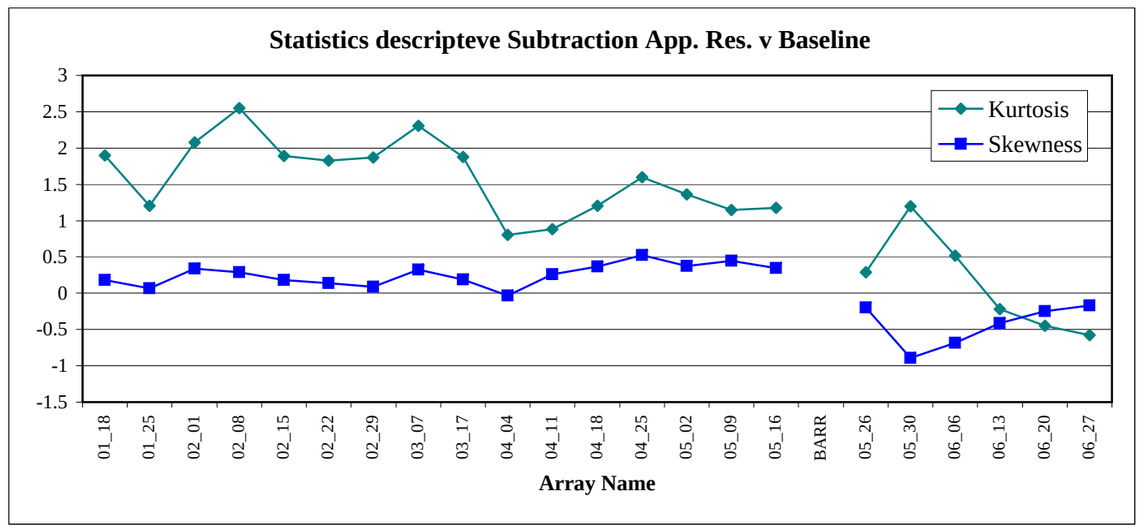

Appendix E

Inverse Model Resistivity Section Images

Inverse Model Resistivity Section Images
First Monitoring Campaign

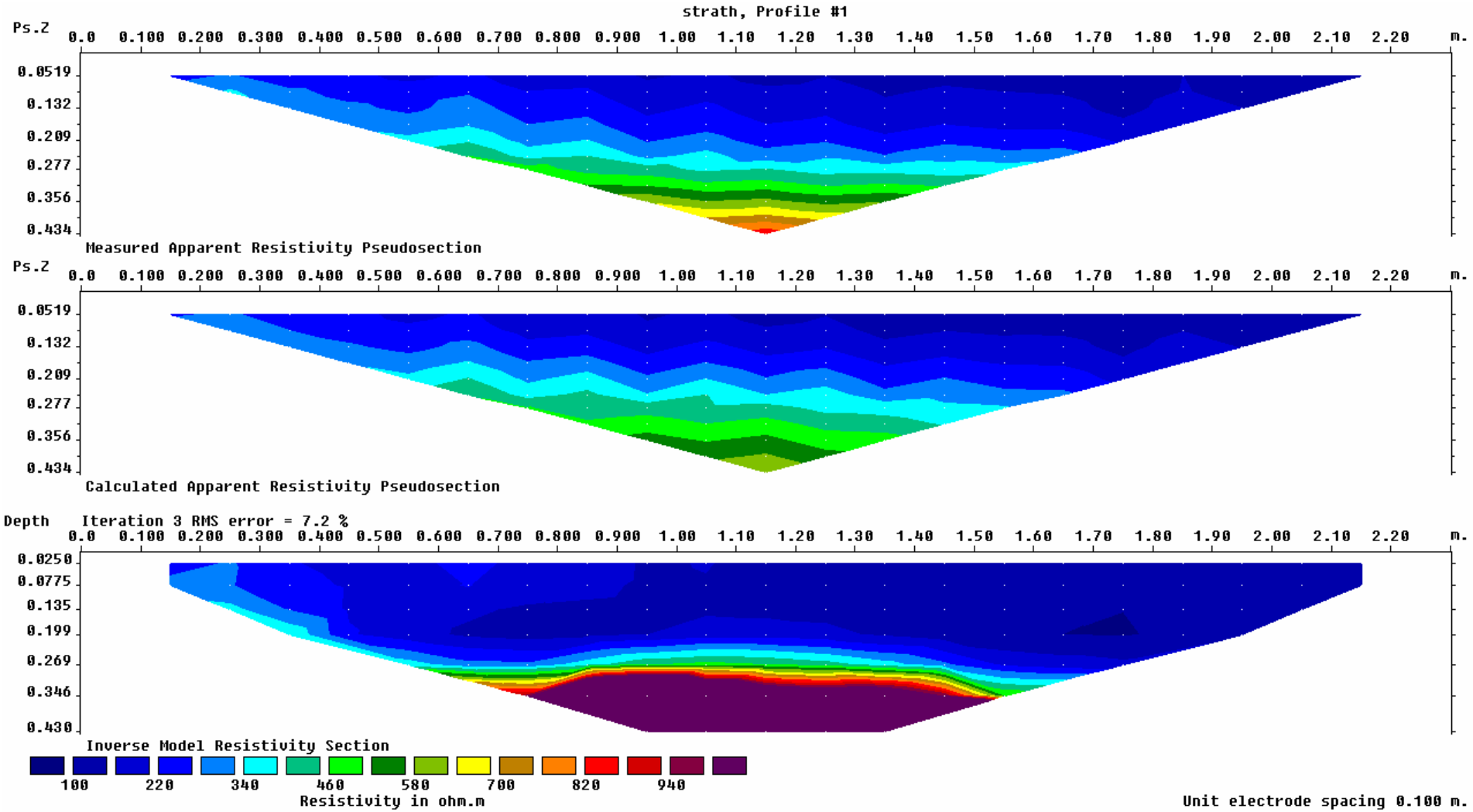

Electrical Resistivity Survey Image "07_17" (17.07.07)

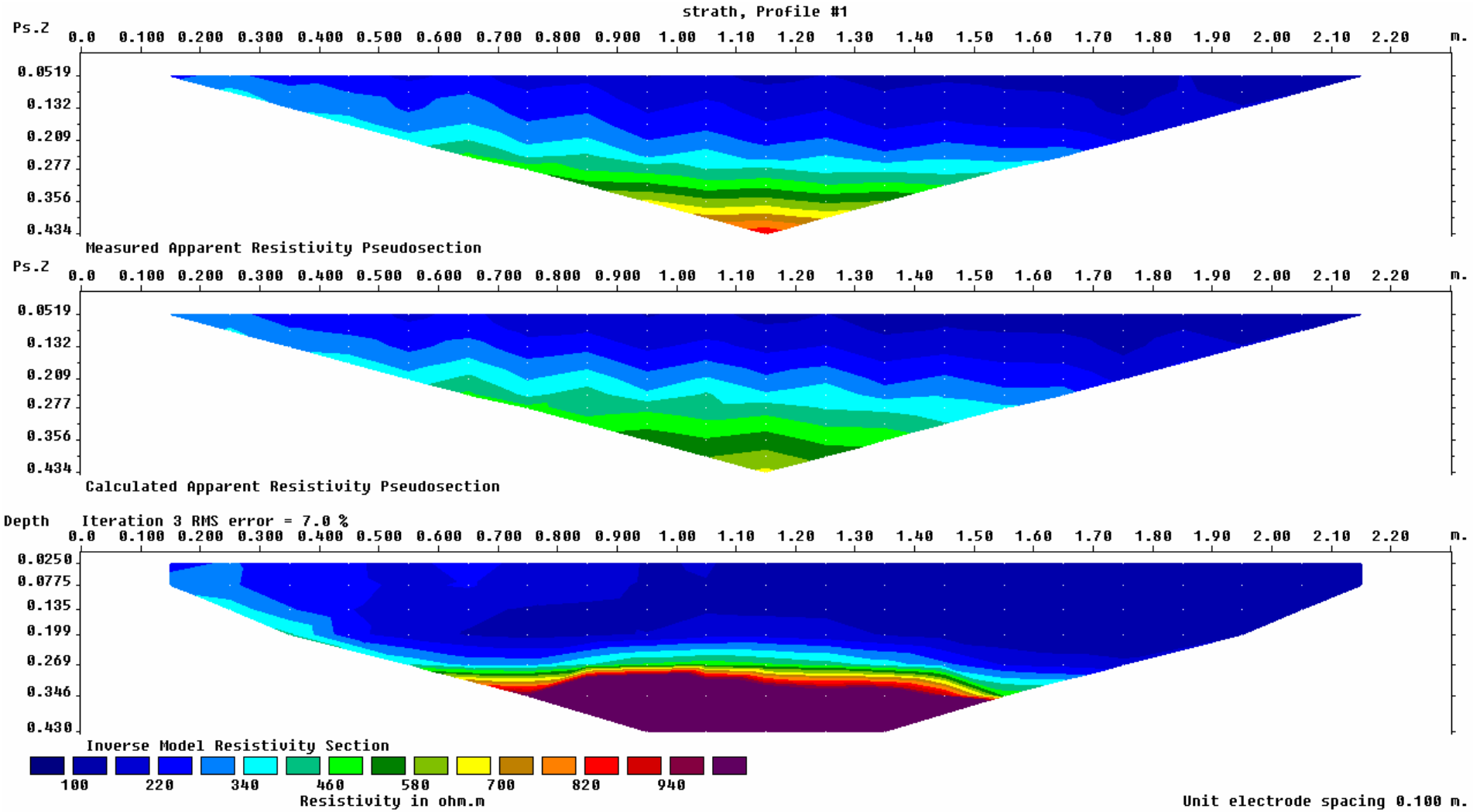

Electrical Resistivity Survey Image "07_17a" (17.07.07)

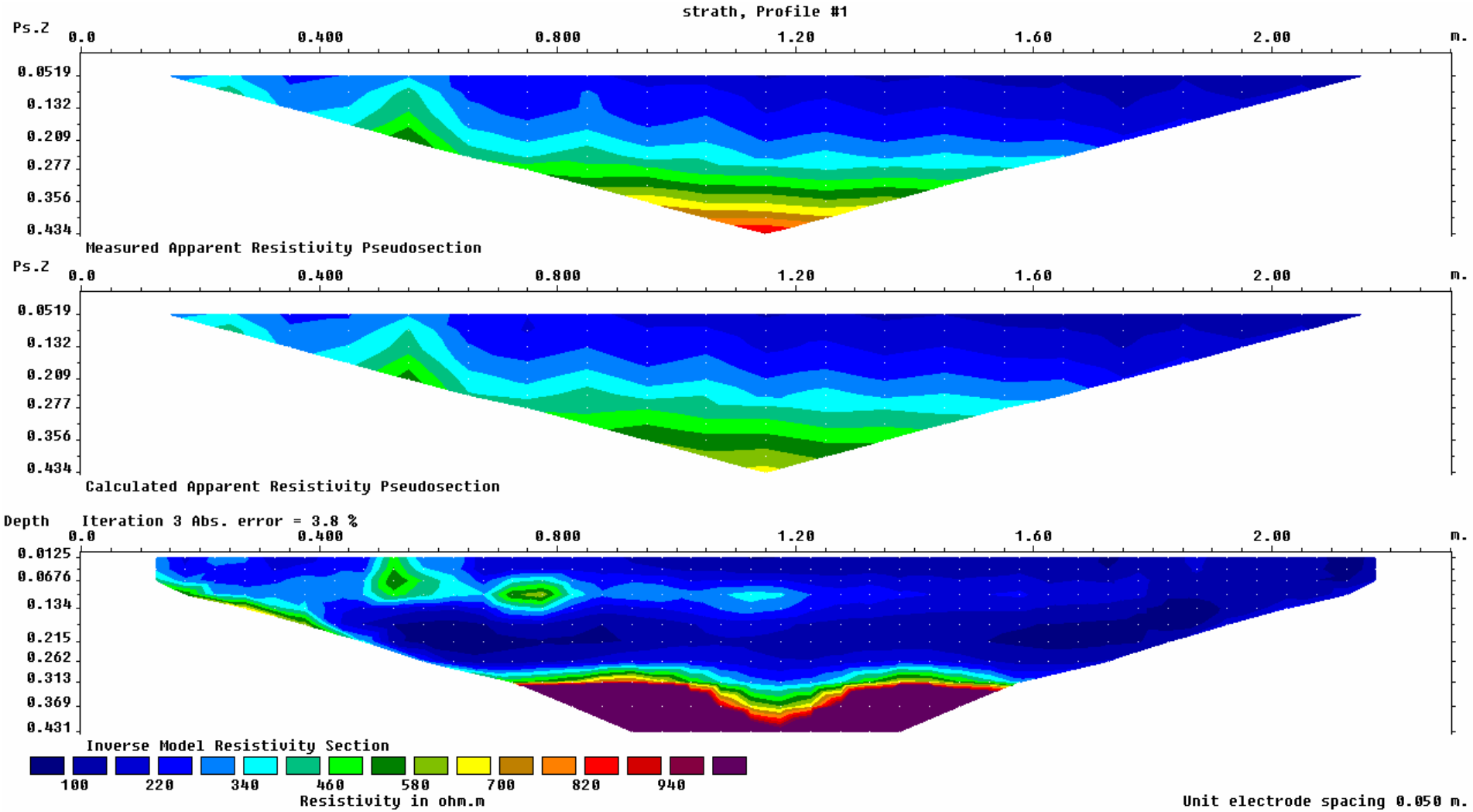

Electrical Resistivity Survey Image "07_18" (18.07.07)

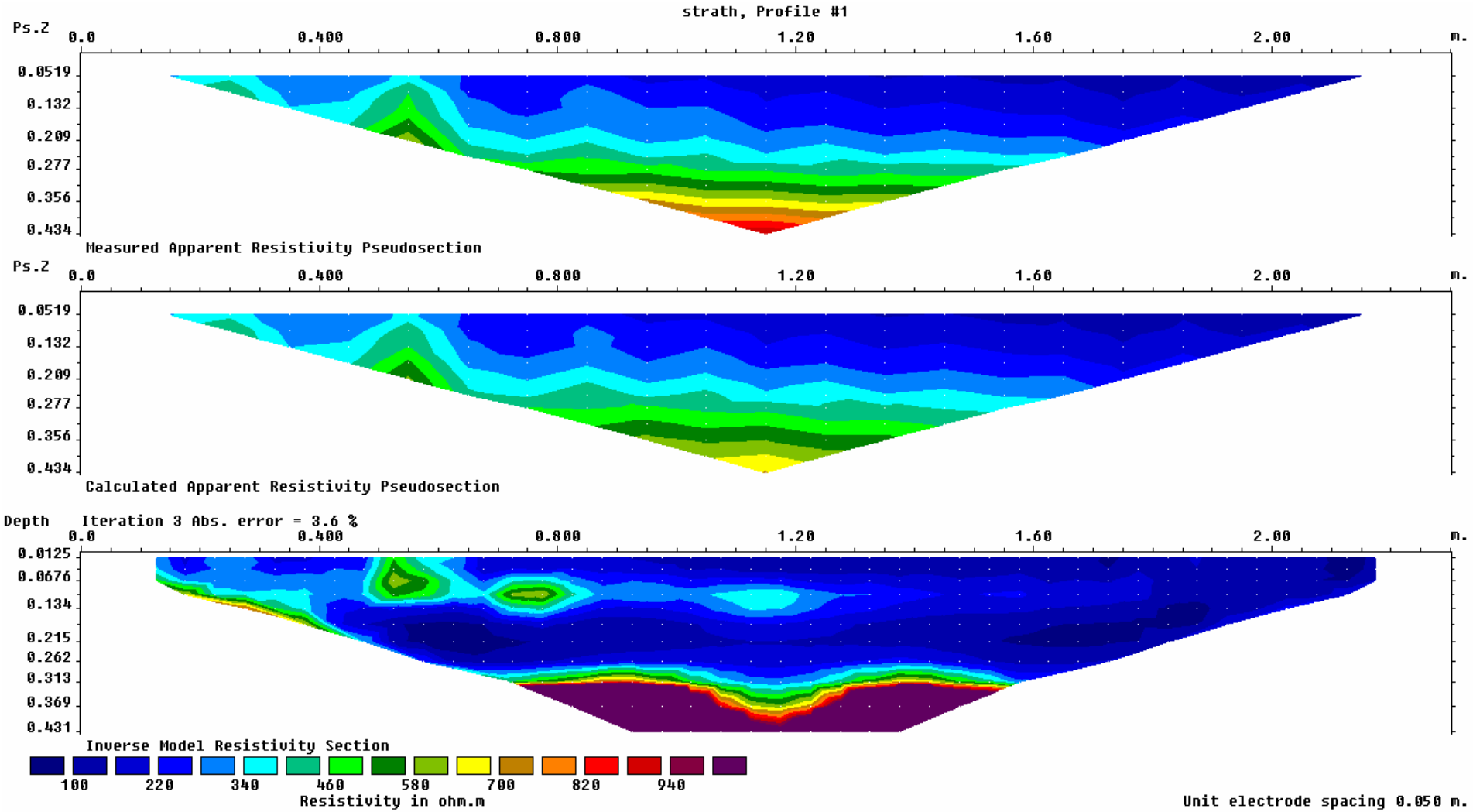

Electrical Resistivity Survey Image "07_18a" (18.07.07)

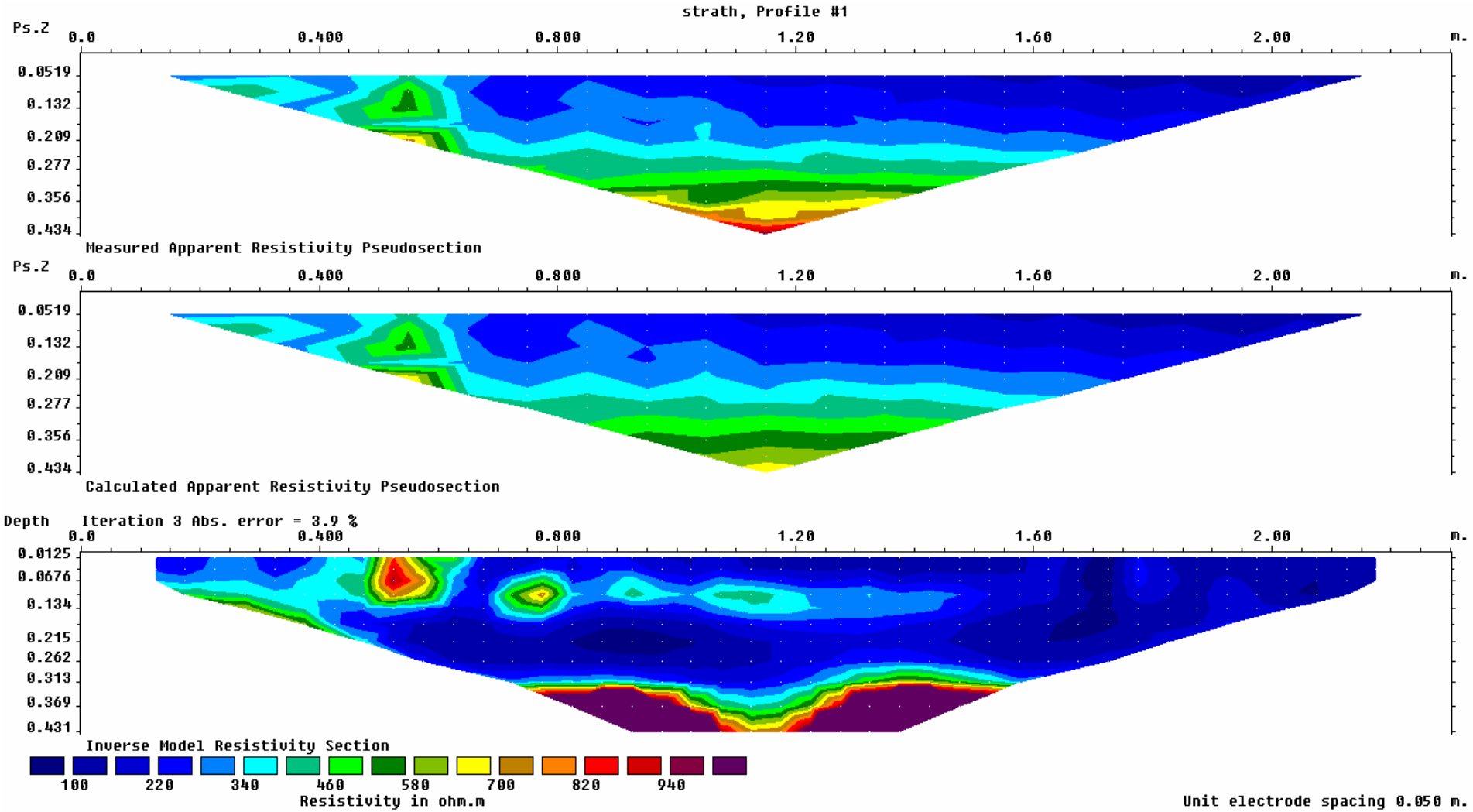

Electrical Resistivity Survey Image "07_19" (19.07.07)

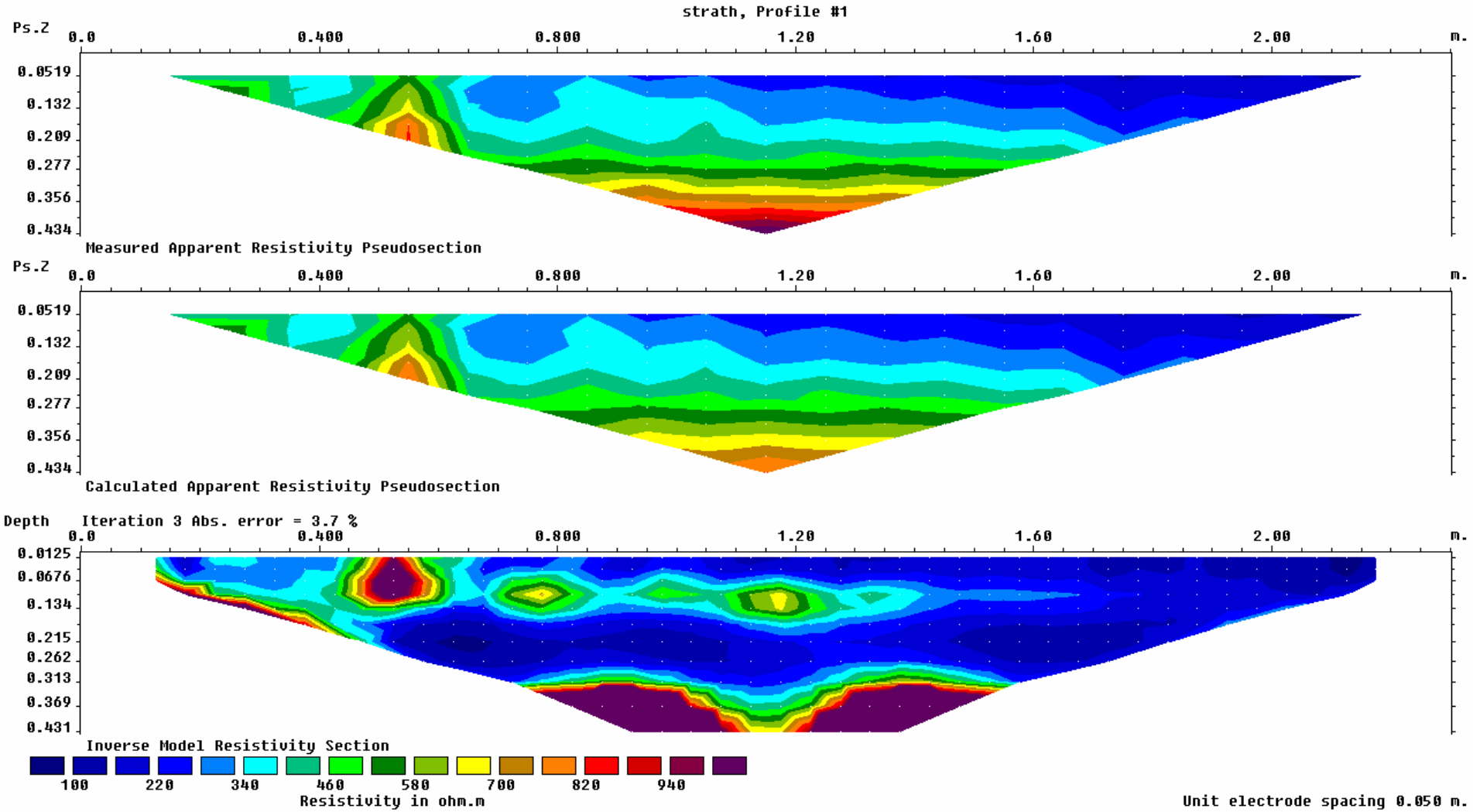

Electrical Resistivity Survey Image "07_19a" (19.07.07)

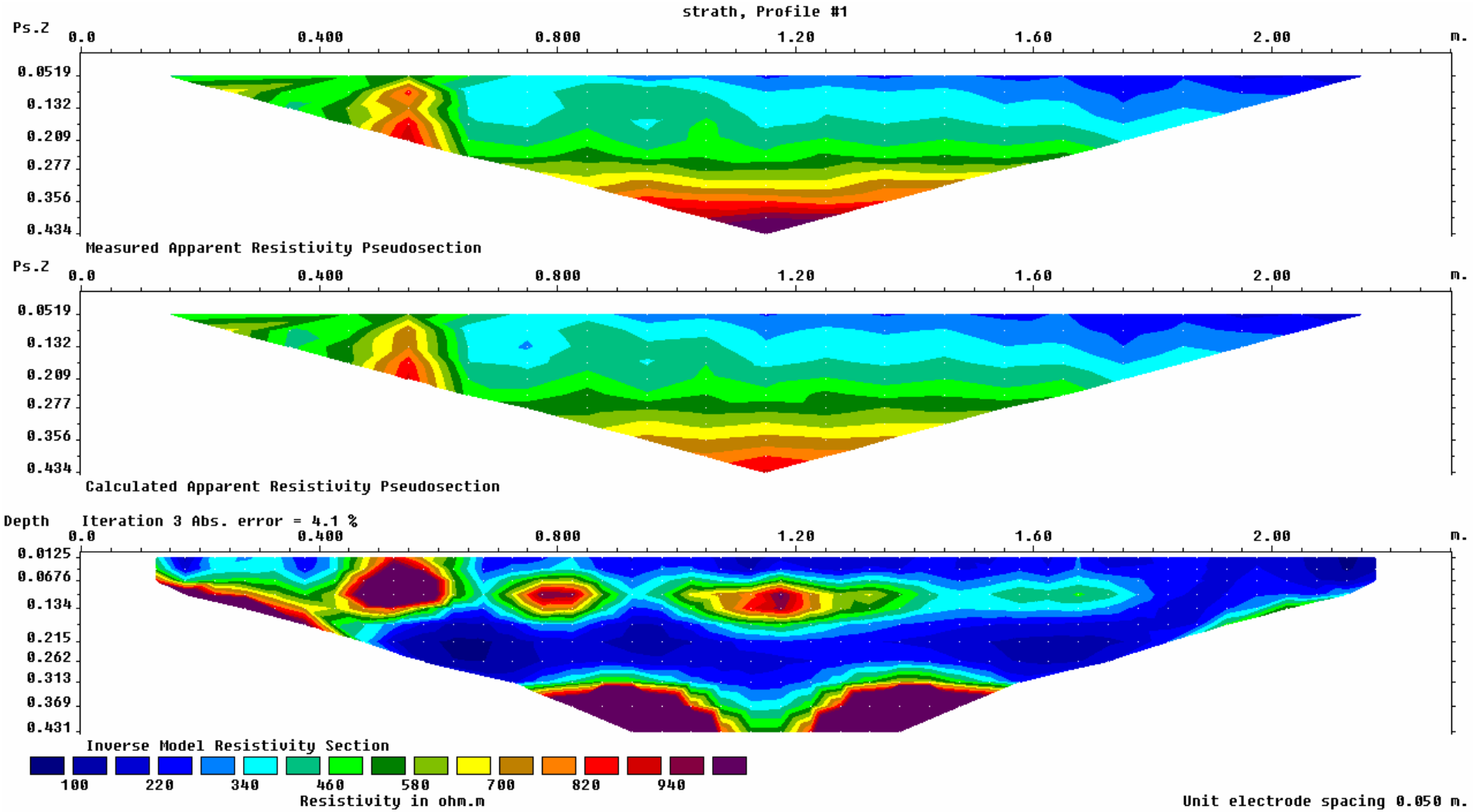

Electrical Resistivity Survey Image "07_20" (20.07.07)

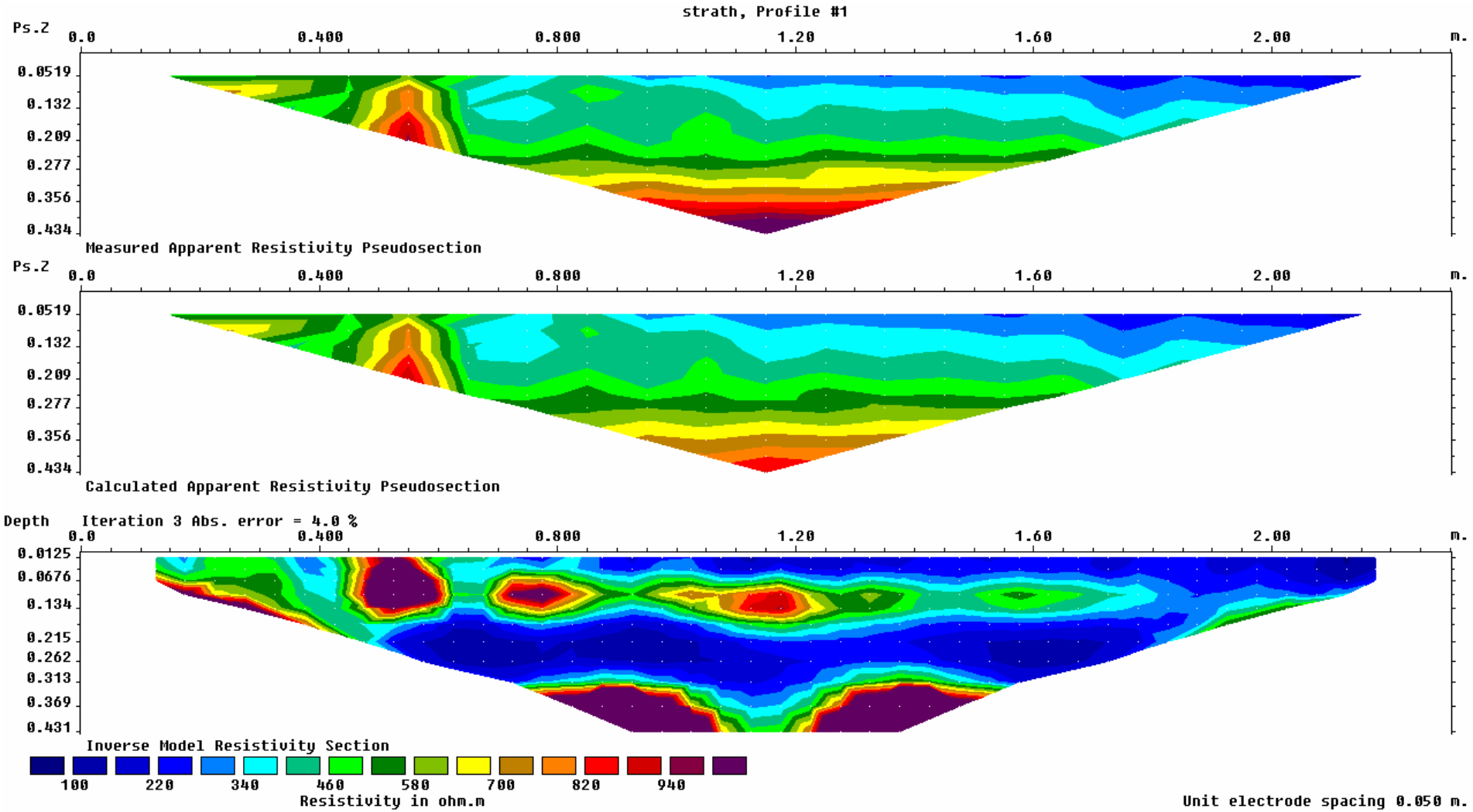

Electrical Resistivity Survey Image "07_20a" (20.07.07)

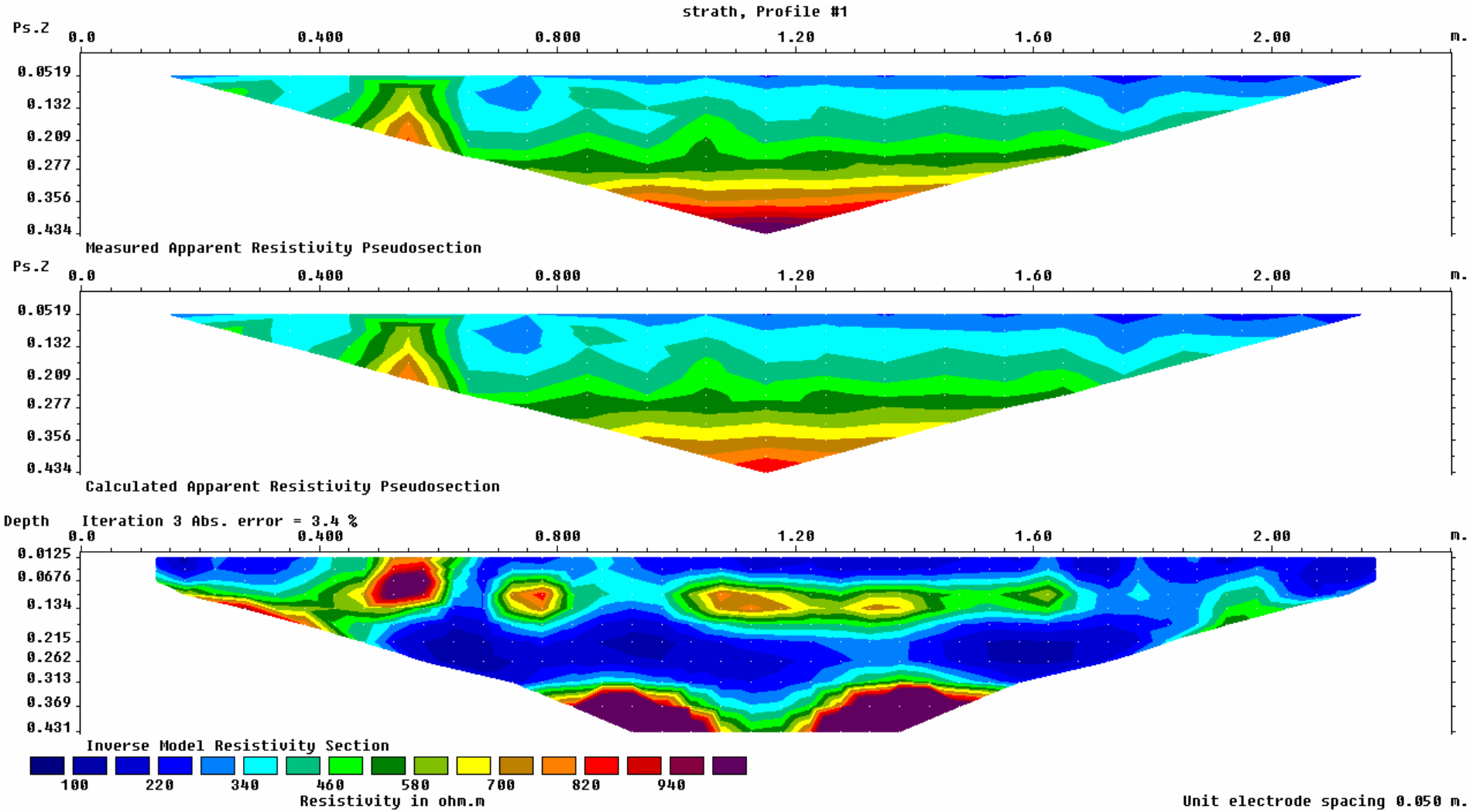

Electrical Resistivity Survey Image "07_23" (23.07.07)

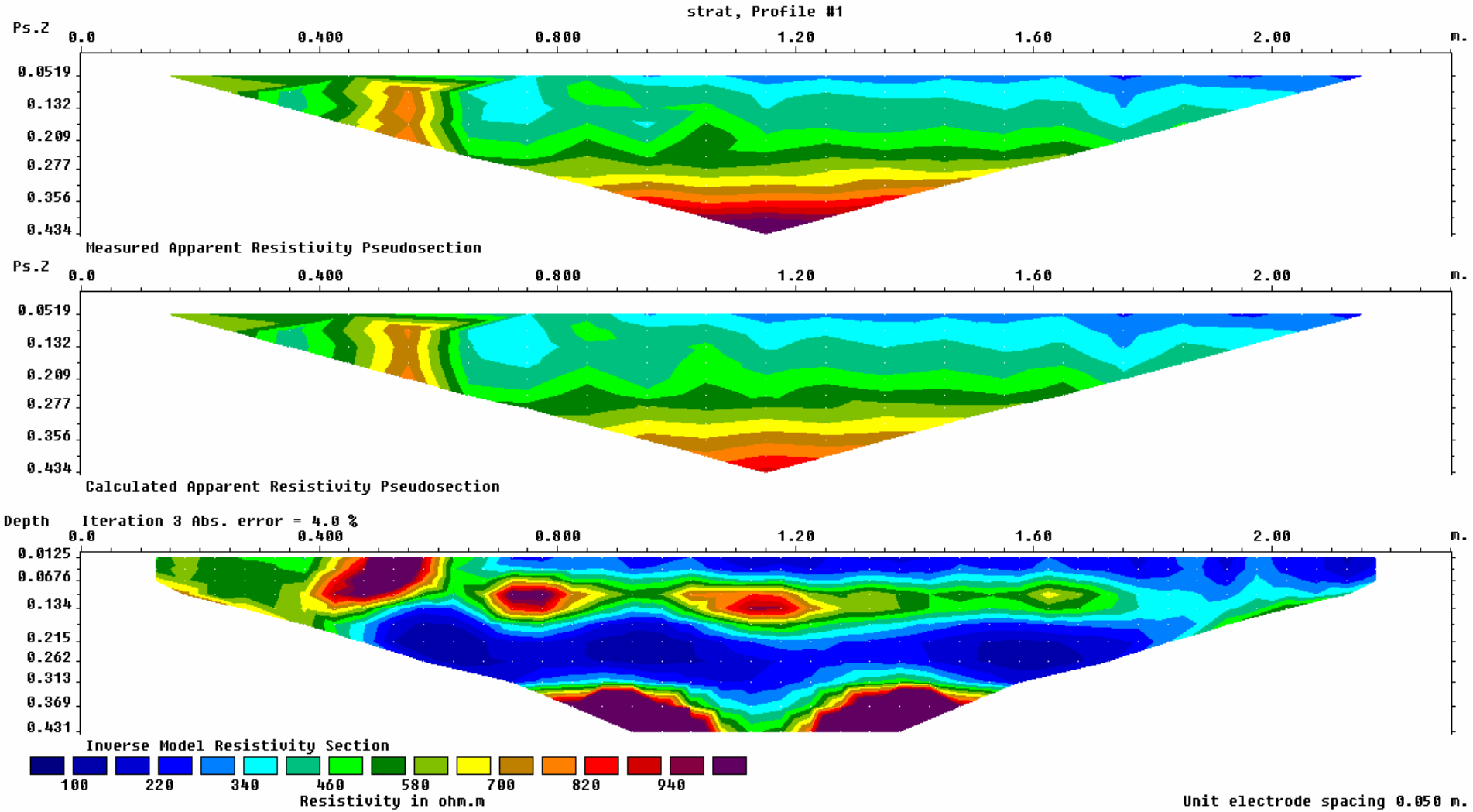

Electrical Resistivity Survey Image "07_24" (24.07.07)

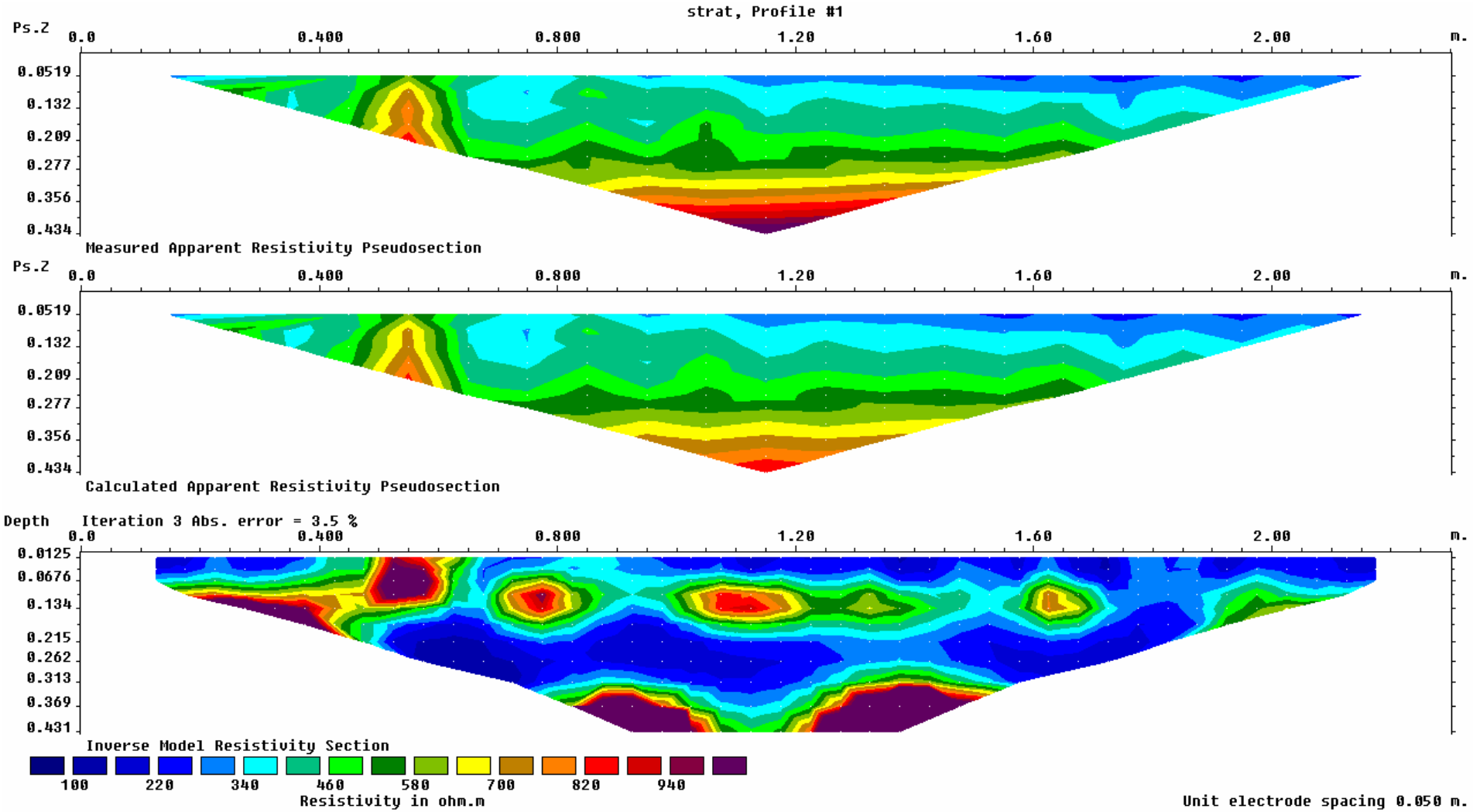

Electrical Resistivity Survey Image "07_25" (25.07.07)

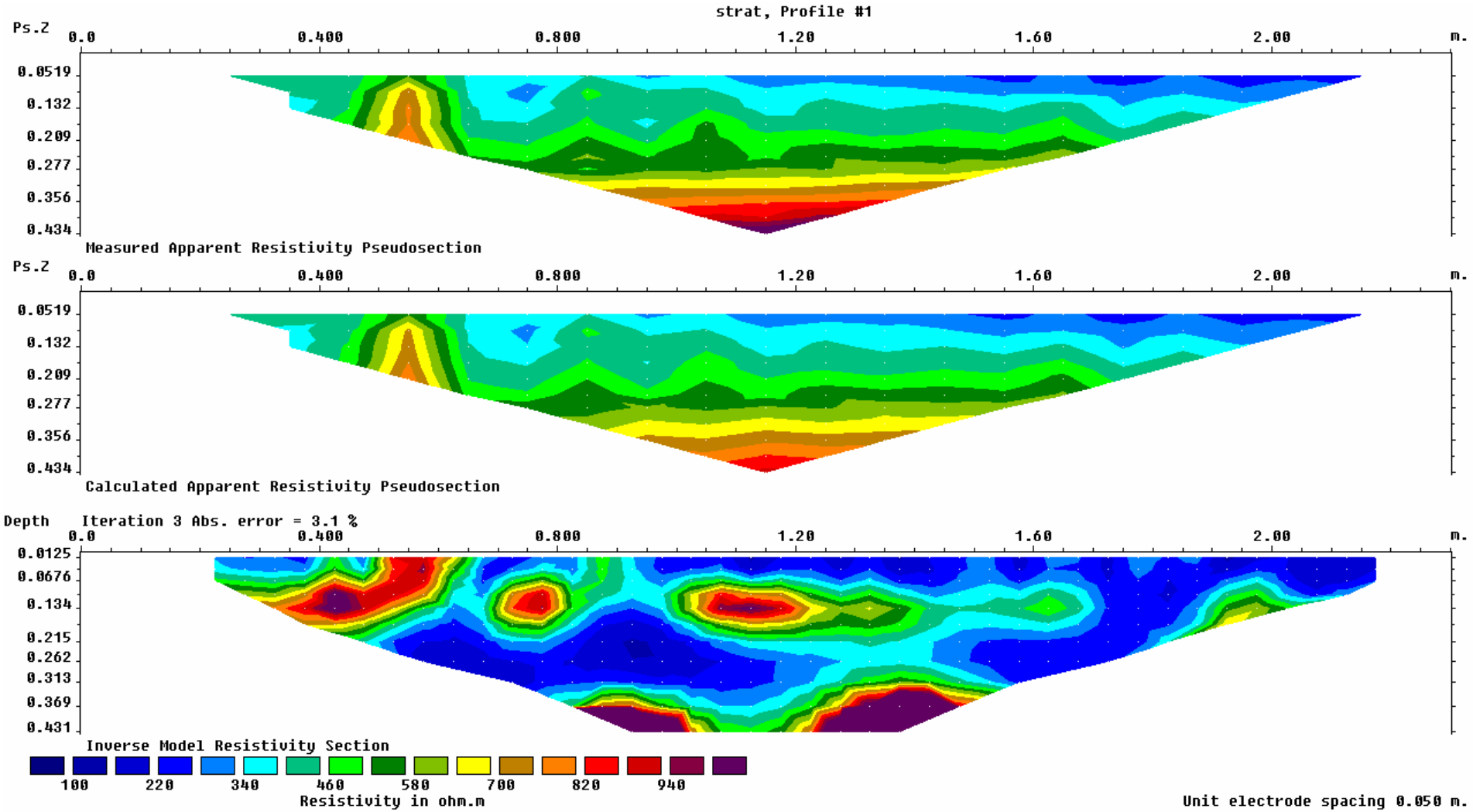

Electrical Resistivity Survey Image "07_26" (26.07.07)

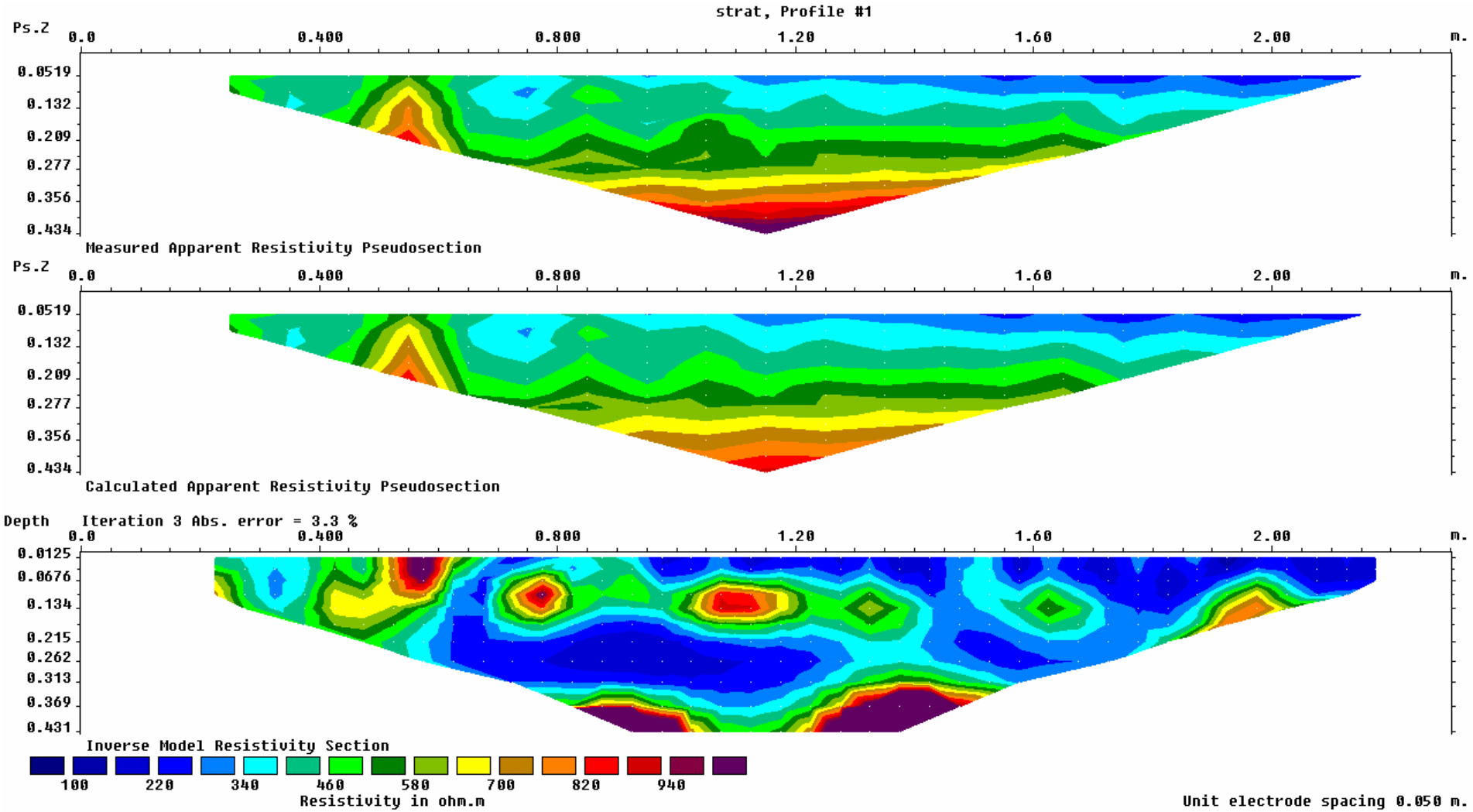

Electrical Resistivity Survey Image "07_27" (27.07.07)

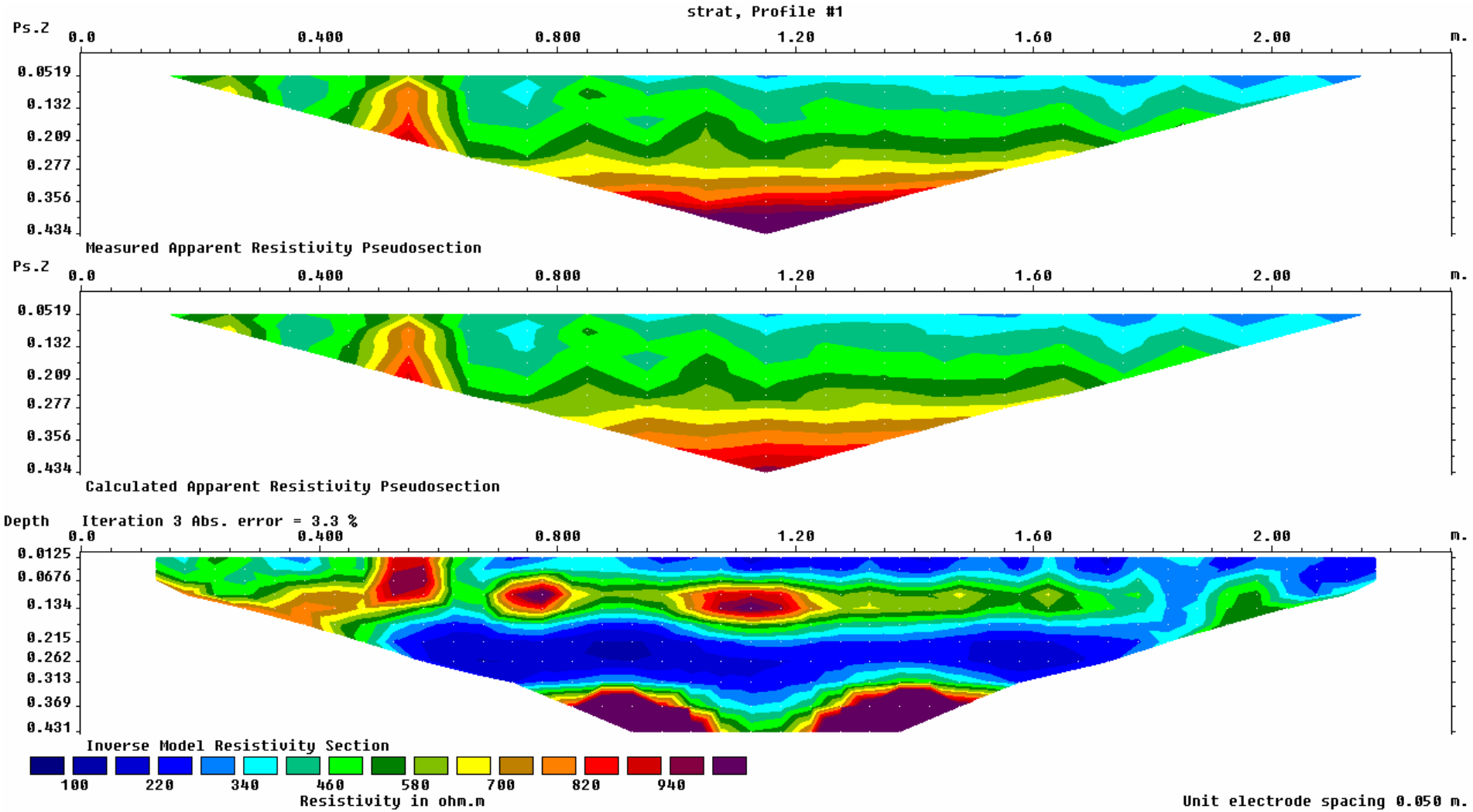

Electrical Resistivity Survey Image "07_30" (30.07.07)

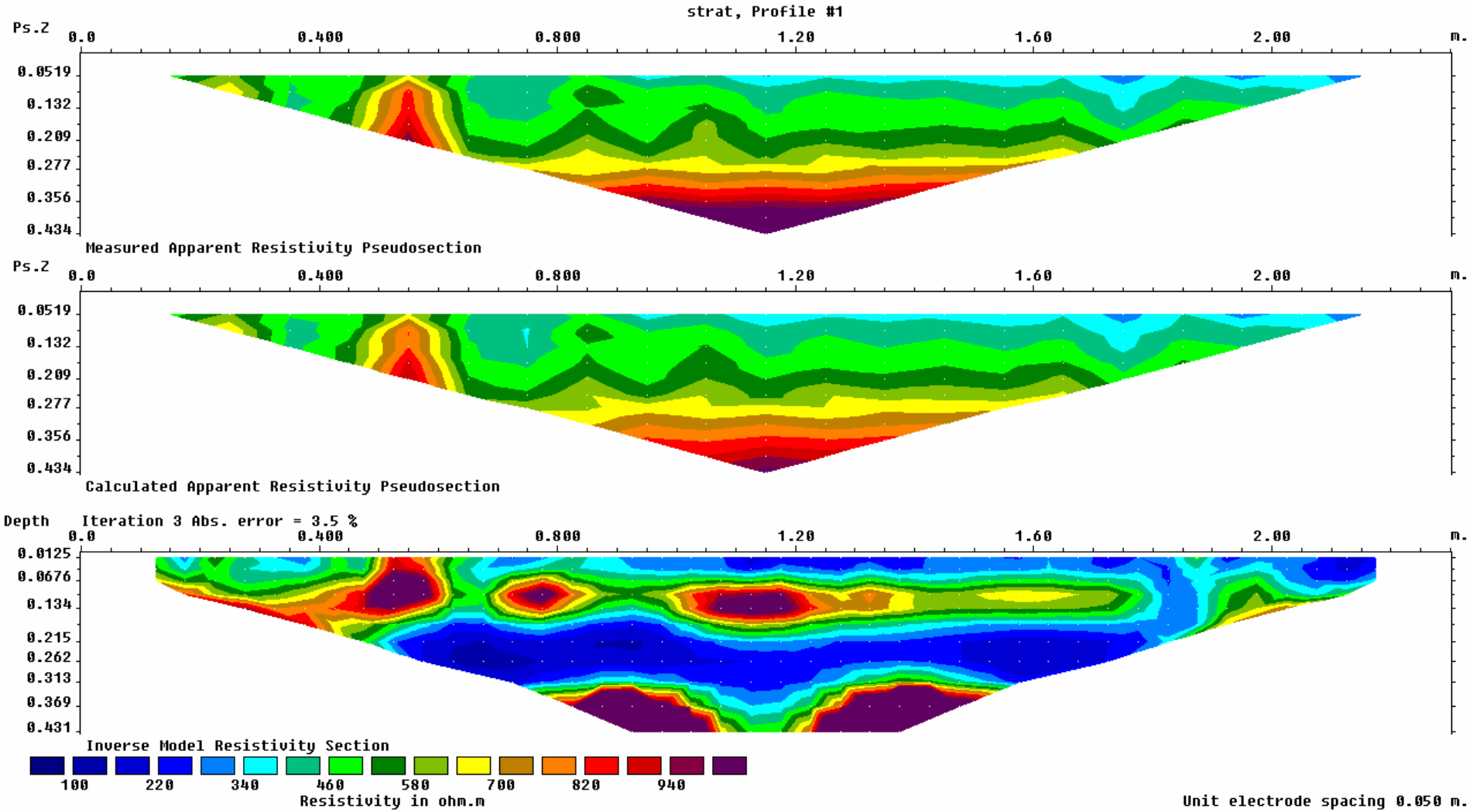

Electrical Resistivity Survey Image "07_31" (31.07.07)

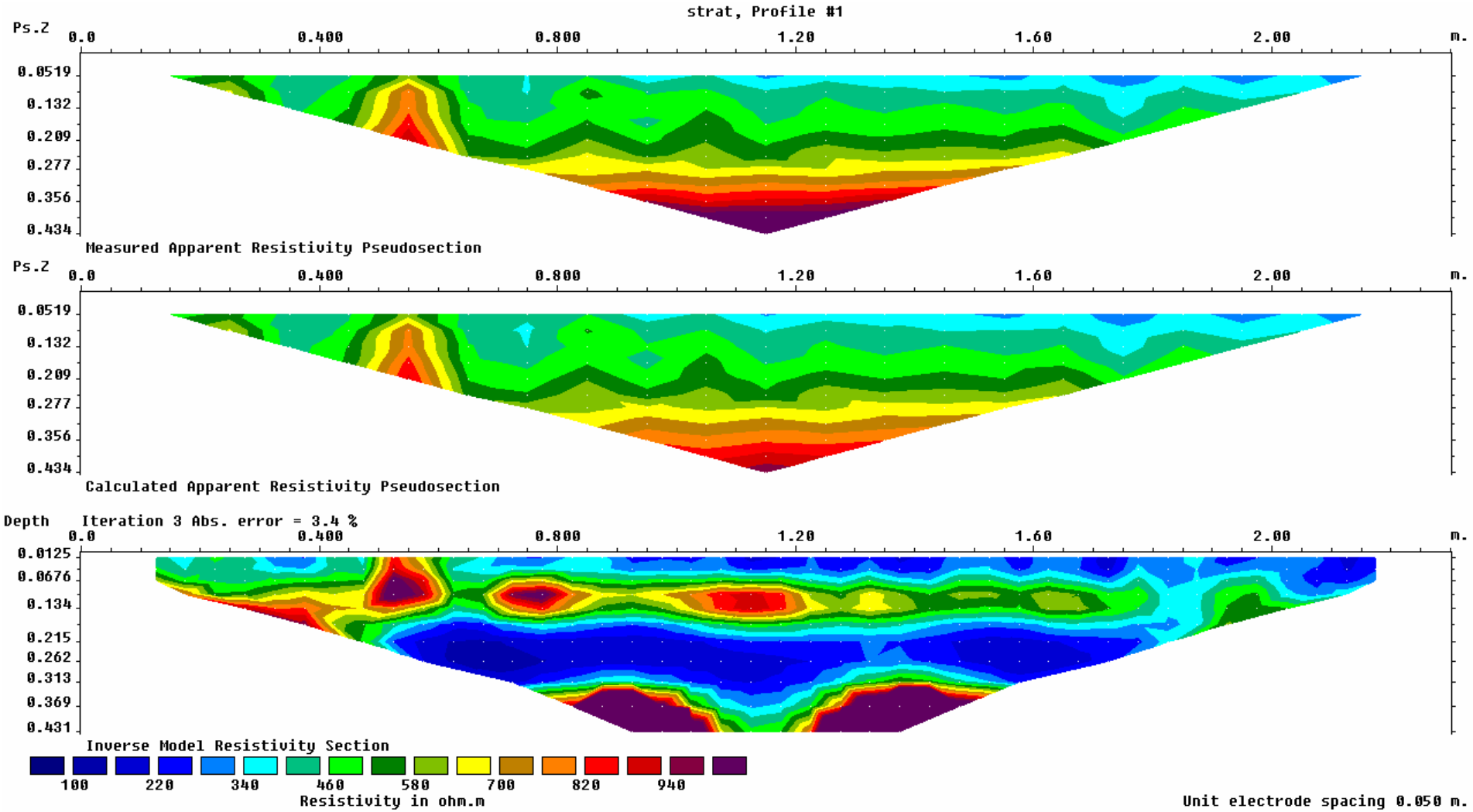

Electrical Resistivity Survey Image "08_01" (01.08.07)

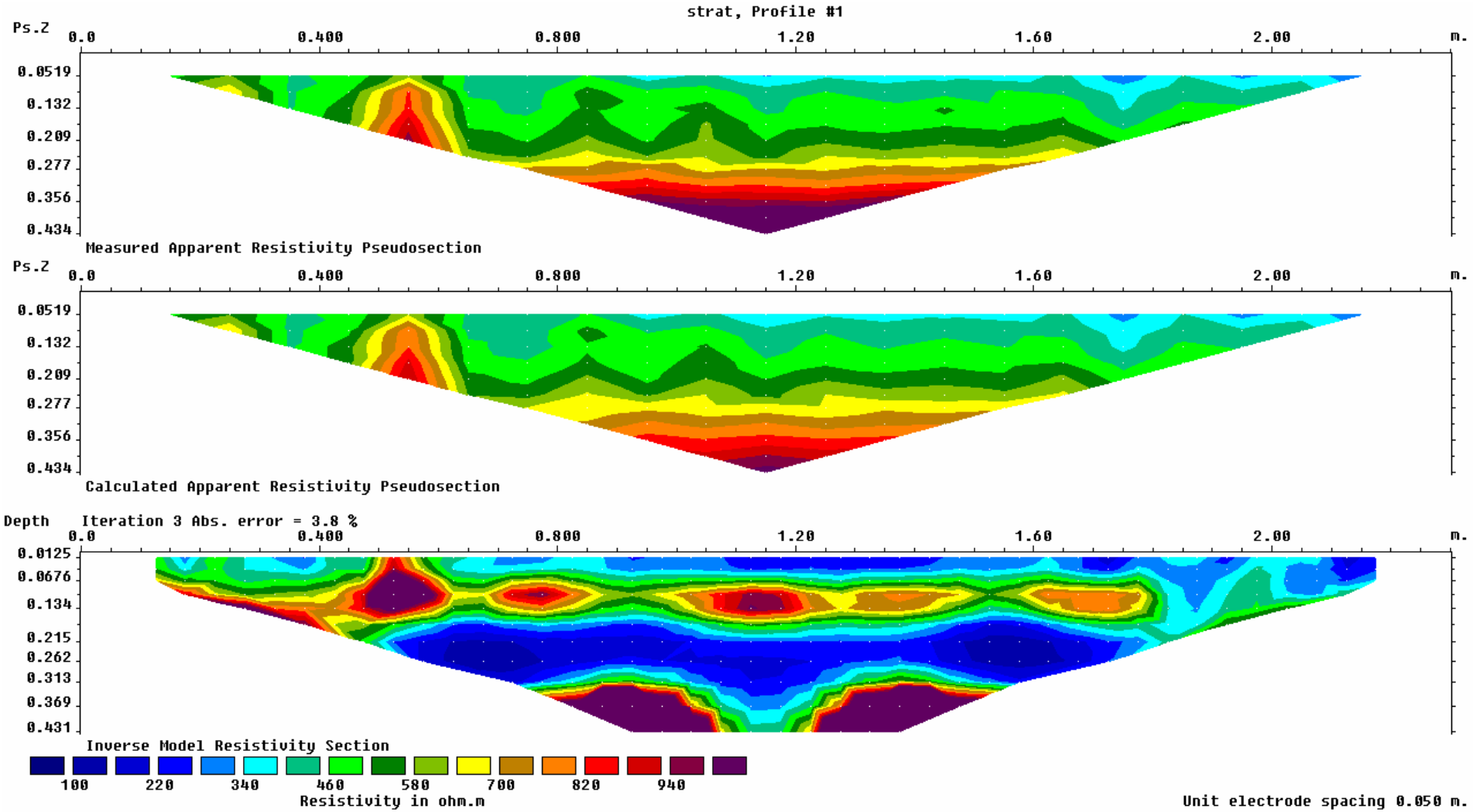

Electrical Resistivity Survey Image "08_02" (02.08.07)

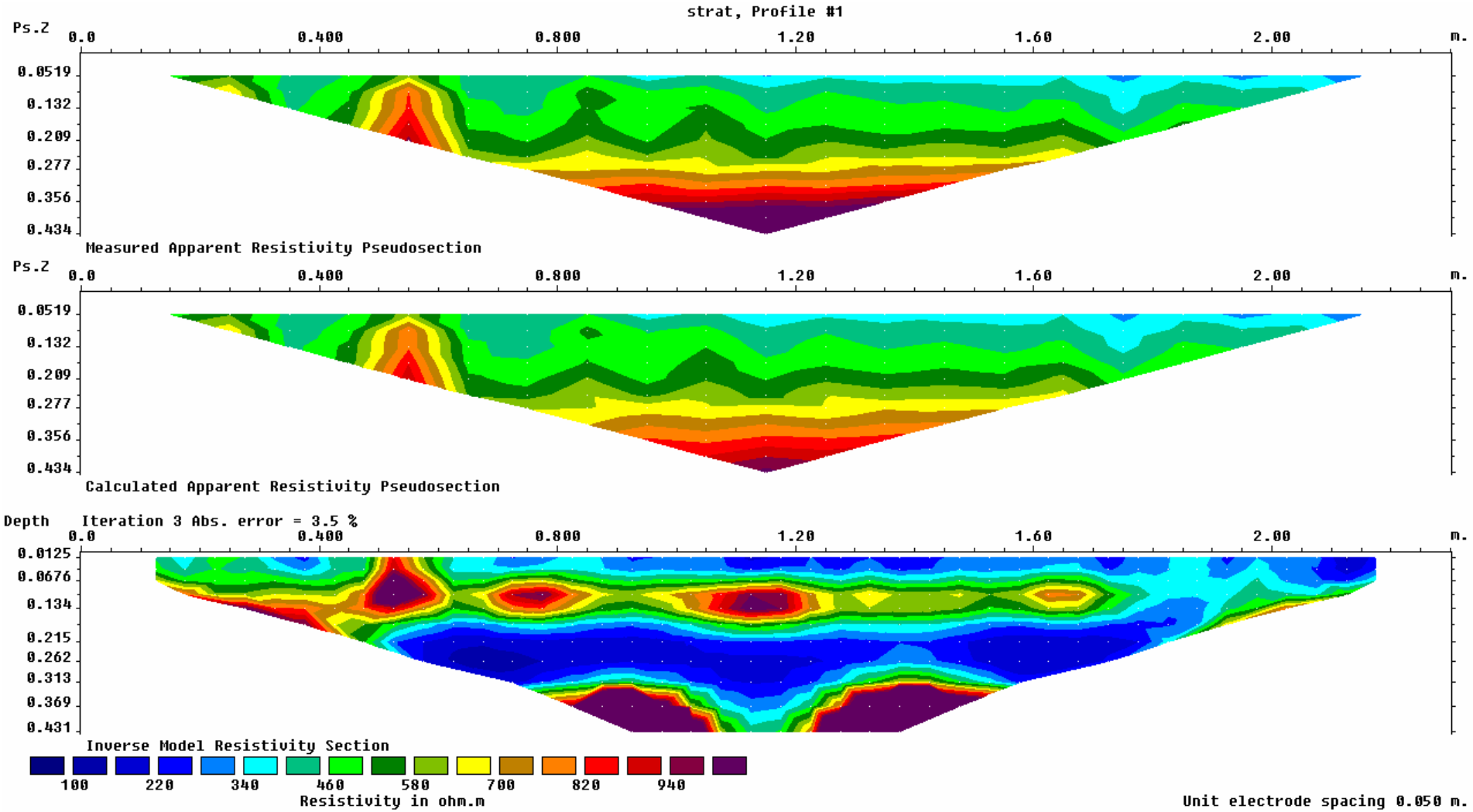

Electrical Resistivity Survey Image "08_03" (03.08.07)

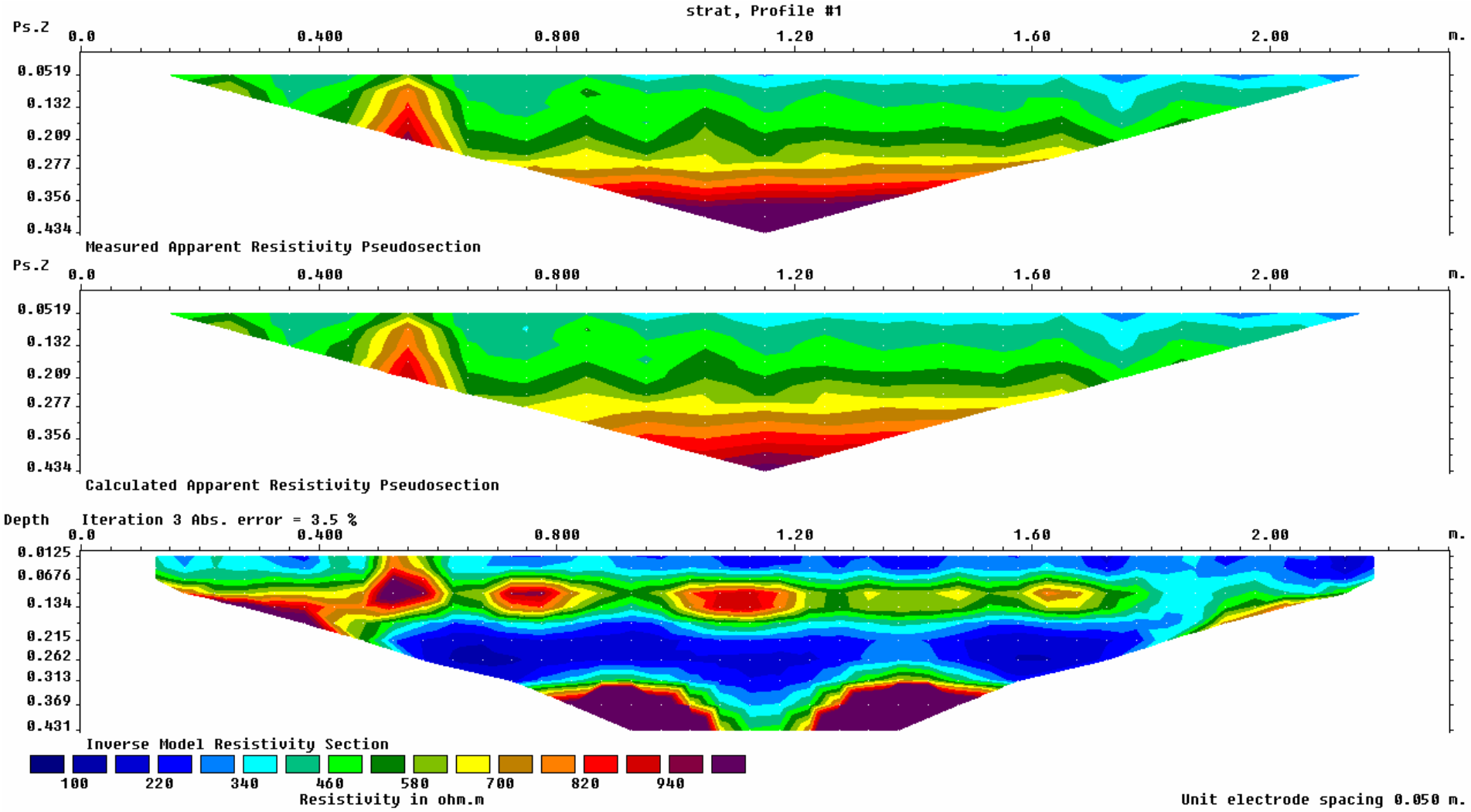

Electrical Resistivity Survey Image "08_06" (06.08.07)

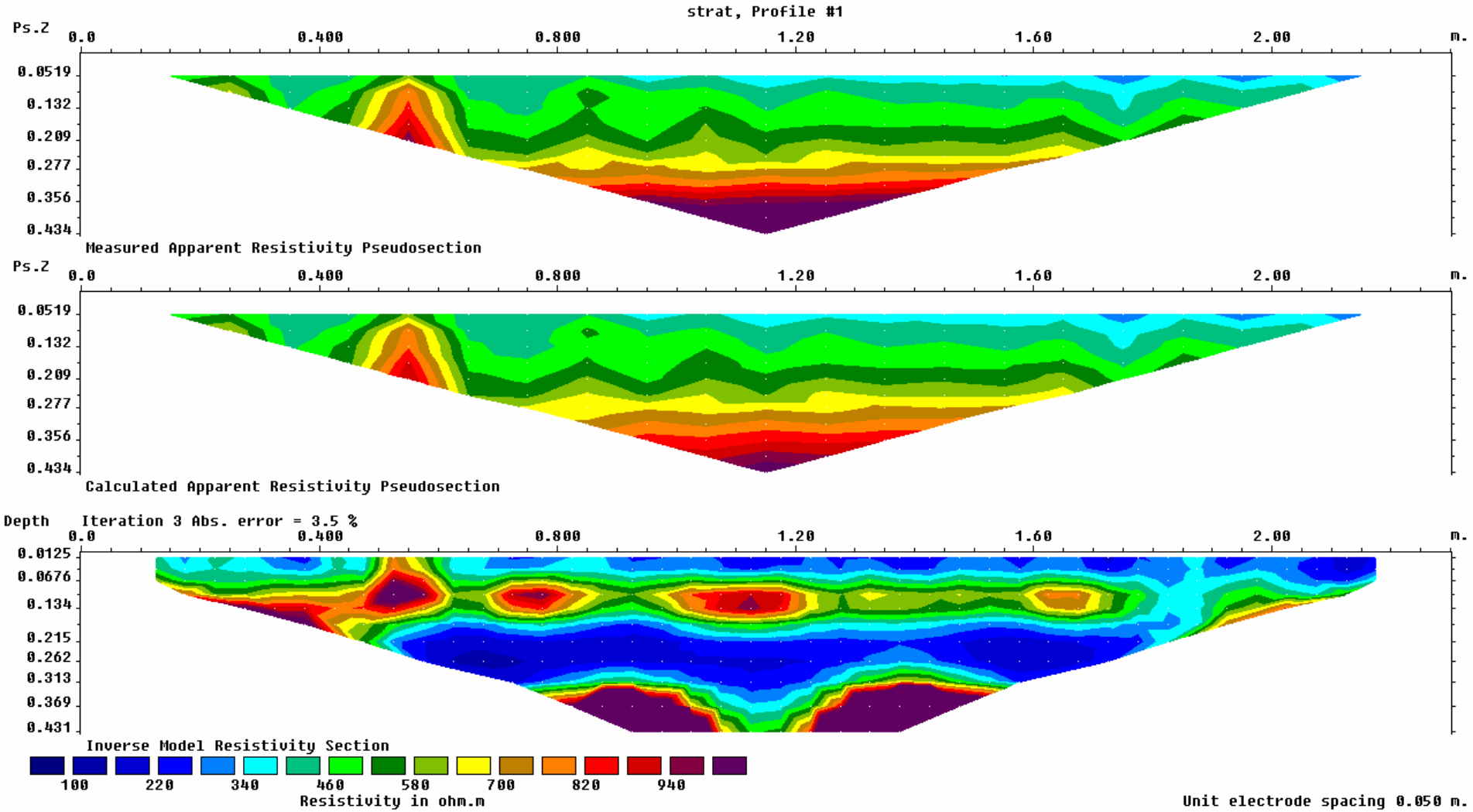

Electrical Resistivity Survey Image "08_07" (07.08.07)

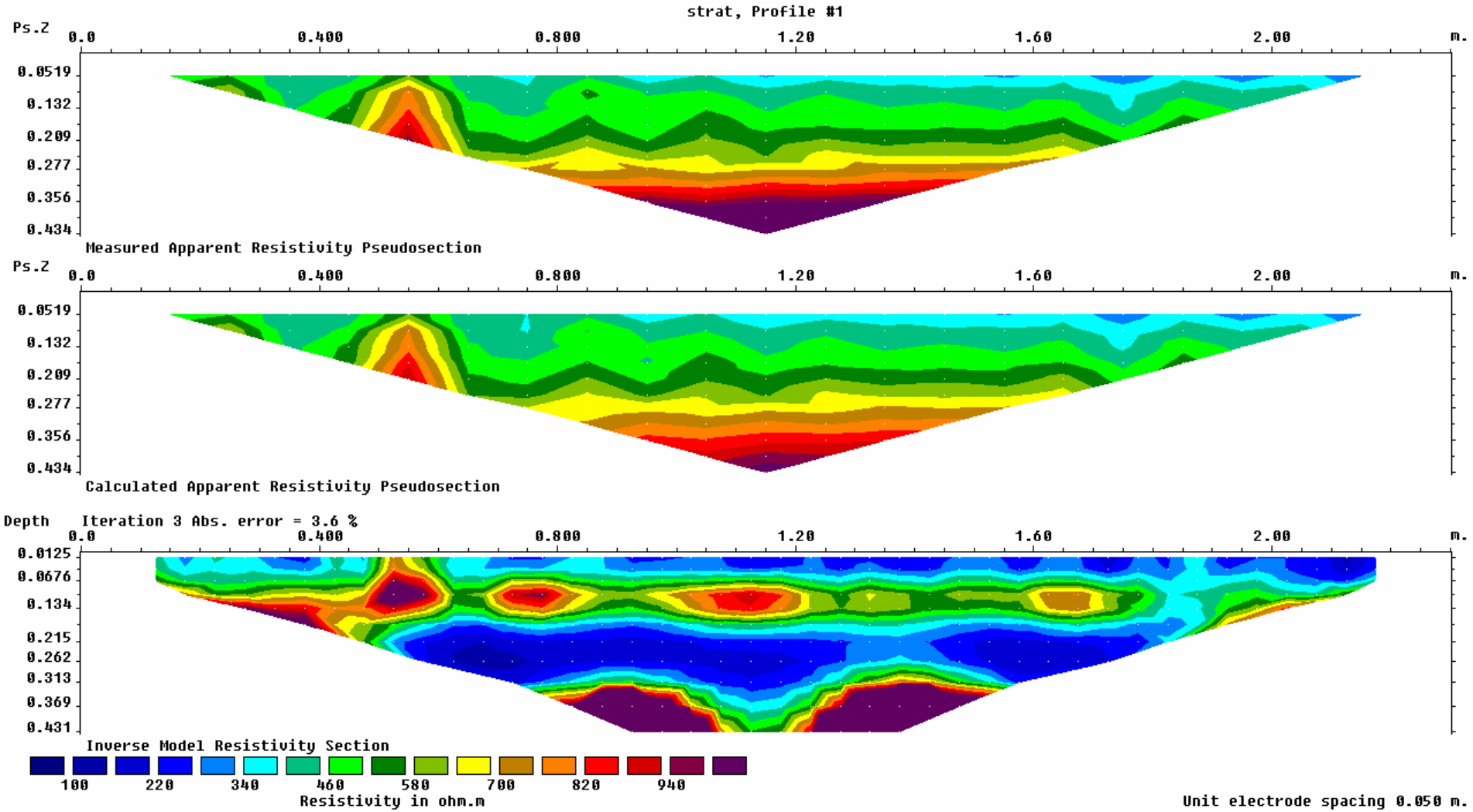

Electrical Resistivity Survey Image "08_08" (08.08.07)

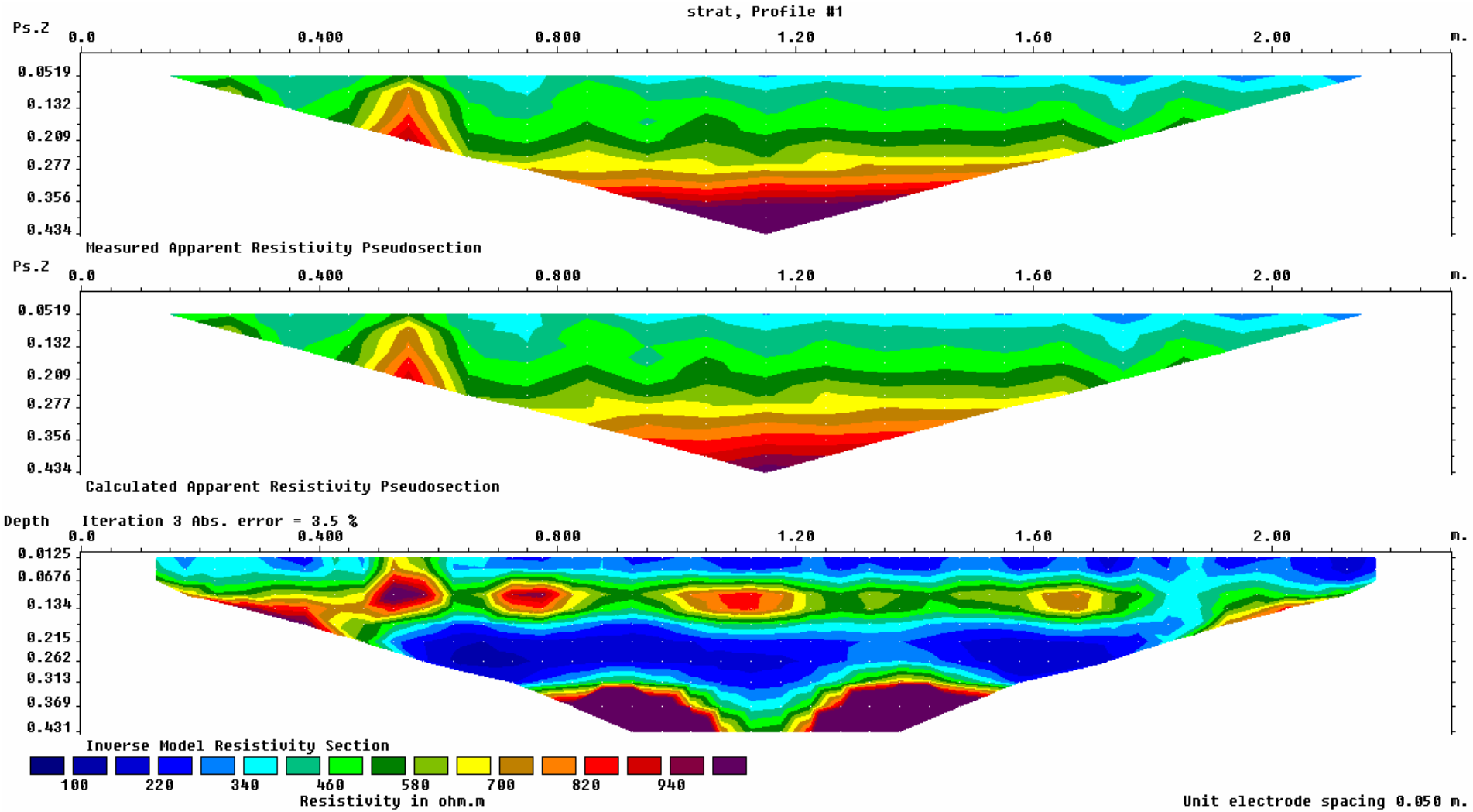

Electrical Resistivity Survey Image "08_09" (09.08.07)

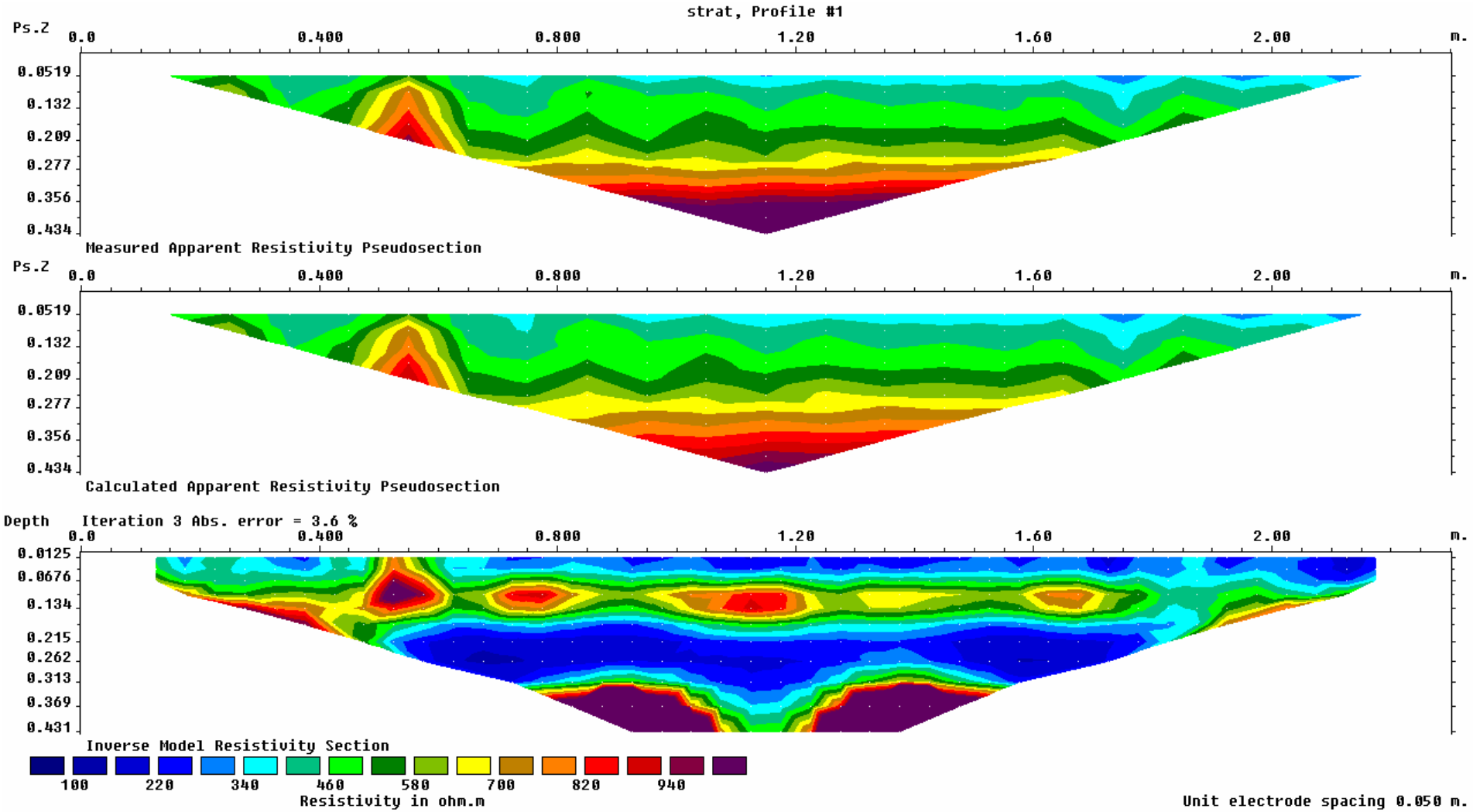

Electrical Resistivity Survey Image "08_10" (10.08.07)

Inverse Model Resistivity Section Images
Second Monitoring Campaign

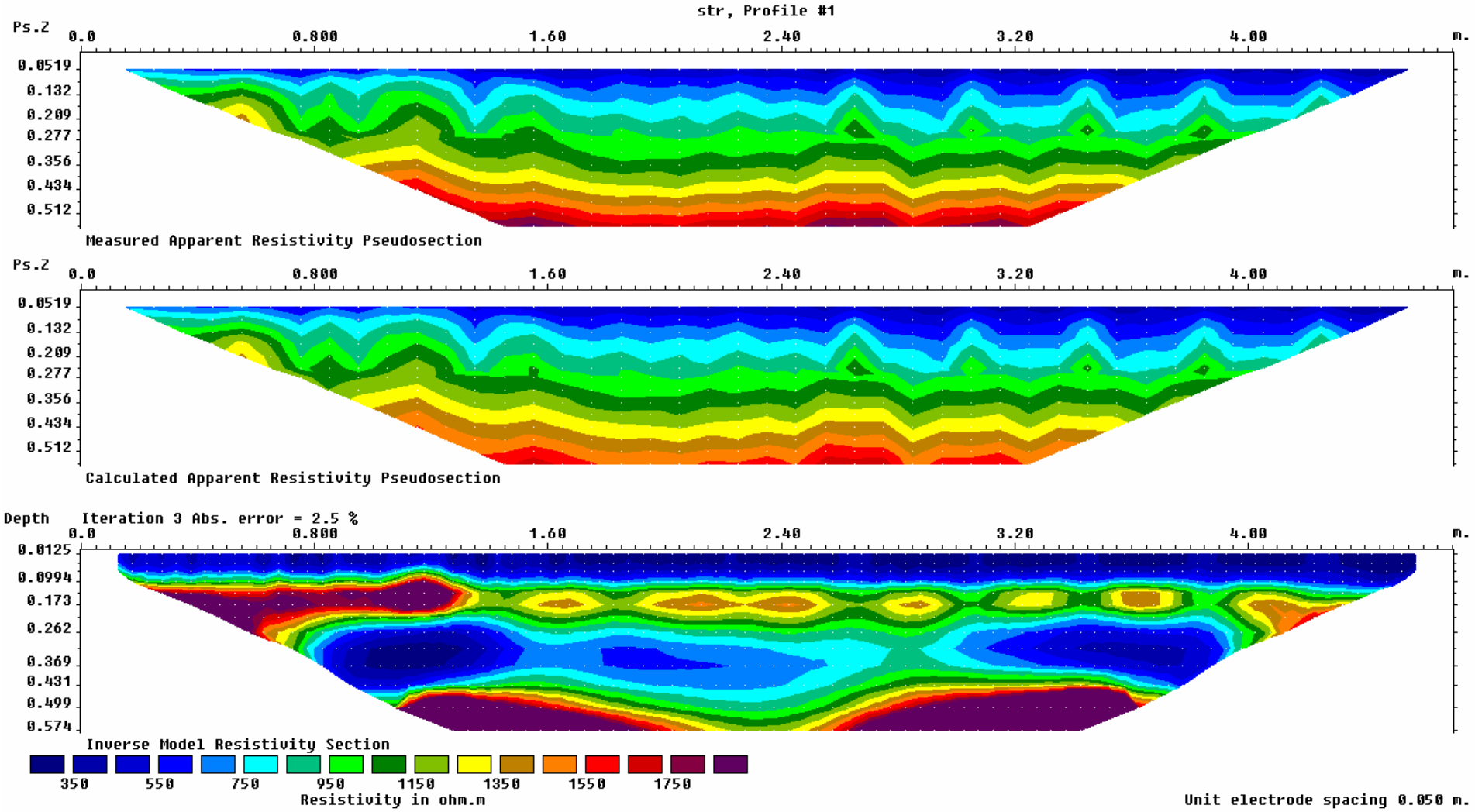

Electrical Resistivity Survey Image "01_11" (11.01.08)

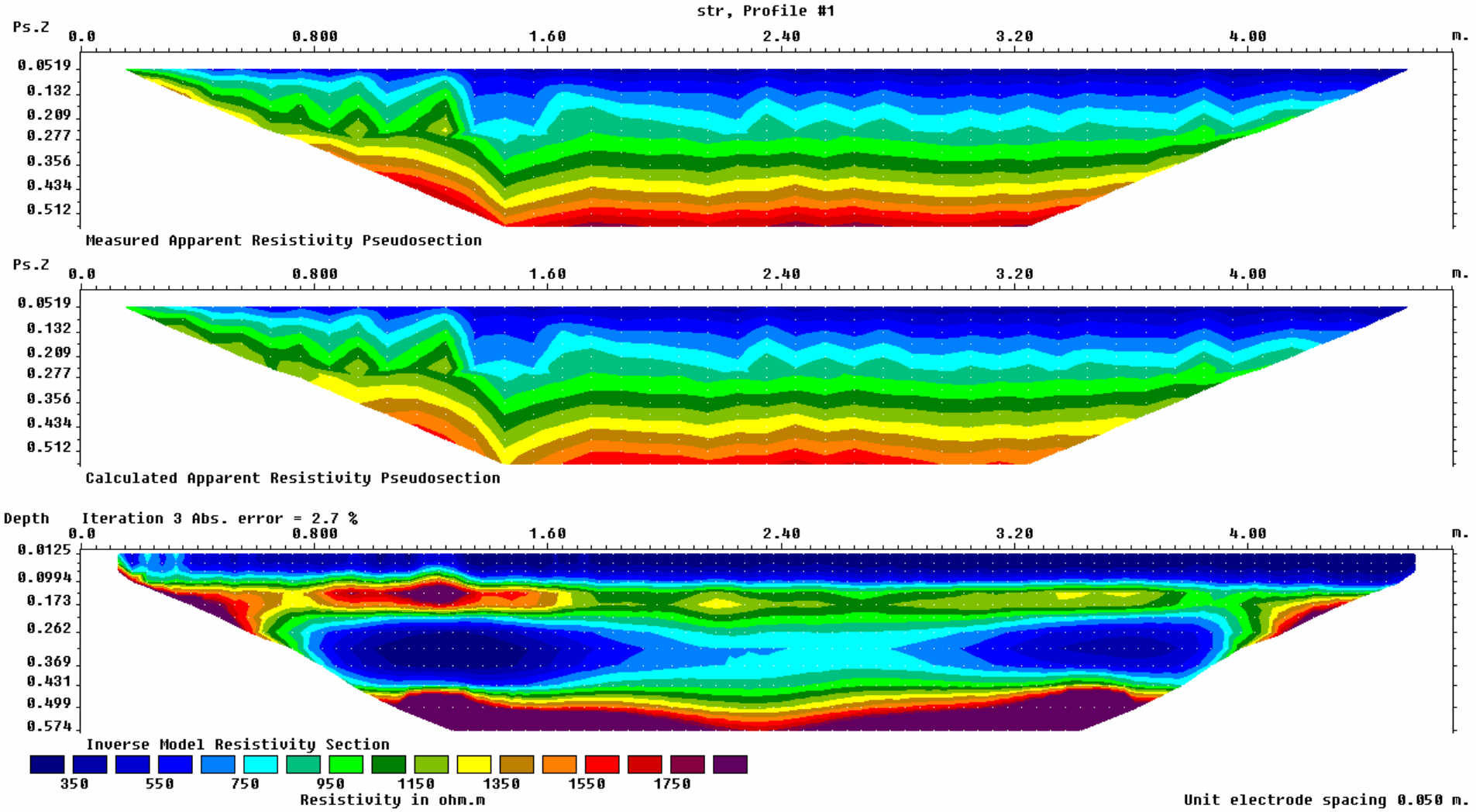

Electrical Resistivity Survey Image "01_18" (18.01.08)

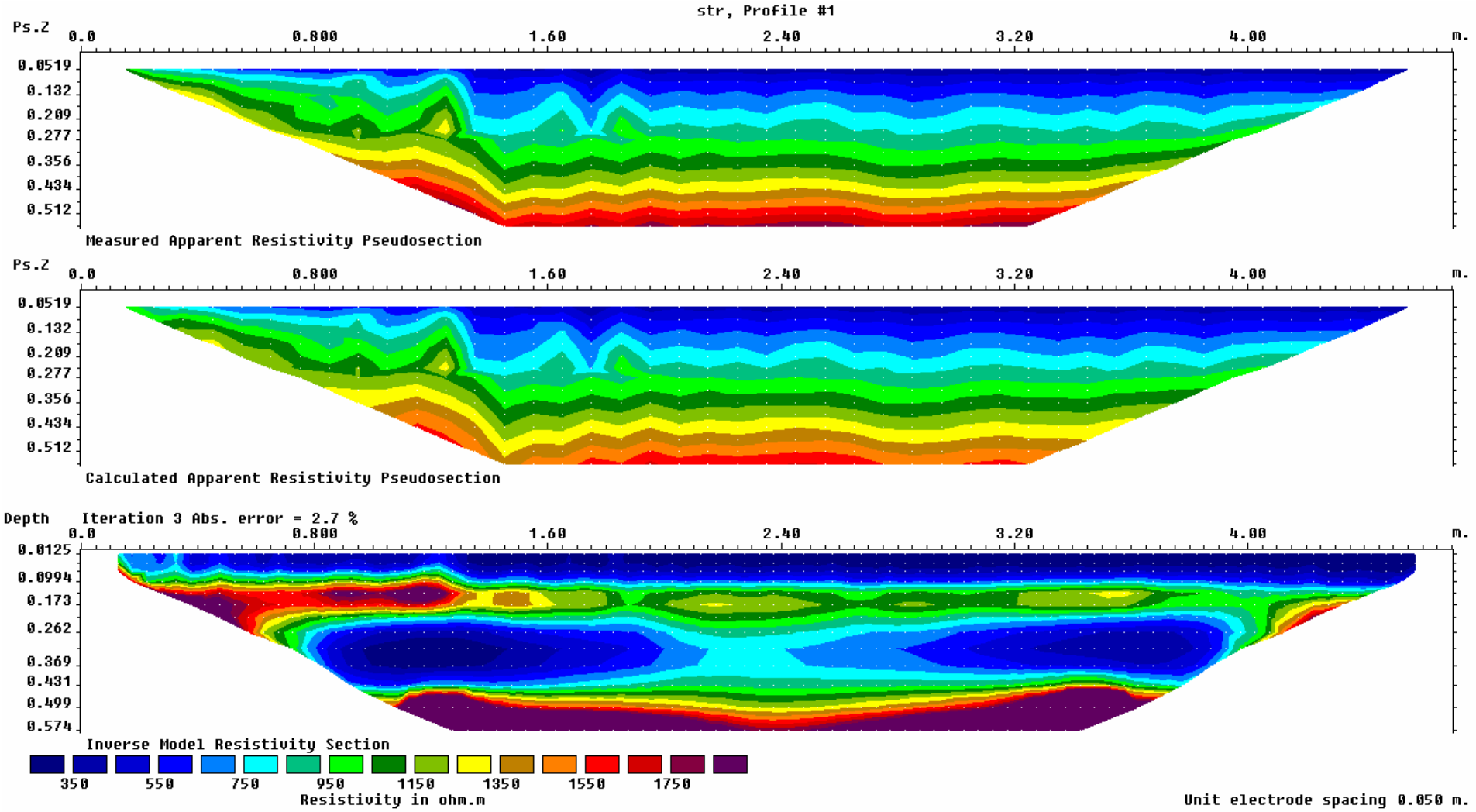

Electrical Resistivity Survey Image "01_25" (25.01.08)

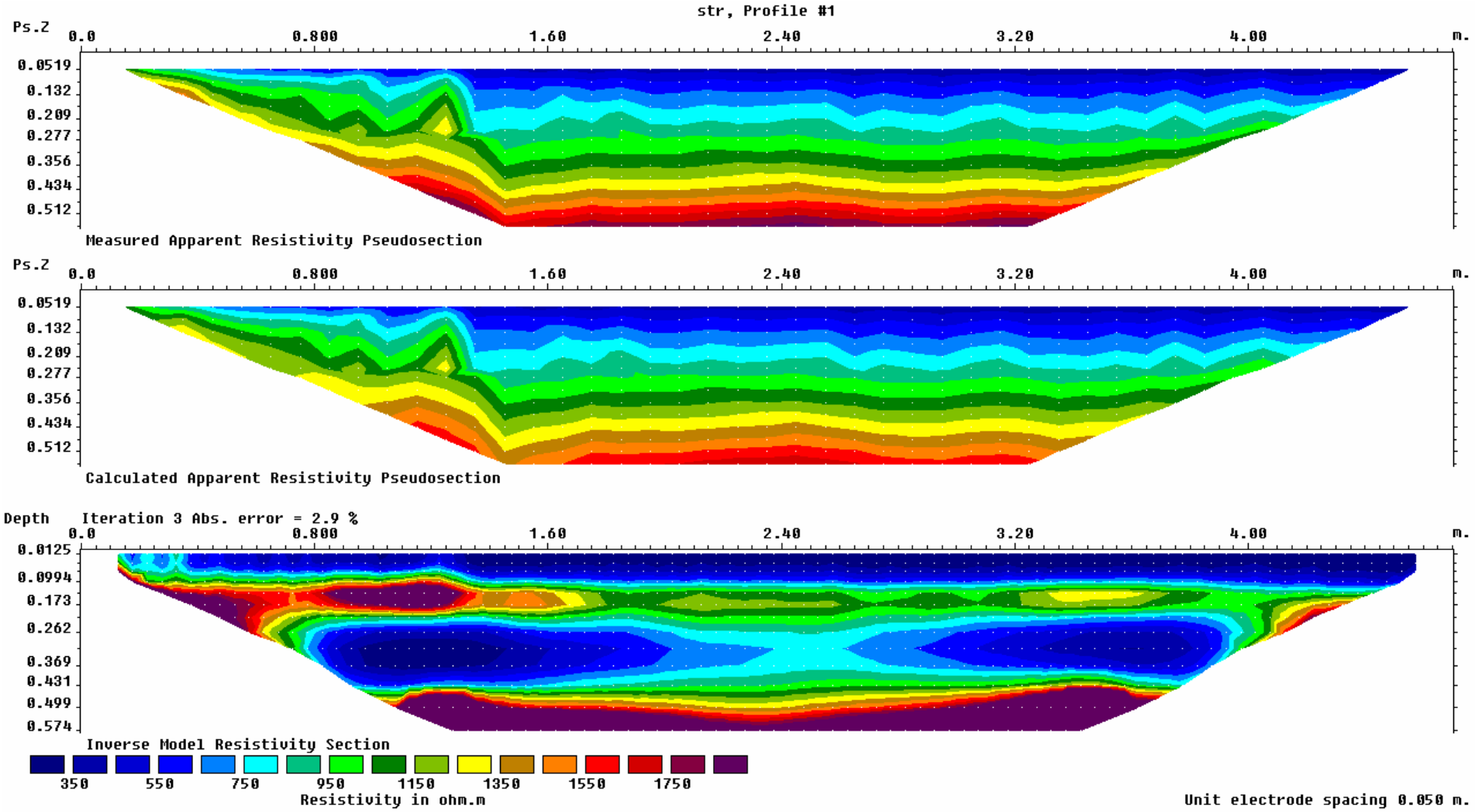

Electrical Resistivity Survey Image "02_01" (01.02.08)

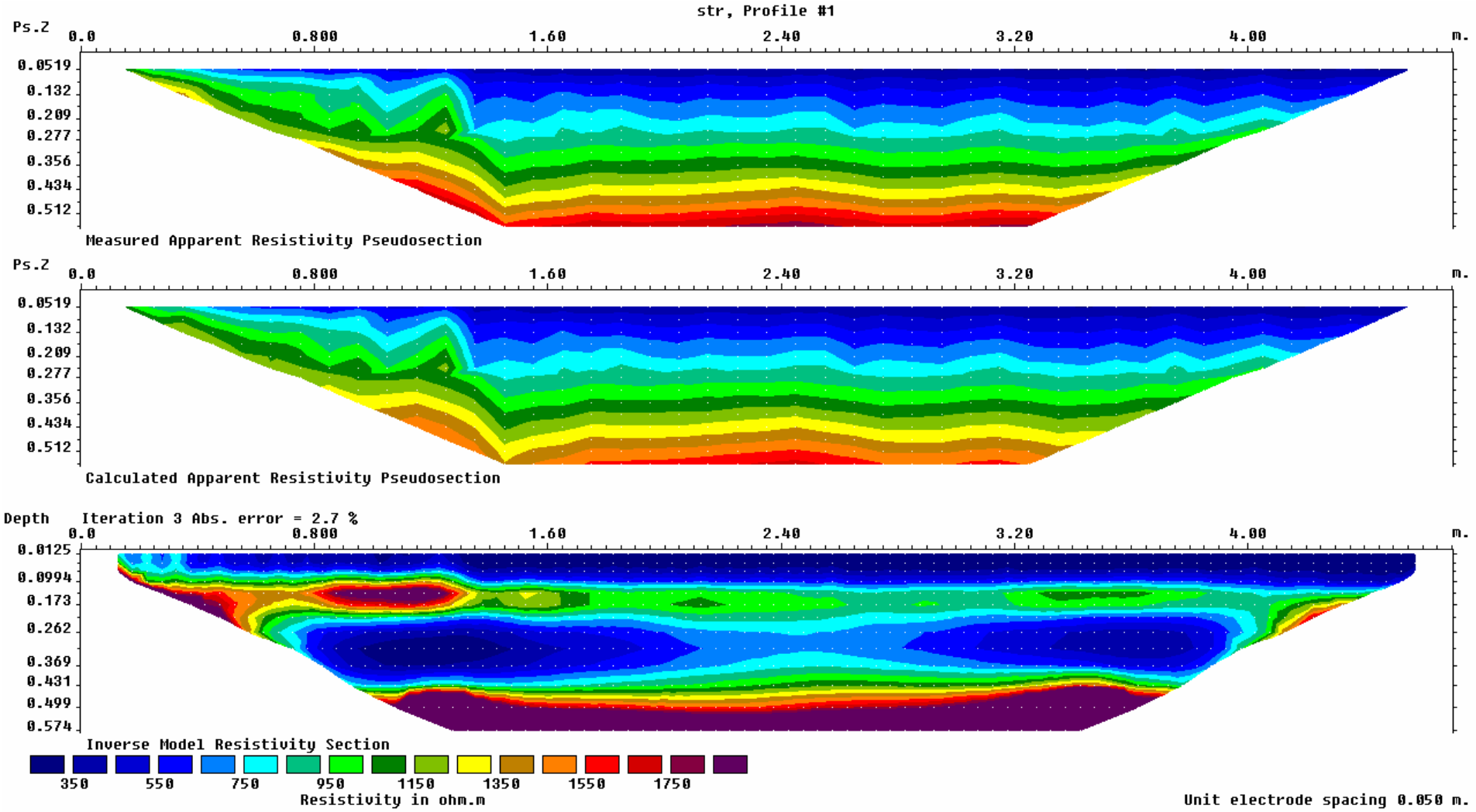

Electrical Resistivity Survey Image "02_08" (08.02.08)

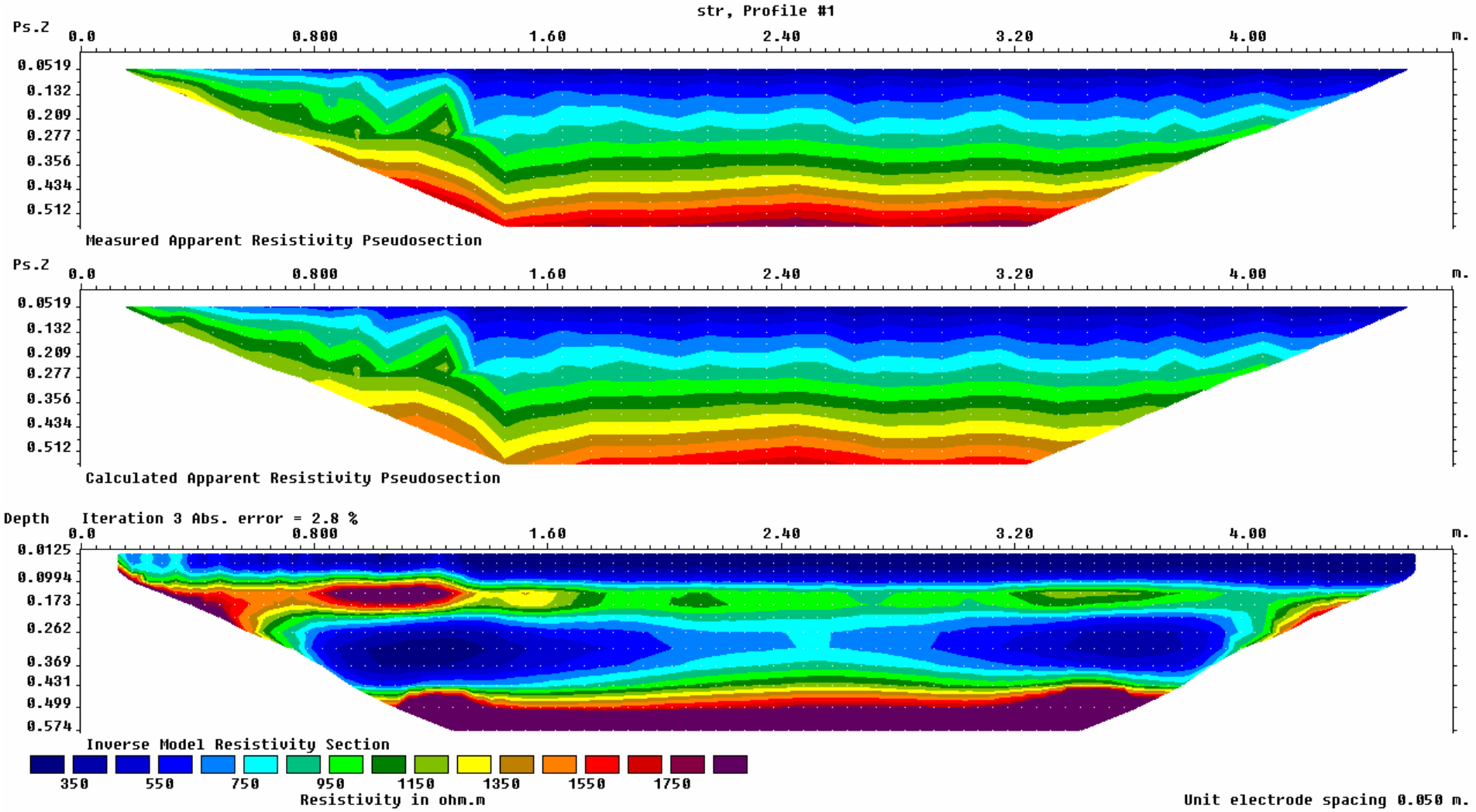

Electrical Resistivity Survey Image "02_15" (15.02.08)

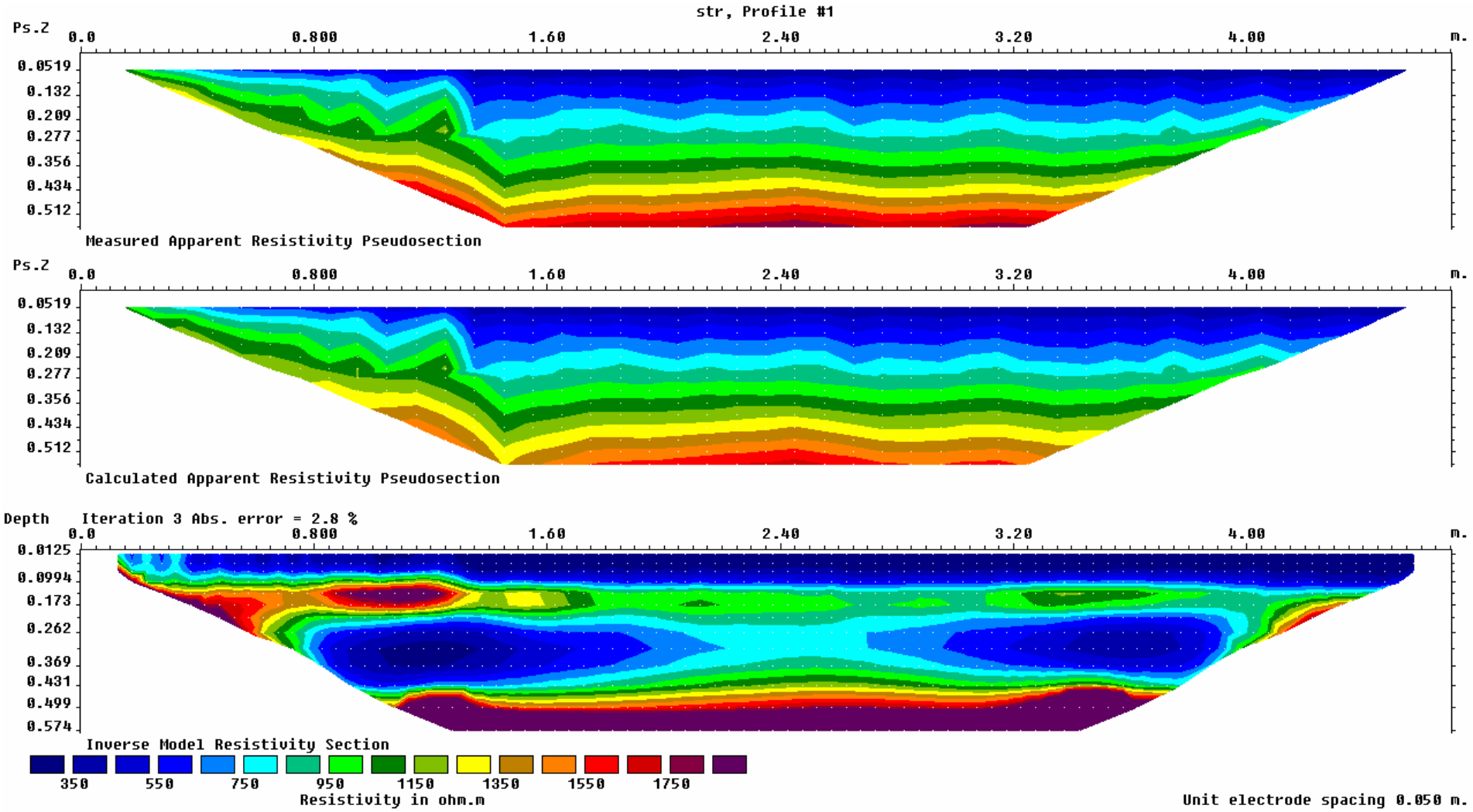

Electrical Resistivity Survey Image "02_22" (22.02.08)

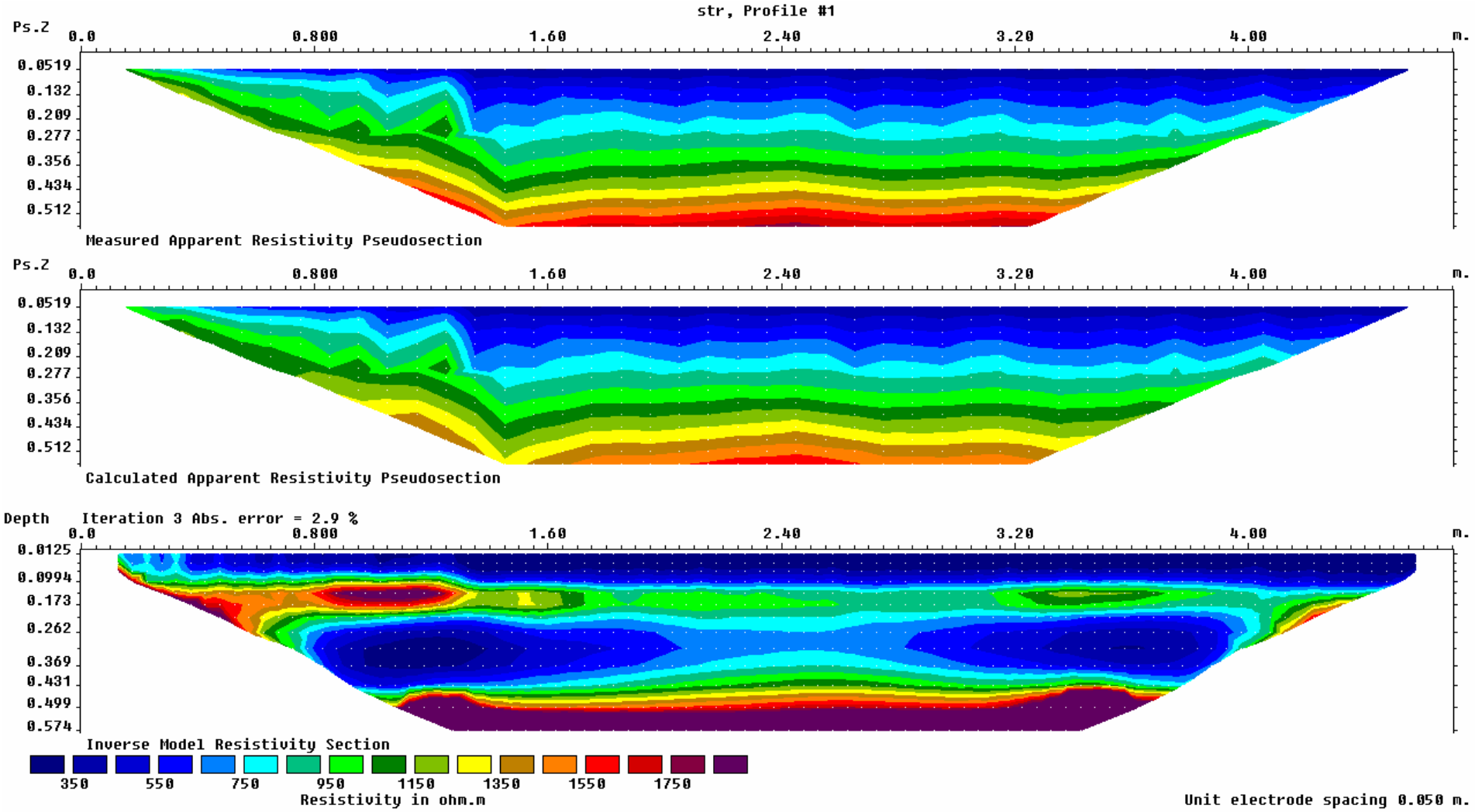

Electrical Resistivity Survey Image "02_29" (29.02.08)

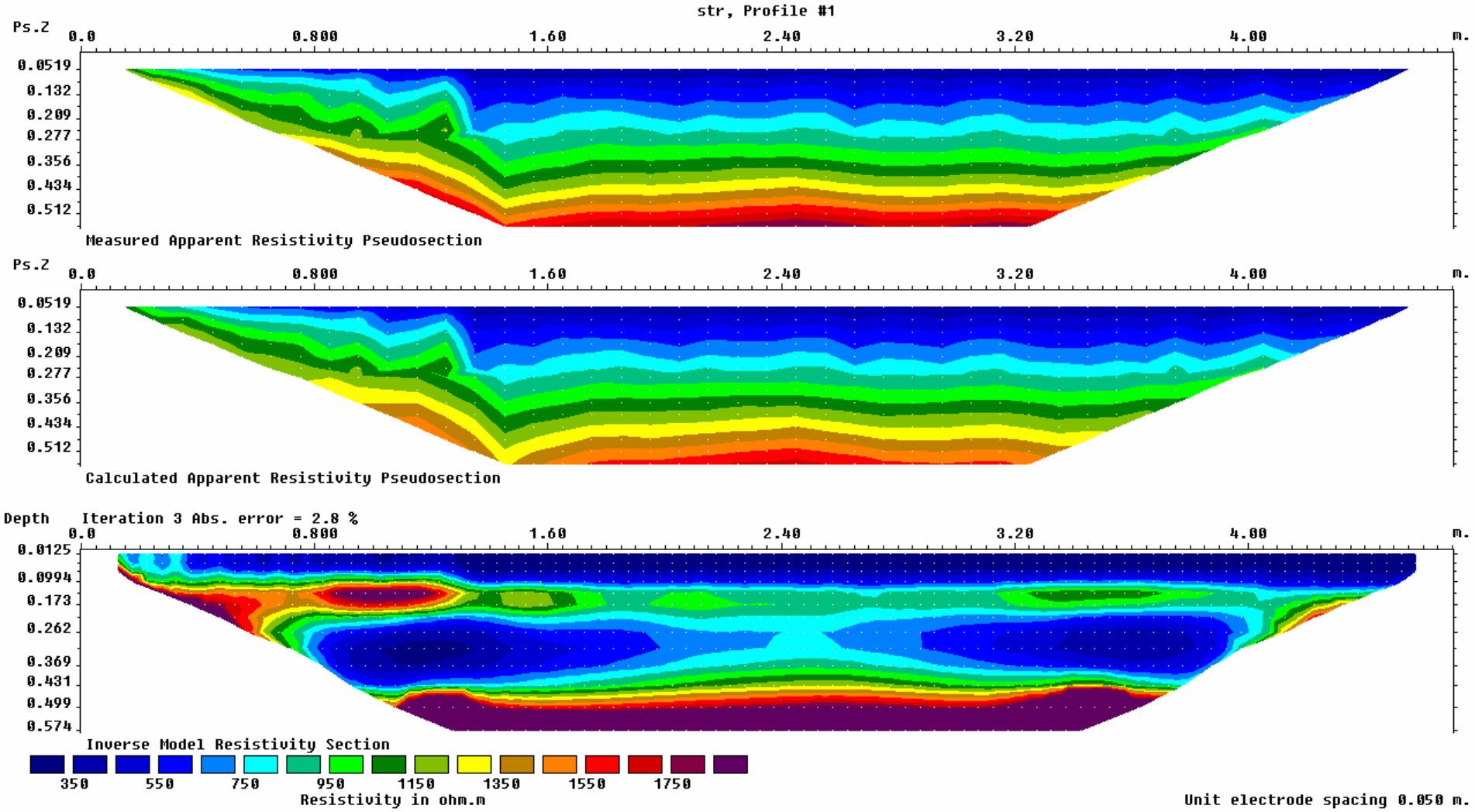

Electrical Resistivity Survey Image "03_07" (07.03.08)

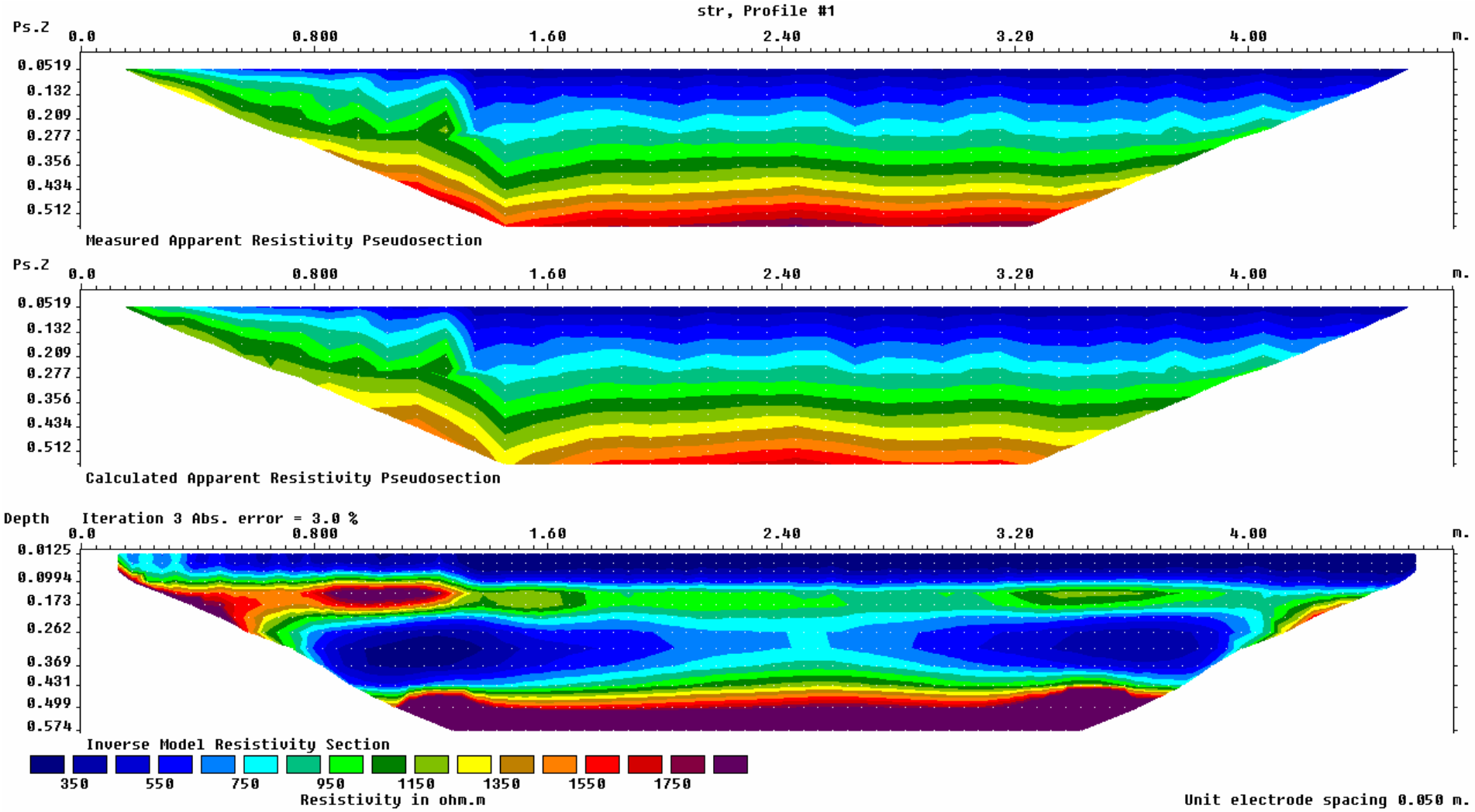

Electrical Resistivity Survey Image "03_17" (17.03.08)

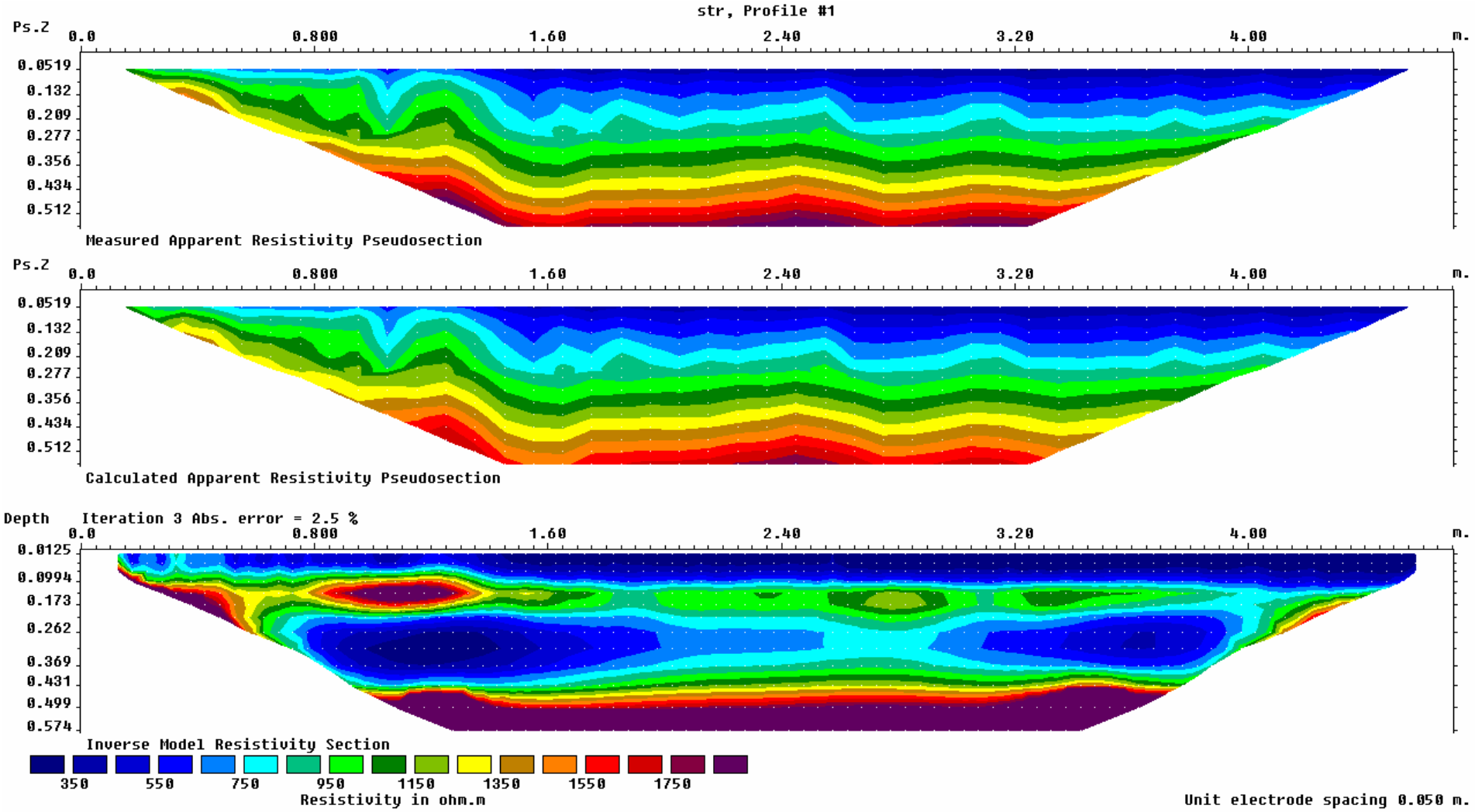

Electrical Resistivity Survey Image "03_28" (28.03.08)

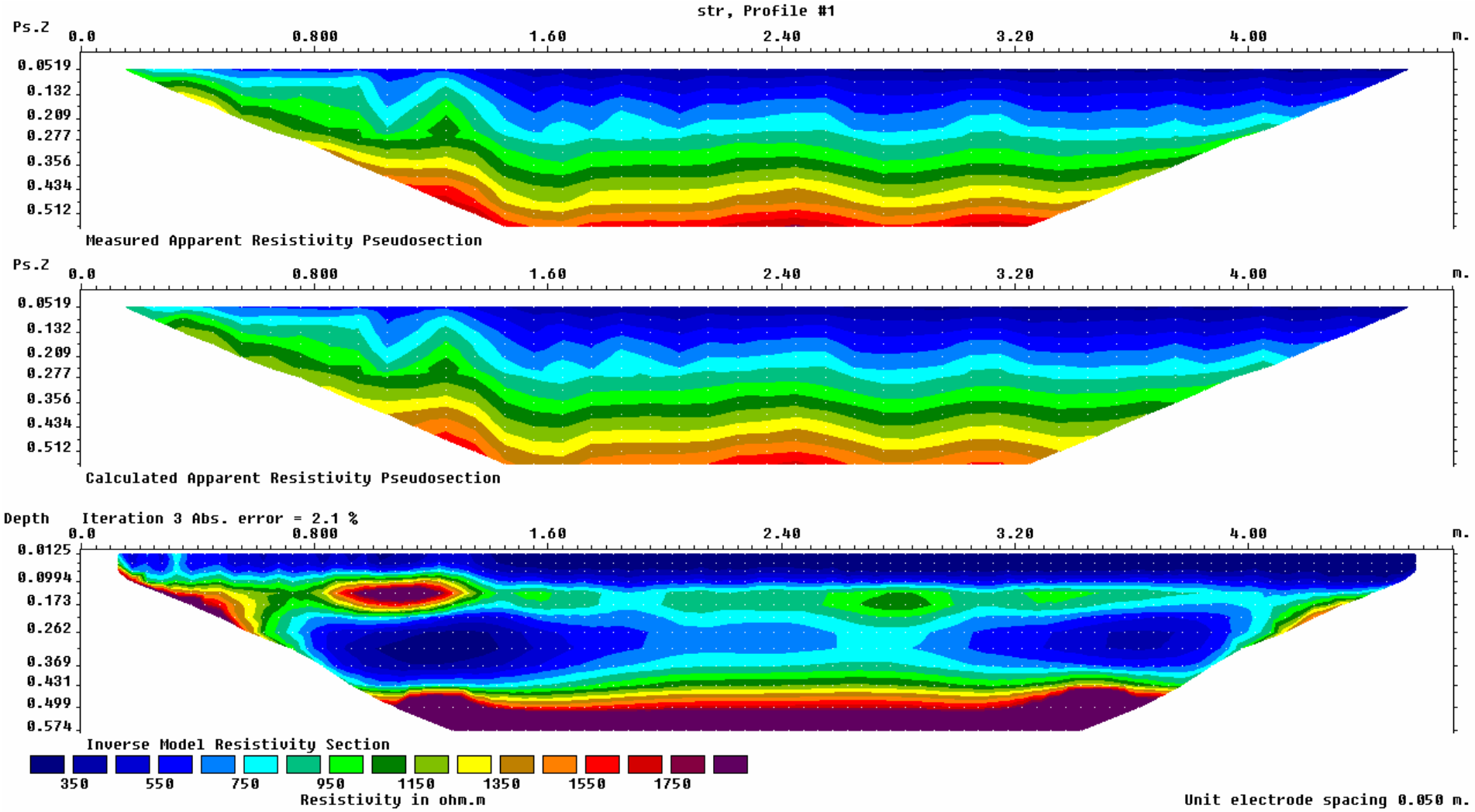

Electrical Resistivity Survey Image "04_04" (04.04.08)

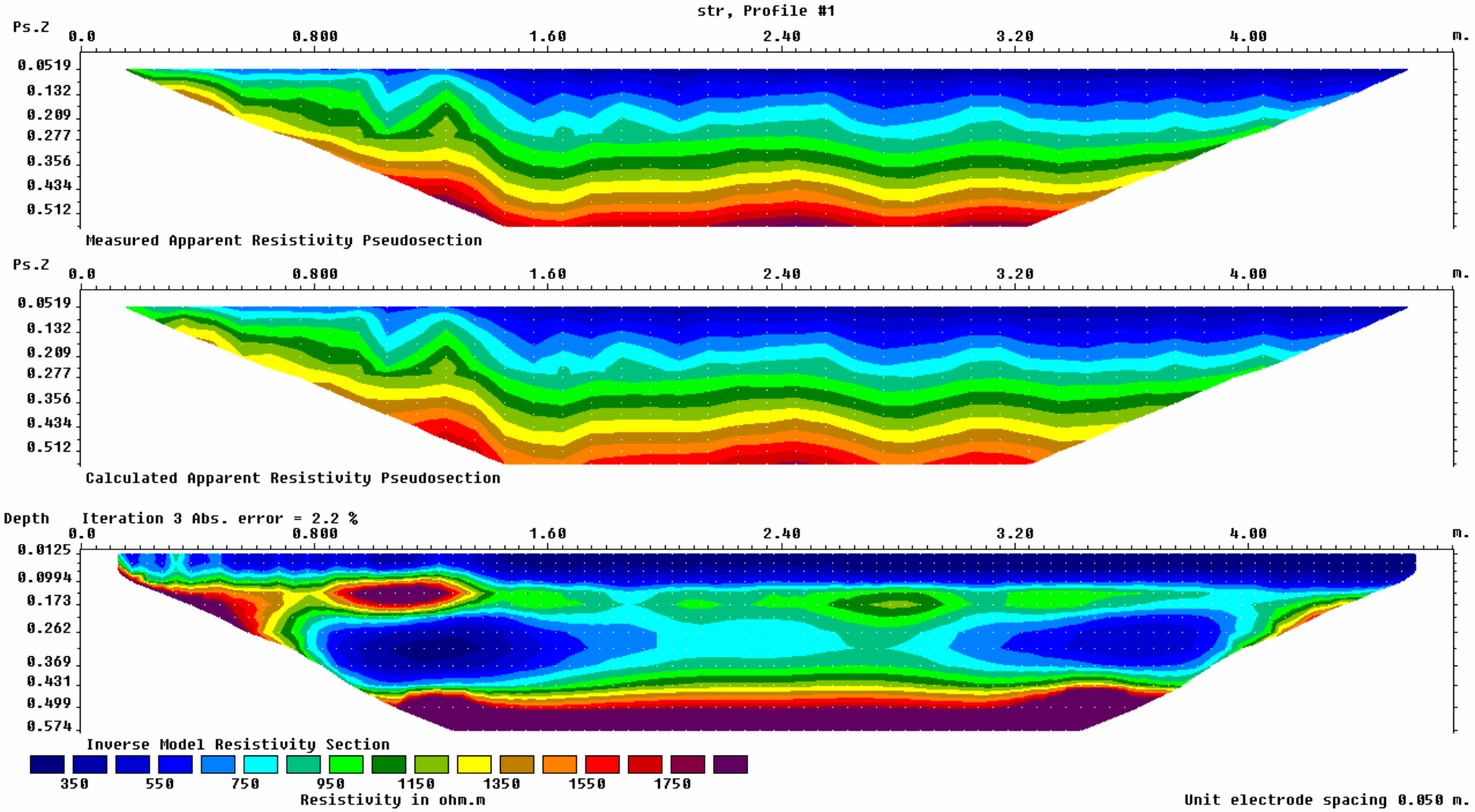

Electrical Resistivity Survey Image "04_11" (11.04.08)

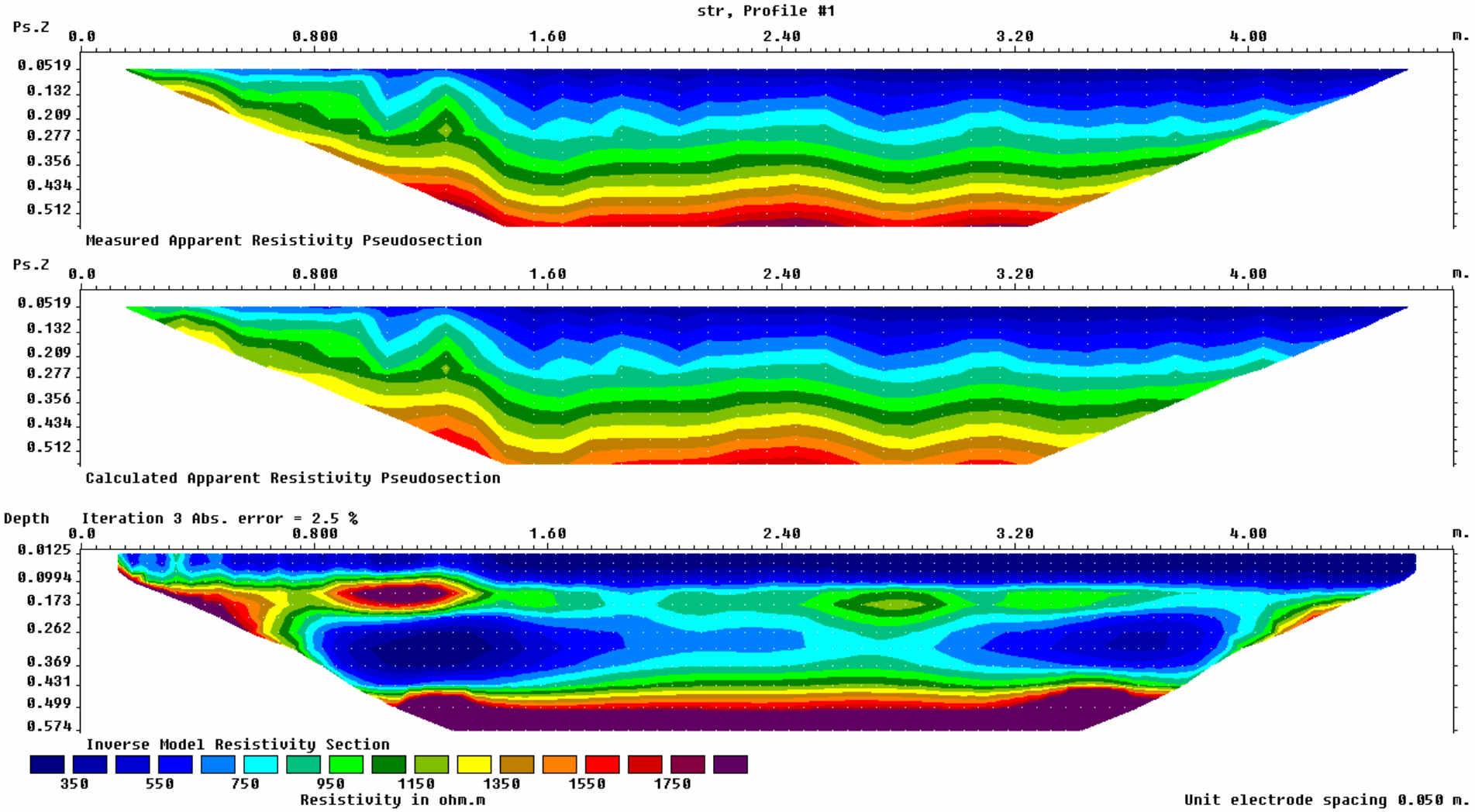

Electrical Resistivity Survey Image "04_18" (18.04.08)

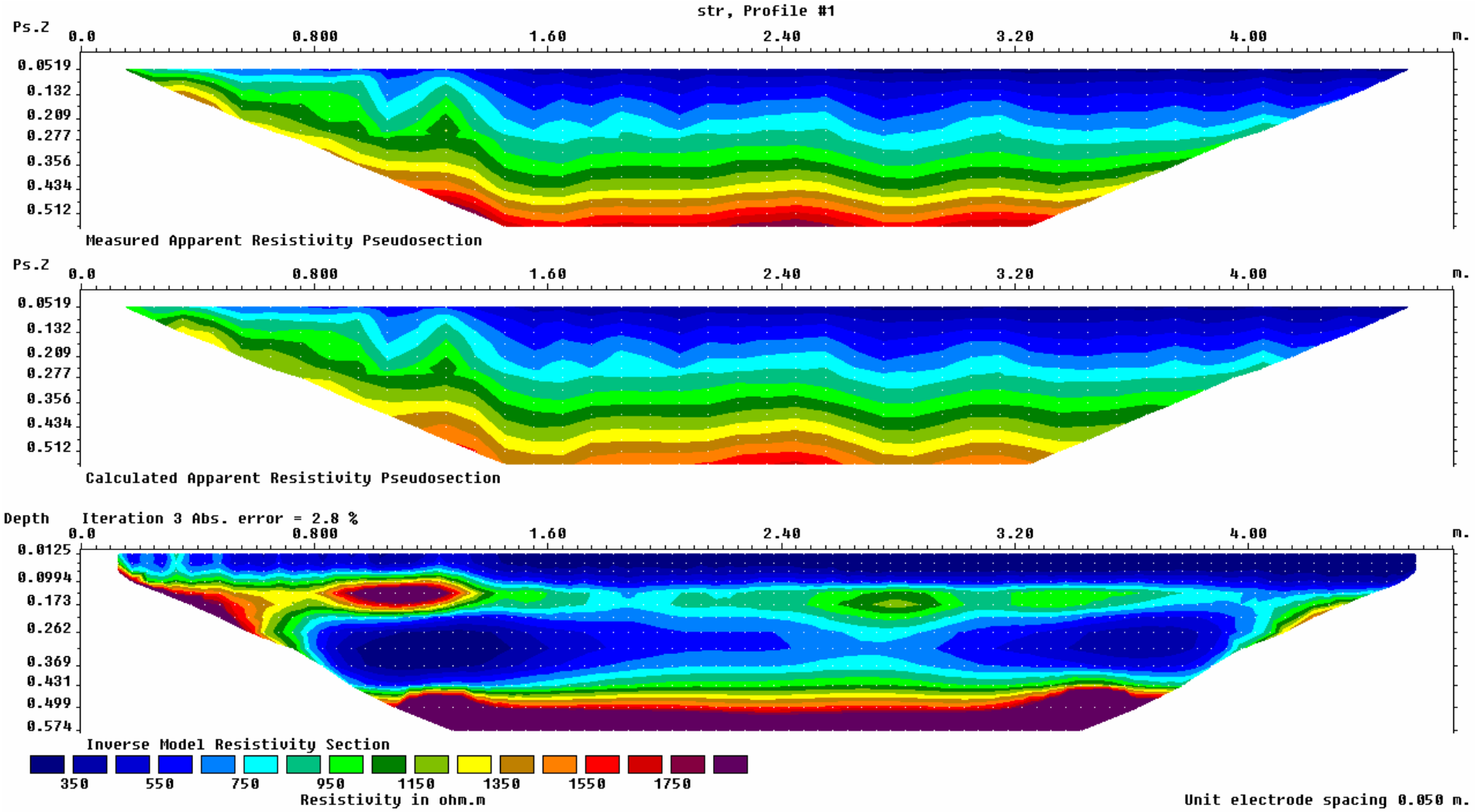

Electrical Resistivity Survey Image "04_25" (25.04.08)

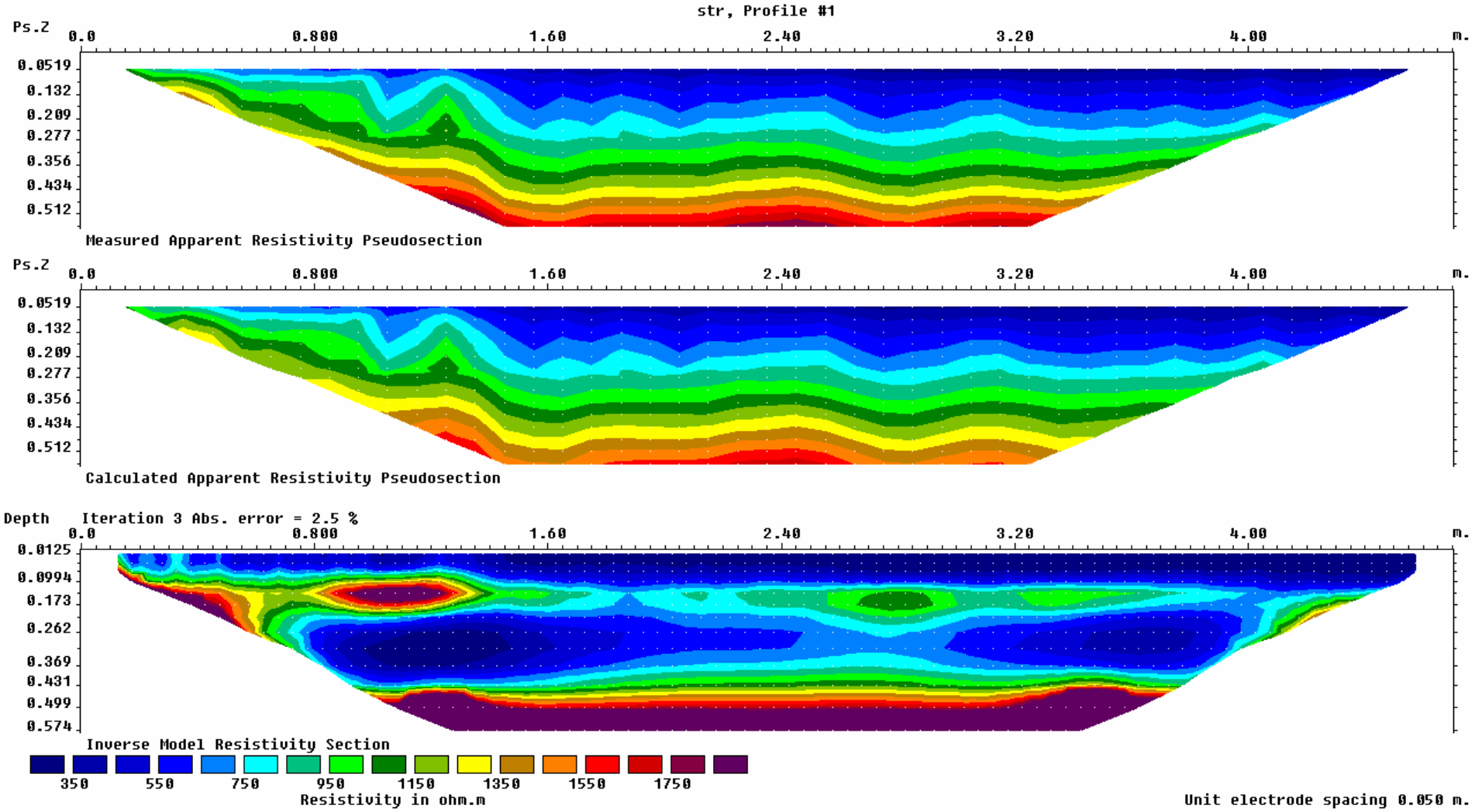

Electrical Resistivity Survey Image "05_02" (02.05.08)

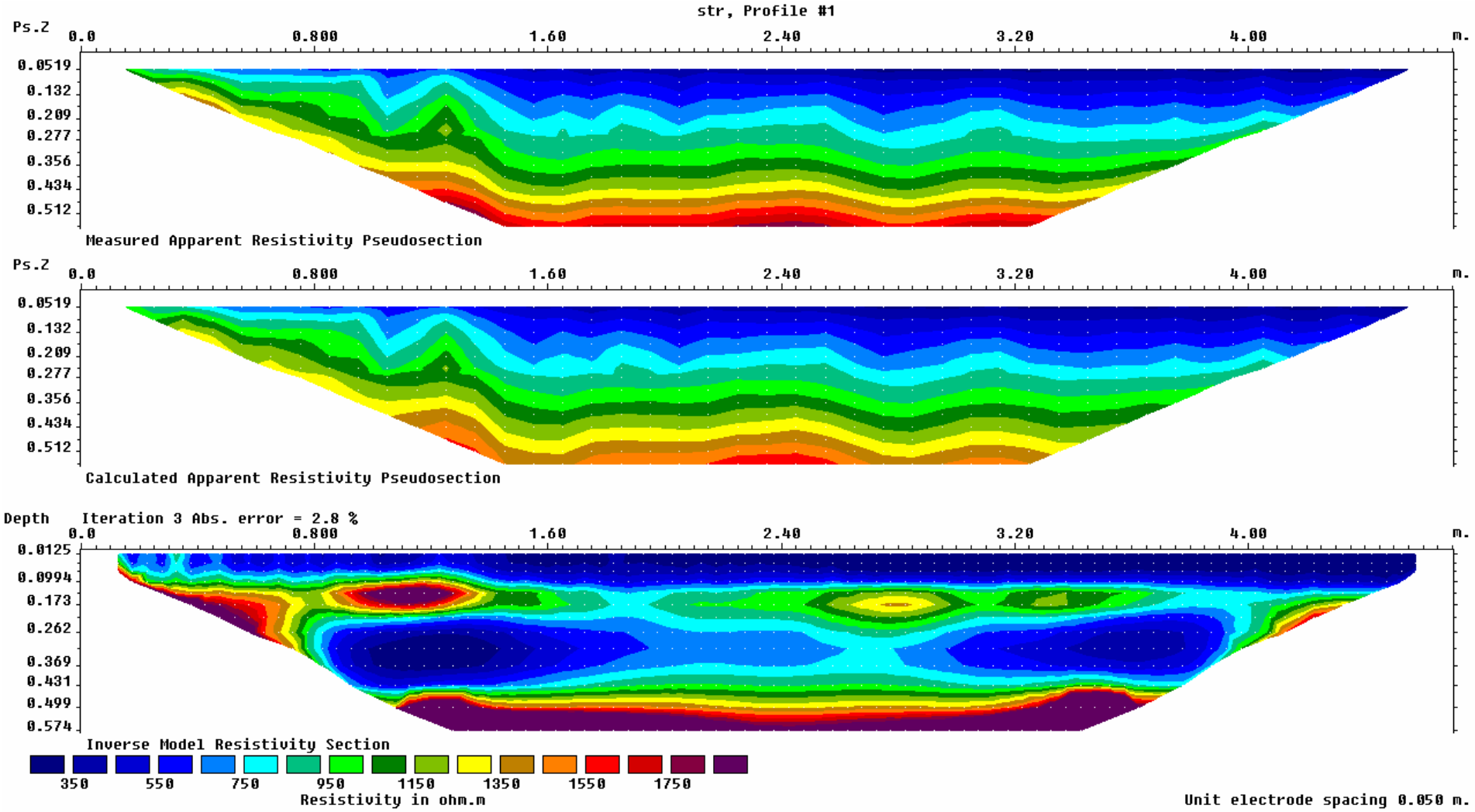

Electrical Resistivity Survey Image "05_09" (09.05.08)

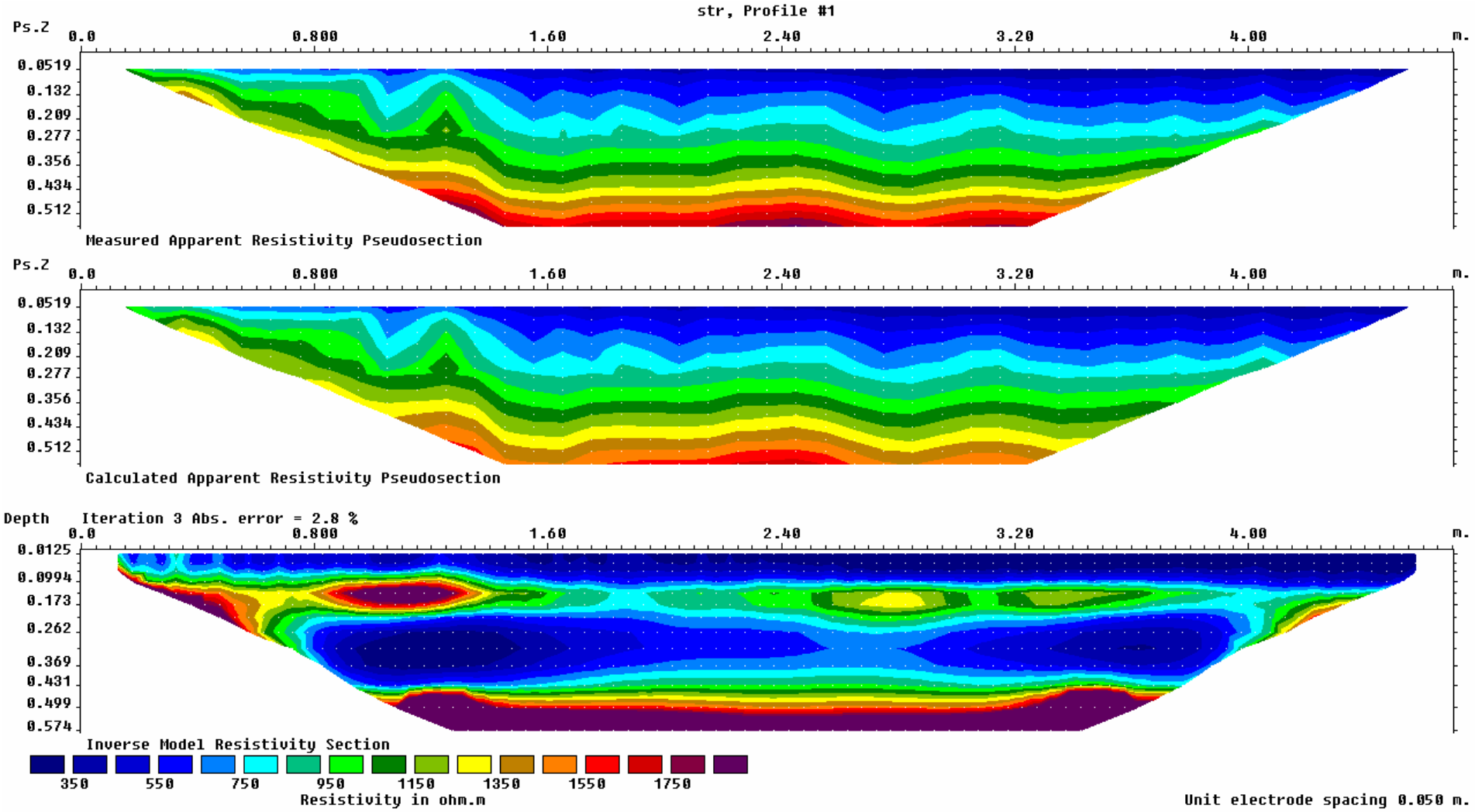

Electrical Resistivity Survey Image "05_16" (16.05.08)

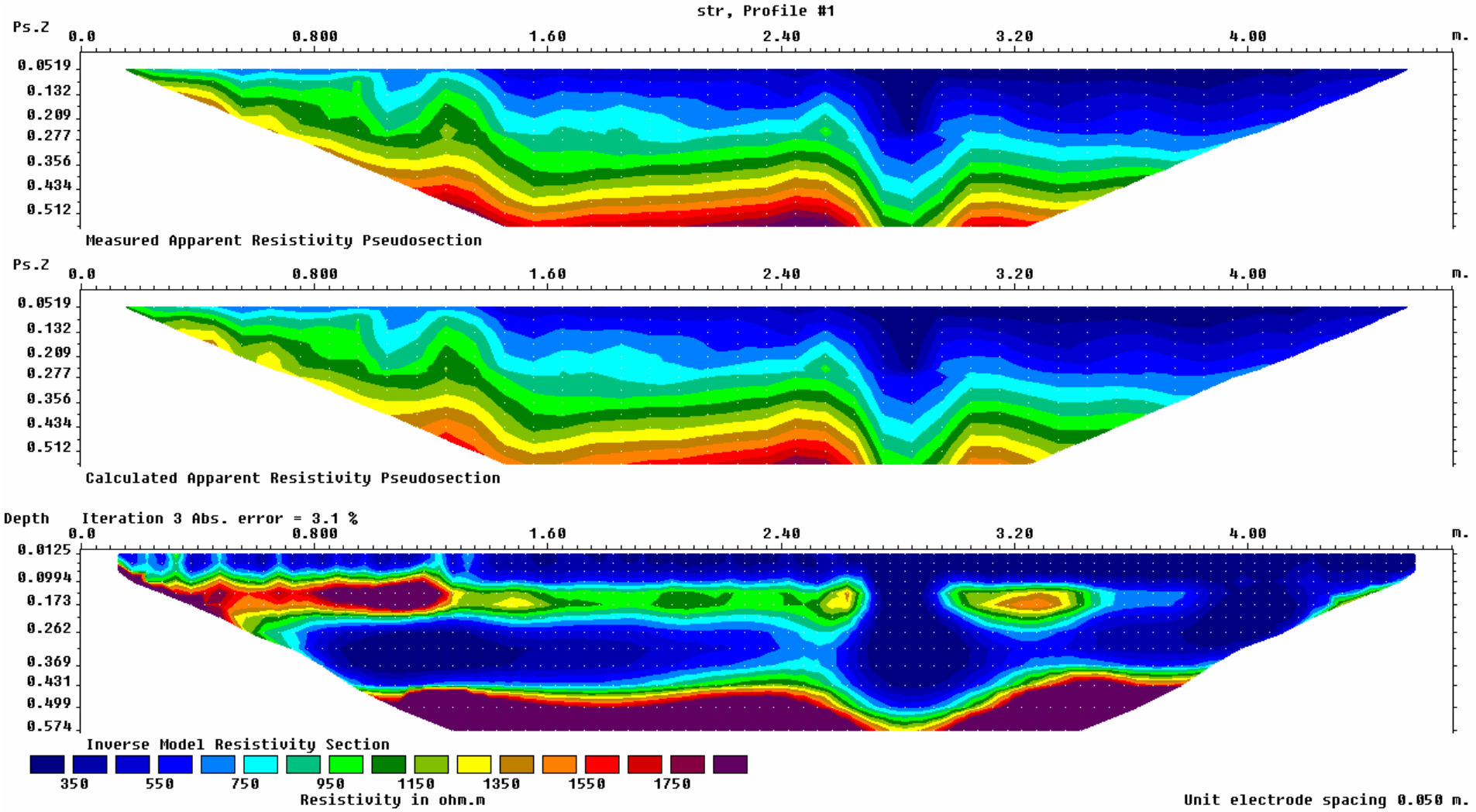

Electrical Resistivity Survey Image "05_26" (26.05.08)

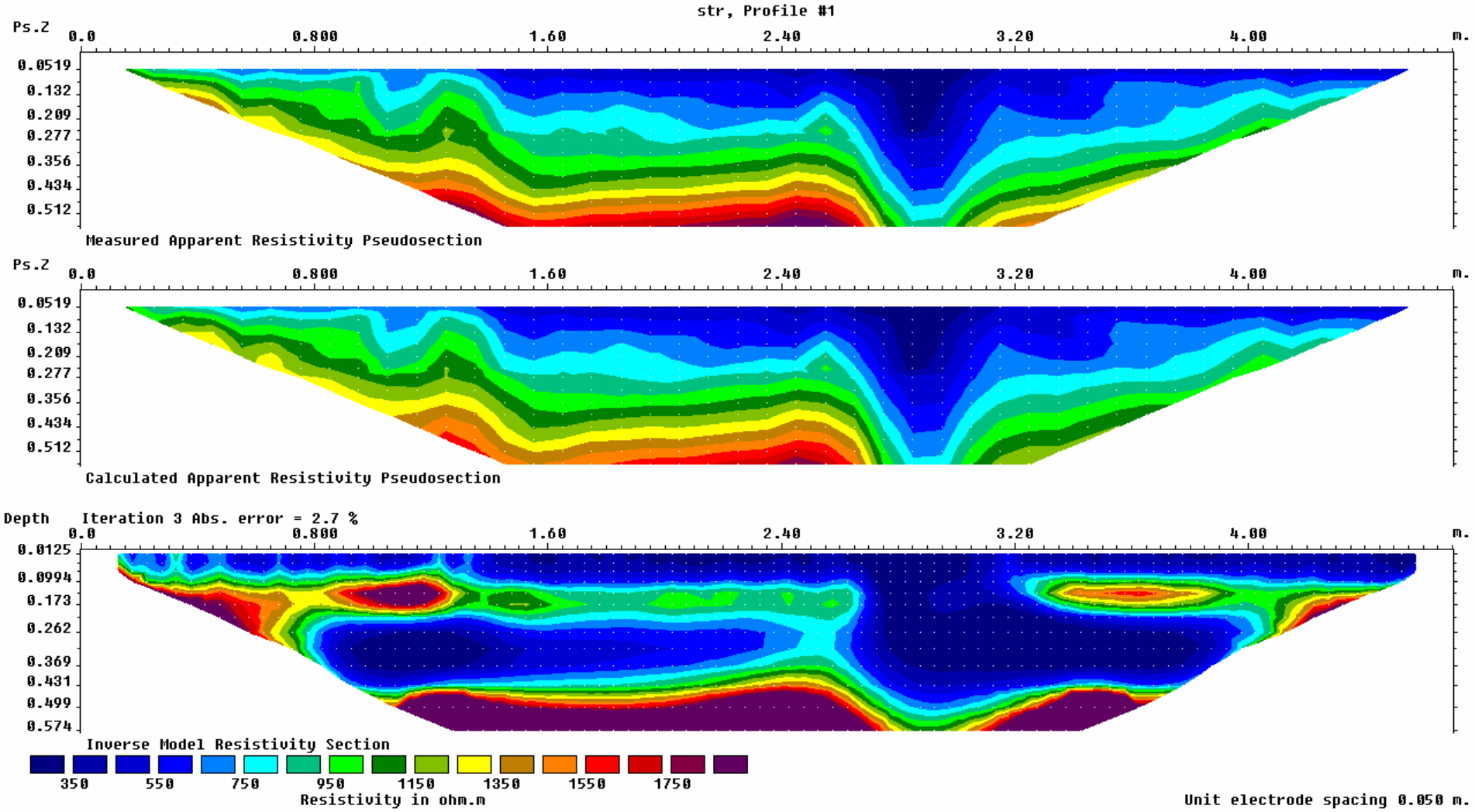

Electrical Resistivity Survey Image "05_30" (30.05.08)

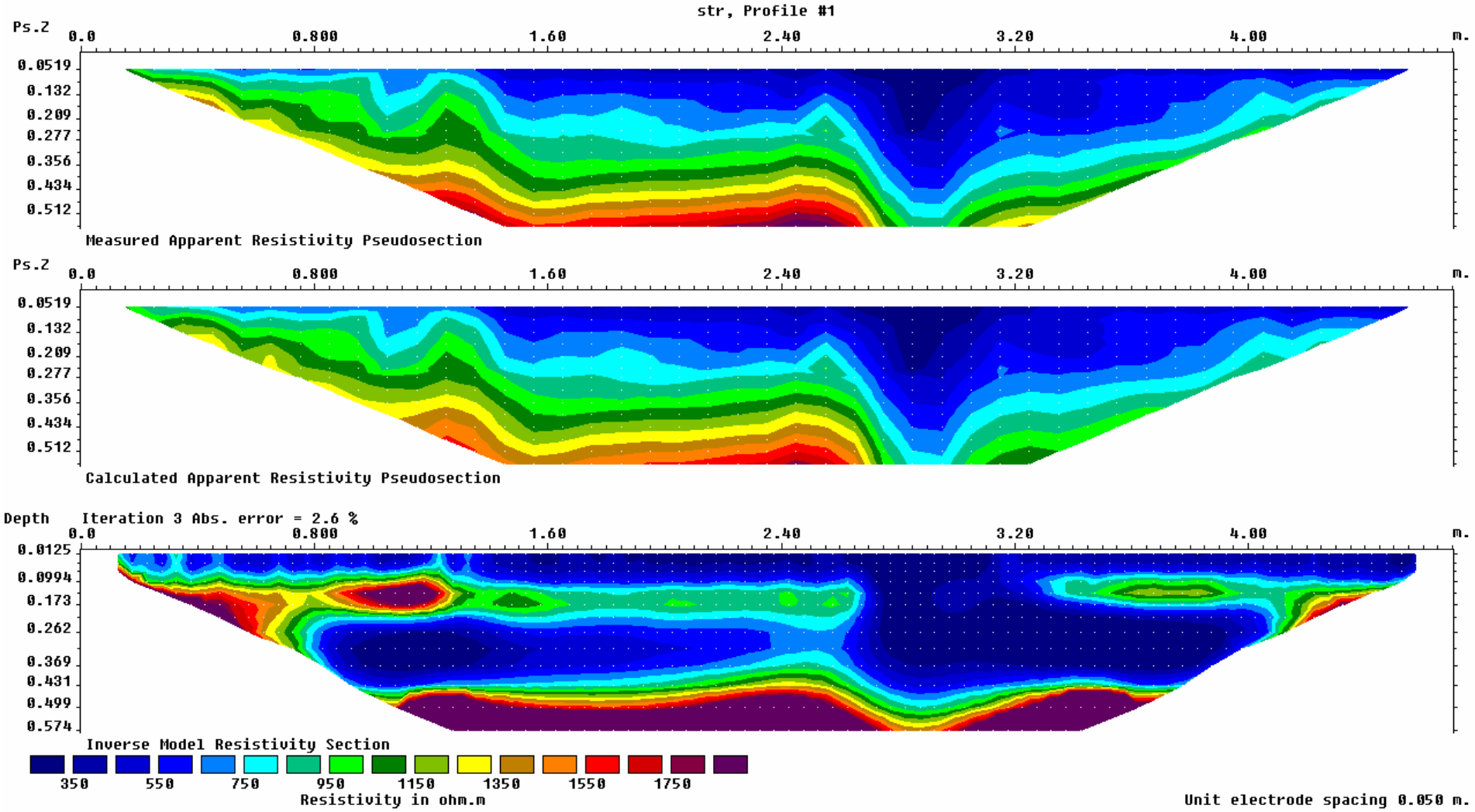

Electrical Resistivity Survey Image "06_06" (06.06.08)

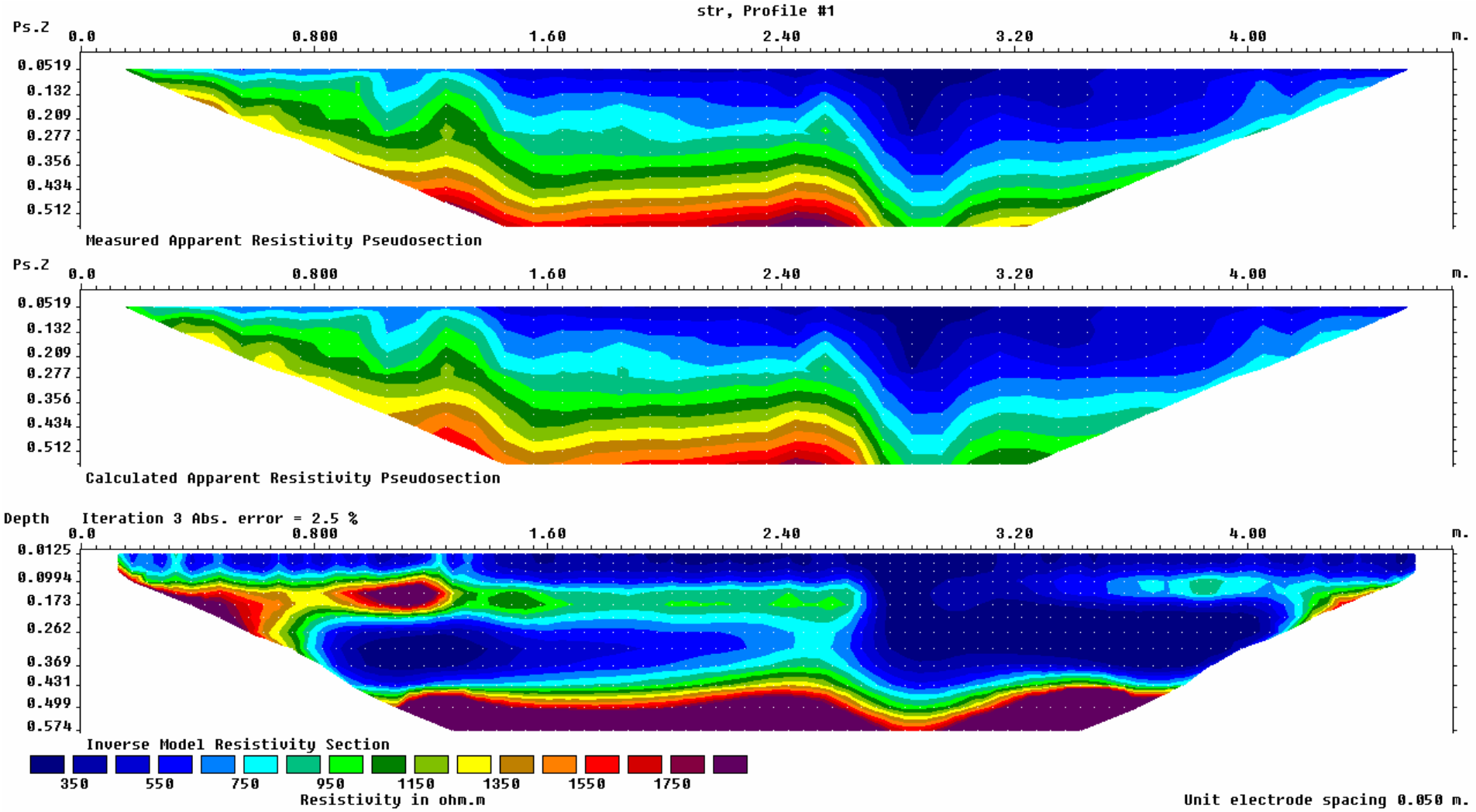

Electrical Resistivity Survey Image "06_13" (13.06.08)

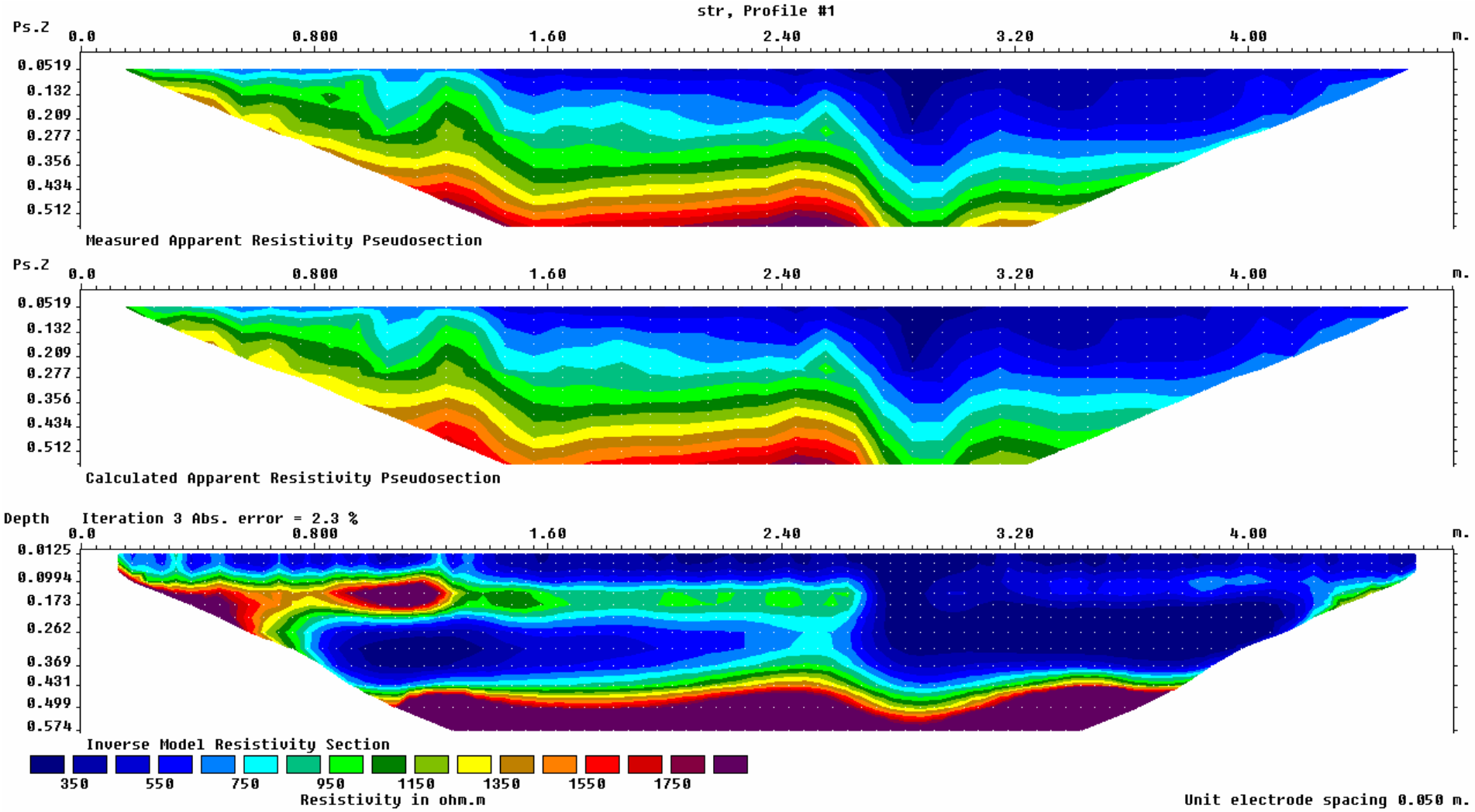

Electrical Resistivity Survey Image "06_20" (20.06.08)

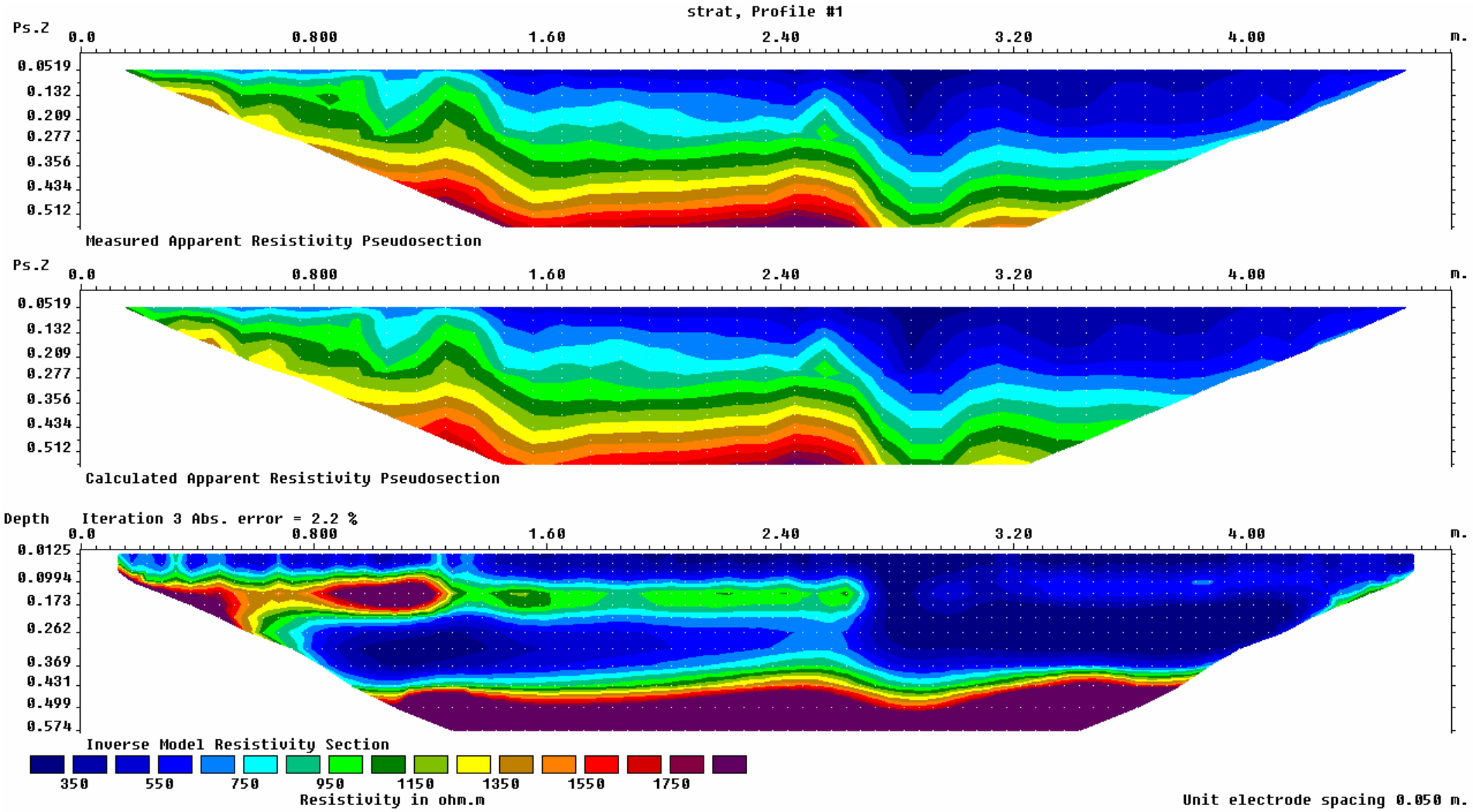

Electrical Resistivity Survey Image "06_27" (27.06.08)